UNIVERSITY OF EXETER
COLLEGE OF ENGINEERING, MATHEMATICS AND PHYSICAL SCIENCES

Noble Metal Nanoparticle Constructs for Applications in Cancer Diagnosis and Treatment

THESIS FOR THE DEGREE OF DOCTOR OF PHILOSOPHY IN PHYSICS

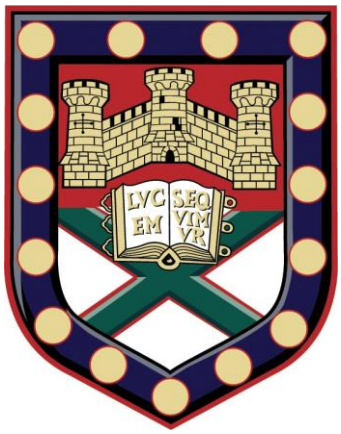

Author:

Fahad Mubarak M Aldosari

Supervisors:

Prof. Francesca Palombo

Prof. Nick Stone

Submitted by Fahad Mubarak M Aldosari, to the University of Exeter as a thesis for the degree of Doctor of Philosophy in Physics, March 2022.

23rd March, 2022 *F. M. M. Aldosari*

ABSTRACT

The deadly nature of cancer and its rising prevalence globally have attracted plentiful studies. Non-invasive means of diagnosing and treating cancer have been among the top area of study. These methods have demonstrated high potential to excellently replace conventional approaches such as surgical excision and medical procedures such as chemotherapy, radiation therapy, or their combination. In addition to invasiveness, these methods solve the inability to remove all cancerous cells during surgery and inoperability related to adjacency to critical tissue structures. Among the non-invasive approaches, thermal medicine (including both diagnostics and therapeutics) has demonstrated promising advantages over conventional approaches owing to its simplicity, and potential applicability to tumours surrounded by vital human organs/regions that are not accessible using the conventional approaches. Nowadays, the deployment of gold-based nanostructures in photothermal therapy (PTT) is increasingly attracting and considered amongst the great achievements for cancer thermal medicine. Furthermore, investigation of novel biodegradable gold nanoparticles (AuNPs) is greatly desired especially for renal clearance, off-target toxicity, biocompatibility and high surface-enhanced Raman spectroscopy (SERS) signals.

This project is aimed at developing biodegradable noble metal nanoconstructs based on hybrid AuNPs and lipid templates (liposomes or lipid vesicles) with added SERS activity and PTT capability. Specifically, the work focuses on the optimisation of the AuNP fabrication according to contemporary protocols, assessment of the NP suitability for SERS application to cell samples, addition of specific ligands to the NP constructs for the investigation of SERS activity and validation of the NP's response to PTT as the strategic way to achieve diagnosis and therapy within the same platform.

To study the effectiveness and potential of AuNPs and liposomes, this project employed a range of experimental techniques including Raman spectroscopy to study the structure, function and chemical composition of the gold nanoparticles (such as nanospheres and nanorods) and liposomes. The results from the synthesised AuNPs demonstrated the strongest SERS signals for *80 nm AuNPs* with biphenyl-4-thiol (BPT) labelling, followed by *60 nm AuNPs* labelled with 4-acetamidothiophenol (4-AATP). Also, the potential of liposome-encapsulated AuNPs for SERS and PTT applications was revealed under different considerations. Analytical techniques such as Transmission Electron Microscopy (TEM), PTT, Dynamic Light Scattering (DLS), UV-visible

spectroscopy and stimulated Raman scattering (SRS) imaging were applied for the characterization of the novel nanohybrids in the context of cancer detection and treatment. The results of different protocols of nanohybrid synthesis revealed low toxicity for the 90-200 nm-sized unilamellar vesicle (ULV) based nanohybrids with small, 5 nm spherical AuNPs. The light-heat conversion efficiency of *5nm AuNPs+BPT+CTAB+liposome* was also investigated by measuring their temperature rise over time during exposure to 808 nm laser radiation. According to our results, the *5nm AuNPs+BPT+CTAB+liposome* constructs exhibits greater temperature increase over time, with an increase in PTT efficiency of 175.52% when compared with *5 nm AuNPs*.

Additionally, the Raman spectral analysis of *5nm AuNPs+BPT+CTAB+liposome* constructs revealed the disappearance of two peaks at 1278 cm^{-1} and 1586 cm^{-1} due to the addition of CTAB, while largest enhanced factor was recorded at 1080 cm^{-1} for *5nm AuNPs+BPT+CTAB+liposome* ($8 \cdot 10^5$ counts) which can be effective for the diagnosis and treatment of cancer in the future.

In another development, the potential application of liposome-encapsulated gold nanorods (AuNRs) combined with SERS and PTT readouts was also investigated. Liposomes showed degradation above the membrane melting temperature (T_m) of around 42°C hence, following their integration in the nanoconstructs, they confer biodegradability by localized temperature increase above the T_m. Whilst small spherical AuNPs are difficult to arrange in larger constructs which exhibit plasmon resonance in the near-infrared (NIR) range, AuNRs have NIR absorption peaks that can be exploited in *AuNRs+CTAB+liposome* constructs with and without BPT labelling.

Overall, the research findings in this thesis will strengthen the development of novel Raman-labelled nanostructures for applications in nanotheranostics. The work will also open a way to the development of hybrid nanostructures for SERS-enabled diagnostics and laser-driven therapy using PTT. Finally, the cell disruption potential of gold nanostructures in non-invasive and biocompatible ways will be established.

DEDICATION

To my father: Mubarak,
my lovely mother: Fatimah,
my wife: Sarah,
my lovely children: Mubarak, Mohammad, Eyad, Amin, Yazan, Fatimah, and Bassam,
my brothers and sisters,
“This project is dedicated to all the lovely people in my life who have put their hopes, trust, blessings and assistance and enabled me to complete this project”

ACKNOWLEDGEMENTS

There are people who deserve my thanks for helping and supporting me throughout the completion of this thesis.

Firstly, my supervisor, Professor Francesca Palombo, who has unconditionally supported and encouraged me in every way possible throughout this difficult journey, deserves special thanks for making my PhD possible. Indeed, being able to work with this fantastic group of researchers makes me feel incredibly lucky. I would like to thank you, Professor Francesca Palombo, for spending so many hours teaching me how to think creatively and write logically. You also provided very effective advice whenever I needed. In addition, I would like to thank you for the weekly meetings with you, and also allowing to attend the weekly group meetings, and the RaNT monthly meetings which helped me develop my discussion skills, and provided us with news and updates on new research. Additionally, I wish to express my gratitude to my second supervisor, Professor Nick Stone, for his advice, support, and suggestions. Both Professor Francesca Palombo and Professor Nick Stone, I am truly grateful for your support in achieving future goals in my research journey.

Secondly, I want to give special thanks to Dr Marzieh Salimi for all her efforts to help me in hyperthermia experiments, to Dr Chun-Chin Wang for helping me in the SE-SRS measurements. It would have been impossible to attain this huge milestone without having adequate help from Dr Marzieh Salimi and Dr Chun-Chin Wang. They have helped me effortlessly in attempting to attain the objectives of this thesis.

Dr Christian Hacker (imaging specialist in the Bioimaging Centre, University of Exeter), your technical assistance with the TEM experiments via imaging of the biodegradable gold nanoconstructs and their evaluation has been an extraordinary impact to my work. I am truly appreciative to have your immense support and guidance through the course of this project.

I would praise Dr Hong Chang as well as she has become one of the main figures to connect and cooperate with during my PhD studies. Without her tremendous wealth of knowledge and practical support in the Imaging Suite, I could not have achieved several of my greatest achievements. Dr Ellen Green, you have been an exceptional colleague as well as a moral supporter. In my PhD programme, I greatly appreciated the teaching and advice you provided at the Biophysics Labs.

Dr Tanveer Tabish (University of Oxford) deserves special thanks and acknowledgment as he has been of great help to measure the *in vitro* cytotoxicity profile of nanohybrids against triple-negative

human breast cancer cell line during my PhD. The conversations we had while you were working at the University of Exeter about experimental details on this were extremely valuable, thank you in advance for your assistance. My doctoral work would not have been completed as swiftly and smoothly without your assistance.

Dr Ben Gardner, your help with the Raman labelling protocol has been important for me to publish my first manuscript titled “Characterization of Labeled Gold Nanoparticles for Surface-Enhanced Raman Scattering” in Molecules. I cannot express you with words how much I am grateful for your assistance. I am grateful to have benefitted from your support and knowledge through the course of this work.

Additionally, my gratitude goes out to all my colleagues who contributed greatly to my project, enabling me to achieve some of the most significant achievements throughout my PhD. I am thankful for the support I have received from several colleagues in the Biophysics Labs, Living Systems Institute Labs, Harrison Labs, and Geoffrey Pope Labs at the University of Exeter. You have been excellent friends and colleagues. I would want to express my gratitude for the enjoyable time we had working together and for assisting me with my research assignments. I am happy for the opportunity to share this wonderful endeavour with you. I believe that the findings from this study will contribute to the pool of empirical evidence.

Most importantly, my great parents are the inspiration and source of my happiness; for their support throughout my PhD programme over the past four years and their love for life; I am eternally grateful. In addition, I would like to thank my wife Sarah. Despite my best efforts, I could not have completed my research here without you. Thank you from the bottom of my heart. My children Mubarak, Mohammad, Eyad, Amin, Yazan, Fatimah and Bassam, you are the secret to my success and perseverance in life, all my love for you. You have kept me motivated and I have always looked up to you for strength and courage.

Finally, I acknowledge financial support from Prince Sattam Bin Abdulaziz University for granting me support across my studying. I also appreciated receiving funding from the UK Engineering and Physical Sciences Research Council (EPSRC), through the “Raman Nanotheranostics—RaNT” Programme Grant (EP/R020965/1; PI: Nick Stone).

PUBLICATIONS

F. M. Aldosari, "Characterization of Labeled Gold Nanoparticles for Surface-Enhanced Raman Scattering," *Molecules,* vol. 27, no. 3, p. 892, 2022.

F. M. Aldosari, A. M. Azzeer, and A. M. Hassib, "An Experimental Analysis to Assess Photo-Acoustic Techniques for Silver Nano-Particles; Considering Physical Properties," *J. Mater. Sci. Res.*, vol. 8, no. 1, pp. 17-24, 2019.

F. M. Aldosari, A. M. Azzeer, and A. M. Hassib, "Analyzing the Preparation and Properties of Silver Nanoparticles; A Photo-Acoustic Study," *Applied Physics Research,* vol. 10, no. 6, pp. 29-37, 2018.

F. M. Aldosari, A. M. Azzeer, and A. M. Hassib, "The Effects of Laser Energy, Repetition of Pulse Laser, Wavelength, and Temperature on Silver Nano-Particles," *Applied Physics Research,* vol. 10, no. 6, pp. 38-44, 2018.

F. M. Aldosari, A. M. Azzeer, and A. M. Hassib, "Optical and Photoacoustic Properties of Colloidal Silver Nanoparticles Solutions," *J. Mater. Sci. Res.*, vol. 7, no. 4, pp. 1-15, 2018.

Table of Contents

LIST OF FIGURES

LIST OF TABLES

LIST OF ABBREVIATIONS

2-NT	2-naphthalenethiol
4-AATP	4-acetamidothiophenol
4-MBA	4-mercaptobenzoic acid
4T1 cells	murine mammary carcinoma cell line from a BALB/cfC3H mouse
ACF	autocorrelation function
Ag	silver
$AgNO_3$	silver nitrate
AgNPs	silver nanoparticles
Au	gold
AuNPs	gold nanoparticles
AuNRs	gold nanorods
BPT	biphenyl-4-thiol
BF	bright field
CCD	charge-coupled device
CE	chemical enhancement
Chol	cholesterol
CO_2	carbon dioxide
CsCl	cesium chloride
CTAB	hexadecyltrimethylammonium bromide
CT	computed tomography
Cu	copper
DF	dark field
DG	diffraction grating
DLS	dynamic light scattering
DMPC	1, 2-dimyristoyl-sn-glycero-3-phosphocholine
DNA	deoxyribonucleic acid
DOP	dioleoylphosphatidylethanolamine
DPBS	Dulbecco's phosphate buffered saline
DSPC	1,2-distearoyl-sn-glycero-3-phosphocholine

EF enhancement factor

EM electromagnetic

EPR enhanced permeation and retention

ESA excited state absorption

FPM fluoroelastomer

FTIR Fourier Transform Infrared

Gg green glass

GCPQ N-palmitoyl-N-monomethyl-N,N-dimethyl-N,N,N-trimethyl-6-O-glycolchitosan

GSD ground state depletion

$HAuCl_4$ chloroauric acid

$HAuCl_4 \cdot 3H_2O$ chloroauric acid trihydrate

H&E hematoxylin and eosin

He-Ne helium-neon

IR infrared

LSPR localized surface plasmon resonance

LUV large unilamellar vesicles

MDA-MB 231 triple-negative human breast cancer cell line

MLV multilamellar vesicles

MRI magnetic resonance imaging

MSNRs mesoporous silica nanorods

MTT 3-(4,5-dimethylthiazol-2-yl)-2,5-diphenyl-2H-tetrazolium bromide assay

MUV massive unilamellar vesicles

MVV multivesicular vesicles

N nitrogen

$NaBH_4$ sodium borohydrate

NaCl sodium chloride

NBR nitrile rubber

Ne neon

NF notch filter

NIR near-infrared

NLO nonlinear Optical

NMR	nuclear magnetic resonance
NPs	nanoparticles
NTA	nanoparticle tracking analysis
NA	numerical aperture
OD	optical density
OLV	oligolamellar vesicles
PAMAM	poly amido amine
PBS	phosphate-buffered saline
PDT	photodynamic therapy
PE	phosphatidylethanolamine
PE	polyethylene
PEG	polyethylene glycol
PET	positron emission tomography
PP	polypropylene
PVC	polyvinyl chloride
PTT	photothermal therapy
PVDF	polyvinylidene fluoride
RNA	ribonucleic acid
RR	Raman reporter
RRMs	Raman reporter molecules
RRS	resonance Raman spectroscopy
R-SH	thiol group
S	sulfur
SAM	self-assembled monolayers
sCMOS	scientific complementary metal oxide semiconductor
SD	standard deviation
SEM	scanning electron microscopy
SERRS	surface-enhanced resonance Raman spectroscopy
SERS	surface-enhanced Raman spectroscopy
SF-TRU	spectral focusing - timing and recombination unit
SH	sulfhydryl

Si	silicon
SL	streamline lens
SORS	spatially offset Raman spectroscopy
SPR	surface plasmon resonance
SRS	stimulated Raman scattering
STEM	scanning transmission electron microscopy
SUV	small unilamellar vesicle
SWNT	single-walled carbon nanotube
TA	transient absorption
T_m	melting temperature
T cell	thymus-originated lymphocyte or T lymphocyte
TEM	transmission electron microscopy
TNBC	triple-negative breast cancer
TRS	transmission Raman spectroscopy
UV	ultraviolet
UV-vis	ultraviolet-visible
WHO	World Health Organization
XPS	x-ray photoelectron spectroscopy
XRD	x-ray diffraction
ZnS	zinc sulfide
ZnO	zinc oxide

CHAPTER 1
INTRODUCTION

1.1 Background

Cancer is the second leading cause of death worldwide after cardiovasculare diseases.[1] The estimated number of new cancer cases reported in 2021 was approximately 1.9 million.[2] Moreover, cancer is one of the most common health concerns, with an estimated 12 million cancer-related deaths annually by 2030.[3] In addition, as forecasted in the next two decades approximately 22 million people will be diagnosed with cancer. It is still one of the leading causes of mortality.[4] According to World Health Organization (WHO), in 2012 there were 14.1 million new cancer cases and about 32.6 million people diagnosed with cancer for over five years.[5] Standard diagnosis method for cancer is histopathologic assessment of biopsies or diagnostic excisions of suspicious tissue. The best way to regulate the rates of cancer is to detect it at early stages. The utilisation of nanomaterials is one approach for determining cancer at an early stage. In consideration of Nanotechnology, the implication of Raman spectroscopy can be implied. Raman spectroscopy combined with a specific nanomaterial is shown to be more effective in detection and mapping of cancer.[4]

Globally, about 1 in 6 deaths is due to cancer.[1] Despite the significant advancements made by researchers, funding agencies, and volunteers worldwide, our ageing population is driving the cancer incidence up. Hence, new strategies need to be developed going forward. An area of unmet clinical need is the early detection and diagnosis of cancers with poor prognosis, e.g breast, lung and oesophageal cancers. In general, the use of ionising radiation to detect cancer, such as in X-ray imaging, may overcome the problem. Raman nanotheranostics (also a research programme within our research group: RaNT EPSRC Programme Grant, PI: Prof. Nick Stone, EP/R020965/1) is a new paradigm in cancer diagnosis and therapeutics delivered through the use of nanostructured agents. Raman spectroscopy is a label-free molecular specific vibrational spectroscopy technique which, utlises safe levels of visible or near-infrared (NIR) radiation to illuminate a sample, provides a chemical “fingerprint” of the constituents. However, Raman signals from biomedical samples are notably weak for various reasons, primarily since the Raman effect (inelastic light scattering from molecular vibrations) is very inefficient and only interests a tiny fraction of the

overall scattered light from a sample. The aim of this thesis is to investigate the effectiveness of noble metal nanoparticles (NPs) in enhancing the Raman signal from biomolecules in the vicinity of their surface, using surface-enhanced Raman spectroscopy (SERS) for cancer diagnosis and treatment.[6]

The gold standard test is histopathology, a diagnostic test or benchmark used in medicine and statistics.[7] Histopathology is "the study of the signs of the disease using the microscopic examination of a biopsy or surgical specimen that is processed and fixed onto glass slides." Tissues need to be removed (biopsy), then sectioned and stained with one or more dyes to be seen under a microscope.
Hematoxylin stains cell nuclei blue and eosin blemish cytoplasm and connective tissue pink. Hematoxylin and eosin (H&E) staining is used by pathologists to make an analysis base on morphological patterns in the tissue section.[8] Histopathology's high effectiveness is the reason why it remains a gold standard in diagnosing diseases such as cancer.[9]

Nanotechnology has extended and occupied almost all the industries in electronics, construction, agriculture, and medicine.[10] Nanoscience is the study of phenomena and manipulation of materials at atomic, molecular, and macromolecular scales, where properties differ significantly from those at a larger scale.[11] SERS is based around active surfaces engineered by nanofabrication or synthesis of metallic NPs, where the presence of a plasmon absorption resonance at the wavelength of incident light generates many orders of magnitude enhancement in the electric field in close proximity to the surface.[12] SERS molecular tags (agents) typically intensify the heterogeneity and regular maturity of the background and significantly improves the Raman scattering, which is beneficial in investigating the Raman fingerprint regions in a wide variety of samples.[13, 14] Over the past few decades, SERS agents have received huge attention owing to their abilities to enhance Raman signals. The schematic diagram of a targeted NPs containing a SERS tag is shown in Figure 1.1.[15] The presence of Raman reporter molecules also provide the gold nanoparticle (AuNP) with a stable capping layer.[16, 17]

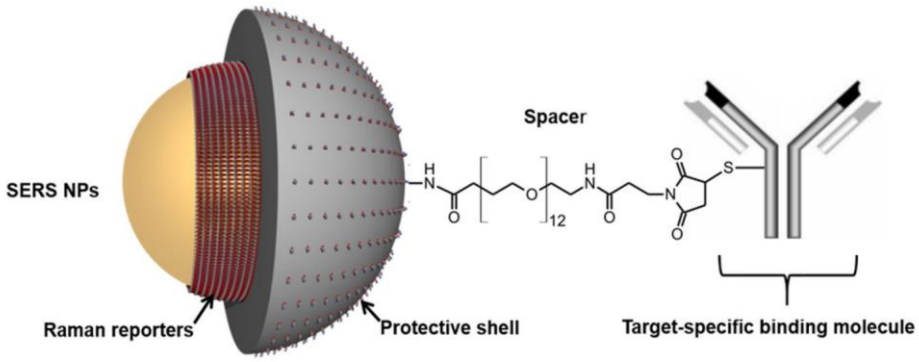

Figure 1.1 Targeted spherical NP (yellow). The Raman reporter molecular layer is shown in red; the passivating coating layer is coloured in grey; oligoethylene glycol is the secondary polymer coating, and the Y-shaped portion is an antibody targeting moiety for active target identification.[15]

1.2 Thesis aims and objectives

This thesis is aimed to develop biodegradable noble metal NP constructs based on AuNPs and liposomes (or lipid vesicles) with added SERS activity and photothermal therapy (PTT) capability to kill cancer cells. This study focused on novel gold nanoconstructs for targeted plasmonic applications in Raman nanotheranostics. The major disease focus is cancer. Therefore, three objectives lay the foundation to this thesis.

The first objective of the research is to optimise the NP constructs accordingly to current protocols. This will enable to expand the NP constructs which are produced and tested using a set of analytical techniques including Raman spectroscopy.

The second objective is to assess the NP suitability for SERS application to cell samples. The SERS effect will be assessed in NP-treated cancer cell lines.

The third objective is to validate the NP response to PTT. The PTT will be validated in solution and in cancer models.

1.2.1 Thesis outline

Chapter 1 discusses the background, introduction to key concepts, as well as aims and objectives of this research work. Chapter 2 provides an overview of literature review including principles and applications of techniques, essentially Raman and PTT. Chapter 3 deals with the detailed description of materials, chemicals, reagents and techniques used. The following three chapters, Chapter 4, Chapter 5, and Chapter 6 are result and discussion chapters, each focusing on a distinct experimental approach. Chapter 4 presents results and characterisation of labelled commercial AuNPs for SERS. The results of this chapter have been published in a Molecules paper. Chapter 5 presents results of AuNP-liposome nanohybrids for SERS and PTT. Chapter 6 shows results of AuNR-liposome nanohybrids for SERS and PTT. Finally, Chapter 7 provides conclusions which cover the whole thesis and a brief description of future perspectives.

CHAPTER 2
LITERATURE REVIEW

2.1 Raman spectroscopy

Raman scattering is a type of vibrational spectroscopy technique. Raman spectroscopy detects optical signals due to vibrational modes of molecules which are initiated by the interaction of light and matter. In addition, the Raman spectroscopy technique challenges the current gold standard when it comes to diagnostics. Each molecule has a unique Raman spectral profile (like a 'chemical' fingerprint) since the vibrational modes are characteristic of its structure and composition. A Raman spectrum can give access to information such as the chemical composition, physical interactions, and concentration of molecules inside the material that is being observed.[12]

Over the years Raman spectroscopy has become increasingly popular due to numerous technical advances.[18] Raman spectroscopy uses laser light to activate the molecular vibrations which then scatter the photons as shown in Figure 2.1. Much more intense than Raman scattering is Rayleigh scattering, which is elastic in that there is no exchange in energy between the photon and the molecule.

In Raman scattering, which is inelastic and hence involves the exchange of energy between photon and molecule, the two possibilities are Stokes and anti-Stokes Raman scattering. The molecule either earns energy (which leads to Stokes Raman scattering) or loses energy (which leads to anti-Stokes Raman scattering) to the scattered photon. This shift in energy (vibrational transition energy) is peculiar of each oscillator, i.e. molecular vibration, and it is called Raman shift.

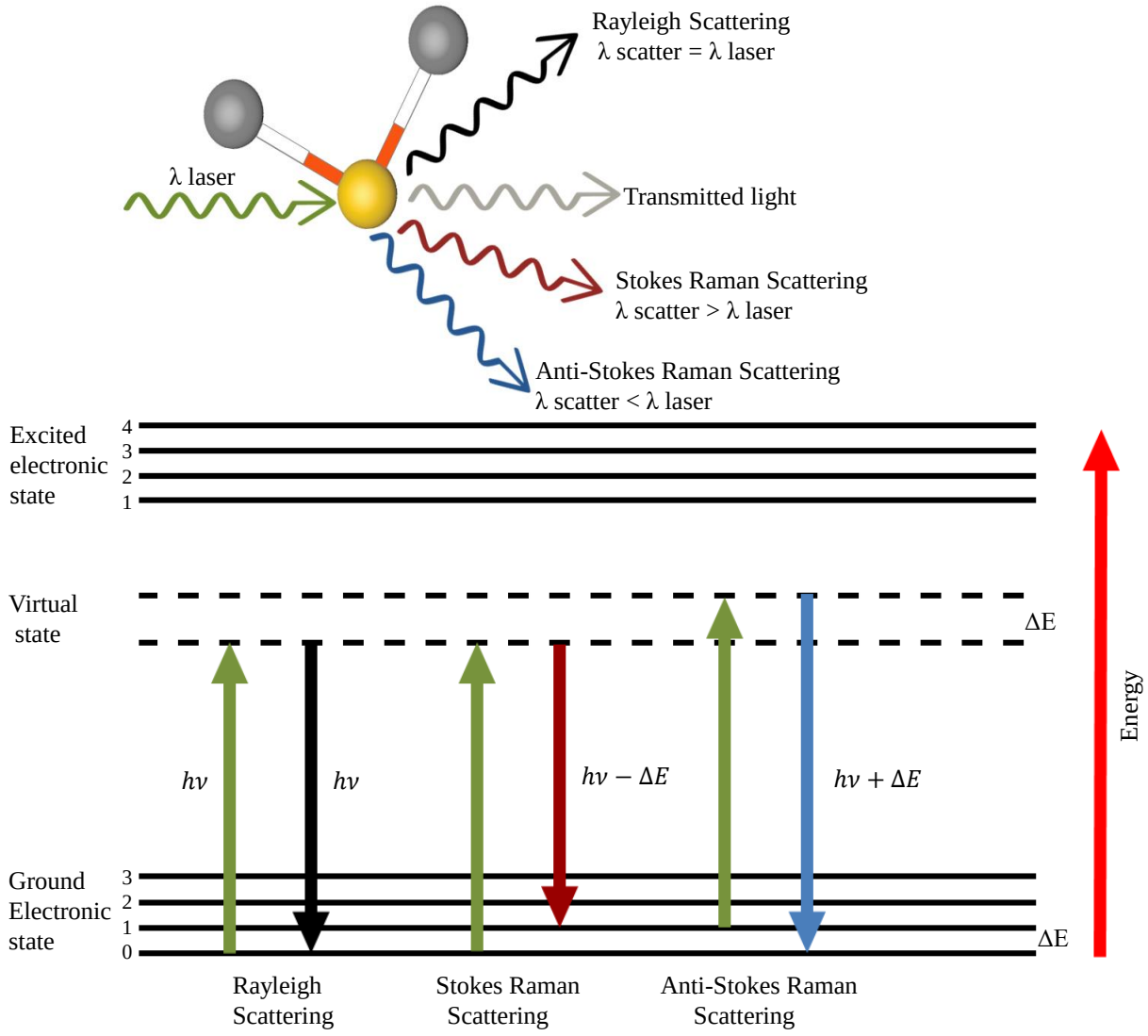

Figure 2.1 Interactions of molecule and laser light with scattering: Rayleigh scattering and Raman scattering.

The common application of Raman spectroscopy for cell analysis is by the use of a Raman spectrometer combined with a confocal microscope.[19] Additionally, Raman spectroscopy is a good candidate for monitoring the effects of different anticancer drugs on cell viability.

2.2 Nanoparticles

Nanotechnology is pervasive in today's life.[20] Artificial nanoparticles are applied in a variety of areas, including disease diagnostics, drug formulations, therapeutic interventions, catalysis, and ecological remediation.[21] Nanoparticles can be categorised based on their size, chemical and physical properties, as well as morphology. Typical examples are carbon-based nanoparticles, metallic nanoparticles, lipid-based nanoparticles, ceramic nanoparticles, and polymeric nanoparticles.

Nanoparticles can be classified as organic and inorganic nanoparticles; the first include dendrimers, liposomes, polymeric nanoparticles, while the latter include fullerenes, quantum dots and noble metal (e.g. gold) nanoparticles.[22] Soft structures such as liposomes, vesicles, and nanodroplets are also nanoparticles. Hard nanoparticles are made of gold, silica dioxide, and titanium dioxide.[23] Gold NP based sensors can detect metal ions by the principle of colour change upon aggregation of gold nanoparticles, a method which is widely used for the analysis of many metals and non-metals including copper, mercury, lead and arsenic in water.[24]

The physical properties of NPs are very important characteristics; for example, NPs are very mobile when they are in a free state (e.g. monodispersed colloidal solution). NPs have specific surface properties, e.g. surface charge, roughness, and morphology. The melting point for AuNPs is lower than for bulk gold, i.e. 300-400°C vs 1064°C, due to surface melting. Bulk gold is inert, however AuNPs are competent catalysts in mild conditions.[25] Optical properties of AuNPs are different from their bulk counterpart. Bulk gold is yellow due to electrons moving so fast that they exhibit relativistic contraction; instead, gold colloidal solutions appear red.

2.2.1 Noble metal nanoparticles

Noble metal nanoparticles with homogeneity in dimension, shape, and surface properties have prospective functions for biomedical diagnosis and therapy.[26] Gold and silver as noble metal nanoparticles demonstrate a diversity of biomedical applications in the field of medical diagnosis, drug and genetic materials delivery, photothermal therapy (PTT), and photodynamic therapy (PDT). Numerous methods are used to prepare the nanoparticles, ranging from grinding, laser ablation and photochemical reduction, through to vapour deposition, thermal decomposition, chemical reduction, coprecipitation, and hydrolysis.

Silver NPs present an electrical conductivity of 10^5 S.cm^{-1} and high operational stability.[27] These NPs can be used for direct printing on a variety of substrates, flexography, including glass, using screen printing; gravure offset lithography, and ink-jet printing.

NPs have been used in nonlinear optics applications, owing to their peculiar optical properties connected with the SPR. Noble metal nanoparticles, such as gold and silver NPs, have been recognised to present improved nonlinear optical (NLO) property and ultrafast reaction times. Their NLO properties have similarly been extensively measured using picosecond and femtosecond lasers.[28] Surface-induced belongings make them a perfect option for bioinorganic hybrid nanostructures in biomedicine and tissue engineering research. AuNPs have good biocompatibility and chemical inertness along with their tunable quantum size.

Although the properties of metallic nanoparticles have not been widely exploited, they have been used in the medical area in the form of nanoconjugates since 1971.[29] Presently, metallic nanoparticles are used in many biomedical applications, such as probes in scanning electron microscopy (SEM) for tracing drug or biological agent distribution (transport and delivery systems for proteins, peptides, DNA, etc.), and for diagnosis and targeted therapies.[22]

Because of surface effects and the dramatic changes in properties of metal clusters in comparison to their bulk counterparts, metal clusters have unique properties (e.g. plasmon absorption, near-IR photoluminescence, superparamagnetism, etc.). The embedding of nanoscopic metal structures into polymeric matrices represents the simplest way to protect metal clusters and take advantage of their physical characteristics.

It has been shown that the use of nanostructure silver materials enhances the inhibitory capacity, likely because nanostructure materials have a high surface area. Embedding of nano-sized metals into biodegradable polymer matrices represents a solution to these stabilisation problems and permits a controlled antibacterial effect.

AuNPs can be obtained by the reduction of chloroauric acid ($HAuCl_4$) by sodium citrate. The reducing agent serves also as a passivating ligand, coating the surface of the nanoparticles. Nanoparticles and their properties are shown in Figure 2.2. Noble metals are widely regarded as non-toxic to humans; in fact, silver nanoparticles are popular for their antibacterial properties.[30, 31]

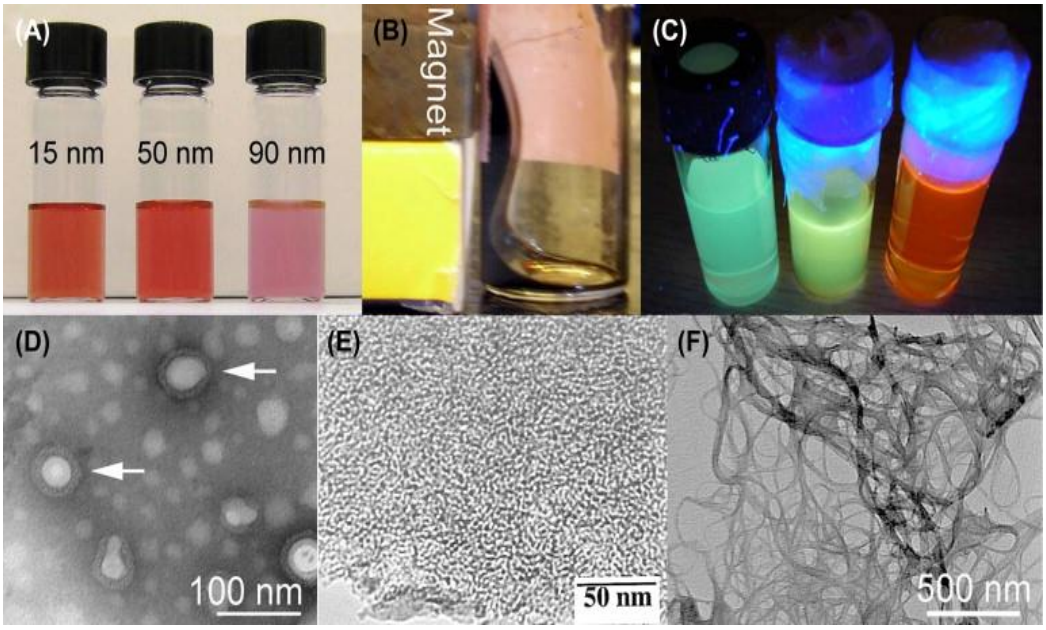

Figure 2.2 Nanoparticles and their properties: (A) gold nanoparticle colloidal solutions experience a colour change with increasing NP size; (B) magnetic nanoparticles are attracted to magnets; (C) quantum dots fluoresce under UV excitation; (D) antibody-conjugated micelles (arrows) are shown in negative TEM (transmission electron microscopy) staining; (E) mesoporous silica containing multiple nanosized pores; (F) TEM image of single-walled carbon nanotubes.[32]

The physical dimension or size is known to have an impact on electronic, thermodynamic, structural, spectroscopic, electromagnetic, biological and chemical properties of nanomaterials; a smaller particle size accounts for a reduced number of free electrons, increased surface area, and quantum confinement effect.[33, 34] Additionally, the size also affects the melting and absorption properties of nanomaterials such as ZnS and ZnO. Furthermore, the semiconductor nanocrystals are in essence zero-dimensional quantum dots in which the spatial allocation of the induced electron-hole pairs is limited within a small volume, which is important to enhance the non-linear optical properties.[35, 36]

Nanoparticles have a lower melting point because the reduced coordination number of the surface atoms greatly increases the surface energy which enables the atom diffusion to occur at relatively lower temperatures. Therefore, as the nanoparticle size decreases, their melting point decrease as well.[37] Researchers are drawn to the effect that surface modification of nanoparticles has on

targeting tumours.[38-40] In addition, it has been found that various surface charges and sizes of AuNPs influence cancer cell migration.[41] Localized surface plasmon resonance (LSPR) of noble metal NPs can enhance light absorption within a specific region which is dependent on size, shape, and separation of the NPs.[42, 43] Additionally the size and shape of the NPs have been known to have a large impact upon the LSPR position, as shown in Figure 2.3.[44] LSPR for branched or nanorod gold shows at approximately 620 nm and 880 nm, respectively. The LSPR of spherical AgNPs appears at 400 nm, while the LSPR of spherical AuNPs is at 520 nm.

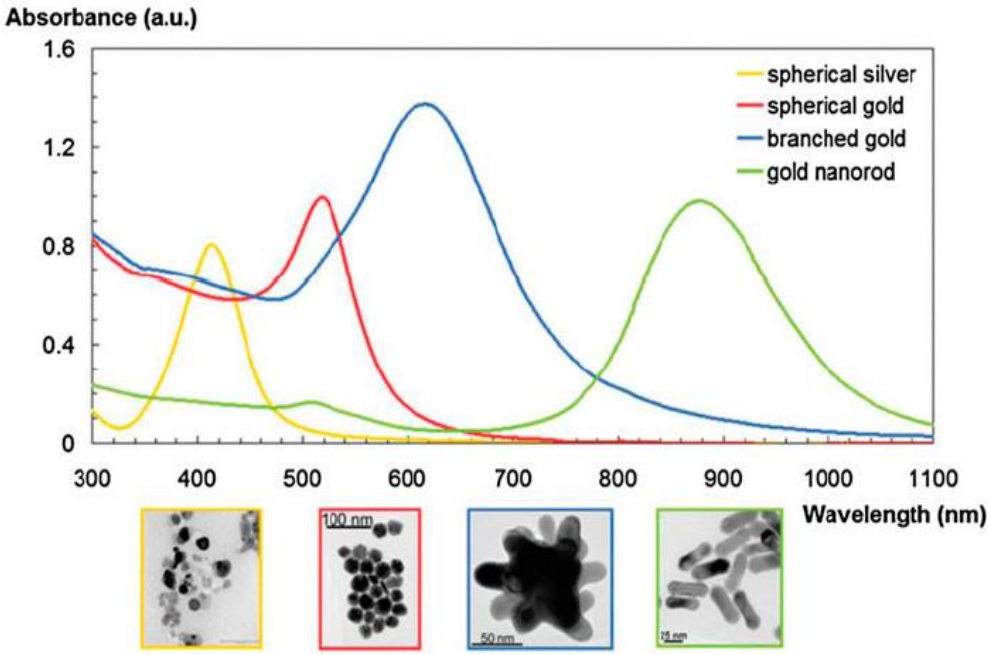

Figure 2.3 Ag and Au NP size and shape determine the LSPR position.[44]

2.2.2 Gold nanorods

Gold nanorods (AuNRs) have been found to be highly effective in various biomedical applications. However, AuNR manufacturing often needs to further purify from the synthesis contaminated cationic surfactant, i.e. cetyltrimethylammonium bromide (CTAB). Such procedures need to be further refined for the purification of AuNRs for their *in vivo* investigations.[45] In our method, having the AuNPs (or nanorods) internalised inside the liposome (with CTAB on the NP surface) effectively shields and reduced the cytotoxicity of the nanoconstructs.

With the help of AuNPs having a particular shape or size, cancer can be treated. They can absorb NIR light, therefore enhancing the Raman signal for increased cancer identification, and convert it to localised heat aimed at cancer ablation. The usage of different AuNRs has become one of the most prominent and broadly used platforms for the creation of new optical imaging methods because of their compact size, facile synthesis and different optical properties.

A few years back, a significant development was made in the nanotheranostics field.[46] Still, the main translational and biological challenge towards nanotheranostics sets a novel model in cancer.[47] The tunable band of SPR from AuNRs permits their optical extinction to be used to match the irradiation wavelength of common NIR lasers employed in therapy and optical imaging.[48] Additionally, their optical absorption permits photothermal conversion that expedites triggered drug release, laser welding, and photothermal therapy.[49] Using different arrangement mesoporous silica nanorods (MSNRs), such nanocarrier will aid in medicine transfer pathway by excellent medicine filling capability or improved cell death efficacy. Versatile nanocomposite by incorporating photothermal and photodynamic agents, along with *in-vivo* imaging (which is two-in-one system) has huge potential to attain anti-cancer optimal therapeutic efficacies. *In vivo* imaging is the type of system which is non-invasive visualisation concerning living organisms for diagnostic and research purposes.[50] Mainly, this technique can be bifurcated into two different areas comprising molecular imaging and morphological imaging based on the different applications used in suitable scenarios. However, different sorts of NPs have recently been analysed to identify the *in vivo* transfer of hereditary constituents.[51] Thus, manufactured gold nanoplexes of different layers via constructing layer over layer of poly-L-lysine and nucleic acid based on electrostatic contact allow sluggish, steady discharge of beneficial genes. The poly amido amine (PAMAM) are also utilised to transfer genes using their great solubility in aqueous solution, clear and distinct form and size, and plenty of primary amino groups on the upper area.

2.3 Raman reporter molecules (RRM)

AuNPs are capable of enhancing the Raman signal from molecules in the vicinity of the NP surface. Typically, SERS nanotags are constructed by immobilising strong Raman active molecules with a large Raman cross-section on the surface of the NPs. Therefore, the sensitivity of the assay utilising the nanotags will depend on the signal intensity generated by the RRMs.

Typical molecules used as RRM are chemisorbed on the NP surface, e.g. through Au–S bond between gold and a thiol group in the reporter, and the large Raman cross-section derives from one or more aromatic groups. Novel Raman reporter molecules are being synthesised to maximise the functional abilities of the RRM: their ability to form self-assembled monolayers improves the Raman signal intensity, and biocompatibility for *in vivo* imaging applications. Self-assembled monolayers (SAM) are densely packed molecular layers that maximise the number of molecules close to the metal surface and thus the SERS signal generated by localised surface plasmon resonance. The aptitude to form SAMs contributes largely to the intensity and reproducibility of the SERS signal. SAM also enables to achieve better molecular orientation and uniform distance of the reporter group to the metal surface. The RRMs are being added to the NPs mainly to enhance their operational capabilities. The thiol-gold chemistry is a simple and versatile route to surface modification; thiophenols, with a thiol group linked to a benzene ring, are small and symmetric molecules that are easily identifiable with only a few characteristic Raman bands. One of the most dependable molecules shown to form self-assembled monolayers is thiophenols.

2.4 Liposomes

Liposomes were introduced in 1965 and were originally used as a model for the study of biological membranes. [52] A liposome is a spherical-shaped vesicle that is composed of one or more phospholipid bilayers. The lipid bilayer closely resembles the structure of a cell membrane.[53] The capability of liposomes to encapsulate hydrophilic or lipophilic drugs has allowed these vesicles to become useful drug delivery systems. Both Moderna and Pfizer COVID-19 vaccines use lipid nanoparticles (liposomes) as drug delivery system.[54, 55] These seem to significantly accumulate within solid tumours by the enhanced permeation and retention (EPR). Liposomes can also form biocompatible and degradable templates for small nanoparticles to assemble within the bilayer, inside their cavity, or on their external surface. The application of liposomes also supports the NP response to PTT in order to fulfill the aim of this study.

2.4.1 Membrane phospholipids

Liposomes, similarly to cell membranes, are typically composed of a phospholipid bilayer. Phospholipids are classified as amphipathic molecules as a result of the presence of both hydrophilic and hydrophobic groups. As shown in Figure 2.4, each phospholipid contains a hydrophilic (i.e. “water-loving”) head group and a lipophilic (i.e. “fat-loving”) tail, which is composed of a long hydrocarbon chain that repels water but attracts other hydrocarbon chains via hydrophobic interaction. The lipophilic tails are repelled by water and hence form a surface, whilst the hydrophilic head groups are oriented towards the aqueous environment. Within a single cell, one layer of the head groups faces the exterior of the cell, whereas another layer of polar head groups faces the internal cellular environment. It has been known that understanding the cellular environment is very important for the properties of the membrane.

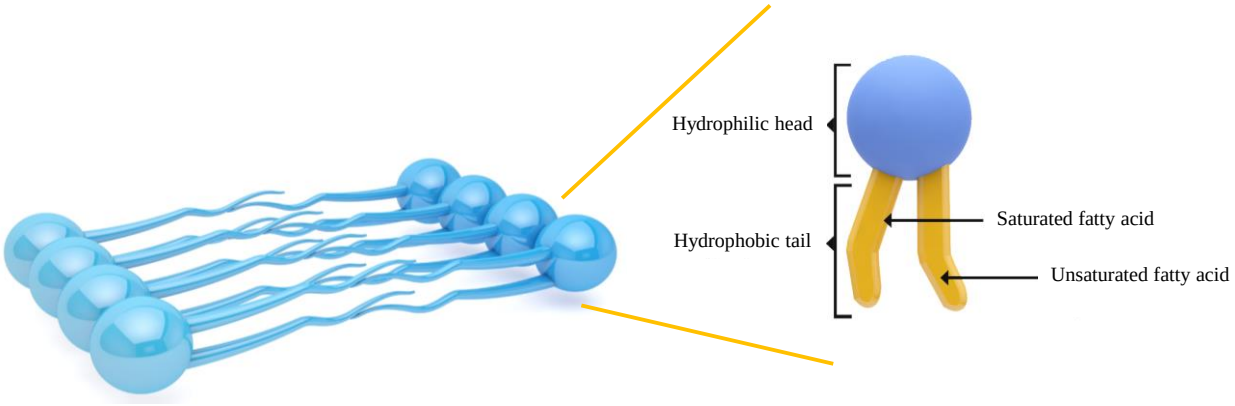

Figure 2.4 Structure of the phospholipid bilayer.

2.4.2 Composition of liposomes

The liposome contains a core of aqueous solution trapped by one or more bilayers. The phospholipid bilayers of a liposome can originate from natural sources, which are biologically inert, and exhibit minimal inherent toxicity. Liposomes are formed by naturally-derived phospholipids with mixed lipid chains, such as egg phosphatidylethanolamine (PE) or dioleoylphosphatidylethanolamine (DOP). There are two main classifications for the phospholipids, one is sphingomyelins and the other is glycerophospholipids. Mainly, the phospholipids of eukaryotic cells are glycerophospholipids, in which glycerol is considered as a backbone.

Previous studies have shown that electrical and physical stimuli can be used as a trigger (e.g. pH, temperature, enzymes, or light).[43-47] The release mechanism is mainly based on controlling the destruction of the lipid pair at the weakest points through stimulation, which will alter the liposome properties. On the other hand, various types of phospholipids such as "1, 2-dimyristoyl-sn-glycero-3-phosphocholine (DMPC) (14:0)" and "1,2-distearoyl-sn-glycero-3-phosphocholine (DSPC) (18:0)", play a vital role for the manufacturing of liposomes. Every lipid has a special phase transition temperature (or melting temperature, T_m). When the temperutre is below T_m, the lipid bilayer will be in regular and uniform arrangement, whilst, if the temperature is above T_m, the lipid bilayer will be in disordered phase, as shown in Figure 2.5. Therefore, at T_m, the lipid structure will change from solid gel phase to liquid phase. The use of DSPC for liposome manufacturing provides more feasibility in comparison with DMPC because the phase transition temperature for DSPC is around 42-43 °C,[56, 57] hence higher than physiological temperature, whereas for DMPC is lower (~23 °C).[58] Furthermore, the longer-chain lipids have higher stability and longer efficiency of the encapsulation as compared to the short-chain lipids. Therefore, liposomes containing DSPC show higher stability and stress over a relatively wide temperature range.

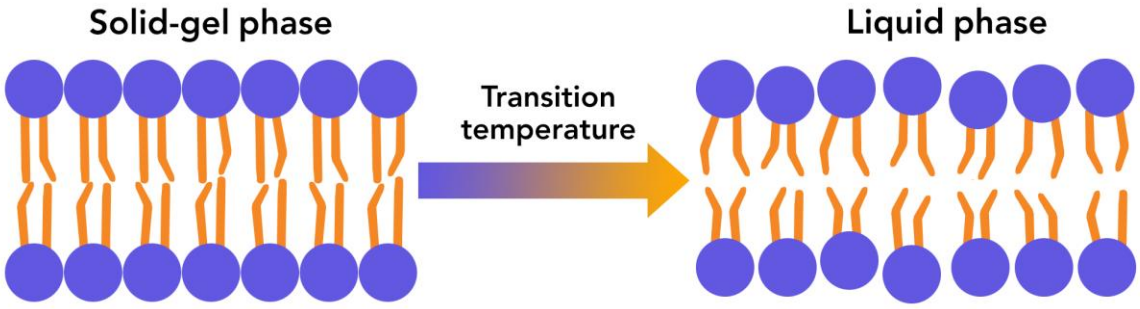

Figure 2.5 Diagram of lipid phase transition at the melting temperature T_m: (a) solid gel phase, and (b) liquid phase.

Cholesterol is found in animal cell membranes, within the so-called membrane rafts, where it enhances constancy and reduces membrane fluidity and permeability to some solutes. The low toxicity, biodegradability, and immunogenicity of lipids make liposomes as important carriers in new drug delivery systems. In addition, liposomes are dynamic and tuneable, so different

structures and T_m can be obtained depending on the membrane composition. The superiority of liposomal nanoparticles as nano-carriers of therapeutic molecules including phytochemicals has led to extensive research on their formulation, modification, stability, and pharmacokinetics. Liposomes are also biodegradable, non-immunogenic, fusogenic and are capable of encapsulating both hydrophilic and lipophilic phytochemicals.[59] The chemical and physical stability of liposomes is affected by many factors and so the efficiency of drug penetration.[60] Therefore, the stability of liposomes is essential for long-term circulation.

2.4.3 Classification of liposomes

The name liposome is derived from the Greek words 'lipos', meaning fat, and 'soma', meaning body. Liposomes can be classified as multilamellar vesicles or unilamellar vesicles. As shown in Figure 2.6, liposomes can be defined as small unilamellar vesicles (SUV, <100 nm), large unilamellar vesicles (LUV, 100-1000 nm), massive unilamellar vesicles (MUV, >1000 nm), oligolamellar vesicles (OLV, 100-500 nm), multilamellar vesicles (MLV, >500 nm), and multivesicular vesicles (MVV, >1000 nm).[61-64]

Both the size and number of bilayers present within the liposome play a role in determining the drug encapsulation volume of liposomes. Liposomes can vary in size from 25 nm up to 2.5 μm.[65] The structure of phospholipid liposomes greatly affects the long-term stability of drug-containing capacity of the liposome. Based on this, the current study has focused on the design and development of biocompatible noble metallic NP constructs based on AuNPs and liposomes (or lipid vesicles) functionalised with Raman tags with potential applications in photothermal therapy.

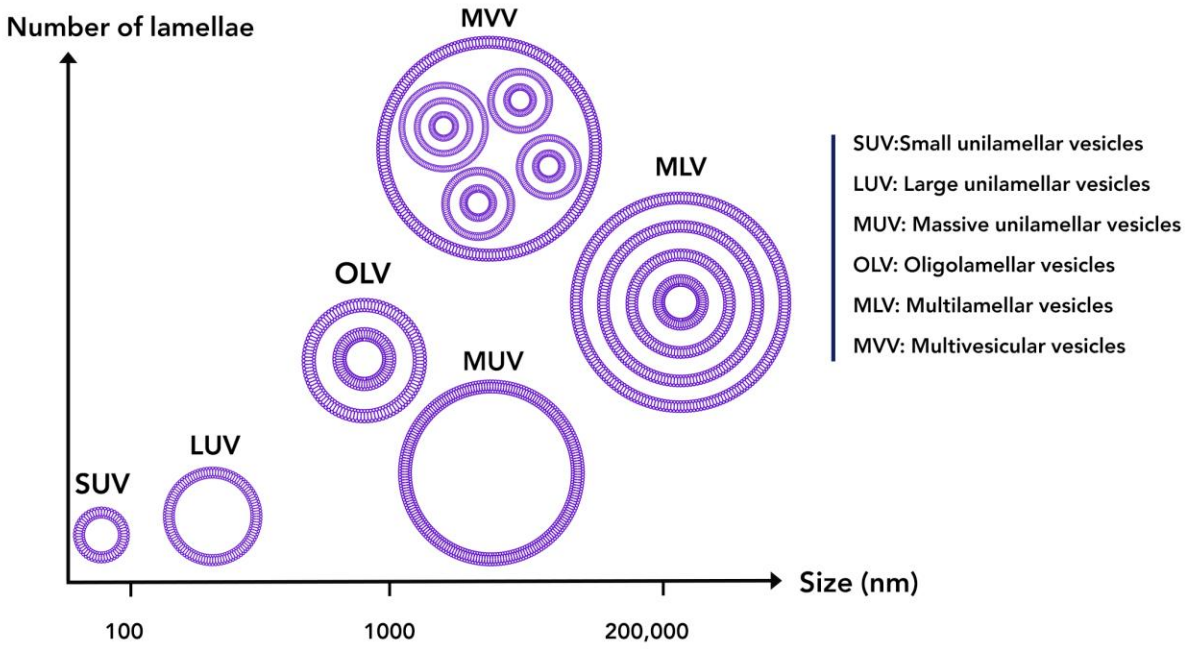

Figure 2.6 Liposome's classification based on size and number of lamellae.

2.5 Surface-enhanced Raman scattering/spectroscopy (SERS)

Surface-enhanced Raman scattering (SERS) combines molecular fingerprint specificity with potential single-molecule sensitivity. SERS also offers high sensitivity for small structural changes in macromolecules, noninvasive sampling capability, minimum sample preparation and high spatial resolution. SERS consists of enhanced Raman signal from molecules in the vicinity of an active metal surface and as such it offers much compensation over other spectroscopic or spectrometric techniques such as Fourier Transform Infrared (FTIR) spectroscopy, NIR absorption, UV-visible (UV-vis) absorption, fluorescence, NMR, X-ray diffraction (XRD), X-ray photoelectron spectroscopy (XPS), and mass spectrometry.[50]

SERS is an attractive tool for sensing molecules in trace amounts within the field of chemical and biochemical analytics. The benefit of SERS includes the ability to extract a significant quantity of scattering directly from complex environments such as biological fluids, living tissues, and cells without any need for prior sample preparation.

2.5.1 Historical background

Increase in Raman intensity is attributed to strong electromagnetic fields induced by excitation of surface plasmon polaritons (SPP) on nanoscale noble metal structures (Au, Ag and Cu) at wavelengths occurring in the visible spectrum. The anomalously enhanced intensity is not attributed to the increased surface area, but due to new phenomena giving rise to the concept of SERS cross-section.

In 1974, Fleischmann et al. discovered anomalously large enhancement of Raman intensity for pyridine molecule adsorbed onto a roughened silver electrode and later it was termed as surface-enhanced Raman scattering.[18] Then the magnitude of the induced molecular dipole is increased, and therefore, the intensity of the inelastically scattered photons increases and greatly enhances the Raman scattering efficiency.[66]

The energy produced due to the enhanced electromagnetic field is transferred to the molecules located near the surface of the nanostructures. To enhance the Raman signal, the molecule must typically be adsorbed on the metal surface, or at least be very close to it (typically ≤10 nm). The electromagnetic model is not the only effect that accounts for all of the SERS activity, the contribution from molecular resonances and charge transfer processes can also contribute to Raman enhancement.

The discovery of SERS has widened the applications of Raman spectroscopy for molecular identification and detection at very low concentrations. This offers a unique capability for the label-free detection and identification of a variety of analytes. An analyte is a substance whose chemical constituents are being recognized and calculated. The dominant effect in SERS is due to the sole property of metal nanostructures and is termed the electromagnetic (EM) enhancement effect. Raman signal enhancement in SERS spans several orders of magnitude as compared to normal spontaneous Raman scattering, hence enabling the detection limit to be reduced to a single-molecule level.

Applications of SERS for quantitative chemical analysis primarily depend on properties of metallic nanostructures with nanometre-scale precision and high reproducibility of Raman enhancement. All of them have an intense effect on the overall capability of the metal nanostructure to enhance the Raman scattering cross-section of molecules adsorbed or in the vicinity of the metal surface. Single-walled carbon nanotubes (SWNTs) are promising materials for *in vitro* and *in vivo*

biological applications, due to their high surface area and inherent NI photoluminescence and Raman scattering properties.[67]

The unique optical property that the metal surface can support is dependent on the size and geometry of the nanostructure, and the dielectric function of the material. Excitation is through the transfer of electrons from the metal to the molecule and back to the metal again. This chemical enhancement is also called charge-transfer enhancement and is less dominant as compared to EM enhancement. It is commonly accepted that the electromagnetic enhancement effect is the dominant factor.

There are two primary mechanisms for SERS enhancement: an EM enhancement and a chemical enhancement (CE). In the EM enhancement, the molecule is adsorbed onto or it is held close to the metal surface, and interaction between the molecule and the surface plasmons occurs. In the case of CE, the molecule is adsorbed and chemically bound to the metal surface, although this effect is much less SERS enhancing than the EM effect.

2.5.2 Mechanisms of surface-enhanced Raman scattering

Mechanisms of surface-enhanced Raman scattering include a positive charge based on the metal side, still the electrons can extend further away from the metallic surface enabling lateral free movement. In addition, the electromagnetic field of a light source causes the electrons to oscillate as a group to the surface, generating the so-called plasmon, shown as a ripple in a sea of electrons in Figure 2.7. The nanoparticle's morphology and the electromagnetic field is intense at edges, leading to strong hot spots,[68] as shown in the nanorods in Figure 2.7(b).

This frequency depends on the excitation wavelength, the size and shape of nanometals, and nature of the surface. Besides, Raman scattering uses Ag and Au because their optimal frequency regions are within the visible and near-infrared ranges. In addition, the SERS arises from two major mechanisms: electromagnetic enhancement and chemical enhancement.[69, 70] Metallic surfaces of Ag and Au have electrons on the surface that arise from the conduction band which are held by positive charges (bare nuclei). Surface plasmons have a resonance frequency at which they absorb and scatter light efficiently.[19]

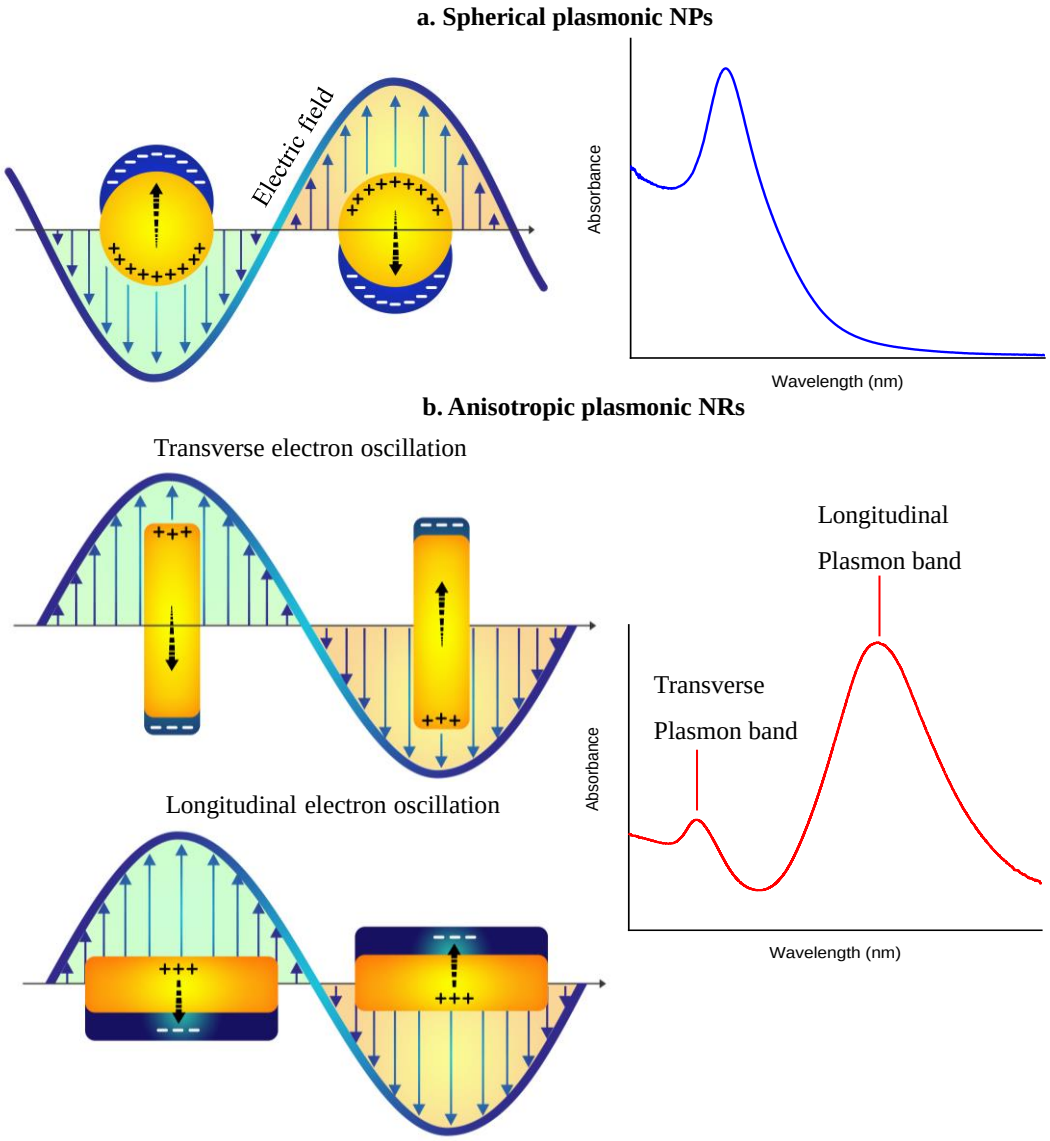

Figure 2.7 Localized Surface Plasmon Resonance for (a) nanoparticles and (b) nanorods in transverse and longitudinal plasmon bands corresponding to transverse and longitudinal electron oscillation.

The Electromagnetic Mechanism (EM) and the Chemical Mechanism (CM) are two mechanisms to describe the SERS effect generally. The EM is a result of the localized surface plasmon resonance of electric fields of the metal nanoparticles because of the surface plasmon excitation.[71, 72] Instead, the CM is regarded to be the consequence of the interaction between

the adsorbed molecules on the metal and the metal surface. This causes the formation of a charge-transfer intermediate state with strong electron coupling between the molecules and the metal surface.[73, 74]

2.5.3 Assembled nanostructures

Solution synthesis of dimers, despite complex, is intrinsically favoured to the lithographic approach because it can reach interparticle gap sizes of 1-2 nm, which are models for maximized signal enhancement. SERS tags can also be engineered to host hot spots at the intermetallic junctions between assembled nanoparticles. The crucial unit of assembly is the dimer. The plasmonic property of dimers has been studied in depth.[75] However, they have for long been out of reach synthetically, at least from the bottom-up. Further, the dimers are preferred for the synthesis of SERS tags because they provide a higher enhancement per particle compared to larger assemblies. As seen before, a single hot spot in a given aggregate will always dominate in terms of enhancement compared to all the others.[76]

The polyol method, in which the inorganic salts (e.g NaCl) are initially used to induce pre-aggregation of the as-made colloids, produces dimers with interparticle gaps of ∼1.8 nm and SERS EFs of $\sim 10^7$.[77] Besides, the dimers are smaller and can therefore be better taken up by targeted cells and tissues. Several approaches have been employed to synthesize dimers of Au nanoparticles in solution.

Further, the gradient centrifugation in CsCl then facilitates the isolation of a clean postponement of the dimers in which the AuNPs are functionalised with 2-naphthalene thiol and induced to aggregate by NaCl. This leads to the polymer-encapsulated and isolation via centrifugation, creating a mixture consisting of 71% monomers, 24% dimers, 3.5% trimers, and 0.5% tetramers.[78]

2.5.4 Biomedical imaging

SERS has been employed in biomedical applications, from protein sensing to DNA detection.[79] Additionally, SERS-based biomedical imaging has been demonstrated by combining traditional methods of Raman microscopy along with the strength and target selectivity of SERS tags. This

leads to SERS being a significant clinical tool to complement MRI, fluorescence imaging, or computed tomography. Indeed, SERS is not meant to replace these methods but to integrate them chiefly because it provides the single-cell sensitivity which most of its diagnostic counterpart's lack, thus promising to become the primary imaging tool for early disease detection or the determination of post-operative outcomes.

SERS imaging has been demonstrated in the literature for *in vitro*, *ex vivo* and *in vivo* applications.[80-82] SERS imaging has also been enabled by technological improvements in the instrumentation, which have lowered costs, increased automation, and reduced size, consequently enabling the first hand-held Raman microscope imaging studies to be carried out in animal models.[83] However, the clinical application of SERS tags is still in its infancy, and only a few examples have appeared for *in vivo* imaging. Nonetheless, this field is rapidly growing, and both *in vitro* cell studies and *ex vivo* tissue analyses have started appearing rather frequently in the literature. Moreover, *in vitro* imaging takes advantage of the SERS tags to recognise diseased cells of specific lineage by exploiting the occurrence of cell surface markers that are specific to the diseased cells.[80] Indeed, by functionalising the nanoparticles with a targeting moiety which has high affinity for the specific receptor, it is possible to successfully target the cell and image it employing a Raman microscope. In addition, it includes the spatial mapping of the peak concentration distribution of a selected vibrational band in the SERS spectrum. Many features of this approach are still being investigated, such as the role of affinity and greed in SERS tag binding to the cell membrane proteins, or the opportunity of rendering these capacities truly quantitative. Nonetheless, SERS imaging has produced some remarkable results, both for single and multiple marker objectives, and demonstrated that SERS tags can surpass fluorescent dyes in both resolution and brightness.[84]

2.5.5 Photothermal therapy (PTT)

The treatment of the tumours has been identified as an area of clinical need. PPT utilises thermal energy produced by light irradiation to kill the cancer cells. PTT is regarded as the effort to utilise electromagnetic radiation for the treatment of different medical conditions such as cancer.[85] [28] In addition, the photosentizers act as an intermediary agent that can convert the NIR photon energy

to other forms to kill cancer cells in the PTT process.[86] Besides, an appropriate amount of oxygen is to make sure sufficient impact of PDT is obtained.

2.5.6 Applications of SERS

For cancer therapy, nanomaterials with capacities to be remotely detected and triggered for therapy could also close the gap between tumour detection and treatment.[87] Moreover, the cellular uptake is in general drastically reduced as the size of the nanoparticles increases, becoming virtually impossible at or above 200 nm.[88]

Furthermore, the traditional non-spherical nanoparticles are gold nanorods, first developed by the groups of Murphy and El-Sayed.[89, 90] These are now widely used in the range of SERS applications both *in vitro* and *in vivo*.[91] Furthermore, gold nanorods have been established to be very useful as SERS tags, mainly due to their size tunability that makes it easy bringing their LSPR into fitting resonance with the laser light.[91]

As a result of the pioneering work of the Nie and Natan groups of,[92, 93] the Stöber method has now been modified to make it possible for silica shells to be easily grown and are widely found in SERS literature as well as commercially.[94]

SERS can give information about adsorption rate of metal surfaces both *in situ* and in aqueous solutions. SERS started off being used to observe DNA and protein and now is used in many biology fields.[53] SERS has been used to detect many biochemical compounds such as nucleic acids, proteins, or small molecules.[24, 95] SERS has been utilized to view the catalytic reaction, monitor the nanoparticle distribution in the live body, and image the tumour and live cell.[96, 97]

2.6 Cytotoxicity

Cytotoxicity is defined as the toxicity due to the activities of chemotherapeutic proxies on the living cells. In the nanoparticles, this type of test is most important as they support the determination of probable biomedical usage. Cytotoxic agents comprise all the components that are poisonous to the cells, including the determinants that prevent their growth and sometimes also result in death as well, and are employed to treat certain disorders.[73] On the other side, the physical agents or biological and chemical substances can cause cytotoxicity by impacting the cells in a diversified manner. When it comes to its features, cytotoxicity is exploited in cancer treatment alongside the therapy and solutions of some autoimmune diseases. For therapy of cancer,

the selective destruction of tumour cells is processed through cytotoxicity and it is counted as one of its major goals.[81]

2.7 Clinical need and significance of the current project

The conventional therapeutic routes for cancer, such as those involving the use of surgery, chemo- and radio-therapy, are not always capable of removing all the cancerous cells or not without damaging normal tissue.[98-104] For example, surgical excision of tumours is limited to large visible tumours, chemotherapeutic medications may target healthy tissue, radiation therapy has harmful effects on normal tissue along the route of radiation. In this regard, there is a clinical need to develop new treatments for cancer that can overcome current limitations.[103-107] Recently, there has been an impetus towards new forms of thermal medicine (e.g. based on PTT) that can be targeted to the tumour location.[104, 108-110] Photothermal therapeutics is an alternative to surgery given that cancer cells are more susceptible to heat (e.g. generated by NIR laser radiation) than healthy cells[111-113] because of the overexpression of heat shock proteins which play a crucial role in cellular defense system. A rise in temperature locally, at the site of action, can induce protein denaturation which in turn damages cancer cells selectively while remaining non-toxic to surrounding healthy cells.[99, 114-120]

Gold nanoparticle-mediated PTT is particularly advantageous in that it can be deployed in combination with Raman detection (based on SERS effect) and at depth.[47, 99, 121-125] In addition, photo-responsive liposomes have proved capable to deliver active molecules and drugs to targeted cells and tissues.[126-128] Furthermore, these liposomes can be decorated or encapsulated with gold nanoparticles to produce hybrid nanoconstructs with new and invaluable properties.[57] Several previous works have developed liposome-based cancer treatments but crucially without the use of Raman detection.[57, 112, 129-132] This project is bridging this gap in the literature by adding SERS to the set of techniques that can achieve non-invasive chemical-specific diagnosis of cancer *in vivo*.

Liposomes or lipid vesicles can be assembled from various membrane compositions, in order to achieve different properties (e.g. tuning the mechanical stability and phase transition temperature). Researchers have previously synthesized biodegradable gold hybrid nanostructures using liposomes made of 1,2-dipalmitoyl-sn-glycero-3-phosphocholine (DPPC).[133-141] The DPPC

membrane's transition temperature of 41°C indicates that it can be used for drug delivery but not to kill cancer cells by hyperthermia (as biological cells only start to die of hyperthermia at 43°C).[142] Here, we synthesised the nanohybrids using 1,2-distearoyl-sn-glycero-3-phosphocholine (DSPC)-cholesterol (LiposAuNPs), with phase transition at 42-43 °C, which enable effective photothermal therapy followed by disassembly of the nanoconstruct to facilitate excretion.[57]

Gold nanoparticles can be engineered to create a complex with the liposome with tuneable size and shape to respond to the use of various wavelengths of light. Song et al.[143] have used 785 nm laser excitation to detect SERS signal of AuNRs (~13 nm × 46 nm)-liposome hybrids. In this project, both 785 nm and 830 nm laser wavelengths were tested for nanoconstructs prepared using commercial AuNPs (5 nm spheres) and AuNRs (15 nm × 55 nm). This is important since a laser wavelength of 808 nm, within the tissue "transparency" window, is normally used for *in vivo* at-depth Raman applications.[122, 125, 144]

Regarding the structure of the nanoconstructs, the complexes can present the AuNPs within the lipid bilayer,[136, 145-147] in the aqueous core,[134, 137, 148-150] or on the surface of the liposomes.[151-153] In this study, the CTAB-coated nanoparticles were mostly identified within the liposome core, with a proportion of the gold nanoparticles attached to the outer surface, which suggests high loading capacity. The nanohybrids were tested at different temperatures across the phase transition to investigate their PTT response and biodegradability.

In summary, based on the state of the art of current literature and with a view on the clinical need, the following gaps were identified: (i) consistent and extensive labelling of gold nanoparticles for use at different NIR wavelengths; (ii) functionalise liposome nanohybrids for use in Raman diagnostics; (iii) achieve the required NIR plasmonic absorption for SERS and PTT. These gaps were respectively addressed in Chapter 4, 5 and 6 of this thesis.

2.8 Conclusion

Metallic NPs have been widely investigated for their potential to address clinical needs, e.g. in diagnostics and therapeutics. Noble metal NPs, such as AuNPs, can produce ultra-sensitive SERS signals with their plasmonic properties in the NIR region of the spectrum, so they are suitable candidates for biomedical Raman applications. In cancer research, AuNPs are particularly

attractive as they provide a platform to which targeting molecules can be introduced for selective detection of tumours and tailored ablation (through e.g. PTT or radiation therapy).

The inspiration for this approach comes from biological systems and smallest objects like nanoparticles where physical and chemical properties can be tuned and adapted to carry out a specific function and achieve detection / treatment as needed. The aim is to prepare the NP constructs accordingly to current protocols. Raman reporters (RR) can be added to the nanohybrids to enable readout via Raman spectroscopy (through SERS effect). Synthesis, characterization and testing of the nanohybrids in the presence of cancer cell lines was performed as part of this project. Overall validation of photothermal therapy by the use of these nanoconstructs was also conducted.

CHAPTER 3
MATERIALS AND METHODS

3.1 Introduction

Cancer is considered a disease pertinent to the genome in a cell. This disease tends to lead toward the reiterative procedure pertinent to sub-clonal and clonal expansion, angiogenesis, clonal selection, and the invasion of tissues.[154] It has been claimed that when the tumour cells tend to migrate from the primary site toward the different organs (forming metastases), then the rate of patient survival decreases. Therefore, early diagnosis and treatment are vital for minimising the effect of malignancy. Present clinical diagnostic tools such as X-ray computed tomography (CT), magnetic resonance imaging (MRI) and positron emission tomography (PET) cannot generally attain single-cell resolution. Thus, this issue prevents them from succeeding in the initial detection of malignancy, or of the tumour after the patient treatment in remission. As asserted by Kong, these techniques can thereby detect the tissues with increased of tumour cell. Moreover, the efficacy of these tools is limited to certain kinds of cancer.[155]

Raman spectroscopy is considered a powerful tool which can measure biochemical modifications of the biological samples at the molecular level. These samples includes tissues, cells and biofluids, such that recent advancements in the field of point-of-care medicine tend to involve *in vivo* Raman needle or fiber-optic probes. These enable measuring the molecular fingerprints of the regions where the tip of the needle is located to analyse the prevalence of cancer.[156] The minimally invasive approach of Raman spectroscopy can also reach deeper regions across the body, by utilising specific illumination-collection geometries (Spatially Offset Raman Spectroscopy, SORS) or the transmission mode (Transmission Raman Spectroscopy, TRS). In SORS, the illumination and collection points are distinct points of tissue surface which assist in reaching many centimetres depth of detection. This modality encompasses distinct applications in numerous fields, which also involve the medicine such as point-of-care medicine.[157] These new tools enable increased precision both *ex vivo* and *in vivo* by measuring molecular biomarkers within the probed volume. With these new tools, more precise diagnosis and therapy are possible using nanoscale contrasting agents.

Single cell resolution is attainable through surface-enhanced Raman spectroscopy (SERS) for the initial stage of cancer detection. Moreover, one of the enhanced techniques for optimizing the intensity of signal is resonance Raman spectroscopy (RRS), which occurs when the excitation wavelength matches an electronic transition in the molecule, for instance the reporter molecule that is further utilised as a label on the nanoparticle metal surface. Subsequently, surface-enhanced resonance Raman spectroscopy (SERRS) can be utilised for the detection of single cells, but not for *in vivo* measurements at depth since these require NIR excitation wavelengths ("transparency" window of tissues).

3.2 Materials

Bare spherical gold nanoparticles of various sizes, 5, 10, 15, 40, 60, 80, and 100 nm (NanoXact, 0.05 mg/mL in aqueous 2 mM sodium citrate), and 55 nm × 15 nm gold nanorods (NanoXact, 0.016 mg/mL, 1 OD in water, 25 mL) were purchased from Nanocomposix. 4-mercaptobenzoic acid (4-MBA; 99% pure), 2-naphthalenethiol (2-NT; 99% pure), 4-acetamidothiophenol (4-AATP; 95% pure), biphenyl-4-thiol (BPT; 97% pure), ethanol (99.5% pure), hexadecyltrimethylammonium bromide (CTAB; ≥98% pure), chloroauric acid trihydrate ($HAuCl_4 \cdot 3H_2O$; ≥99.9% pure), sodium borohydrate ($NaBH_4$; 99.99% pure), sodium citrate tribasic dehydrate (≥99% pure), ascorbic acid (≥99% pure) were all purchased from Sigma-Aldrich. methanol (>95% pure) and chloroform (>99% pure) were Fisher Scientific products. Silver nitrate ($AgNO_3$, >99.8% pure) was purchased from Fosher Chemical. 1,2-distearoyl-sn-glycero-3-phosphocholine (DSPC; synthetic, >99% pure) and cholesterol (ovine wool, >98% pure) were purchased from Avanti Polar Lipids (Alabaster, AL) and used as received without further purification. An amphiphilic polymer, N-palmitoyl-N-monomethyl-N,N-dimethyl-N,N,N-trimethyl-6-O-glycolchitosan (GCPQ) (20191207-RM-GCPQ-01 (GCPQ19) M_w= 286.22 g/mol; 20201029-RM-GCPQ-01 (GCPQ20) M_w= 327.44 g/mol), was generously provided by Ryan Mellor and Prof. Ijeoma Uchegbu at UCL School of Pharmacy as part of the EPSRC RaNT Programme Grant. Ultrapure MilliQ water (18.2 MΩ.cm) was obtained in our laboratory. All glassware was cleaned with ethanol, then Hellmanex® III and rinsed with water before use.

3.3 Methods

3.3.1 Liposome synthesis

One of the most conventional and common synthetic method for obtaining liposomes involves suspension of the dry powder lipid within an organic solvent, purification of the resultant liposome, and resuspension in aqueous media, followed by characterisation of the end product.[158] Liposomes are widely utilised for studying the physical behaviour pertinent to the biological membranes. They include the lipid orientation in bilayer, the ion transport across biomembrane and the physico-chemical characterisation of lipid. However, the liposome is utilised widely for the delivery as they meet the good delivery vehicle requirement. Liposomes are biocompatible, biodegradable and are also stable in colloidal solutions. Moreover, these also protect the degradation of drugs and lower their non-specific toxicity and can be formulated and produced for the particular delivery.[159]

To produce small unilamellar vesicles (SUV, size range 20-100 nm, good size homogeneity/monodispersity feature), it was used the thin film hydration method of multilamellar vesicles (MLV, size >500 nm) followed by sonication and purification as shown in Figure 3.1.

The same step-by-step protocol can be used to generate different types of vesicles by stopping the process at different steps. For example, the method enables MLVs (up to step E), LUVs (step G) or SUVs (step H) to be produced. In this work, step A to I was followed to produce SUVs of ca. 100 nm diameter.

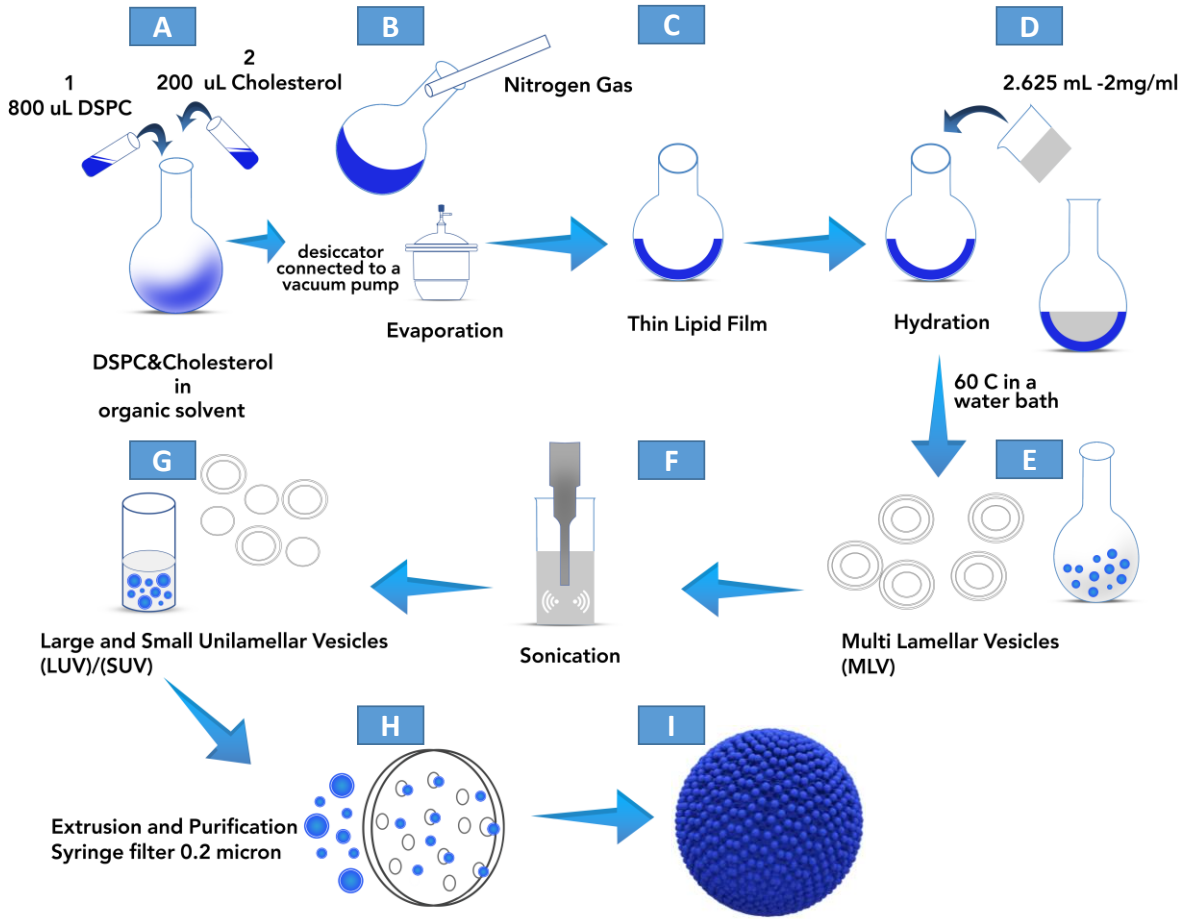

Figure 3.1 Diagram showing the liposome preparation steps.

Formation of Multilamellar Vesicles (MLV):

The multilamellar vesicles are prepared through shearing a lamellar phase that is composed of a surfactant and the lipids. Liposomes have largely revolutionised the therapy of cancer through their extensive clinical applications. The liposomes can address the limitation of chemotherapy by enhancing the stability and the bioavailability of the drug molecules. This is generally done by minimising the side effects through targeted drug delivery. The liposomes can thereby be developed by sonicating the dispersion of amphipatic lipids which also include phospholipids in water. The lower shear rates tend to develop the multilamellar liposomes. Moreover, the sonication is largely recognised as the method of gross preparation. It is due to the fact that it can damage the

drug structure in order to be encapsulated. In the MLV, the vehicles tend to encompass the onion structure. The liposome can target the tumour tissues actively which can be utilised through the approach which is based on antibody. These are done by inserting several antibodies toward the surface of liposome that are also known as immunoliposomes. These are thereby specific toward the cancer cell toward the pertinent to the tumour vasculature.[160]

The liposomes (multilamellar vesicles, MLV) made up of DSPC:Chol with molar ratio 8:2 at a concentration of 2 mg/ml were prepared by thin-film hydration method.[57] 10 mM DSPC stock solution, 10 mM cholesterol stock solution, then 10 mM lipid mixture stock solution were prepared. Mixture of DSPC and cholesterol with different molar ratio was dissolved in a 2:1 chloroform:methanol mixture. 1 mL of lipid mixture 10 mM (DSPC:Chol 8:2) was put in a 25 mL round bottom flask. The solvent was let to evaporate under a stream of dry nitrogen first and then, to enable all the organic solvent to completely evaporate, it was left for 20 minutes under vacuum (using a desiccator connected to a vacuum pump). This procedure leads to the formation of a thin lipid film. The lipid film was then hydrated at 60°C in a water bath (above the main phase transition temperature of DSPC) adding 2.625 ml Milli Q water to reach the lipid concentration of 2 mg/mL and vortexing for some minutes (until all the lipid film is dissolved in water). This procedure leads to the formation of multilamellar vesicles (MLV).

Formation of Small Unilamellar Vesicles (SUV):

Unilamellar vesicles are spherical vesicles with a single bilayer and an aqueous solution inside the cavity. The vesicle size tends to dictate the curvature of the membrane which is a significant factor to study the fusion protein. Small unilamellar vesicles (SUV) have a size below 100 nm, whilst large unilamellar vesicles (LUV) are typically between 100-1000 nm. LUV and SUV are widely utilised to deliver distinct type of drugs. Whereas, GUV are large enough to be visualised by traditional florescence microscopy. SUV are recognised as sonicated vesicles that are prepared through sonication e.g. using a probe tip sonicator. Instead, LUV can be prepared through several different methods that also involve the extrusion and the detergent dialysis. The unilamellar vesicles are thereby prepared from large multilamellar vesicles. It has been further found that the LUV are largely stable over the storage. However, the SUV tend to spontaneously fuse while they

drop below the transition phase temperature.[161] The MLV suspension was sonicated for 3 cycles at (20% intensity for 6 min, in water bath for 5 min) using a probe sonicator (UP100H, Hielscher Ultrasonics GmbH, Teltow, Germany). Each sonication cycle was performed for 2 minutes with 1 s on/off pulse, to obtain small unilamellar vesicles (SUV) of 100 nm diameter. Then, a syringe filter with 0.2 μm pore size was used for purification. The SUV were then stored in a fridge for maximum a month and, before use, the solution was sonicated for 30 s.

3.3.2 Labelled gold nanoparticles

Noble metal nanoparticles (NP) such as gold nanoparticles (AuNPs) can produce ultrasensitive Surface Enhanced Raman Scattering (SERS) signals owing to their plasmonic properties. In this work, labelled AuNPs in suspension were characterised in terms of size dependency of their localized surface plasmon resonance (LSPR), dynamic light scattering (DLS) and surface-enhanced Raman scattering (SERS) activity. The study was conducted using a set of four Raman labels or *reporters*, i.e. small molecules with large scattering cross-section and a thiol moiety for chemisorption on the AuNP, namely 4-mercaptobenzoic acid (4-MBA), 2-naphthalenethiol (2-NT), 4-acetamidothiophenol (4-AATP), and biphenyl-4-thiol (BPT), to investigate their viability for SERS tagging of spherical AuNPs of different size in the range 5 nm to 100 nm.

In this study, a 100 mM stock solution of each Raman label was prepared by adding 15.4 mg, 16 mg, 16.7 mg, or 18.6 mg of 4-MBA, 2-NT, 4-AATP, or BPT, respectively, to 1 mL ethanol. Each solution was mixed in a Vortex Varimix shaker (SciQuip) and diluted 1:99 in ethanol to make up a 1 mM label solution. Then 100 μL of label solution was added to 1 mL AuNPs to a final label concentration of $9.1 \cdot 10^{-5}$ M. The labelled AuNP solution was then centrifuged using a Hettich Mikro 22 centrifuge for 10 to 30 minutes, after shaking by hand for 5 minutes, vortexing for 1 minute and sonicating in a water bath at 30°C for 5 minutes. Table 3.1 lists the centrifugation speeds used with all NP solutions; higher speeds were required to effectively mix smaller AuNP solutions to obtain a pellet. The supernatant was then carefully removed and the pellet was resuspended in distilled water.

Table 3.1 Centrifugation rate and time used in the preparation of labelled gold nanoparticle solutions.

AuNP size (nm)	4-MBA		2-NT		4-AATP		BPT	
	Speed (rpm)	Time (min)	Speed (rpm)	Time (min)	Speed (rpm)	Time (min)	Speed (rpm)	Time (min)
5	10 K	10	4 K	10	4 K	10	10 K	30
10	4 K	10	4 K	10	4 K	10	10 K	30
15	4 K	10	4 K	10	4 K	10	10 K	30
40	3 K	10	3 K	10	3 K	10	4 K	30
60	3 K	10	3 K	10	3 K	10	4 K	30
80	3 K	10	3 K	10	3 K	10	4 K	30
100	3 K	10	3 K	10	3 K	10	4 K	30

Each solution was then transferred into a 2 mL Eppendorf tube (Figure 3.2) and stored for approximately 12 hours at 4°C in darkness before characterization.

(a) 4-MBA labelled AuNPs

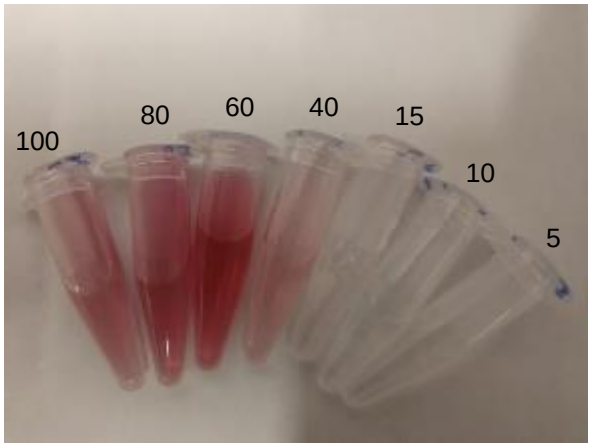

(b) 2-NT labelled AuNPs

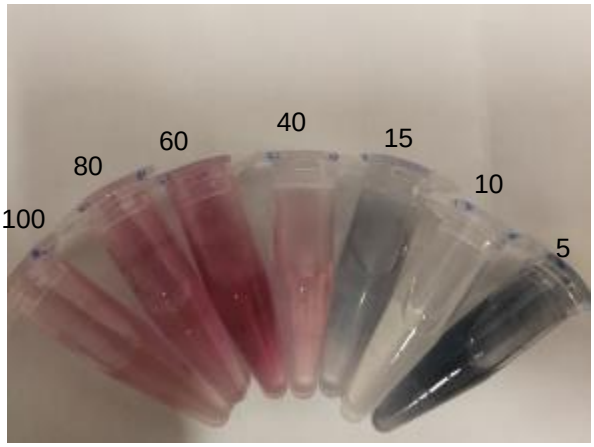

(c) 4-AATP labelled AuNPs

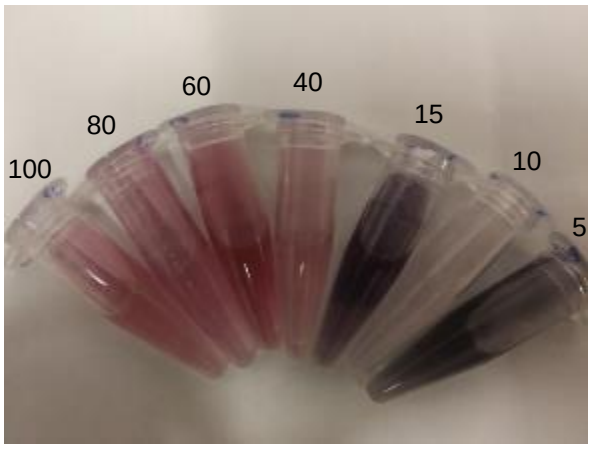

(d) BPT labelled AuNPs

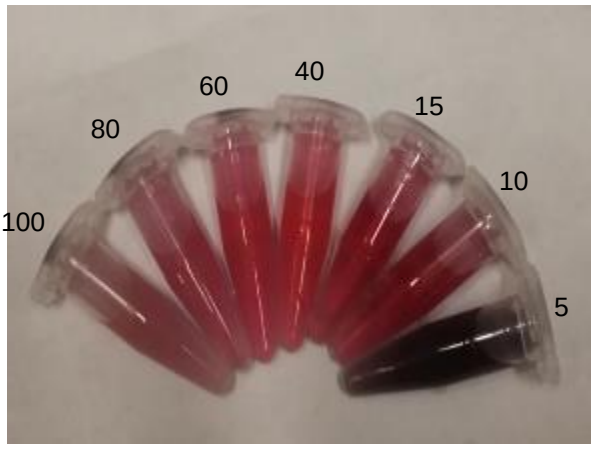

(e) AuNPs

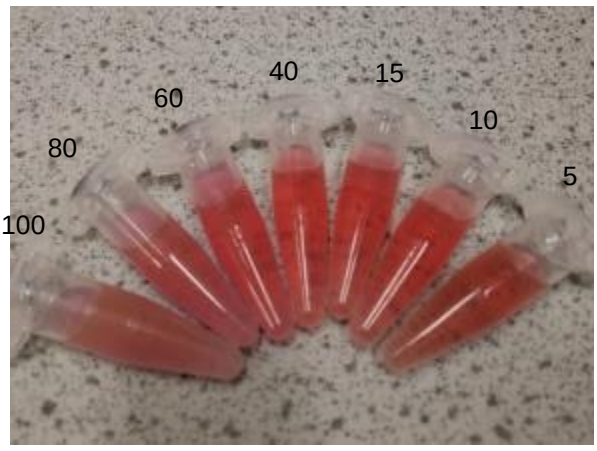

Figure 3.2 Solutions of AuNPs labelled with (a) 4-MBA, (b) 2-NT, (c) 4-AATP, (d) BPT, and (e) unlabelled AuNPs. Numbers indicate the particle size. Dark solutions in (b-d) denote aggregation for small sized NPs, 15 nm and 5 nm.

3.3.3 Gold nanoparticle (AuNP) synthesis

This protocol follows an early publication.[162] The NPs of size 5 nm were synthesised by using a reducing agent of the chloroauric acid solution of 100 mL and of $0.3 \cdot 10^{-3}$ M at room temperature followed by addition of 1.2 mL of 0.1 M freshly prepared ice-cold sodium borohydride in the presence of 4 mL of 1% (w/v) sodium citrate (as the stabilizer). Vortexing was required for every solution, using a vortex for 1-2 minutes until dissolved in water, then used a bath sonicator for 1 minute. The solution was stirred at 600 rpm speed at room temperature for 10 min which resulted in orangeish red colloid. The colloid exhibited an LSPR at 510 nm, [Au] concentration of $0.237 \cdot 10^{-3}$ M and NP concentration of $4.3 \cdot 10^{12}$ NPs.mL^{-1}.

Note that, after preparing the 100 mM chloroauric acid ($HAuCl_4$) solution, this needed to be stored in the fridge wrapped in aluminum paper to protect from light. Water before adding 4.54 mg sodium borohydride powder must be cold. The sodium borohydride is a very strong reducing agent. An ice bath is needed to slow down the reaction and give proper control over reaction. Glass bottles and milli-Q-water were used.

After obtaining the AuNP solution, this was transferred in a glass bottle wrapped in aluminum paper. It wasstored for a few months at 4°C in darkness before characterization (see Figure 3.3).

Figure 3.3 Glass bottle containing the AuNP solution.

3.3.4 Gold nanorod (AuNR) synthesis

The tunable aspect ratio of the gold nanorods has been increasingly obtained through modified synthesis method. Ascorbic acid was employed as the shape controller to induce the growth of anisotropic structures. This regulated the aspect ratio of the synthesise gold nanorods. This protocol follows nearly a publication by Yang et al. [163] with modifications.

Reagents

For the $HAuCl_4$ solution (0.01 M), 393.8 mg of $HAuCl_4 \cdot 3H_2O$ is weighed, transferred in a volumetric flask (100 mL) and (100 mL) water is added to dissolve the powder. The solution is then transferred into a glass container for storage.

For the CTAB solution (0.1 M), 2.19 g of CTAB is weighed, transferred in a beaker (100 mL) and 60 mL of water is added. The beaker is put in a water bath (30°C) to dissolve the CTAB. The solution should be colorless before use. If the process of dissolution is too slow, the temperature of water bath can be increased.

Preparation of seed solution

9.75 mL of CTAB solution (0.1 M) is added in a glass vial (28 mL) and stirred slowly at 30°C (water bath). Meanwhile, 3.78 mg of $NaBH_4$ is weighed into a glass vial (28 mL) and 10 mL of water is added. The solution is shaken vigorously to dissolve the solid. Then it is inserted in ice for at least 10 min to keep the solution ice-cold. The 0.25 mL of $HAuCl_4$ solution (0.01 M) is added into the former glass vial containing CTAB solution. After this, 0.6 mL of $NaBH_4$ solution is added and stirred vigorously. The colour of the solution changes from bright yellow to brownish yellow immediately. After 7 minutes, the stirring is stopped and the solution kept undisturbed for 1h. During all the addition processes care must be taken to prevent making bubbles.

Growth of gold nanorods

9.5 mL of CTAB solution (0.1 M) is added in a glass vial (28 mL) and stirred slowly at 30°C (water bath). Meanwhile, 88 mg of ascorbic acid is weighed into a glass vial (28 mL) and 5 mL of water is added, then shaken vigorously to dissolve the solid. 17 mg of $AgNO_3$ is weighed into a glass vial (28 mL) covered with aluminium foil and 10 mL water is added, then shaken vigorously to dissolve the solid. The glass vial is then stored in the dark. 160 µL of $AgNO_3$ solution (0.01 M) is added in the former glass vial containing CTAB solution. Then 0.5 mL of $HAuCl_4$ solution (0.01 M) is added. After this, 55 µL of ascorbic acid solution (0.1 M) is added. The colour of the solution changes from bright yellow to colorless. Lastly, 12 µL of seed solution is added. After 1 minute, the stirring is stopped and the solution is kept undisturbed for 1 h. During all the addition processes care must be taken to prevent making bubbles.

After an hour, the solution is transferred into an Eppendorf tube and Millipore water is added to a total volume of 15 mL. Then the solution is centrifuged at 30°C and 8500 rpm for 15 minutes. The supernatant is removed and 10 mL of phosphate-buffered saline (PBS) is added.

Key is to maintain the reaction in darkness, at constant temperature of ca. 30°C, using the sequence above for the addition of the reagents, and dosing the silver nitrate based on the obtained results. Silver nitrate is a very labile reagent and is photosensitive, hence each bottle is different and need to be replaced frequently.

Generally, the reaction works better by producing small amounts in 10-20 ml vials rather than in large flasks.

3.3.5 Synthesis of AuNPs/AuNRs with BPT and CTAB

3.3.5.1 BPT-labelled AuNPs/AuNRs:

BPT-labelled AuNPs/AuNRs were prepared as shown in Figure 2.4. A 100 mM stock solution of BPT was prepared by adding 18.6 mg to 1 mL ethanol. Then the solution was mixed in a Vortex Varimix shaker and diluted 1:99 in ethanol to make up a 1 mM BPT solution. Afterwards, 100 µL of BPT solution was added to 1 mL AuNPs to a final BPT concentration of $9.1 \cdot 10^{-5}$ M. Finally, the solution was shaken by hand for 5 minutes, vortexed for 1 minute and sonicated in water bath at 30°C for 5 minutes.

3.3.5.2 CTAB/GCPQ-coated BPT-labelled AuNPs/AuNRs:

The liposomes are negatively charged, and so are the gold nanoparticles. Enabling gold nanoparticles to interact with SUVs requires reversing the surface charge of nanoparticles, for instance by using a positively charged molecule such as CTAB or GCPQ.

After preparing the BPT solution as shown in Figure 2.4, a 75 mM solution of positively charged molecules (CTAB or GCPQ) is prepared using glass bottles. After vortexing the CTAB solution for a minute until dissolved in distilled water and sonicating in water bath at 30°C for 10 minutes until the solution is colourless, a 0.3 mL of CTAB solution is added to 1 mL of gold nanoparticle solution. Afterwards, the BPT-labelled AuNPs with CTAB/GCPQ solution undergoes vortexing for a minute, and sonication for 10 minutes in water bath at 30°C. Then the solution is left for approximately 15 to 20 hours at room temperature using aluminum paper to protect it from light. Two samples of CTAB/GCPQ-coated BPT-labelled AuNP solution are prepared so that a higher concentration of AuNP solution can be achieved in the next step.

The gold solutions (CTAB/GCPQ-coated BPT-labelled AuNPs or AuNRs) are then centrifuged at room temperature at 55K rpm for 30 minutes or 10K rpm for 15 minutes, respectively. The supernatant is removed carefully, due to the presence of bubbles, and the pellet with only 50 µL of solution is retained. In order to get high concentration of gold solution, the second sample of CTAB/GCPQ-coated BPT-labelled AuNP solution that was prepared previously is added to the pellet, and then this is centrifuged and another pellet is obtained and retained with only 50 µL of gold solution.

3.3.6 Synthesis of liposomal nanoconstructs

The lipid solution is generally dissolved by ether-methanol or diethyl mixture which is gradually and slowly injected in the aqueous solution. These solutions are generally encapsulated at 55°C to 65°C temperature or under lowered pressure. The constant eradication of ether under vaccum leads toward the liposome creation.[164]

After sonicating multilamellar vesicles (MLVs) and obtaining small unilamellar vesicles (SUVs) as described in section 3.3.1 and illustrated in Figure 3.1, different volumes of 2 mg/ml liposome solution were added to CTAB/GCPQ-coated BPT-labelled 5 nm AuNPs or 55 nm/15 nm AuNRs

to obtain different concentration ratios [liposome:AuNPs/AuNRs] which are [1:5], [1:20], [1:200], [1:500], [1:1K], [1:3K], [1:6K], [1:16K], and [1:32K], as shown in Figure 3.4. After addition of the liposomes to the nanoparticle solution, the mixture is sonicated in water bath for 30 s, and then left for 6 hours at room temperature. After that, it is stored in fridge at 4°C for 12-15 hours. A specific plastic tube, Eppendorf LoBind microcentrifuge tube, was used to avoid NPs sticking on the walls of the tube. Aluminum foil is used to protect the sample from light.

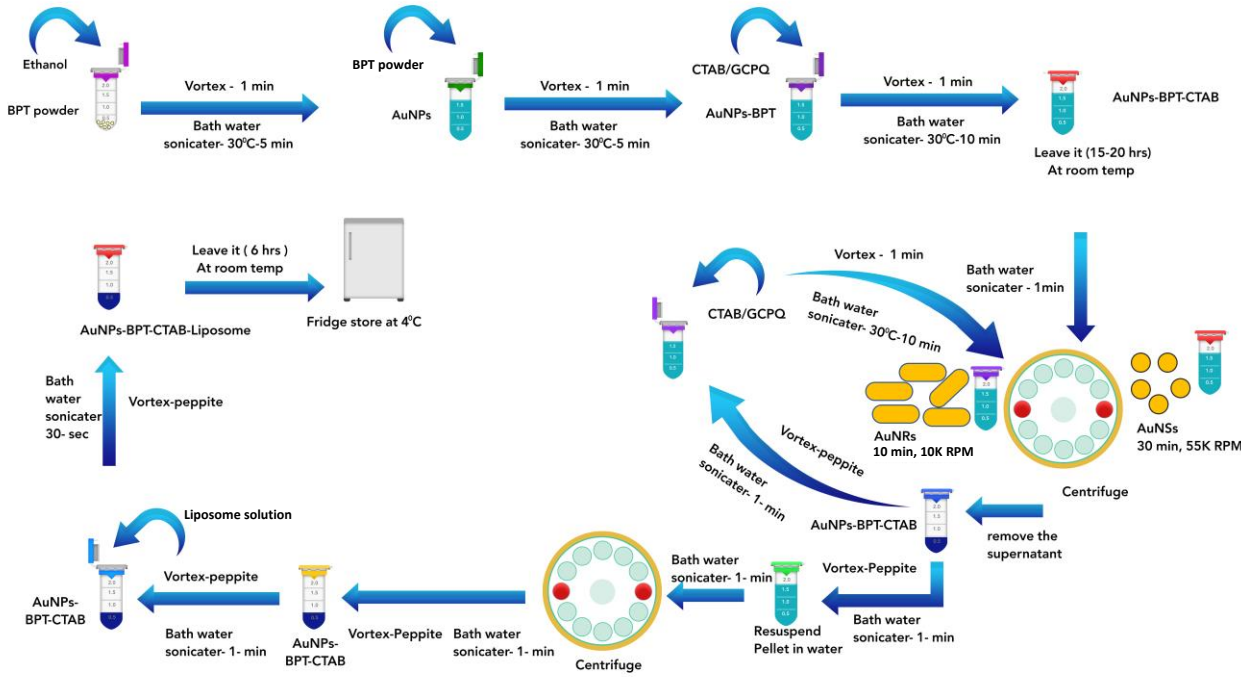

Figure 3.4 Diagram illustrating the synthesis of liposomal nanoconstructs.

3.3.7 Gold solution cytotoxicity

3.3.7.1 Cell culture work: triple-negative human breast cancer cell line (MDA-MB 231)

The cell culture largely refers toward the removal of the cell from the plant or the animal along with the growth in more favourable environment. Under this stage, the cell is largely and widely sub-cultured by transferring them into novel vessel with novel adequate and new growth medium for offering the room toward continued growth. The Triple-Negative Breast Cancer (TNBC) is widely based on lack of three molecular markers. More commonly, the hormone receptor expressed by the breast cancer encompasses more favourable prognosis as compared to the HER-

2/Neu amplification. The TNBC display that approx. 10 to 15% of the breast cancer, and the patient encompassing TNBC have poor result as compared to the other breast cancer subtypes. More interestingly, the TNBC incidence is being higher in African American women as compared to other ethnic groups. The reason behind this increase is still not elucidated.[164]

As part of this work, the cytotoxicity studies were carried out on cells seeded in a 96-well plate *(Merck, Sigma Aldrich, UK).* Imaging measurements were performed in glass bottom dishes (35 mm dish diameter, 14 mm glass diameter, MatTek Life Sciences, USA). The cells were plated in a 96-well plate at a density of $1 \cdot 10^4$ cells per well, whilst cells for imaging were incubated in glass bottom dishes at a density of $1 \cdot 10^6$ cells per dish. The multi-well plate and glass bottom dishes with the cells were incubated for 24 hours prior to the experiments. After incubation, cells were again incubated after treatment with and without 0.05, 0.025, 0.01 and 0.0125 mg/ml of nanohybrids (by labelling them as A, B, C, D, E, F, G, H, I, J which denote *AuNPs+BPT* (100 nm size), *AuNPs+BPT* (80 nm), *AuNPs+BPT* (60 nm), *AuNPs+BPT* (40 nm), *AuNPs+BPT* (15 nm), *AuNPs+BPT* (10 nm), *AuNPs+BPT* (5 nm), *Liposome+AuNPs+CTAB*-1:5 lipo:NPs, *Liposome+AuNPs+CTAB*-1:10 lipo:NPs, *Liposome+AuNPs+CTAB*-1:20 lipo:NPs, respectively). Cell viability of treated and untreated (control) cells was evaluated using MTT assay (Sigma Aldrich, UK) according to the manufacturer's instructions and as previously reported by our group.[165] The concentration of solution was evaluated by optical density (OD) measurements using an xMark™ microplate absorbance spectrophotometer (Bio-Rad) at a wavelength of 570 nm (reference wavelength at 630 nm). The results were expressed as percentage cell viability. Three independent experiments were performed for each sample and all measurements were performed in triplicate.

Statistical Analysis: The data has been statistically analysed through the GraphPad Prism 5.04 for assessing the viability of the cells and were expressed as the mean cell count ± standard deviation (SD), where Mann Whitney *($p < 0.05$) was taken statistically significant.

3.3.7.2 Cell culture work: Primary Normal Human Dermal Fibroblast cells (NHDF)

Primary Normal Human Dermal Fibroblast (NHDF) cells were seeded at a density of $4 \cdot 10^5$ in a 6-well plate fitted with a coverslip and were cultured in fibroblast growth medium (Promocell). Cells

were maintained in 37°C and 5% carbon dioxide (CO_2) until 80%-90% confluent. Prior to treatment, cells were washed twice with 1X Dulbecco's phosphate buffered saline (DPBS) then 1 ml of growth media was added to each well. 50 µL of (NL1-3 and NR1-3) were added to the cells and incubated for 24 hours. Post treatment, cell were washed twice with 1X DPBS and fixed using 4% paraformaldyhide for 15 minutes.

3.4 Instrumentation

The present study is aimed to characterize colloidal AuNPs of different sizes and with different Raman labels or *reporters* using Transmission Electron Microscopy (TEM), UV-visible absorption, Dynamic Light Scattering (DLS), Nanosight, and Raman micro-spectroscopy.

3.4.1 UV-visible spectrophotometry

Ultraviolet-visible spectrophotometry is based on the absorption of UV-visible light by chemical compounds.[166] These tend to result in distinct spectra production for given chromophores. The spectroscopy is largely based on the interaction between matter and the light.[167] The UV spectroscopy is extensively utilised technique in most of the science area that range from drug identification, bacterial culturing and the nucleic acid purity check along with the quantitation. Thus, the quality control in the beverage industry along with the chemical research, the spectroscopy complementary encompasses sensing depth and can thereby interrogate directly with the pre-cancerous growth and the primary invasive carcinomas in the cervix, anus, neck and the head along with the recurrent disease of chest wall in the breast cancer.[163]

Absorption spectra in the UV-visible spectral range can be taken with an UV-visible spectrophotometer. The energy of absorbed photon leads to electron excitation from the ground state to an excited state. As a result, the absorption spectrum, measured with the spectrometer, gives information on the chromophore's structure. The absorbance is directly proportional to concentration via the Beer-Lambert law:

$$A = log\ (I_0/I)\ = \varepsilon cL$$

where A is the absorbance, I_0 is the intensity pertinent to the incident light, I is the intensity pertinent to the transmitted light, ε is the molar absorption coefficient (or extinction coefficient), c the compound concentration in solution (in molar concentration, M), and L is the optical pathlength (cm).

A volume of 1 mL AuNP solution was transferred into a quartz cuvette with a 1 cm path length and a UV-visible absorbance spectrum was acquired using a Thermo Scientific Evolution Array UV-visible spectrophotometer (Thermo Fisher Scientific). Spectra were acquired in the range 185–1100 nm, with 30 scans and 1000 ms integration time. The wavelength of maximum absorbance and shape of the localised surface plasmon resonance (LPSR) were analysed using OriginPro software.

3.4.2 Transmission Electron Microscopy (TEM)

3.4.2.1 Jeol JEM- 2100 Transmission Electron Microscope

The JEOL 2100 TEM system is a sophisticated instrument that runs at 200 kV and can provide molecular quality pictures of nanomaterials, thinner coatings, layers, granules, flaws, and structure of ultra-thin specimens.[164] It has a pinpoint resolution of 0.25 nm and a crystal resolution of 0.14 nm in principle. It can function in both TEM and Scanning transmission electron microscopy (STEM) modalities, as well as bright field (BF) and dark field (DF) formats. It is equipped with an Oxford Instrument X-MAXN EDS sensor, which enables characteristics as fine as a handful nanometres to be analysed. Unit cell characteristics, alignment, and alignment connections may all be determined using selected area diffraction.[168]

The size and morphology of labelled AuNP samples were investigated using Transmission Electron Microscopy (TEM) with a TEM-JEOL 2100 instrument at an operating voltage of 200 kV. Prior to the measurements, two drops of each solution were deposited onto a 300 mesh holey carbon film coated copper grid (carbon film-Cu TEM grid; Agar Scientific, Stansted, UK) and left to dry in an oven at 80°C for 4 hours.

3.4.2.2 Jeol JEM-1400 Transmission Electron Microscope

The JEM-1400 TEM system is utilised in several sectors, including biological sciences, nanomaterial, polymeric science, and innovative technologies. When inspecting biological samples such as macromolecular components, medications, pathological segments, and viral infections, the whole view of body tissue, constructions, intended areas, and inspection area are often validated at minimal resolution before fine formations of interest are cautiously examined at

higher resolution. Growing needs for simpler observation procedures to capture higher-throughput picture data are rising in order to seamlessly advance to this sequence of observations.[169]

The JEM 1400 TEM system is operated at 120 kV and fitted with a Gatan ES1000W (4008X2672 pixel) charge-coupled device (CCD) camera on the side that enables for quick observation and purposes that require a broad area of vision. This enables quick picture acquisition, random sampling, and extremely precise measurement. Qualified personnel were approached for getting assistance on all major aspects of TEM.[164] This microscopic device is part of the Bioimaging Centre, and is used to support the College of Life and Environmenal Sciences, the Living Systems Institute as well as other Colleges at the University of Exeter. It has been used to produce high-resolution micrographs from biological and inorganic specimen.[169]

In order to visualise liposomes and nanogold particles using TEM, a modified negative staining method was applied. Small volumes of the samples in solution were transferred onto pioloform-coated 100 mesh copper EM grids for 3 minutes by floating the grids upside down on small droplets of the sample solution placed on parafilm. After washing grids 4 x 3 minutes on droplets of deionised water, the bound structures were contrasted in a solution of 2% (w/v) uranyl acetace and 2% (w/v) methyl cellulose (UA:MC mixed to 1:9 ratio) on ice for a total duration of 9 minutes. Grids were then picked up in a small metal wire loop from the contrasting solution and excess staining solution carefully removed on a filter paper. The grids were then air dried in the loop. Once the UA:MC film is dry, the grids are carefully removed from the loop with tweezers and are ready for inspection with the TEM. After preparing the liposomal nanoconstuct samples, they are stored in fridge for 30 minutes to 1 hour. Prior to the TEM imaging, solutions were sonicated in a water bath at 30°C for 30 s every 10 minutes for 30 minutes (total is 90 s).

To be able to image cross-sections of liposomes, samples were also embedded in resin to enable the production of ultrathin sections for TEM analysis. Samples in solution were therefore mixed with 12% pig skin gelatine in PBS. After the samples solidified in the gelatine, small cubes of the sample were fixed in 2% glutaraldehyde and 2% paraformaldehyde in 0.1 M sodium cacodylate, pH 7.2. The samples were then washed 3 x 5 minutes in cacodylate buffer before post-fixing for 1 hour in 1% osmium tetroxide (reduced in 1.5% potassium ferrocyanide) in cacodylate buffer. After 3 x 5 minutes washes in deionised water, the sample cubes were dehydrated in a graded ethanol

series (30, 50, 70, 80, 90, 95, 2 x 100% ethanol, 10 minutes per step) before embedding in Durcupan resin. The sample blocks were cured in an oven at 60 degrees for 24 hours and could then be sectioned using an ultramicrotome (Leica EM UC7) to produce 70 nm thin sections. The sections were picked up on EM grids (see above) and were contrasted in Reynold's lead citrate for 10 minutes. Dried grids were then ready for TEM imaging.

3.4.3 Dynamic Light Scattering (DLS)

Dynamic light scattering (DLS) is a physics methodology for determining the dimension dispersion characteristic of tiny objects suspended in liquid or polymeric fluid. The brightness or particle auto-correlation measure is commonly used in DLS to examine temporal variations.[170] The autocorrelation function (ACF) in frequency zone evaluation normally decomposes from a zero-latency period, and quicker movements owing to finer particles result in quicker decorrelation of dispersed illumination tracing.[171] The concentration ACF has been demonstrated to be the Fourier conversion of the energy spectral range, implying that DLS observations may be done equally effectively in the spectral dimension. DLS may be employed to investigate the behaviour of complex liquids such as saturated polymeric mixtures.[170]

A Malvem Zetasizer Ultra running DTS software and 4 mW helium-neon (He−Ne) laser at 633 nm was used for performing DLS measurements. A constant temperature of 25°C was adjusted for the analysis at 173° and 90° scattering angles. A zeta potential cell was used for measuring zeta potential, whereas size was measured through disposable cuvettes of 1 cm optical path length. Data were collected in three phases and presented in the form of median and average values.

Before DLS measurement, the colloid was passed through a 0.2 μm polyvinylidene fluoride (PVDF) membrane. Dust is one of the most common difficulties in DLS observations, and it can mislead the findings. The dispersion solution should be screened to prevent dust infiltration during dispersion. Professional syringe filtration with particle diameters varying from 1mm to 20 nm is accessible for usage. Whatman™ Puradisc 25mm Syringe Filters have polypropylene housings with female luer lock inlet and male luer outlet.

In this work, I used Hellmanex® III for cleaning glassware; a previous study has highlighted that the interfacial pressure of water is greatly reduced with Hellmanex III.[172] It explained that the excellent soaking effect of a Hellmanex III watery treatment also ensures the elimination of dirt particles, whereas its strong coagulant and dispersion properties avoid the released particles from being re-deposited. After the cleansing of glassware, special surface-active chemicals make it easier to rinse them without leaving any residue. Hellmanex III was filtered to a depth of 1 mm, making it nearly particle-free.[173]

The ideal dilution (typically 0.5 to 2 vol%) is determined by several factors, including the hardness of the water, the amount and kind of pollution, the temperature, and so forth. The cleansing properties are improved when demineralized water is used.[168]

The cleansing procedure is accelerated as the temperature rises. Nevertheless, it is vital to prevent heat damage at warm temperature. Before submerging the cuvettes in hot washing liquids, they should be pre-warmed.[174]

Hellmanex III can be used on glass, crystal, sapphires, porcelain, ceramics, plastics, and magnetic materials when dissolved to a practical concentration of 2%. It may also be applied to materials that are prone to rust, such as aluminum as well as other non-ferrous elements. Stainless steel, polyethylene (PE), polypropylene (PP), polyvinyl chloride (PVC), fluoroelastomer (FPM), or nitrile rubber (NBR) containers can be used to hold the concentration.[175] Here, cuvettes were soaked for a whole night (15-16 hrs).

3.4.4 NanoSight

The NanoSight LM10 instrument employs a laser illumination output to spotlight nano elements inside a 0.3 ml specimen supplied to the observing unit via a disposable syringe. Nanoparticles emerge as point-scatterers flowing with Brownian movement, aided by a near-perfect black backdrop. The NanoSight LM10 has a high sensitivity camera for the measurement of size of dispersed particles and molecules in solution, typically between 10 nm and 2000 nm. This package comprises of an adapted microscope, a scientific complementary metal oxide semiconductor (sCMOS) camera and Nanoparticle Tracking Analysis (NTA) software suite. Real-time interactive nanoparticle visualisation, particle-by-particle assessment, molecule numbering and resizing,

particle diameter dispersion shown as histograms, data export to spreadsheets, and video clip recording are all features of the NTA Analytical Software package.

The imagery processing Nanoparticle Tracking Analysis (NTA) application package allows researchers to monitor and measure nanoparticles autonomously. In addition, picture video snippets can be generated and preserved for subsequent use.[176]

In this study, a NanoSight LM10 equipment comprising a 532 nm beam, HS sCOMS camera, 565 nm long passing output filtering, and NTA syringe pump was used.

3.4.5 Raman micro-spectroscopy

The AuNP solutions were transferred onto a quartz Hellma 96-well microplate (volume of each well is 300 μL) and measurements were conducted using a Renishaw inVia Raman microscope. The system comprises two NIR diode lasers (785 nm and 830 nm), various objectives (5x, 10x, 20x, and 50x), and three diffraction gratings (300, 600 and 1200 l/mm). A motorized xyz stage was used to control and change the sample position. Spectra were acquired at room temperature (21 ± 2 °C) using both 785 nm and 830 nm excitations, the 600 l/mm grating and 50x objective (NA 0.75) in the range 283–2493 cm^{-1} at full laser power (20-30 mW at the sample), with 10 s acquisition time and 16 accumulations per spectrum. As a concentration gradient is expected for the solution in each well, depth-resolved Raman measurements were conducted (along the z axis) starting from the surface and then down 100, 200, 300, 400, 500, and 600 μm into the solution. The largest signals were observed for 400 μm depth and hence these spectra were retained for analysis. WiRE 4.1 software was used for data acquisition and handling.

The system was calibrated using different standards such as silicon (Si), neon lamp (Ne), and green glass (gg) before measuring and analyzing samples.

Different optical parts of the InVia Raman microscope and paths of the laser photons and Raman photons are presented in Figure 3.5.

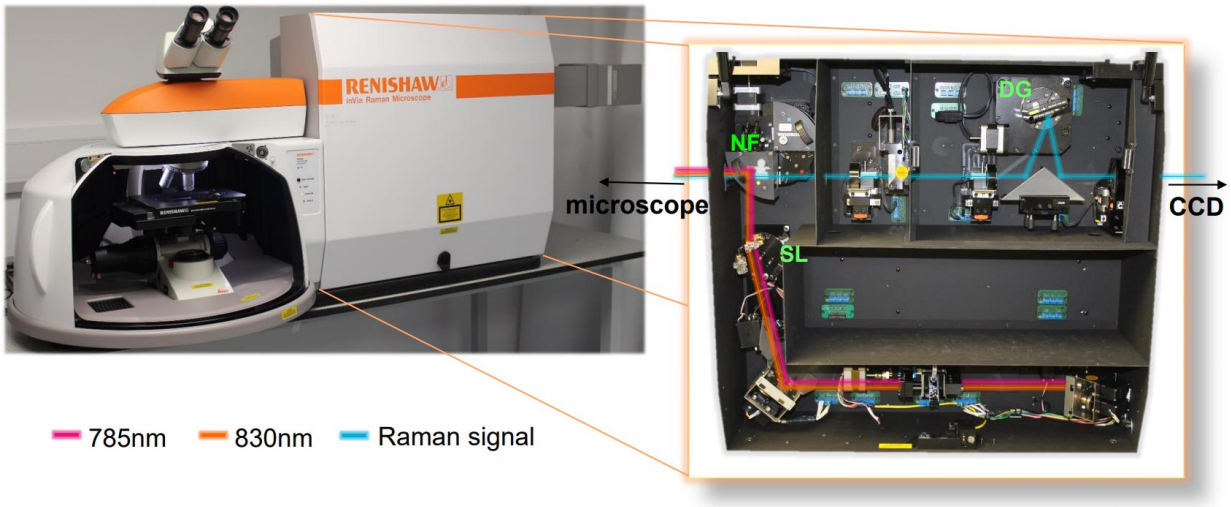

Figure 3.5 The Renishaw inVia Raman microscope and interior components of spectrometer, with the ray paths for Raman signal and 785 and 830 nm lasers [SL: streamline lens, NF: notch filter, DG: diffraction grating].[177]

The white light passes through a series of transmissions and reflections to visualize sample using camera on the top of the microscope (Leica Microsystems, Milton Keynes, UK). A Hellma all-quartz 96 well microplate (300 μL volume of each well) was used for obtaining the Raman measurements of the AuNPs solutions (Figure 3.6).

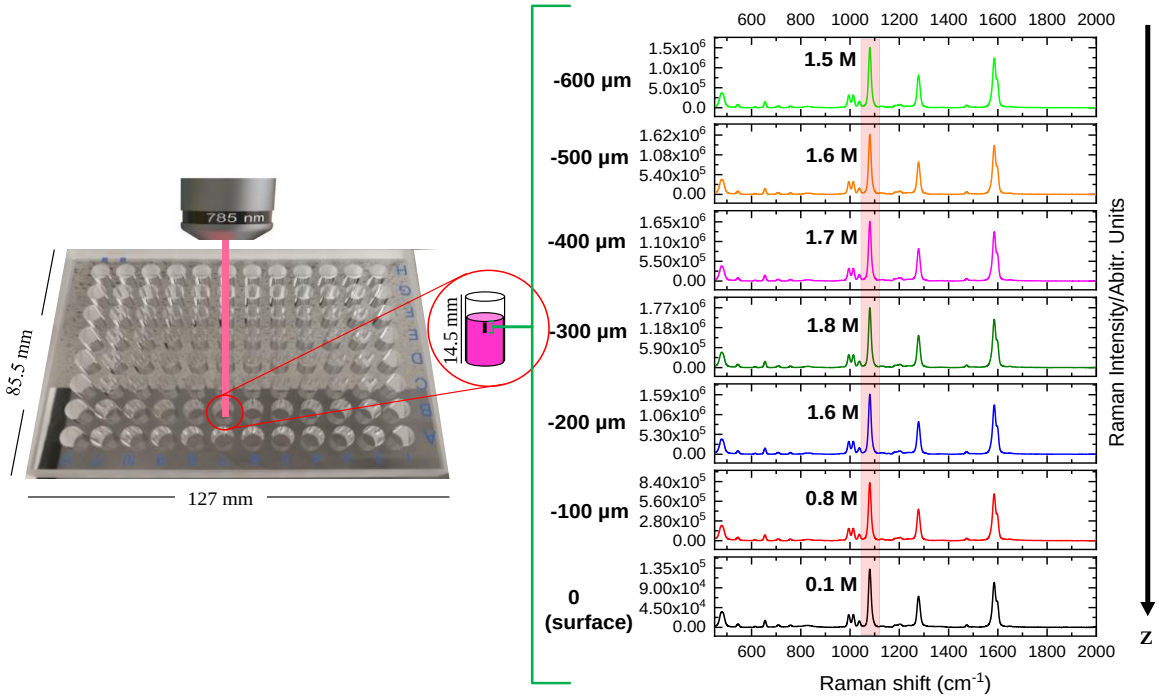

Figure 3.6 Raman spectra obtained with a 96-well quartz microplate (Hellma, Germany, 730.009-QG, volume of 300 µl) at various depths (0 depth, which is the surface, -100, -200, -300, -400, -500, and -600 µm depth) for 80 nm AuNPs-BPT using a 785 nm laser.

OriginPro software was used to analyse the Raman spectra. Figure 3.7 shows the procedure applied to each spectra, starting with (i) the raw Raman spectrum, then (ii) baseline anchor points subtraction, and (iii) baseline-corrected spectrum.

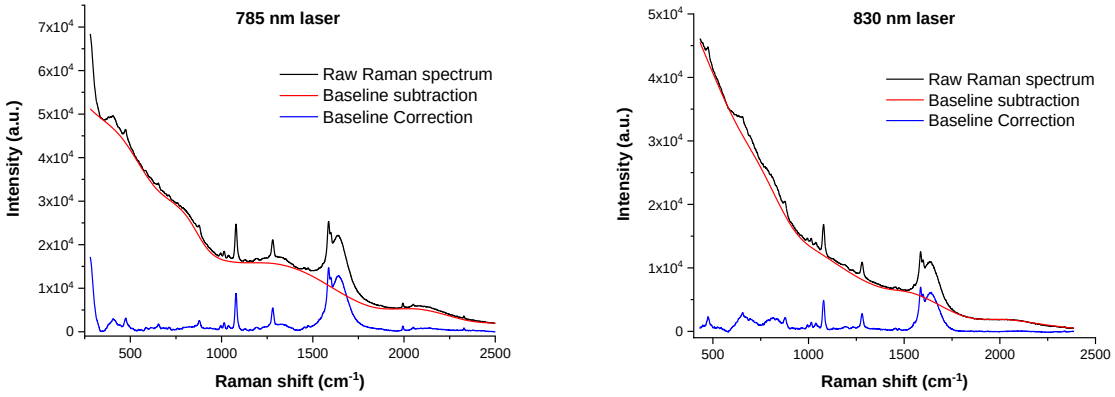

Figure 3.7 Data processing applied to the Raman spectra at 785 and 830 nm of a 5 nm AuNPs-BPT solution: raw spectrum (black), baseline (red), and baseline-corrected spectrum (blue).

The SERS enhancement factor (EF) is a key parameter for performance evaluation of SERS-active substrates. Various definitions of EF have been proposed.[178-180] In this study, the following method was used to assess the EF of Au nanoconstructs: 1 μL droplet of solution containing the labelled nanoconstructs was deposited on the surface of a quartz microplate and measured with Raman microscopy (single spectrum) at both 785 and 830 nm; the EF was then evaluated for each of the three most prominent peaks of the Raman reporter benchmarked against the same peaks of the Raman label aqueous solution in the absence of NPs:

$$EF = \frac{I_{SERS}/N_{SERS}}{I_{Normal}/N_{Normal}} \qquad (3.1)$$

where I_{SERS} and I_{Normal} are the peak height intensities of the SERS and Raman signals of Raman reporter molecules, respectively, whereas N_{SERS} and N_{Normal} are the number of Raman reporter molecules calculated in the presence of gold nanoparticles (SERS) and in the absence of them (Raman spectroscopy).

For the Raman experiment, the number of reporter molecules in one drop of reporter aqueous solution (at $9.1 \cdot 10^{-5}$ M concentration) was calculated from the equation:

$$N_{Normal} = \frac{\mathrm{m}}{M_w} \times N_A \qquad (3.2)$$

where m, M_w, and N_A are the mass of Raman reporter (in units of g) obtained by multiplying the volume by the density (1.3 g/cm^3 for 4-MBA; 1.2 g/cm^3 for 2-NT and 4- AATP; 1.1 g/cm^3 for BPT),[181-184] the molecular weight (g/mol) and Avogadro constant (molec/mol).

For the SERS experiment, Eq. 3.2 was used to calculate the number of Raman reporter molecules in the nanoparticle solution. After determining these values, they were substituted into Eq. 3.1 to obtain the EF for the NPs.

Note that the assumption here is that all Raman reporter molecules added to the NP solution are attached to the gold nanoparticles. In other words, the N_{SERS} is equal or less than what is calculated because some of the Raman reporter molecules might not be attached to the gold nanoparticles and, consequently, the final EF can be more than what was calculated.

3.4.6 SRS

The cells in glass bottom dishes were imaged using Stimulated Raman Scattering (SRS) after treatment with nanohybrids and Raman reporter molecules. SRS imaging was largely carried out using an InsightX3 femtosecond laser in the form of excitation (Newport SpectraPhysics), 802 nm (pump beam) and 1045 nm (Stokes beam), as previously reported.[185, 186] The power intensity at the samples was 1 mW and 2 mW for the Stokes and pump beam, respectively. The beams were then further chirped in order to generate the picosecond pulses. The delay between the pump and the Stokes beams was also controlled within the unit; changing the delay allows different Raman vibrations to be probed within an approximately 250 cm^{-1} range for hyperspectral data acquisition. Moreover, the temporal overlay was scanned through the spectral focusing - timing and recombination unit (SF-TRU). These generate the coherent spectra of coherent Raman scattering of samples. The experiment had specific parameters in which settings had to be placed. As shown in Table 3.2, 802 nm as a wavelength for the pump beam in the high wavenumber (CH stretching) region with proper delay positions (91.02 mm for SRS and TA in cells and gold nanorods (AuNRs) imaging; and 92.21 mm for TA in AuNRs imaging) for 3D imaging, with the scanning speed of 8 µs/pixel, or with a starting position of 90.25 mm and end position of 92.5 mm were set for the hyperspectral imaging. Lastly, all SRS images of 4T1 cancer cells and AuNRs samples were taken at 5.3X magnification. The SRS signal was collected in the forward direction using a modified confocal microscope (Olympus FV3000) which includes a 1.2 NA water immersion objective (Olympus UPlanSApo/IR 60X). The coherent anti-Stokes Raman scattering (CARS) signal was filtered out using a long pass dichroic beam splitter (Chroma DC/T760lpxr) followed by two filters (Chroma ET650/45x) and detected using a photomultiplier tube (PMT, Hamamatsu R3896).[185] The SRS signal was further recorded in the forward direction with a 1.4 NA oil immersion condenser (Nikon D CUO DIC). The signal was detected through a lock-in amplifier and photodiode (APE SRS detection set), and 1045 nm was blocked through the photodiode by utilising the following filters: Chroma CARS 890-210 and Edmund Optics 950 nm 4OD short pass filter.

Table 3.2 Experimental parameters used in SRS imaging measurements.

Wavelengths	802 nm and 1045 nm
Delay positions for 3D imaging	91.02 mm = 2928 cm^{-1} for SRS and TA (4T1 cancer cells and AuNRs imaging) 92.21 mm = 3141 cm^{-1} for TA (AuNRs imaging)
Pump power	2.0 mW
Stokes power	1.0 mW
Start delay position of the hyperspectral scan	90.25 mm = (2788.8 cm^{-1})
End delay position of the hyperspectral scan	92.25 mm = (3148.8 cm^{-1})
Speed	8 µs/pixel
Zoom	5.3X

In the data analysis of SRS measurements, the method of Multivariate Curve Resolution (MCR) analysis described in ref. [187] was used to decompose spectra from different cellular structures or AuNRs. MCR analysis is a decomposition method whereby a matrix of concentration for each component and the corresponding spectrum is computed. The MCR analysis with the constraint of non-negative concentrations and spectra gives rise to different components that contribute to the hyperspectral stack.

3.4.7 Photothermal Therapy Setup

Figure 3.8 shows the PTT setup which involves a 808 nm laser, sample with the thermocouple inserted into the nanoparticles solution; the sample stirrer is inside the cuvette to stir the nanoparticles solution during the laser exposure, and power meter. The setup also includes a laser fiber for exposing the sample, the component for measuring the elastic scattering, the component for measuring the inelastic scattering (Raman spectroscopy) and a power meter for measuring the power of laser irradiation at the sample.

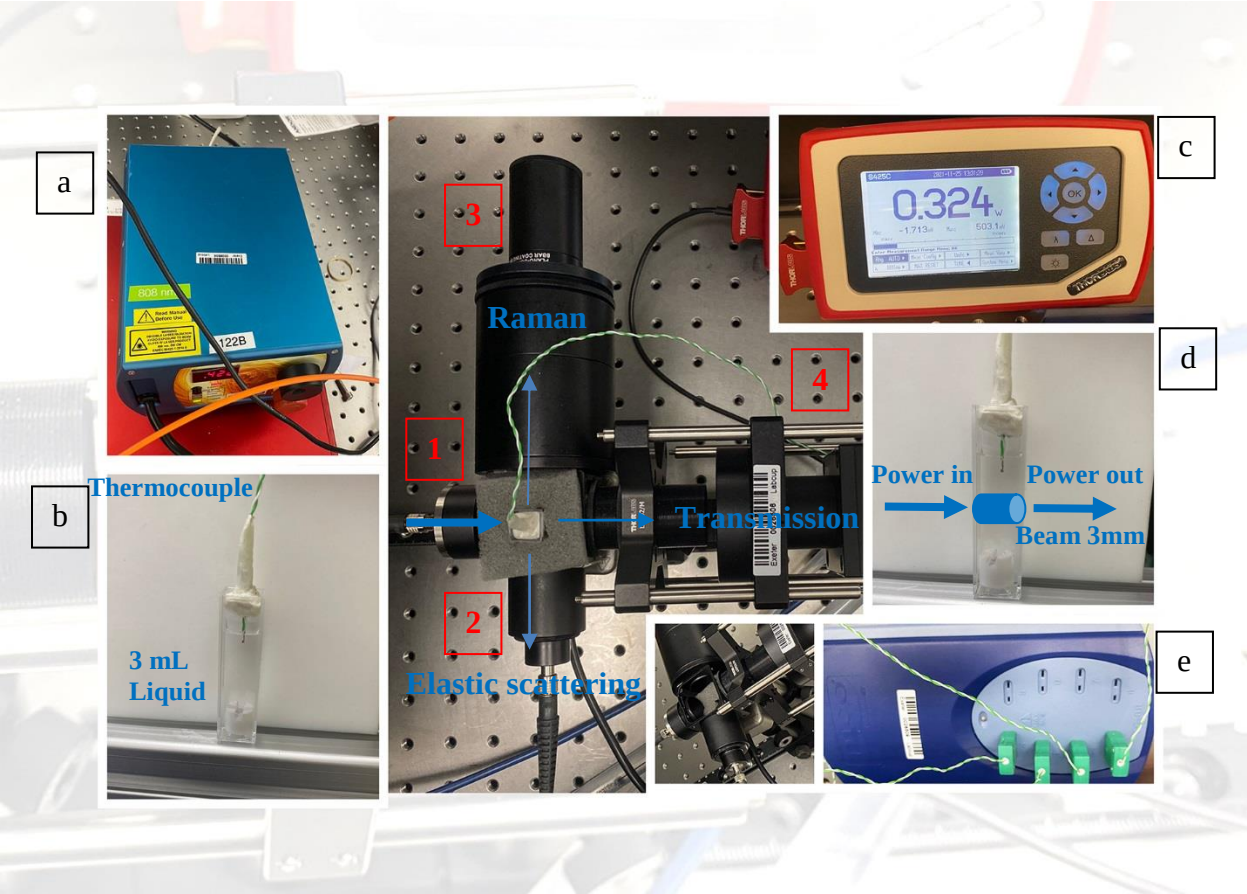

Figure 3.8 The PTT setup which consists of ; (a) laser 808 nm for (1) exposing the sample, (b,d) Sample of nanoparticle solution with magnetic stirrer and used (2) UV- visible spectrometer for measuring the elastic scattering and (3) The spectrometer for measuring the inelastic scattering (Raman spectroscopy), (c) Power meter for (4) measuring the power of laser passed the sample in the cuvette. (e) digital thermometer to measure the temperature into the solution.

Temperature measurements

A plastic vial containing nanoassemblies solution (3 ml) was put in the sample holder and exposed to the laser beam (~3 mm diameter). The temperature was recorded by a digital thermometer using a thermocouple probe with an accuracy of 0.1°C (Pico Technology, Cambridgeshire, UK) inserted into the solution. The metallic head of the thermocouple was mounted away from the laser path to not have any significant contribution to heat generation in the sample. To obtain a uniform

temperature increase through the whole sample, a small magnetic stirrer was mixing up the solution in the cuvette during the experiment. All measurements were performed three times.

Laser power dissipation

The power of the laser beam passed through the sample was measured by a power meter (Thorlabs, Newton, NJ, USA). The power dissipated in the sample (both scattered light and absorbed light) was calculated by subtracting the output measured power from the initial laser power (500 mW). The temperature increase in the solution was due to the light absorbed by the AuNPs and the water and vial holding the sample.

Elastic scatting measurements

Part of the dissipated laser energy would be absorbed by the nanoassemblies and subsequently converted to heat, while the other part would be elastically scattered by the NPs within the sample cuvette. To measure the relative number of elastically scattered photons, a fraction of the scattered photons were collected at 90° to the illumination beam and measured by a UV-vis-NIR spectrometer (Ocean optics, St. Petersburg, FL, USA), demonstrating that this was elastically scattered light and not fluorescence or Raman photons.

CHAPTER 4
CHARACTERIZATION OF LABELLED GOLD NANOPARTICLES FOR SURFACE ENHANCED RAMAN SCATTERING

4.1 Introduction

Cancer is a major concern for our society as it is the second leading cause of death worldwide, with around 10 M deaths estimated in 2018.[1] Despite the cancer burden continuing to grow, the survival rate of many cancers is improving thanks to early detection. Amongst the techniques that have shown potential to improve cancer diagnosis, Raman spectroscopy is especially advantageous in that it is nondestructive and chemically specific, hence providing a molecular fingerprint of the sample, with quantitative information. A drawback is the intrinsically small scattering cross-section of biomolecules or the change in biomolecular signal between tumour and healthy cells, which makes it challenging to accurately detect pathology-specific signatures using conventional spontaneous Raman techniques.

When combined with a given nanomaterial, Raman spectroscopy has been shown to be more effective in detection and mapping of cancer cell models.[4] For many years, scientists in multiple research areas of physics, chemistry, material science and life sciences have applied the Surface Enhanced Raman Scattering (SERS) technique to detect specific molecules present in small concentrations in biological media. SERS has several advantages over traditional vibrational spectroscopy techniques as it has enhanced molecular sensitivity, selectivity, and accuracy. Sensitivity in SERS spectroscopy is improved by amplification of Raman signals of biomolecules in the vicinity of active surfaces such as silver, gold, or nanostructures (nanofibres, nanowires, nanowhiskers, nanorods, and nanostars). The marked signal enhancement of the order of $10^4 – 10^{10}$ that originates from the localized surface plasmon resonance (LSPR) can allow single molecule detection of species that are in close proximity to the nanomaterial's active surface. Therefore, specific Raman signatures with strong sensitivity can effectively be disentangled from the much weaker spectrum of other non-proximal molecules.

SERS-based techniques have been used in affordable, field-transferable, qualitative and quantitative detection of biomarkers.[188, 189] In prostate tumour cells, nanoparticles have been deployed to enable a viable SERS-based method for differentiating tumour and normal cell

lines.[190] According to Szekeres and Kneipp,[191] the formation of nanoaggregates which can significantly augment the SERS detection can be impaired due to multilayer protein adsorption (protein "corona") and high viscosity on the nanoparticles surface for providing high SERS response, when estimating cellular protein concentrations. In this regard, further positioning and development of intracellular aggregates can produce high SERS signals in live cells. Owing to their critical surface concentration or area, gold nanoparticles (AuNPs) become optimal when their size is around 50 nm in diameter. Furthermore, minimum toxicity has been shown for AuNPs of 50 nm size with biomolecules at biological concentrations.[192] Therefore, the introduction of a minimum amount of gold can be suitable for detecting essential biomolecules at biological concentrations when using SERS with the lowest possible toxicity.[193] Precisely, the advantages of SERS-active nanoparticles include providing higher sensitivity, unparalleled multiplexing abilities, and accurate signal specificity as compared to conventional imaging models.[194]

Previous works have investigated the LSPR and SERS activity of AuNPs in a similar range of sizes as studied here, using rhodamine 6G,[195] malachite green isothiocyanate[196] or oxalate salt,[197] but crucially not with sets of different Raman labels to single out optimal candidate(s) for SERS tagging.

The present study is aimed to characterize colloidal AuNPs of different sizes and with different Raman labels or *reporters* using Transmission Electron Microscopy (TEM), UV-visible spectrophotometry, Dynamic Light Scattering (DLS), and Raman micro-spectroscopy. 4-MBA, 2-NT, 4-AATP and BPT were selected as they are organic probe molecules with a thiol and aromatic groups, as well as an amide in 4-AATP and a carboxylic group in 4-MBA which can form self-assembled monolayers (SAM) that can be used for development of SERS sensors. Results are discussed and a selection is made for the AuNP candidates to be used in further SERS application to nanotheranostics. The novelty of this work is in a comparability study of different size nanoparticles with four Raman labels. It is the first time that this has been performed to test these Raman labels at two NIR excitation wavelengths, 785 and 830 nm. All the work in this chapter has been conducted by the author.

4.2 Results

Figure 4.1 shows the transmission electron micrographs of 4-MBA, 2-NT, 4-AATP and BPT labelled AuNPs. It can be seen that the AuNPs are spherical in shape, and the label produces some grey shadowing on the nanoparticle surface.

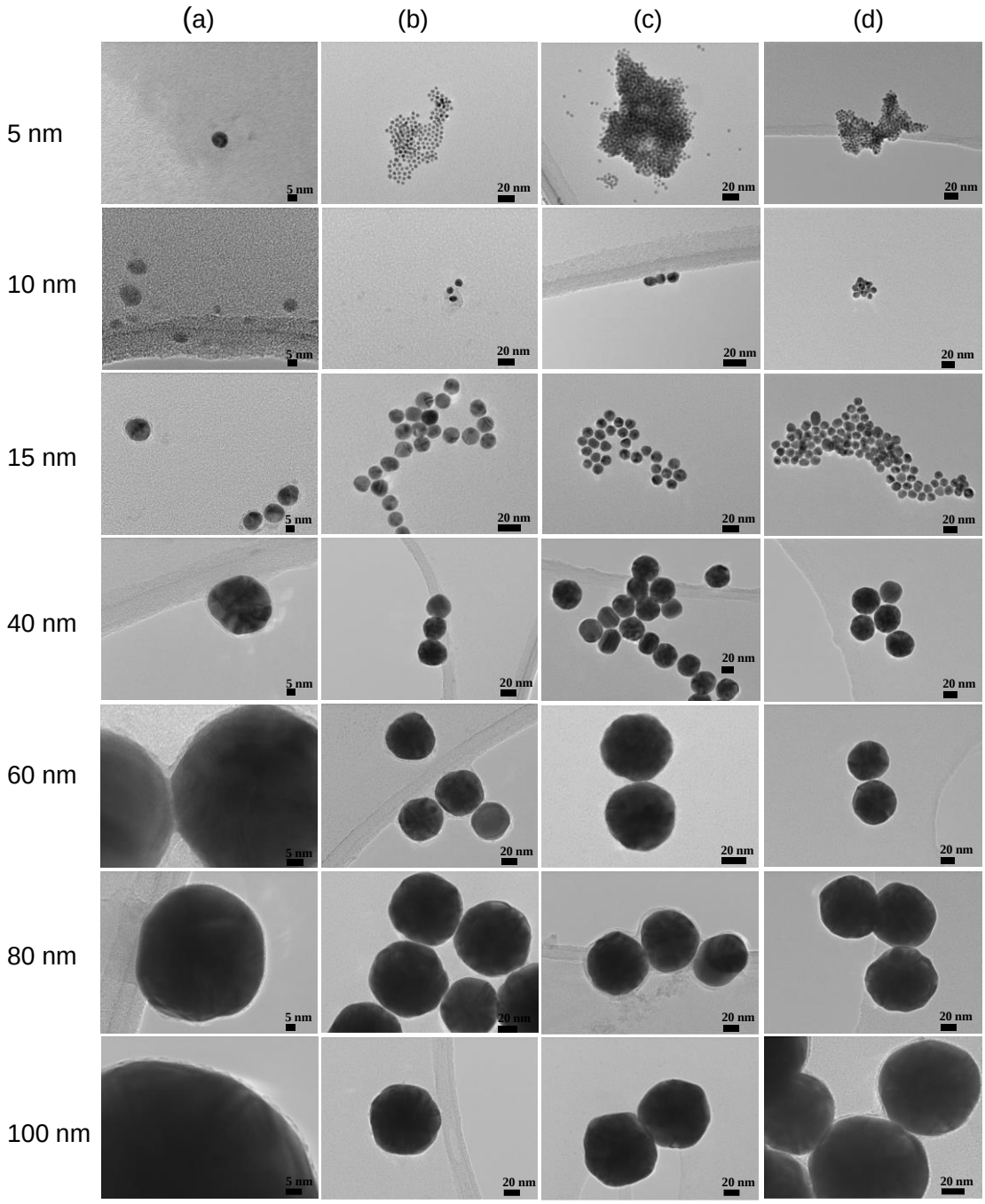

Figure 4.1 TEM images of (a) 4-MBA, (b) 2-NT, (c) 4-AATP and (d) BPT labelled AuNPs of different size ranging between 5 nm and 100 nm. Scale bar: 5 nm in (a); 20 nm in (b-d).

Figure 4.2(a) illustrates the UV-visible spectra of the bare AuNP solutions showing the redshift of the LSPR shifts with increasing NP size, as it is expected for these solutions. Figure 4.2(b) is a plot of the LSPR maximum wavelength versus AuNP size for all the solutions in this study. It shows that 2-NT and BPT labelling produce the largest redshift (~14 nm) in LSPR compared to 4-MBA and 4-AATP (Larger shifts observed for 5-15 nm 2-NT, 4-AATP, and BPT labelled AuNPs may be due to aggregation).

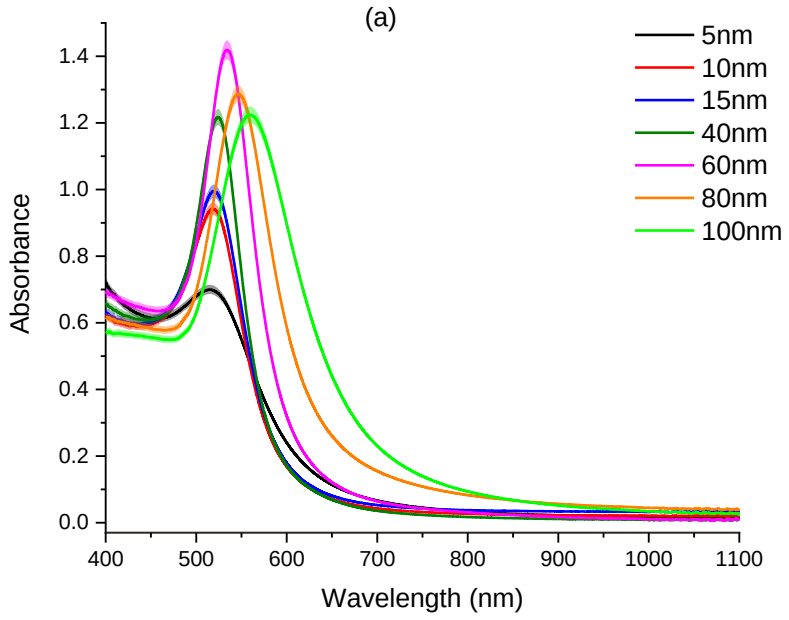

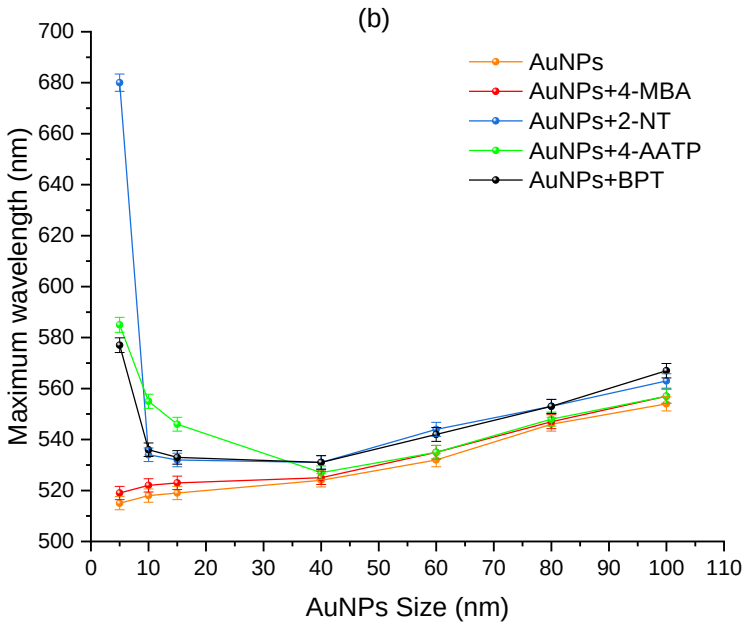

Figure 4.2 (a) UV-visible spectra of colloidal AuNPs of different size ranging between 5 nm and 100 nm. (b) Plot of the localized surface plasmon resonance maximum wavelength vs. AuNP size for all the solutions. Error bars denote the standard deviation.

Figure 4.3 illustrates the results of DLS measurements of all AuNP solutions. In the absence of a label, the measured particle sizes essentially reproduce the nominal sizes of AuNPs. In contrast, in the presence of a label, the particle sizes are consistently larger, especially with 2-NT and BPT labels that have two benzene rings.

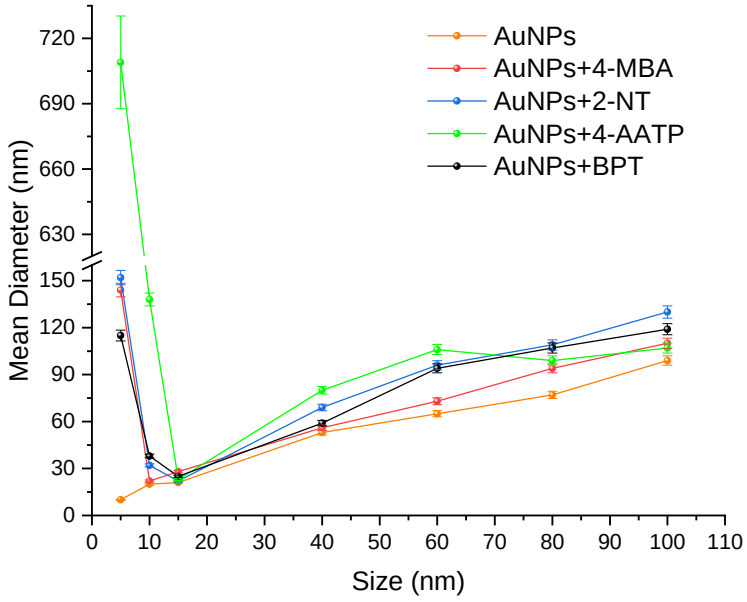

Figure 4.3 Plot of the DLS-derived AuNP size vs. nominal size for all the solutions. Error bars: standard deviation.

When comparing different sizes of AuNPs, based on Figure 4.2 and Figure 4.3, it appears that only nanoparticles with a diameter above 15 nm do not show aggregation. Therefore, a meaningful comparison can only be made with larger nanoparticles.

Figure 4.4 shows plots of the localised surface plasmon resonance maximum wavelength vs. DLS-derived AuNP mean diameter for (a) raw AuNPs and NPs labelled with (b) 4-MBA, (c) 2-NT, (d) 4-AATP, and (e) BPT. In most cases, apart from Figure 4.4d and a few outliers, the plots show a regular increase of the LSPR maximum wavelength with increasing size of the AuNPs.

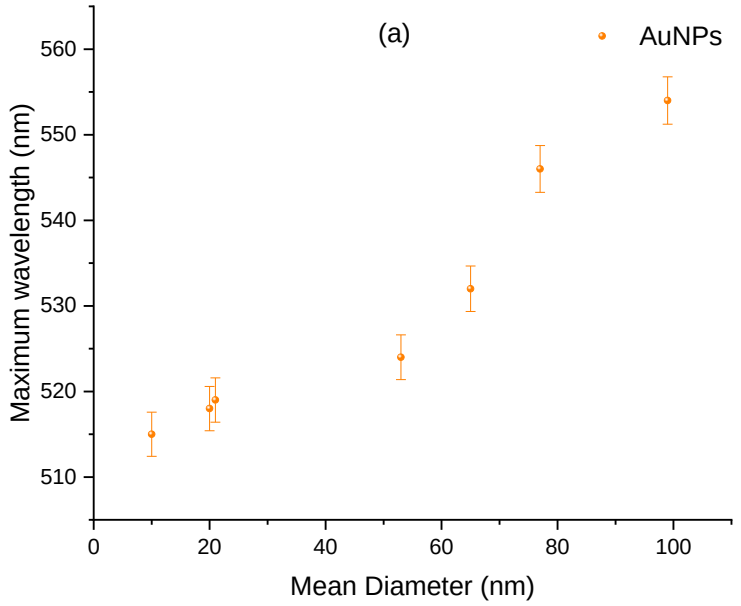
(a)
AuNPs
Maximum wavelength (nm)
Mean Diameter (nm)
510
520
530
540
550
560
0
20
40
60
80
100

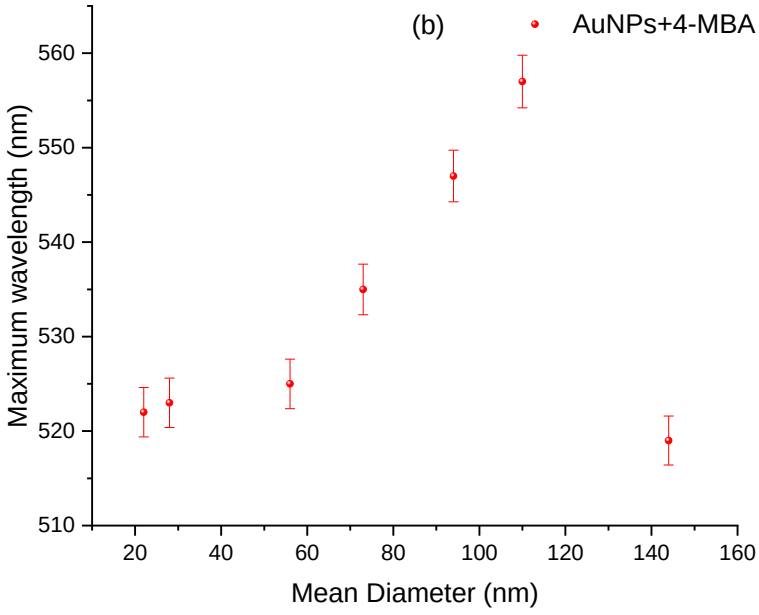
(b)
AuNPs+4-MBA
Maximum wavelength (nm)
Mean Diameter (nm)
510
520
530
540
550
560
20
40
60
80
100
120
140
160

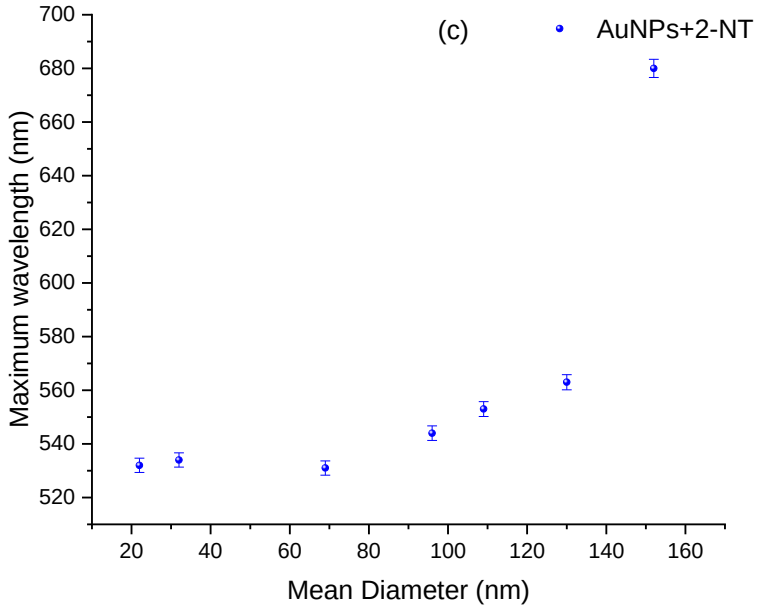
(c)
AuNPs+2-NT
Maximum wavelength (nm)
Mean Diameter (nm)
700
680
660
640
620
600
580
560
540
520
20
40
60
80
100
120
140
160

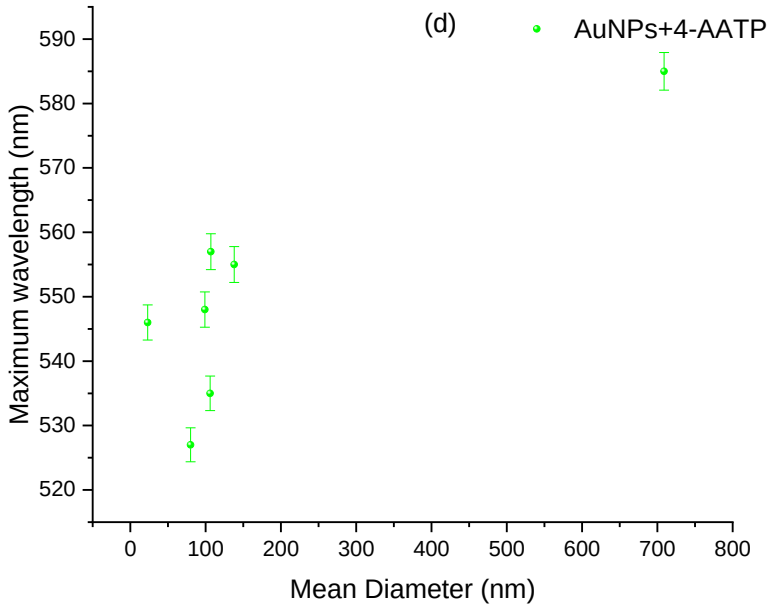
(d)
AuNPs+4-AATP
Maximum wavelength (nm)
Mean Diameter (nm)
590
580
570
560
550
540
530
520
0
100
200
300
400
500
600
700
800

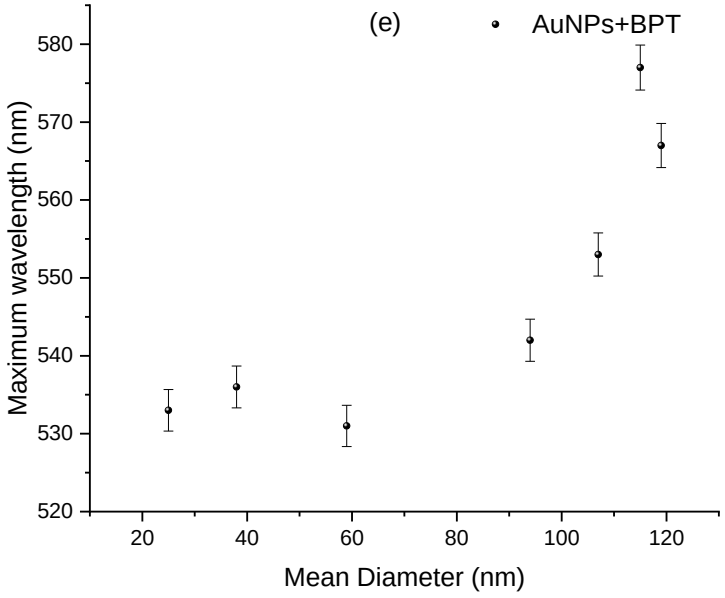

Figure 4.4 Plot of the localized surface plasmon resonance maximum wavelength vs DLS-derived AuNP mean diameter for (a) bare AuNPs, (b) 4-MBA, (c) 2-NT, (d) 4-AATP and (e) BPT labelled NPs. Error bars: standard deviation.

The surface charge (zeta potential) of the gold nanoparticles before and after adding the Raman reporter was negative, and the highest charge was observed for 60 nm AuNPs labelled with 4-MBA (–61 mV), as shown in Figure 4.5.

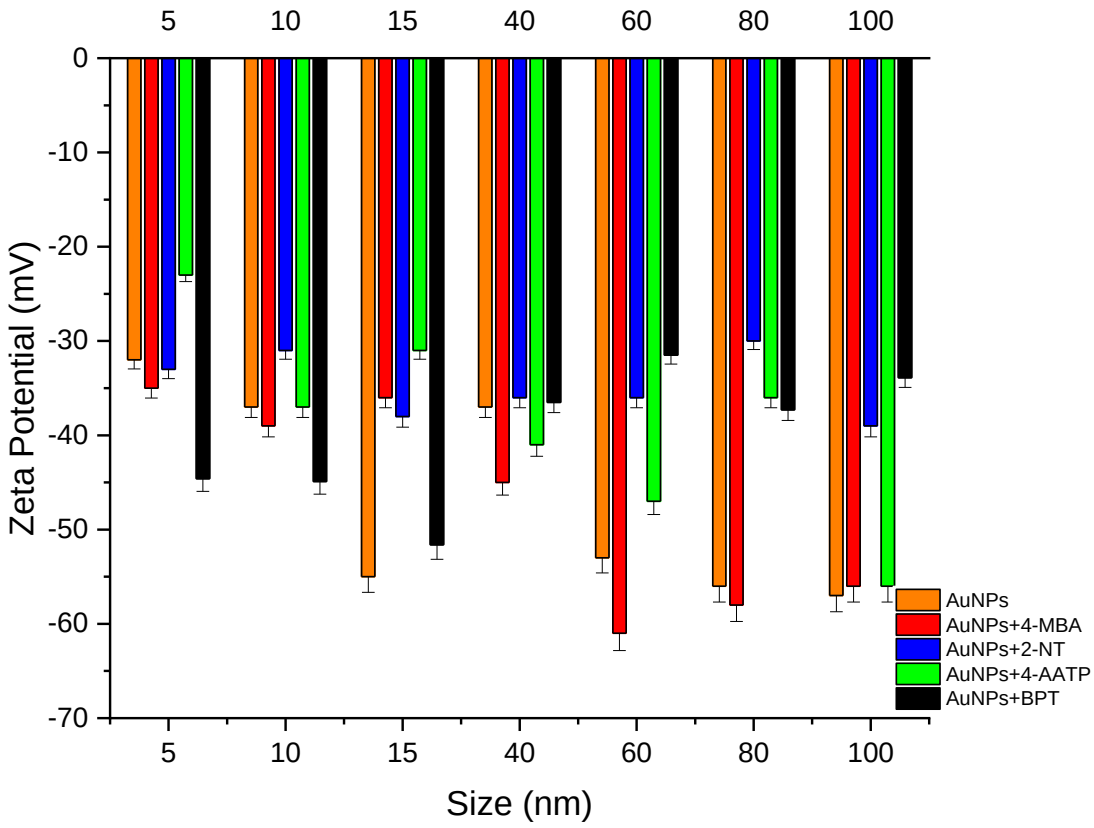

Figure 4.5 Zeta potential of (orange) bare AuNPs, and in the presence of a label: (red) 4-MBA, (blue) 2-NT, (green) 4-AATP, and (black) BPT for different NP sizes. Error bars: standard deviation.

Figures 4.6-4.9 present the Raman spectra of labelled AuNP solutions prepared using different NP sizes and measured at two wavelengths, 785 nm and 830 nm. For comparison, the spectrum of the BPT label dissolved in ethanol solution (at the concentration of $9.1 \cdot 10^{-5}$ M) is also shown. Note that there was no Raman signal arising from the AuNPs themselves when reporters were not added (see "water" spectrum).

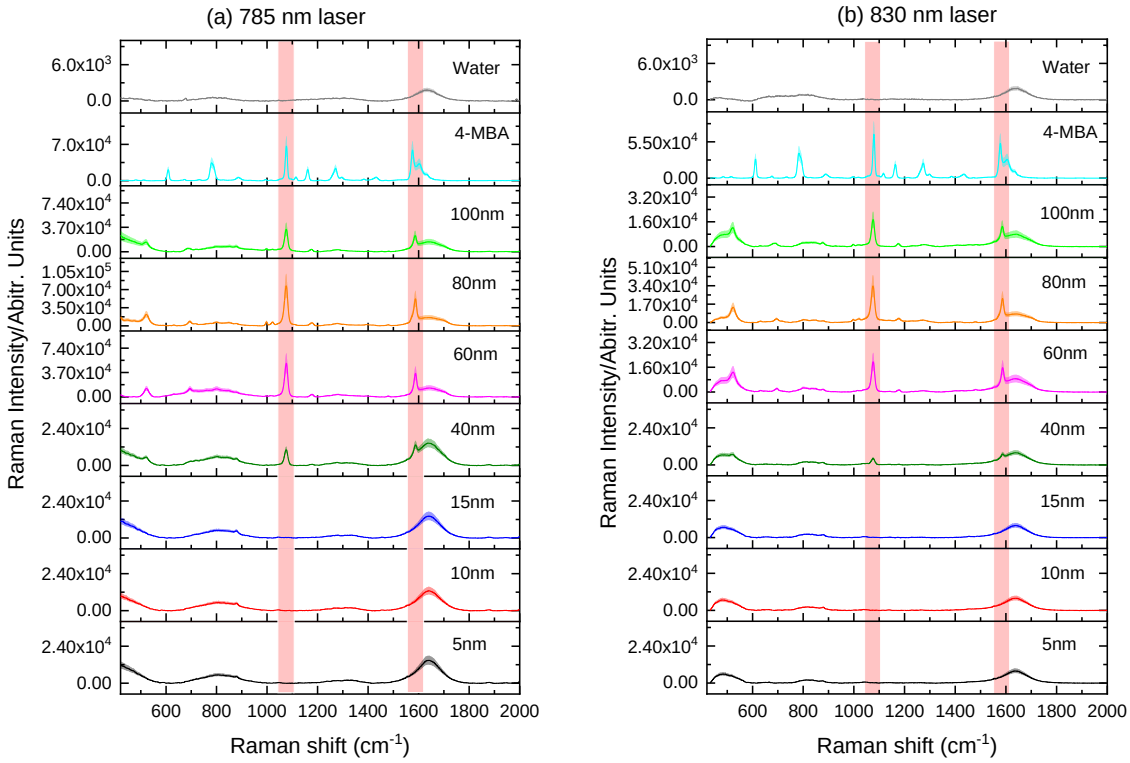

Figure 4.6 Raman spectra of 4-MBA labelled AuNP solutions measured at (a) 785 nm and (b) 830 nm. Dashed lines denote the two most prominent signals of 4-MBA, at 1078 and 1588 cm^{-1}. Shading: standard deviation.

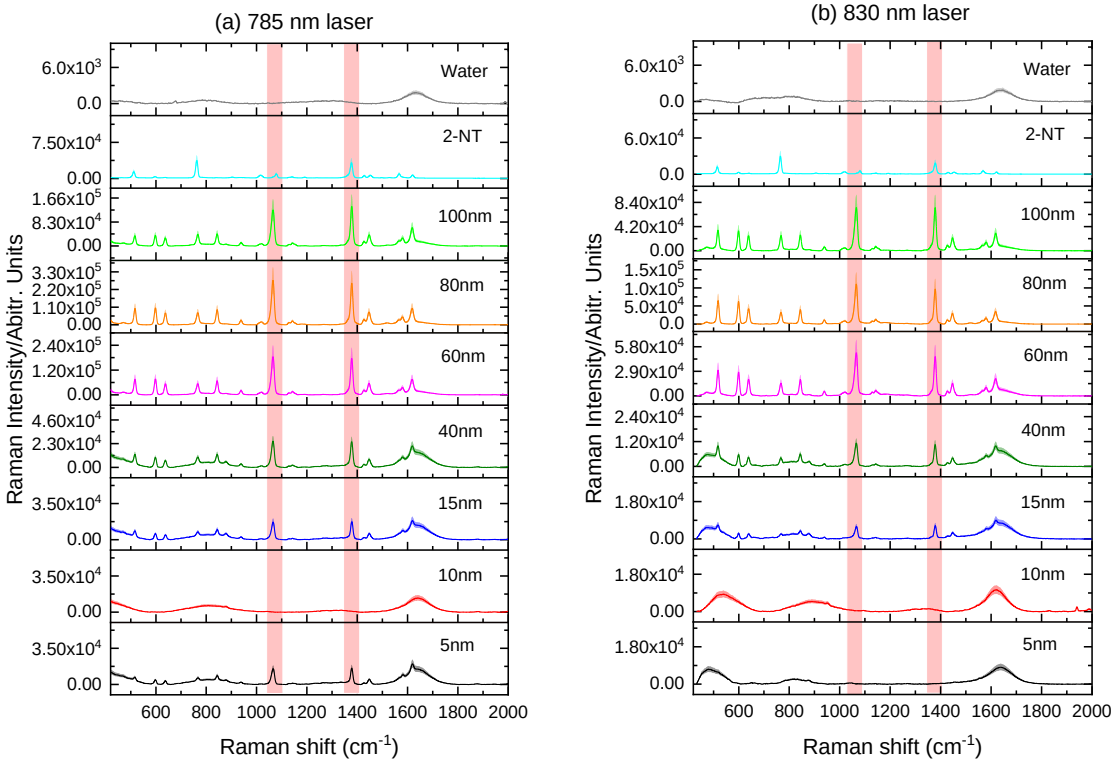

Figure 4.7 Raman spectra of 2-NT labelled AuNP solutions measured at (a) 785 nm and (b) 830 nm. Dashed lines denote the two most prominent signals of 2-NT, at 1066 and 1380 cm^{-1}. Shading: standard deviation.

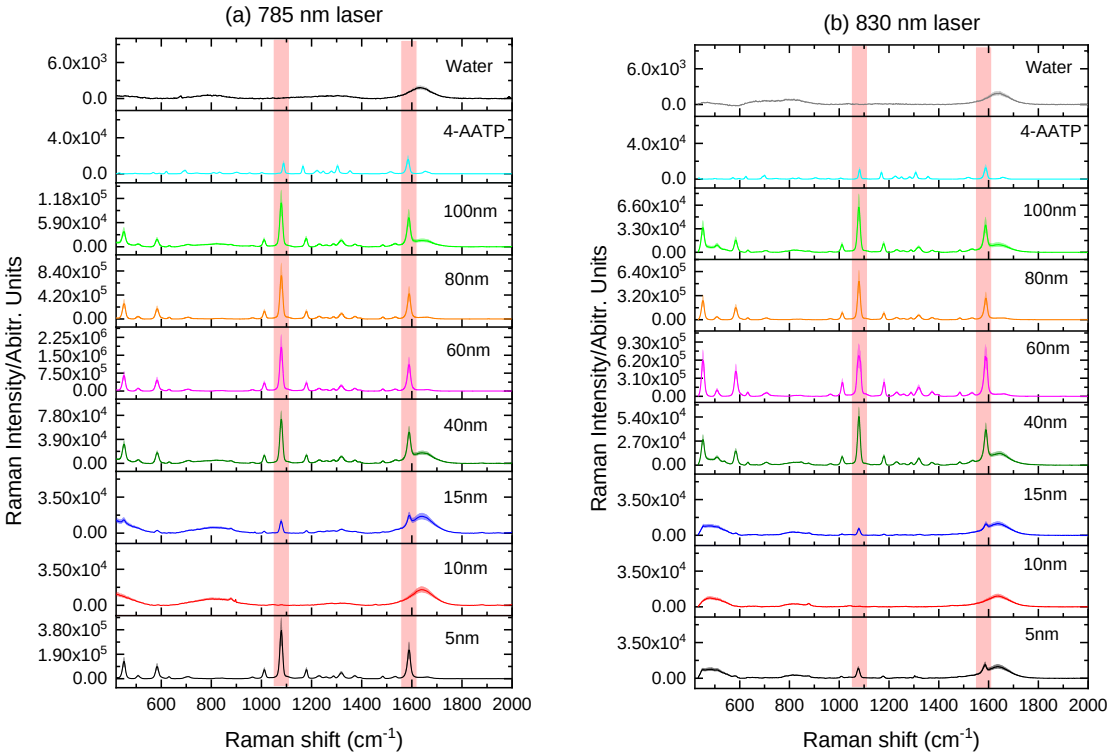

Figure 4.8 Raman spectra of 4-AATP labelled AuNP solutions measured at (a) 785 nm and (b) 830 nm. Dashed lines denote the two most prominent signals of 4-AATP, at 1080 and 1589 cm^{-1}. Shading: standard deviation.

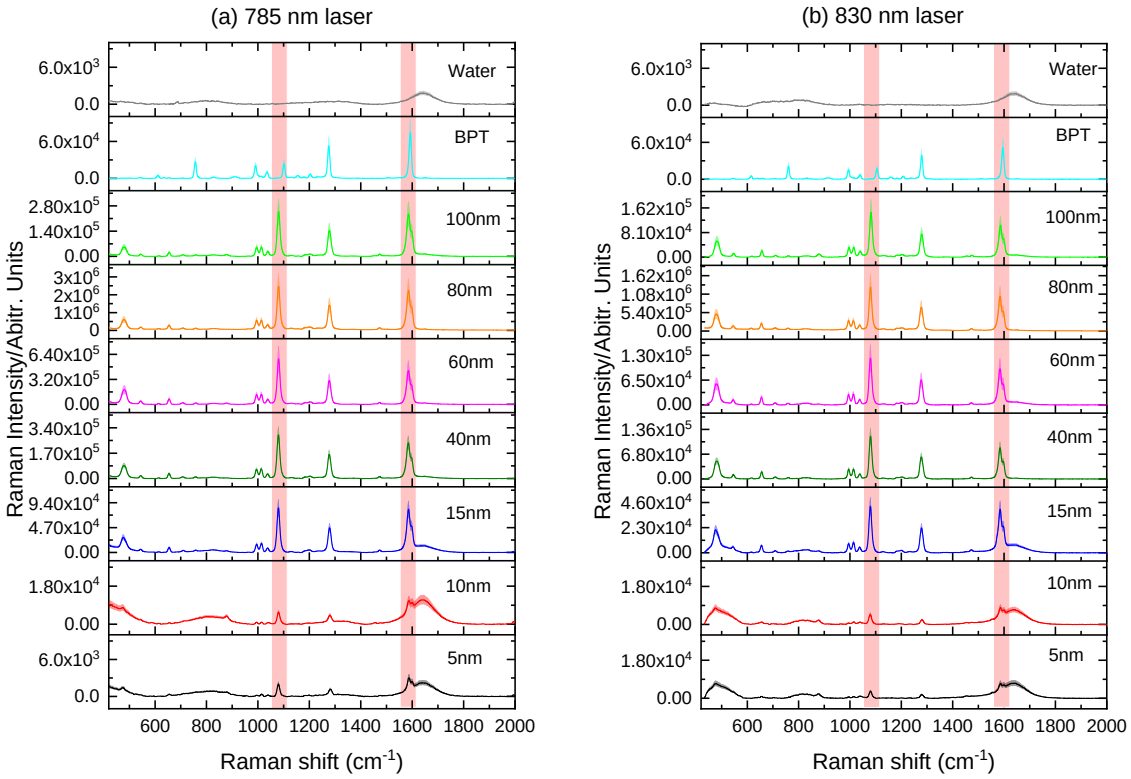

Figure 4.9 Raman spectra of BPT labelled AuNP solutions measured at (a) 785 nm and (b) 830 nm. Dashed lines denote the two most prominent signals of BPT, at 1080 and 1586 cm^{-1}. Shading: standard deviation.

To assess the SERS signals for each individual label, the two dominant vibrational lines corresponding to the C–H rocking (1080 cm^{-1}) and in-plane stretching of the benzene rings (1380 and 1586 cm^{-1}) were selected.[198]

As it can be seen in Figures 4.6-4.9, the occurrence of broader peaks accompanying the SERS signals observed for labelled colloidal gold below 40 nm could be due to aggregation.[199] Conversely, the SERS signal was strong for AuNPs of size comprised between 40 nm and 100 nm, as shown in Figure 4.10.

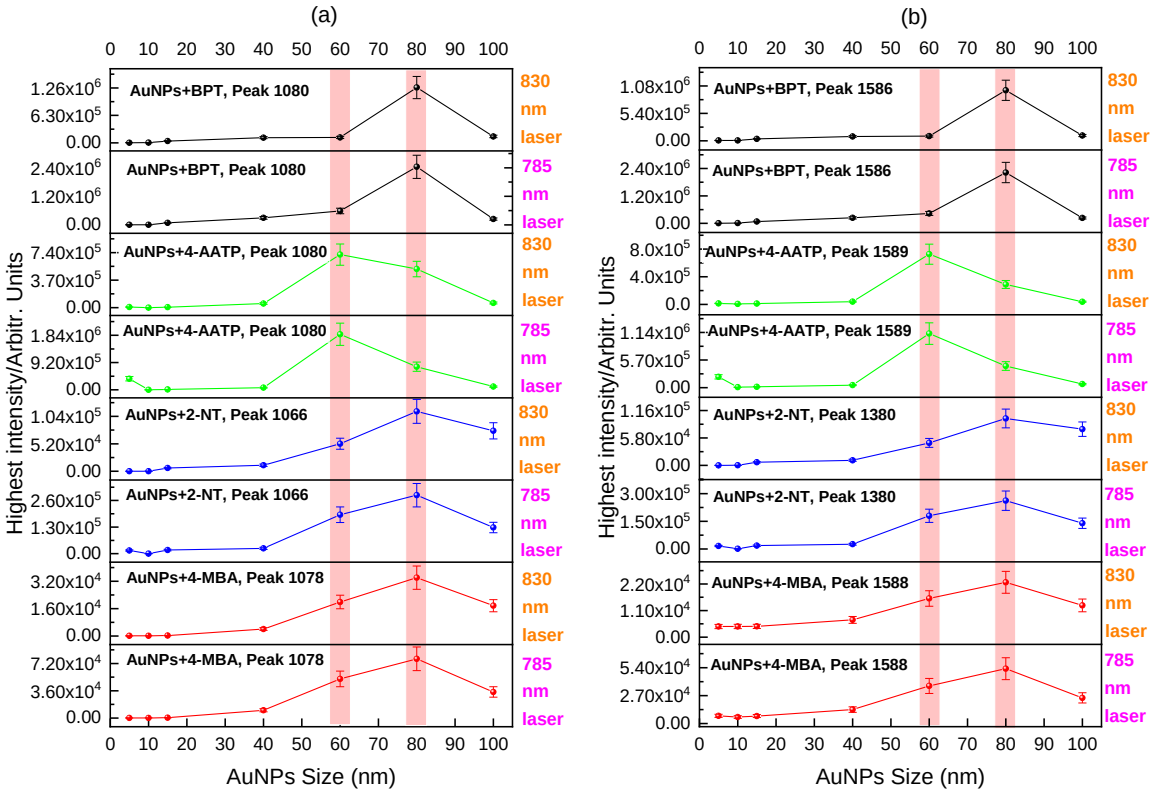

Figure 4.10 Plot of the intensity (height) of the two main peaks at (a) lower and (b) higher wavenumbers for labelled AuNP solutions vs. NP size at 785 nm and 830 nm excitation.

Excitation at 785 nm was found to produce larger signals than those obtained with 830 nm excitation, as it is expected from the wavelength dependence of the scattering intensity.[200] The largest signal was found for BPT labelled 80 nm AuNPs ($2.6 \cdot 10^6$) followed by 4-AATP labelled 60 nm AuNPs ($2.2 \cdot 10^6$) using the 785 nm laser, suggesting that BPT and 4-AATP are the best candidates for Raman labelling of spherical AuNPs with sizes in the range 5 nm to 100 nm.

Figure 4.11 shows the SERS enhancement factor (EF) plotted against NP size at 785 and 830 nm. This graph illustrates the evaluated SERS at the two highest peaks. Peak 1 is at 1078, 1066, 1080, and 1080 cm^{-1} for 4-MBA, 2-NT, 4-AATP, and BPT, respectively, which can be seen in Figure 4.11a. Peak 2 is at 1588, 1380, 1589, and 1586 cm^{-1} for 4-MBA, 2-NT, 4-AATP, and BPT, correspondingly, as shown in Figure 4.11b. It can be seen that the highest EF (of the order of 10^7) is obtained using peak 1 intensities for BPT labelled 80nm AuNPs and 4-AATP labelled 60nm AuNPs, with better sensititivity when employing a 785 nm laser (Figure 4.11a). Slightly lower EFs were obtained using peak 2 intensities (Figure 4.11b).

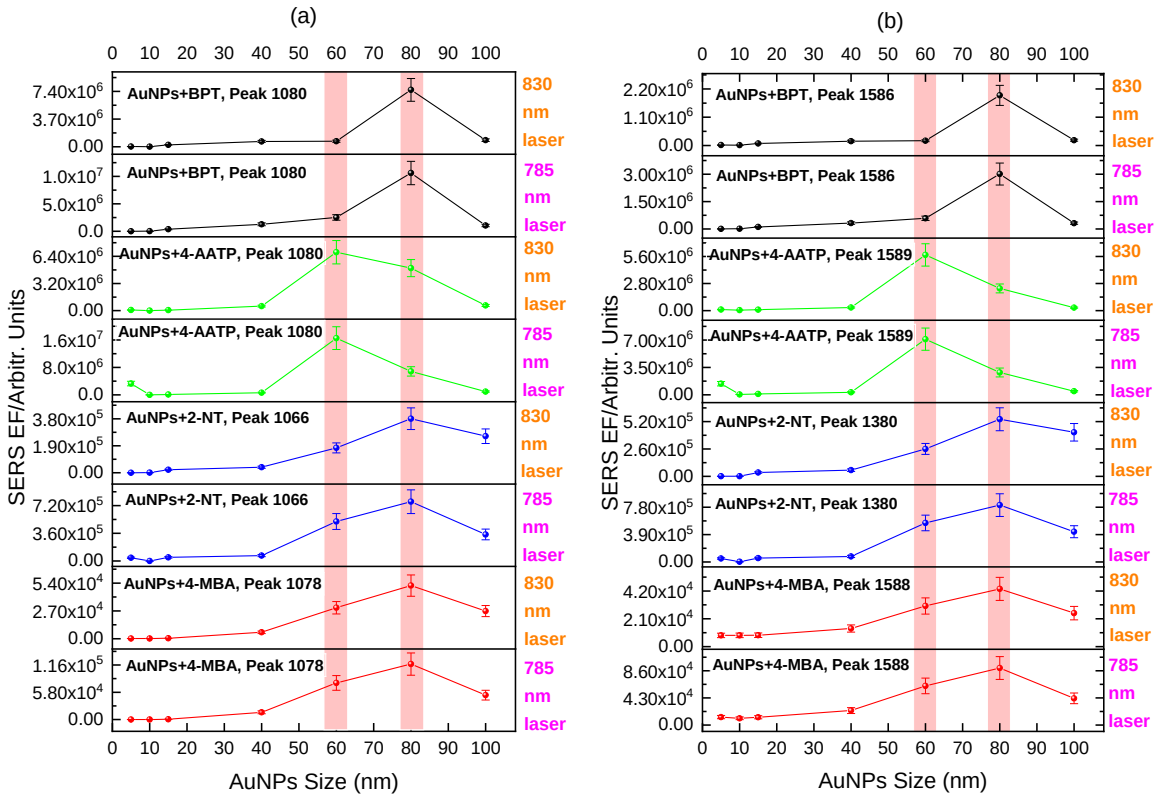

Figure 4.11 Plot of SERS EF of the two main peaks at (a) lower and (b) higher wavenumbers for labelled AuNP solutions vs. NP size at 785 nm and 830 nm excitation.

This study investigated the physical and spectroscopic properties of commercial spherical gold nanoparticles with diameters ranging between 5 nm and 100 nm in aqueous solution with four different Raman reporters, 4-MBA, 2-NT, 4-AATP, and BPT chemisorbed on the nanoparticles surface. The effect of size is very important for nanoparticle-based SERS active substrates. Therefore, it is essential to select the appropriate NP size and the matching excitation wavelength to excite the localized surface plasmon resonance (LSPR) and obtain the best signal from SERS. Results from UV-visible spectrophotometry showed that 2-NT and BPT labelling produce the largest redshift in LSPR. The surface charge (zeta potential) derived from DLS for the gold nanoparticles before and after adding Raman reporters was negative.

Results obtained from Raman measurements on AuNPs with 4-MBA labelling were compared with previous findings on gold nanotips by Gao et al.[201] The authors have observed the highest SERS signals for tips with 40 nm apex diameter using 4-MBA as the probe molecule and an

intensity decrease for tips with 60 and 80 nm. The discrepancy with our data for 4-MBA, which show the strongest signal intensity for gold spheres with 80 nm diameter (Figure 4.10), is plausibly caused by a difference in curvature and associated molecular packing on the gold substrates.

Sizeable signals from all labels were observed with increasing AuNP size above 40 nm (Figure 4.10). Excitation at 785 nm was found to produce larger signals than those obtained with 830 nm excitation, as expected. The largest signal was found for BPT labelled 80 nm AuNPs followed by 4-AATP labelled 60 nm AuNPs, suggesting that BPT and 4-AATP are a preferable choice over 2-NT and 4-MBA for Raman labelling of spherical AuNPs with sizes in the range 5 nm to 100 nm and can therefore be employed in applications of gold-mediated Raman nanotheranostics.

4.3 Conclusion

This study applied Raman spectroscopy along with complementary analytical techniques to characterize and validate the use of four different Raman probing molecules with colloidal gold nanospheres in the range 5 nm to 100 nm as SERS substrate. The results show the strongest SERS signals for 80 nm AuNPs with BPT labelling, followed by 60 nm AuNPs labelled with 4-AATP. Going forward, we expect these findings will underpin the development of novel nanostructures-label conjugates for applications in nanotheranostics.

Raman spectroscopy has been shown to offer the most promise among the different methods used to identify cancer since it is chemically specific and non-destructive. It should be mentioned that, since Raman spectroscopy offers a molecular fingerprint as well as quantitative information about the material, it is regarded as highly beneficial for cancer detection. Furthermore, SERS has several advantages over traditional vibrational spectroscopy techniques, including the ability to improve the Raman signal amplitude of biomolecules. When Raman signals are efficiently disentangled with significant sensitivity, this approach enables to distinguish prominent spectra from molecules in close proximity with the nanosurface versus a considerably weaker spectrum derived from non-proximal molecules, according to empirical evidence. Furthermore, SERS-based approaches are cost-effective, quantitative and qualitative in biomarker detection, and field transportable.

The study's focus was on characterising different sizes of colloidal AuNPs with distinct Raman labels or reporters utilising TEM, DLS, UV-visible spectrophotometry, and Raman micro-

spectroscopy. In this study, 4-MBA, 2-NT, 4-BPT, and 4-AATP were used as Raman labels. Two most prominent vibrational lines were used in the current investigation to assess the SERS signals for each of the unique labels of AuNP particles. The best results in terms of SERS EF were achieved with 80 nm AuNPs labelled with BPT, followed by 60 nm AuNPs labelled with 4-AATP.

Based on UV-visible spectra, the level of absorption for 4-AATP labelled 60 nm AuNPs and BPT labelled 80 nm AuNPs at 785 and 830 nm (wavelengths used in the SERS experiments) is higher than that for the corresponding 100 nm AuNPs. This finding explains the larger SERS enhancement factor observed for these two types of NPs. In a previous work, researchers have investigated Raman labelled gold nanoparticles of different sizes in the range 40.7 nm - 99.64 nm and found that with a laser wavelength $\lambda = 633$ nm the maximum Raman enhancement was achieved for a diameter of gold nanoparticles of ~76 nm.[202] Others have found that Raman labelled 50-to-60 nm gold nanoparticles provided the strongest enhancements.[193, 203] This result has been explained based on the fact that, at 60-80 nm threshold size, the external and internal energy modes are closest, hence resulting in greater SERS activity.

CHAPTER 5
AuNP-LIPOSOME NANOHYBRIDS FOR SURFACE ENHANCED RAMAN SCATTERING AND PHOTOTHERMAL THERAPY

5.1 Introduction

Metallic nanoparticles (NPs) have been widely investigated for cancer diagnostics and therapeutics owing to their good biocompatibility, high binding affinity, high penetrability and targeting ability, as well as low toxicity. Noble metal NPs, e.g. AuNPs, have the ability to produce ultra-sensitive SERS signals, owing to their plasmonic properties in the NIR region, which make them ideal candidates for nanotheranostics. In cancer research, AuNPs are particularly attractive as they provide a platform to which target molecules can be further introduced for selective detection of tumours and tailored ablation via photothermal therapy (PTT) or radiation therapy. In this chapter, the focus is to assess the design and development of biocompatible noble metal NP constructs based on AuNPs and liposomes (or lipid vesicles) functionalised with Raman tags for potential applications in photothermal therapy. This section of the study also emphasises determining why it is preferred to use gold nanospheres with small sizes (e.g. 5 nm diameter), since they are not toxic and do not accumulate in the body. Moreover, this section of the study involves analysis through which it is determined how essential it is for the nanoconstructs to produce a NIR plasmon absorption for improved photothermal therapy. Additionally, it is emphasised assessing the use of liposomes (composition: DSPC:cholesterol 80:20), since they are biodegradable (at temperatures >42-43 °C), safe and can encapsulate active agents such as NPs and drugs. Therefore, various protocols were tested and optimised to prepare these nanohybrids in a range of sizes between 90 and 200 nm made of a template of unilamellar vesicle (ULV) and small AuNPs (5 nm nanospheres) to enable aggregation and prevent toxicity effects when systemically delivered to a living system. Additionally, it was validated that the use of biphenyl-4-thiol (BPT) as Raman reporter molecule provides significant enhancement in SERS signals when used with AuNPs at correct doses and ratios. Furthermore, the analysis also included the use of different polymers such as CTAB and GCPQ to enable binding between gold nanoparticles and liposomes. Optimal SERS signals were observed by using different polymers such as CTAB, GCPQ19, GCPQ20 for enabling AuNPs to attach to the surface of unilamellar vesicles (ULVs) of approximately 100 nm diameter. The size distribution of nanohybrids was measured by DLS and by Nanoparticle Tracking Analysis (NTA).

The nanohybrids were characterised by using TEM, DLS, UV-visible spectrophotometry and Raman micro-spectroscopy. The light-heat conversion efficiency of BPT-tagged AuNPs with liposome were also investigated by measuring their temperature rise over time under 808 nm laser exposure. Additionally, we investigated the toxicity effects of these nanohybrids against triple negative breast cancer cell line (MDA-MB-231) in a concentration dependent manner which showed whether liposome-AuNP constructs are more or less toxic towards cancer cells. Based on this, we investigated whether the hybrid nanostructures are promising in delivering PTT for light-mediated therapy and potentially SERS for Raman diagnostics.

The novelty of this work is in a comparability study of AuNP-liposome constructs based on small (5 nm) spherical gold nanoparticles, with different polymers (CTAB, GCPQ19, GCPQ20) and at different NP:liposome ratios. It is the first time that light-heat conversion efficiency is evaluated for these nanohybrids relative to 5 nm AuNPs alone.
PTT data were collected and analysed by Dr Marzieh Salimi, a former BioSpec team member. SRS imaging measurements and data analysis were performed by Dr Jessica Mansfield at the "CONTRAST" facility. Finally, cytotoxicity tests and data analysis were conducted by Dr Tanveer Tabish, a former BioSpec team member. Everything else is the author's work.

5.2 Results

5.2.1 Synthesis and characterization of liposome

Various protocols were tested and optimised to prepare the liposomes as shown in Figure 5.1a. The liposomes (multilamellar vesicles -MLV) composed of DSPC:Chol with a molar ratio of 8:2 and concentration 2 mg/ml were produced by one of the most common methods for liposome preparation called thin-film hydration method. The composition was selected such that the liposome membrane presents a phase transition at T = 42–43 °C. [116] When sonicated for 3 cycles of 6 mins duration, the size distribution of ULVs was approximately 100 nm diameter as shown in Figure 5.1b (measured by using DLS). The surface charge was negative at around – 15mV, as shown in Figure 5.1b. In addition, the size distribution and concentration of liposomes in suspension were analysed using NanoSight LM10. The NTA software produced the graphs shown in Figure 5.1c. The liposome size was approximately 93 (±4) nm. The estimated liposome concentration was reported as 6.48×10^{9} particles/ml. Figure 5.1d shows transmission electron

micrographs of the liposomes at different concentrations: 2 mg/ml liposome stock solution, diluted 1:500 and diluted 1:1000. It can be seen that some liposome structures appear as flat liposomes that are tilted upright in the methyl cellulose/uranyl acetate film. Because of creating a film that embeds the liposomes, they will end up in various orientations and some of them can be seen as flat liposomes rather than round structures.

Furthermore, NanoSight was utilised to record the video data of liposomes in aqueous solution. Screenshots show optimal light that is scattered off the vesicles (Figure 5.1e): from left to right- at 5 and 60 sec. A number of at least five 60 s videos of the vesicles undergoing Brownian motion were recorded by NanoSight. These recordings were then analysed for size distribution and particle concentration utilising the integrated NTA v 3.4 software.

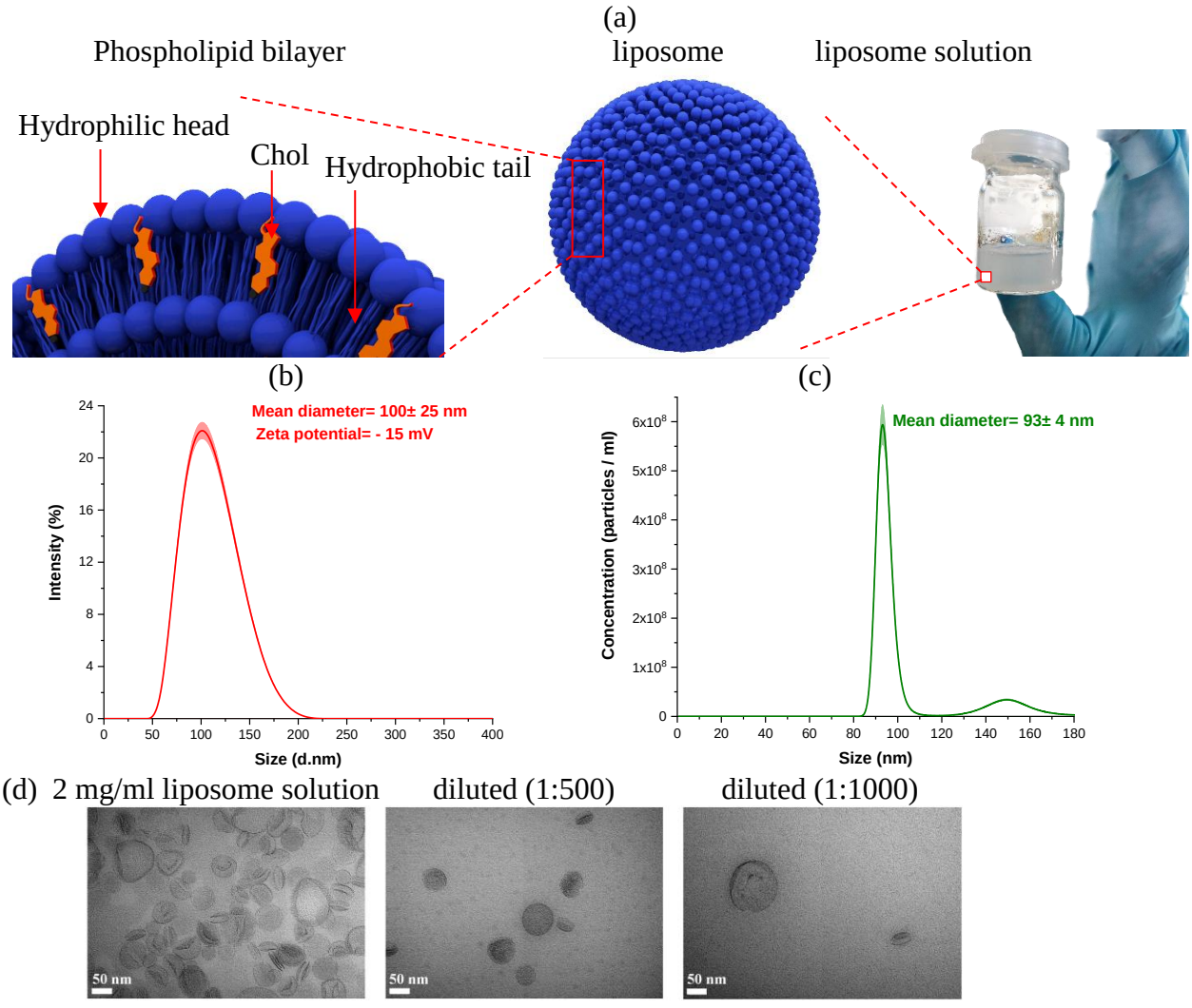

(e) 5 s exposure 60 s exposure

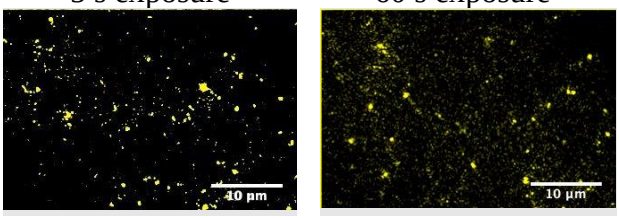

Figure 5.1 Characterization of liposome solutions. (a) Liposome composition: DSPC:Chol (8:2 wt%). (b) DLS particle size distribution of a 2 mg/ml liposome solution. (c) Liposome size distribution plotted in terms of concentration in 10^7 particles/ml by Nanosight Nanoparticle Tracking Analysis (NTA). (d) TEM images of a 2 mg/ml liposome stock solution, diluted (1:500) and (1:1000). Scale bar: 50 nm. (e) NTA images showing light scattered off liposomes; acquisition time: 5 s and 60 s. Scale bar: 10 µm.

In this work, BPT-labelled liposome−AuNP hybrids using DSPC:Chol liposomes and surface-functionalized AuNPs were synthesised by self-assembly utilising the methodology of lipid film hydration and sonication. As the phase transition of our nanohybrids occurs at T = 42–43 °C, the heat generated at 43°C can destroy the cancer cells and simultaneously degrade the nanohybrids in a process that is efficient in clearing the 5nm AuNPs through renal filtration.

5.2.2 Design and characterization of nanohybrids

Herein, the thin lipid film hydration method followed by sonication, purification, and addition of different compounds was used to design the novel liposome-gold nanohybrids. The following sections will provide more details of the sample preparation.

5.2.2.1 Nanohybrid design

Liposomes have a negative surface charge, and bare AuNPs are negatively charged as well. Therefore, Hexadecyltrimethylammonium bromide (CTAB polymer) was added to reverse the surface charge of the AuNPs. Figure 5.2 shows the achieved nanohybrid structure which consists of (a) liposome made of DSPC:Chol (8:2) (negatively charged), (b) AuNPs (negatively charged), (c) BPT (with thiol group) as Raman reporter (negatively charged), (d) CTAB linker (positively charged).

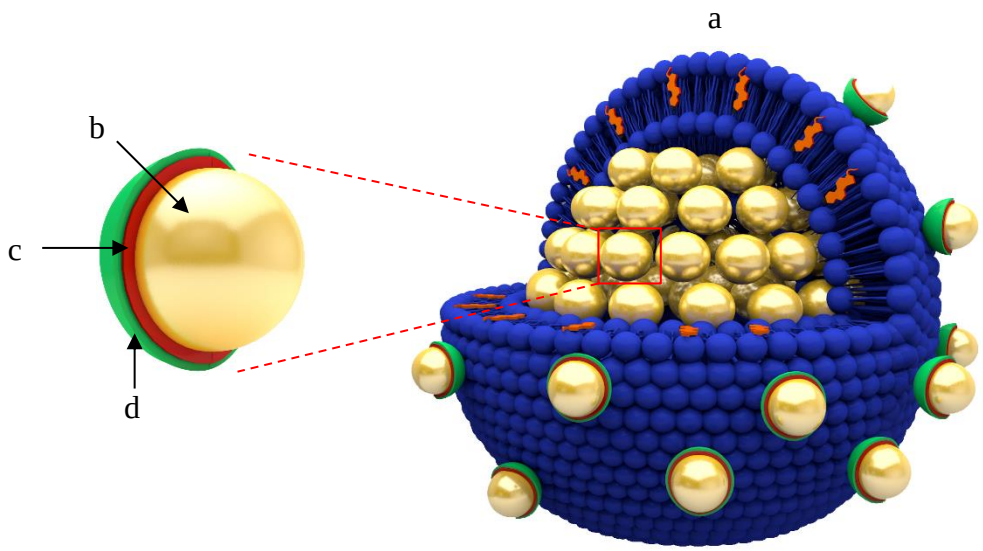

Figure 5.2 Schematic illustration of (a) liposome with (b) gold nanoparticles both on the surface and within the liposome cavity. The NPs are labelled with (c) the Raman reporter BPT and (d) CTAB or GCPQ.

Gold nanoparticles were prepared or used in two different shapes and sizes:

I. 5 nm AuNPs (both supplied from Nanocomposix and synthesised in the lab)
II. 55/15 nm Au nanorods (both supplied from Nanocomposix and synthesised in the lab), and
   A. Nanohybrid with AuNPs encapsulated within the aqueous core of the liposome.
   B. Each commercial or synthetic 5 nm AuNP is
   C. BPT-labelled for Raman signal (SERS) monitoring, and
   D. CTAB-coated, resulting in positive AuNP

According to the random packing density in a 3D model of sphere packing is 64%, each 100nm-diameter liposome should contain ca. 5,120 5 nm AuNPs.[204]

As the Au nanorods have strong absorbance in the NIR region, the nanohybrids will have a response in the NIR range of the electromagnetic spectrum. In this study, AuNPs have the size of 5 nm in diameter (comparable to the thickness of the lipid bilayer, ~5 nm). The hydrophilic CTAB-coated AuNPs added to the liposome solution end up being encapsulated within the aqueous core of the liposome. In fact, the liposomal membrane is of ~5nm thickness, and CTAB polymer is a long chain molecule with a positively charged hydrophilic head. When CTAB is added as a coating to the AuNPs, hence reversing their surface charge (from negative to positive), the nanoparticles

are capable of transmigrating across the liposomal membrane and passively encapsulate within the aqueous core preferentially.[126, 137]

Note that for the AuNPs to be directly deposited on the surface of liposome, they need tethering e.g. by DNA hybridization or the MLVs should be suspended in a solution of AA to which the $HAuCl_4$ is added. AA reduces the valent state of $HAuCl_4$ from Au3+ to Au0 which then leads to the deposition of AuNPs on the surface of the liposomes. These deposited AuNPs can be easily further used as the seed for Au nanoshell growth on the surface of liposomes.

BPT proved to give the highest SERS enhancement compared to 4-MBA, 2-NT, and 4-AATP, and hence it was used as the Raman reporter of choice in the remainder of the study.

5.2.2.2 *DLS and NanoSight measurements*

Various protocols have been used throughtout the literature to prepare gold nanohybrids made of unilamellar vesicles (ULVs) and smaller AuNPs (5 nm spherical) in a range of sizes between 90 and 200 nm.[57, 137, 146, 205, 206] The size distribution of liposomes and liposomal nanohybrids (*5nmAuNPs+BPT+CTAB+liposome*) was approximately 100 (±25) nm and 108 (±45) nm, respectively, as shown in Figure 5.3a (measured by DLS). Furthermore, the surface charge was reversed from -15 mV for liposomes to +51 mV for *5nmAuNPs+BPT+CTAB+liposome* due to the positive charge of CTAB (as shown in Figure 5.3b). Compared with Nanosight results, the particle size was approximately 124±31 nm. *5nmAuNPs+BPT+CTAB+liposome* concentration was estimated as $3.52 \cdot 10^9$ particles/ml, with a mean size of 124 ±31 nm, and a mode size of 143.3 nm (Figure 5.3c). Figure 5.3d shows the screenshot of video from NanoSight which shows the optimal light dispersion from *5nmAuNPs+BPT+CTAB+liposome* -From up to down-at 05and 60 sec for *5nmAuNPs+BPT+CTAB+liposome* for of 20:1 NPs: liposome. The morphologies of *5nmAuNPs+BPT+CTAB+liposome* is taken by a JEOL TEM 1400 operated at 120 kV. The images were taken with a digital camera (Gatan ES1000W).

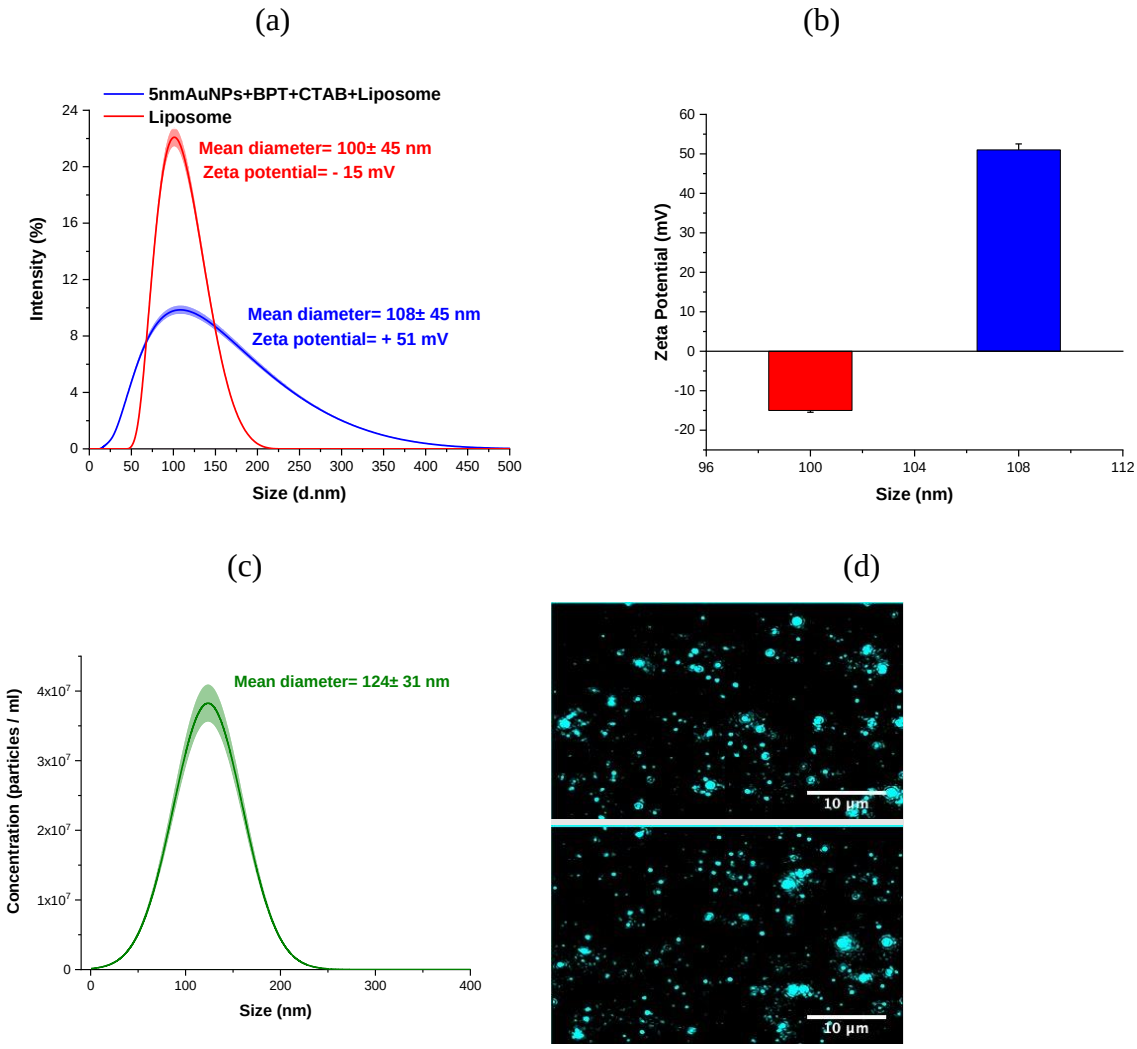

Figure 5.3 Characterization of *5nmAuNPs+BPT+CTAB+liposome*. a) *5nmAuNPs+BPT+CTAB+liposome* particle size distribution. b) Zeta potential of *5nmAuNPs+BPT+CTAB+liposome* obtained by using DLS. c**)** *5nmAuNPs+BPT+CTAB+liposome* size distribution plotted in terms of concentration in 10^7 particles/ml using NTA. d) Screen capture of NTA video showing optimal light dispersion from *5nmAuNPs+BPT+CTAB+liposome* -top to bottom-at 5 and 60 sec for *5nmAuNPs+BPT+CTAB+liposome* for of 20:1 NPs: liposome. Scale bar: 10 µm.

Figure 5.4 shows TEM images of liposomes (I) and *5nmAuNPs+BPT+CTAB+liposome* samples with different (low) number ratios of 5nmAuNPs:liposome: (II) [5:1], (III) [10:1] and (IV) [20:1]. In these images it can be seen that NPs tend to colocalise with liposomes, plausibly encapsulated inside its cavity.[126]

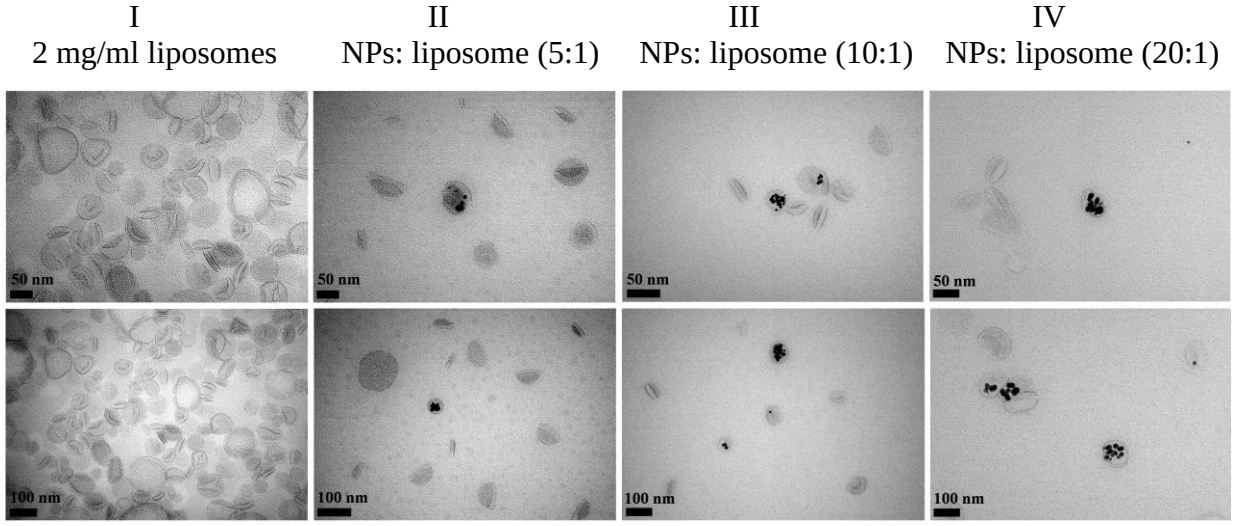

Figure 5.4 TEM images of liposome (I) and *5nm AuNP:liposome nanohybrids* with low number ratio: II) [5:1], III) [10:1] and IV) [20:1]. (scale 50 nm and 100 nm).

Increasing the NP:liposome number ratio from [20:1] to [500:1] and [1k:1] gave better results, as shown in Figure 5.5. It reveals that AuNPs samples (at a ratio of 500:1) are more concentrated with the liposome structures whereas, in the 1k:1 ratio, some of the gold nanoparticles seem to just adhere (stick fast to a surface) to one edge of the liposome and then form large clumps. In the 1k:1 hybrid, we notice fewer NPs per frame compared to the more concentrated dilutions. For electron microscope imaging, the liposomes with the 500:1 ratio worked better because of the higher density of liposomes on the EM grid. Therefore, it made it far easier to analyse the sample and to obtain representative images.

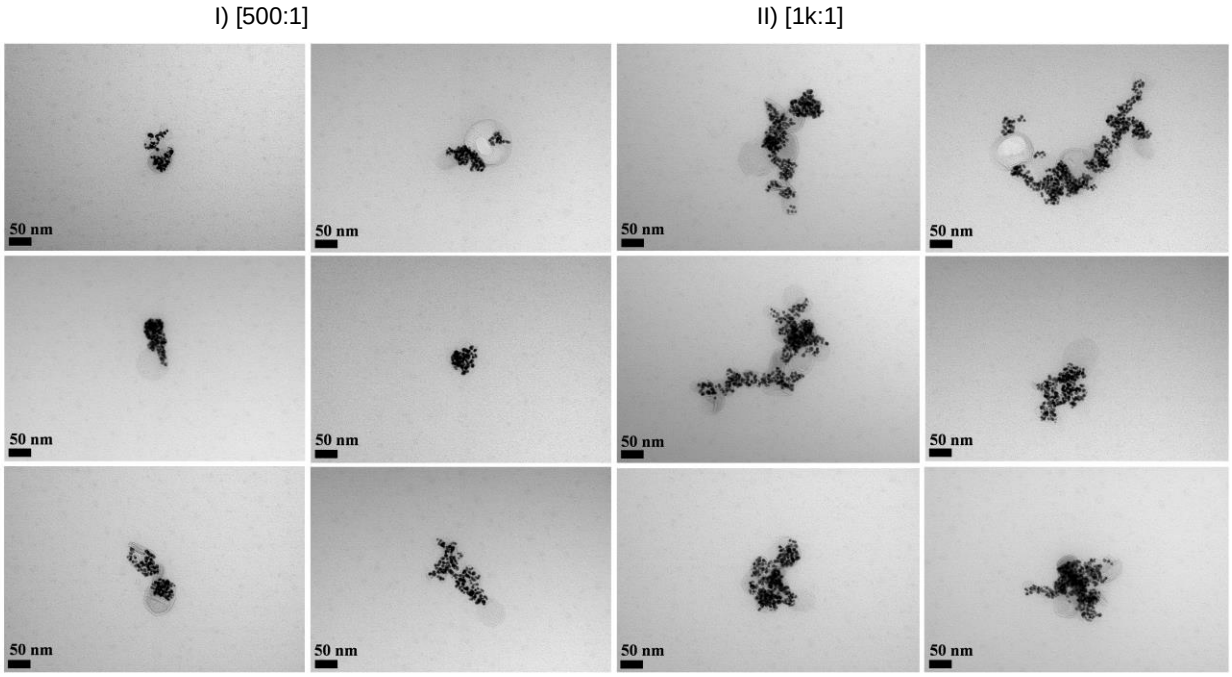

Figure 5.5 *5nm AuNP:liposome nanohybrids* with number ratio I) [500:1] and II) [1k:1]. Scale bar: 50 nm.

Figure 5.6 illustrates good colocalization of AuNPs (putatively inside the cavity) with the liposomes in the case of [16k:1] ratio. Based on ImageJ analysis, the most common structures have a mean NP number of 36 ± 1. Results look much more promising with respect to the *5nmAuNPs+BPT+CTAB+liposome* obtained using a similar number ratio but centrifuging the NPs before adding CTAB, as seen in Figure 5.7.

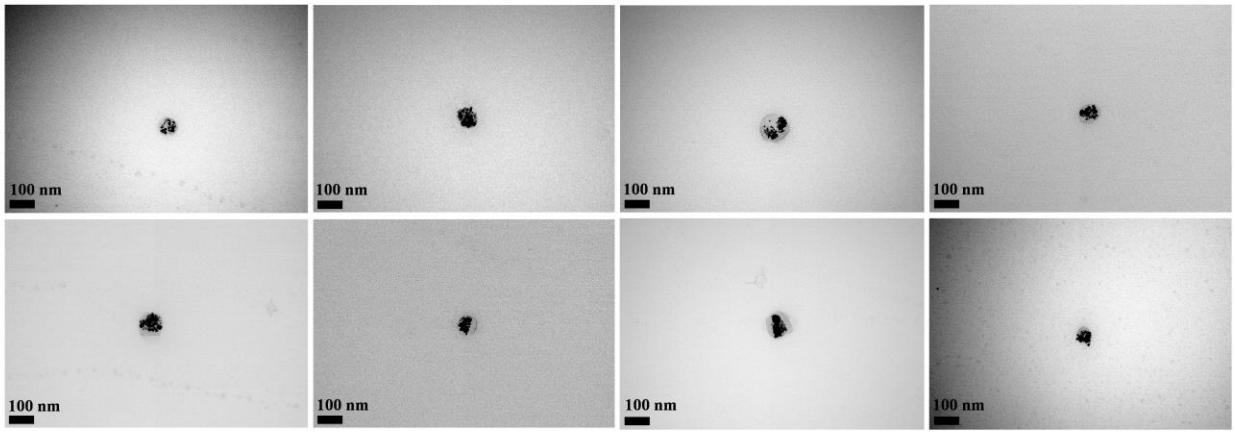

Figure 5.6 *5nm AuNP:liposome nanohybrids* with number ratio of [16k:1]. Scale bar: 100 nm.

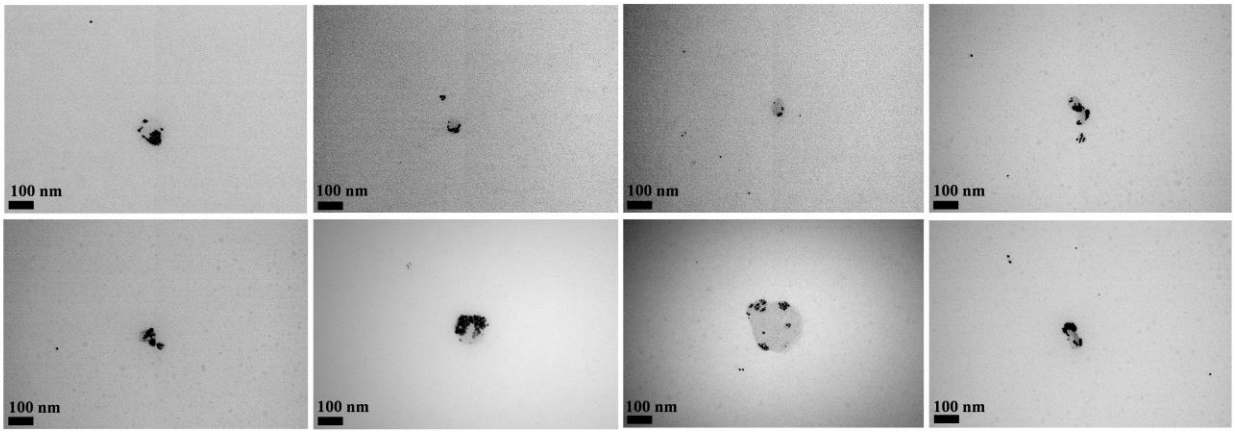

Figure 5.7 *5nm AuNP:liposome nanohybrids* with number ratio of [16k:1] obtained by centrifuging the NPs before adding CTAB. Scale bar: 100 nm.

The case of [32k:1] ratio looks slightly different, as shown in Figure 5.8. The larger number ratio results in larger gold nanoparticle aggregates without observation of the liposomes.

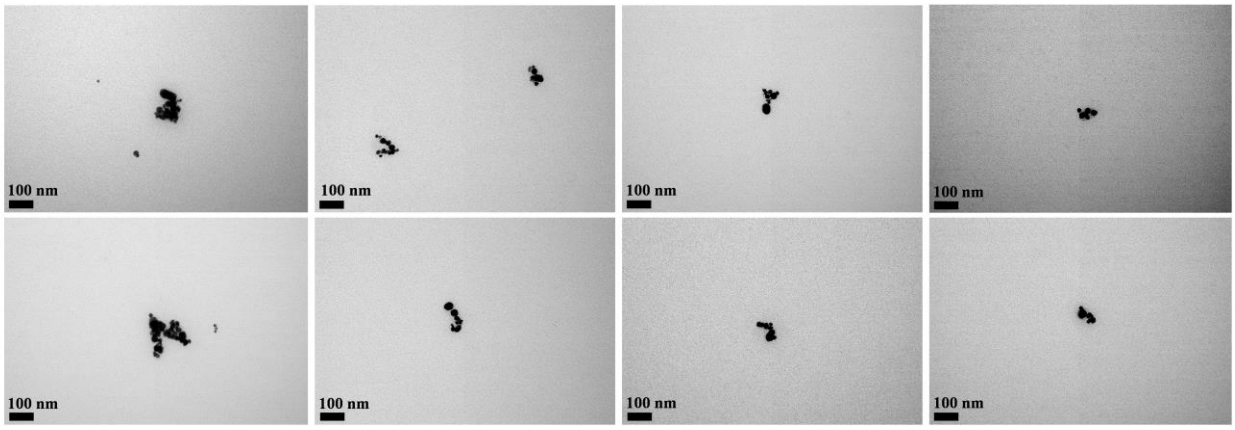

Figure 5.8 *5nm AuNP:liposome nanohybrids* with number ratio [32k:1]. Scale bar: 100 nm.

Overall, the CTAB-coated *5nm AuNP:liposome nanohybrids* with a [16k:1] ratio seemed to offer the best option in our experiments. However, above the critical micelle concentration (>1 mM) CTAB is a toxic compound which can lead to uncontrolled cell death.[207-210] In addition, CTAB causes nonspecific electrostatic interactions with the cell surface. The interaction between CTAB and the cell membrane can lead to bubbles and defect holes forming on the membrane, thus killing the cell. Therefore, either encapsulation of the nanohybrids using e.g. PEG coating or

different compounds should be tested. Another compound, the polymer GCPQ (synthesised in our collaborator Prof Ijeoma Uchegbu's lab at UCL), was applied, as shown in Figure 5.9, because it is safe and can overcome the CTAB toxicity on control and target cells before the PTT procedure. The polymer GCPQ forms a network of micelles with a diameter of 20 to 40 nm in aqueous media by self-assembly.[211-213] A self-assembling polymer (GCPQ), which is likewise cationic in composition, has been employed to efficiently solubilize and distribute hydrophobic compounds systemically. Cationic nanoparticles have the advantage of being readily internalised by engaging with the anionic surface of the cell. However, only a few of these types of nanoparticles have been tested in 3D *in vitro* cancer models, and most of these models were cancer cell spheroids.[214] Furthermore, these attempts show that aggregates of GCPQ-coated AuNPs are formed in the 1:1000 dilution, whilst in the 1:100 dilution, there are small clusters of gold but it is hard to identify liposomes. There appear to be small round structures (similar to micelles) all over the grid but not defined clusters with gold.

GCPQ is a linker which enables aggregation of smaller nanoparticles to create larger nanoconstructs. However, it has been shown [215] that GCPQ causes membrane damage to cell lines, which would thus explain why there is no evidence of liposomes in GCPQ-NP-liposome solutions as shown by TEM measurements.

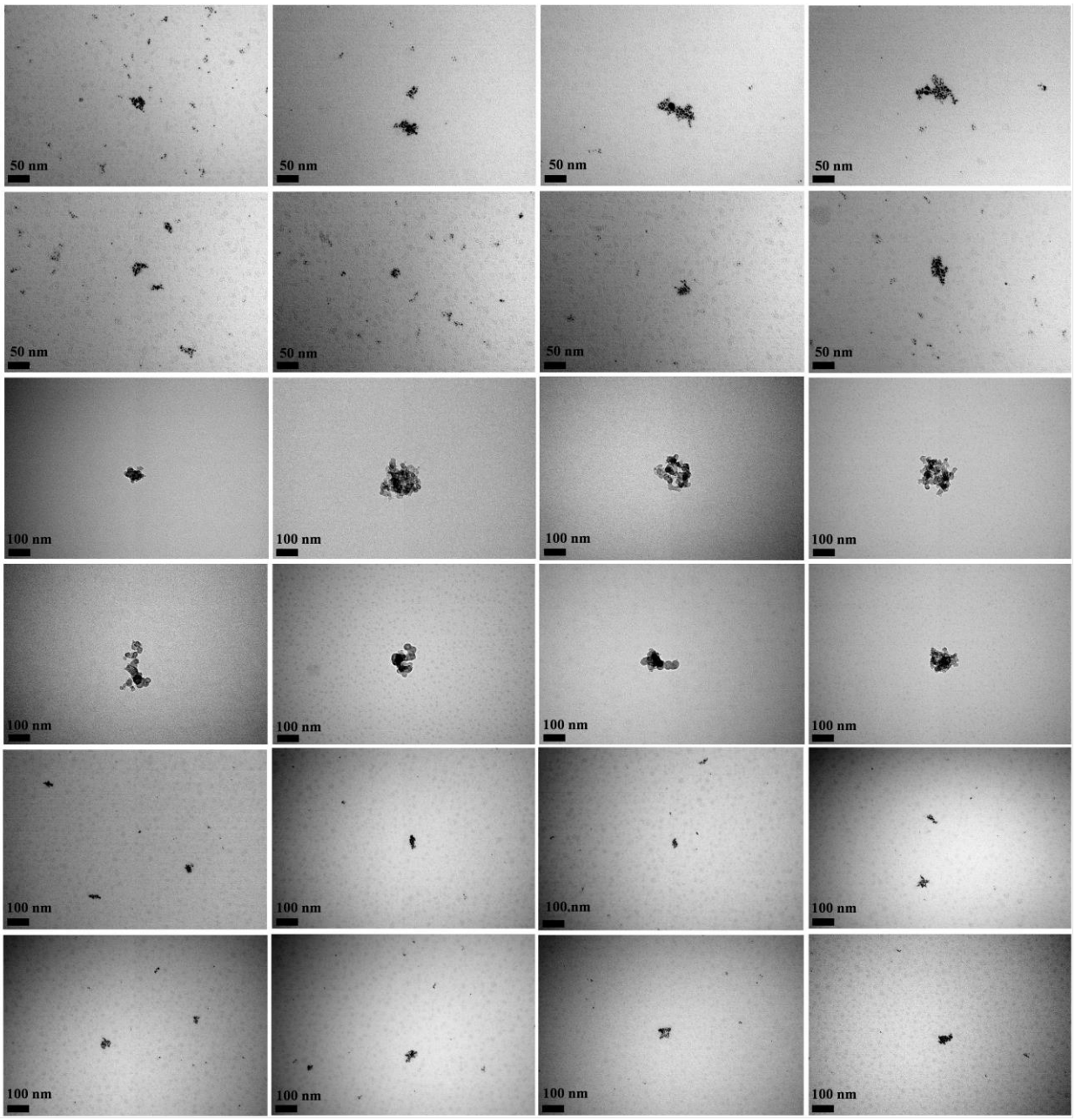

Figure 5.9 *GCPQ20-coated 5nm AuNP:liposome nanohybrids* with [16k:1] number ratio. Scale bars: 50 and 100 nm.

GCPQ is safer than CTAB, but CTAB is a suitable candidate as it preserves the nanohybrid structure; its cytotoxicity can be mitigated through PEG coating. When comparing the use of CTAB in Figure 5.6 and GCPQ in Figure 5.9, for 3 times the saturation limit of the liposome aqueous core, there are AuNP aggregates but not liposomes by using GCPQ20.

5.2.3 Potential photothermal therapeutic responses

Tables 5.1 and 5.2 list the results of photothermal experiments conducted on nanohybrids using a PTT system. *5nm AuNPs+BPT+GCPQ20+liposome* and *5nm AuNPs+BPT+CTAB+liposome* at [16k:1] present a higher differential temperature over time compared to the solution with liposomes alone (as shown in Figure 5.10). All curves has subtracted from water heating. The calculated Q/E (laser- heat conversion efficiency) is 12.9% for *5nm AuNPs+BPT+CTAB+liposome*, 15.3% for *5nm AuNPs+BPT+GCPQ20+liposome* and only 7.8% for AuNPs 5 nm. The efficiency of transduction has also shown variance, as one value has not been calculated for any of the samples. For *5nm AuNPs*, it is at 0.02, which is lower than *5nm AuNPs+BPT+CTAB+liposome*, which has been measured at 0.06. Values of transduction efficiency are also highest at 0.07, for *5nm AuNPs+BPT+GCPQ20+liposome*. In other words, our results revealed that *5nmAuNPs+BPT+GCPQ20+liposome* and *5nmAuNPs+BPT+CTAB+liposome* [16k:1]) are capable of increasing (by ca. 226.78%, 175.52%, respectively) the light/heat conversion efficiency in the case of AuNPs of 5 nm in size. When compared with gold nanoshells possessing a high light/heat transduction efficiency at 808 nm (near-infrared), the efficiency of *5nmAuNPs+BPT+GCPQ20+liposome* and *5nmAuNPs+BPT+CTAB+liposome* are expected to increase with increasing number of AuNPs per liposome because of getting close to a large cluster or gold nanoshell structure. As AuNPs are 5nm diameter and each liposome is 100 nm in size, increasing the NP:liposome ratio to [16k:1] provide a similar structure to the gold nanoshells and boost its light/heat conversion efficiency in the NIR window. Conditionally those nanospheres are on the surface of liposome. In summary, the hybrid nanostructures appear promising in delivering PTT for light-mediated therapy, particularly as they are biodegradable.

Table 5.1 Parameters used in calculating the light-heat conversion efficiency of *5nmAuNPs*, *5nmAuNPs+BPT+CTAB+liposome, 5nmAuNPs+BPT+GCPQ20+liposome*.

Laser power (P) / W	**0.5**
Laser beam diameter / mm	3
Cuvette thickness (I) / mm	10
Heating volume (Vh) / cm^3	0.070686

Specific heat capacity (c) water/ J. kg^{-1}. K^{-1}	4200
Specific heat capacity (cAu) Au/ J. kg^{-1}. K^{-1}	130
Volume of liquid in cuvette / ml	2.2

Table 5.2 The light-heat conversion efficiency calculated from the initial slope of the differential temperature-time curve (first 60 s). The transduction efficiency per µg of *5nmAuNPs*, *5nmAuNPs+BPT+CTAB+liposome, 5nmAuNPs+BPT+GCPQ20+liposome* were also calculated using the mass of Au in the heating volume.

	5nmAuNPs:Liposome (CTAB)	**5nmAuNPs:Liposome (GCPQ20)**	**5nmAuNPs**
Temperature increase in first time period / K	0.308	0.365	0.186
First time period (t) / s	60	60	60
Initial gradient of heating slope / dK.dt^{-1}	0.005	0.006	0.003
Q/E	0.129	0.153	0.078
Efficiency of transduction (Eff) / ug^{-1} Au	0.061 (SD=±0.014)	0.072 (SD=±0.005)	0.022 (SD=±0.004)

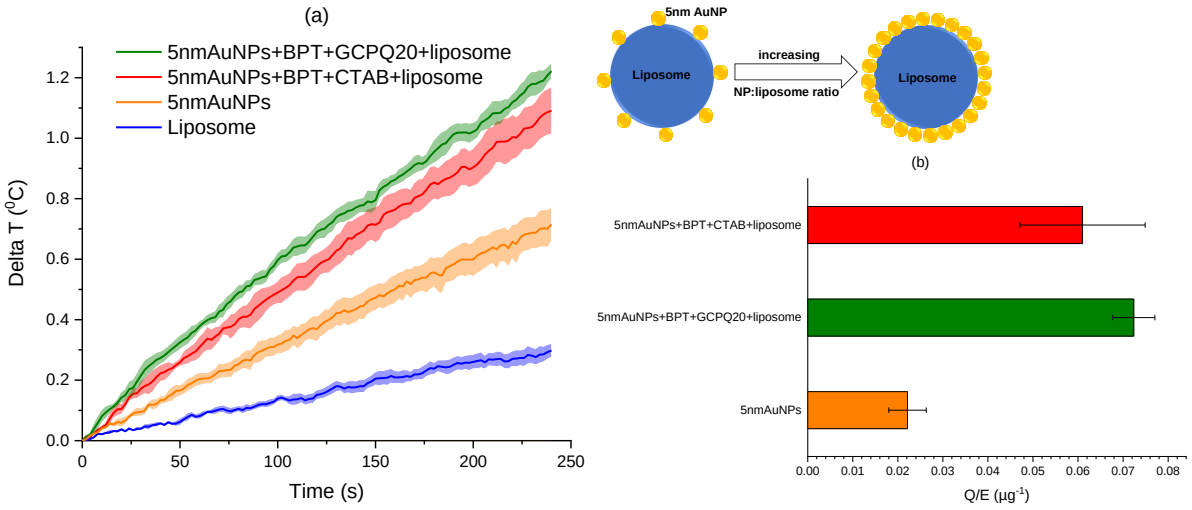

Figure 5.10 a) Differential temperature-time curves and b) Q/E for *5nmAuNPs*, *5nmAuNPs+BPT+CTAB+liposome, 5nmAuNPs+BPT+GCPQ20+liposome* and liposome

solutions. During the 808 nm laser exposure, the temperature of samples was measured using a thermocouple thermometer.

5.2.4 Plasmonic light absorption

To gain an insight in the process of AuNP assembly in the presence of lipid membranes, we investigated different concentrations of liposomes and AuNPs. The five ratios yielded different nanoassembly morphologies (Figures 5.4 and 5.5) with various absorbance profiles as shown in Figure 5.11a. The citrate-stabilized 5 nm NPS (as a control) were measured when the linker (CTAB) was not present. The control sample (5nm AuNPs) presented an LSPR peak at 515 nm and -55 mV surface charge as shown in Figure 5.11a (navy spectrum) and Figure 5.11c, which mainly indicates that this is a monodispersed colloidal solution of citrate-capped bare nanospheres (no assembly occurs in the absence of the linker polymer). Additionally, the liposome solution has no absorption peak in that region, as shown in Figure 5.11a (red spectrum). After coating with CTAB, the surface charge was modified from -55 mV to around +34 mV, as shown in Figure 5.11c. The UV-visible spectrum of CTAB-coated 5 nm AuNP solution displays an LSPR peak at 530 nm with negligible NIR absorbance (Figure 5.11a, blue spectrum). Redshift was observed to the bare 5 nm AuNPs of around 15 nm. Before centrifugation (Figure 5.12a, blue spectrum) and after centrifugation at a speed of 55000 rpm of CTAB-coated 5 nm AuNPs (Figure 5.11a, olive spectrum) made no difference to the LSPR at 530 nm, only a loss of absorbance which is no AuNPs pellets lost after centrifugation. However, using liposomes with 5 nm AuNPs and CTAB at different concentration ratios, 5:1, 10:1, 20:1, 500:1, and 1k:1, led to redshift of the LSPR peak from 515 nm to 534 nm, 536 nm, 535 nm, 537 nm and 535 nm (redshift of 19, 21, 20, 22, and 20 nm respectively) (Figure 5.11a, magenta, orange, green, wine, and cyan spectrum respectively). This redshift could be indicative of aggregation induced by the added CTAB. However, centrifugation of the latter sample (Figure 5.11a, purple spectrum) leads to an LSPR peak at 544 nm, which demonstrates that there is an effect of centrifugation. Figure 5.11d exhibits photos for samples 1, 2, 3, 4, 5, 6, 7, 8, 9, 10 which represent liposome (composition: DSPC:cholesterol), *5nm AuNPs* (Nanocomposix), *5nmAuNPs+BPT+CTAB* at 25mM (before centrifugation), *5nmAuNPs+BPT+CTAB* at 2.5 mM (after centrifugation), *5nmAuNPs+BPT+CTAB+liposome* at different ratios, [5:1], [10:1], [20:1], [500:1], [1k:1] and [10:1] after two cycles of centrifuge. For

5nmAuNPs+BPT+CTAB+liposome the LSPR is around 544 nm, which is similar to the value for a 80 nm AuNP solution.

Comparison between *5nmAuNPs+BPT+CTAB* and *5nmAuNPs+BPT+CTAB+liposome* shows that the presence of liposomes determines an increase in absorbance, indicating the significance of this nanoassembly morphology over the *5nmAuNPs+BPT+CTAB* alone. However, the polymer linker (CTAB) is a comparatively large macromolecule (>1 nm), and the flexible polymer chains and multiple anchoring end groups further assists in the packing of *5nmAuNPs+BPT+CTAB*, which as a result helps in the reduction of gaps between NPs and potentially in hot spot formation.

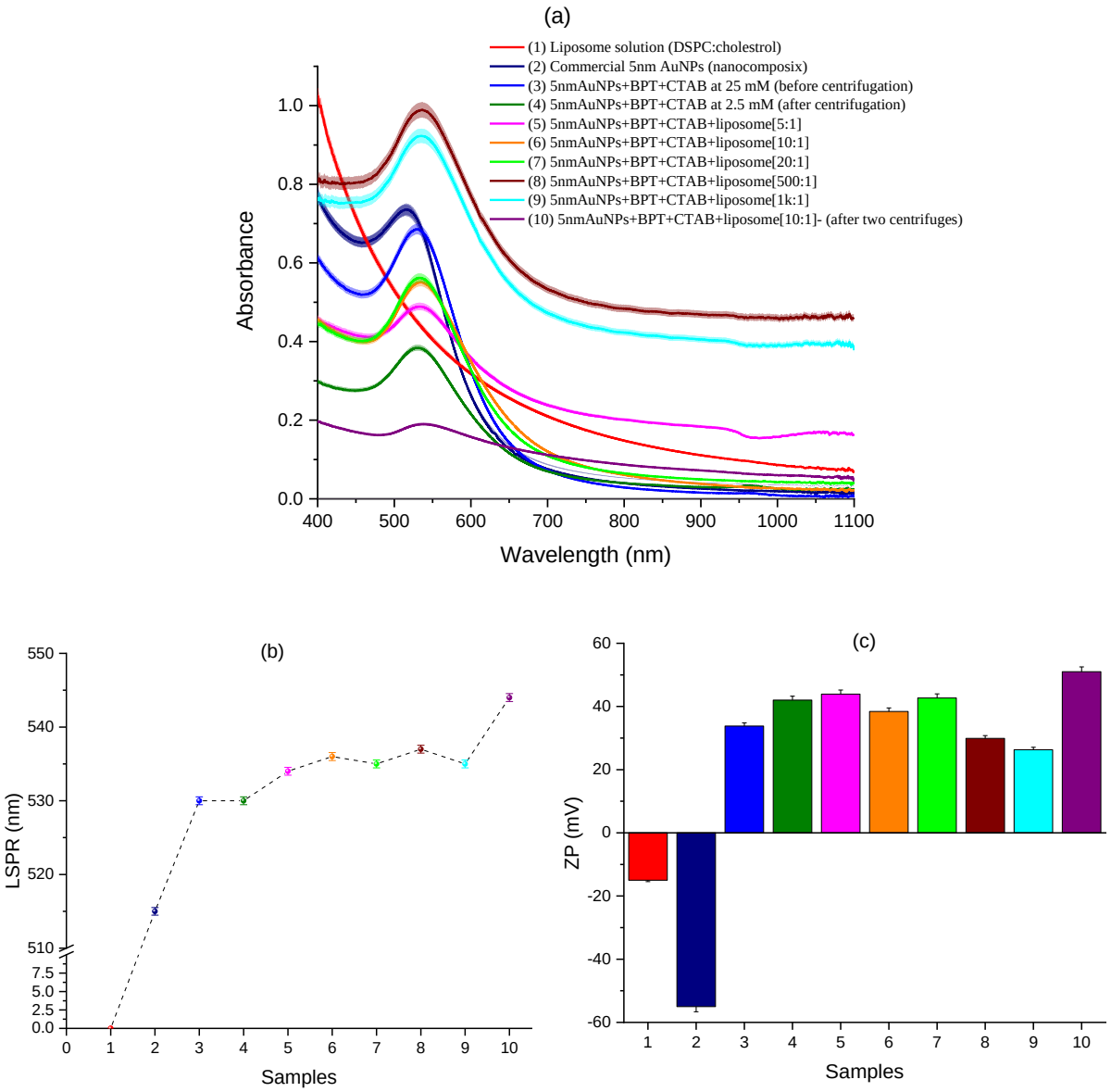

(d)

Figure 5.11 a) UV-visible absorption spectra of different colloidal NP:liposome solutions (1-10 samples) which represent liposome solution, commercial *5nm AuNPs* (Nanocomposix), *5nmAuNPs+BPT+CTAB* at 25mM (before centrifugation), *5nmAuNPs+BPT+CTAB* at 2.5 mM (after centrifugation), *5nmAuNPs+BPT+CTAB+liposome* at different ratios: [5:1], [10:1], [20:1], [500:1], [1k:1], and [10:1] after two centrifugations. b) Plasmonic peak maximum and c) zeta potential for samples 1, 2, 3, 4, 5, 6, 7, 8, 9, 10.

Figure 5.12 shown UV-visible absorption spectra of *5nmAuNPs:liposome nanohybrids* using a) CTAB, b) GCPQ19 or c) GCPQ20 at different linker:NP ratio: [20:1], [500:1], [1k:1], [3k:1], [6k:1], [16k:1], and [32k:1].

In Figure 5.12d, using liposomes with 5 nm AuNPs and CTAB at different concentrations, 20:1, 500:1, 1k:1, 3k:1, 6k:1 and 16k:1 led to increasing the wavelength of the LSPR peak from 515 nm to 535 nm, 536 nm, 537 nm, 537 nm, 538 nm and 553 nm (redshift of 20, 21, 22, 22, 23, and 38 nm respectively).

Using liposomes in the presence of 5 nm AuNPs and GCPQ19 at different concentration ratio, 20:1, 500:1, 1k:1, 3k:1, 6k:1 and 16k:1, led to increasing the LSPR peak wavelength from 515 nm to 518 nm, 521 nm, 519 nm, 520 nm, 520 nm and 519 nm (redshift of 3, 6, 4, 5, 5, and 4 nm respectively). However, using GCPQ20 instead at the same concentration ratios led to a further increase in the LSPR peak wavelength from 515 nm to 529 nm, 531 nm, 536 nm, 554 nm, 540 nm and 531 nm (redshift of 14, 16, 21, 39, 25, and 16 nm respectively).

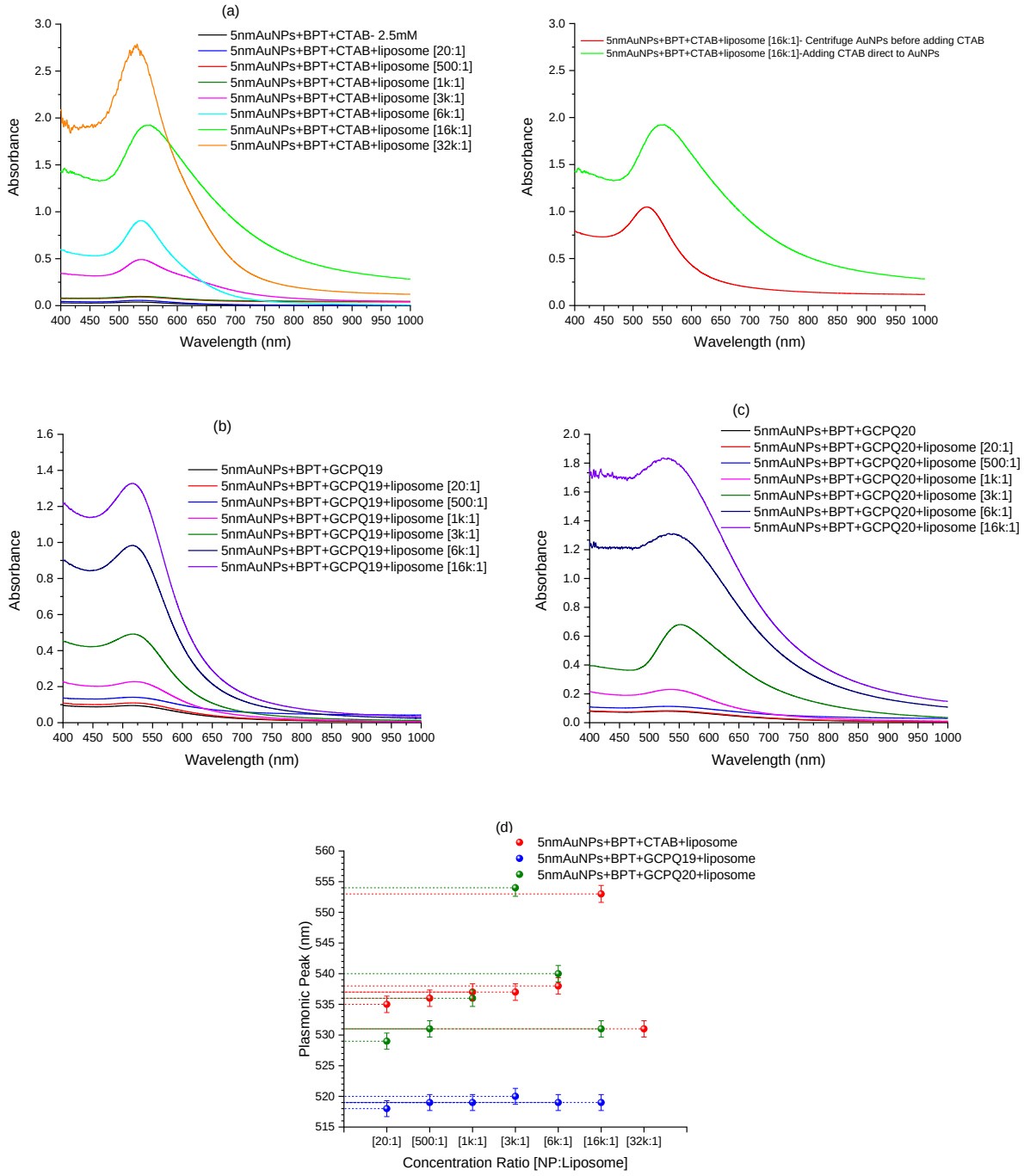

Figure 5.12 (a) UV-visible absorption spectra of *5nmAuNPs:liposome nanohybrids* using CTAB at different ratio to the AuNPs: [20:1], [500:1], [1k:1], [3k:1], [6k:1], [16k:1], and [32k:1]. (b) UV-visible absorption spectra of *5nmAuNPs:liposome nanohybrids* using GCPQ19 at different ratio: [20:1], [500:1], [1k:1], [3k:1], [6k:1] and [16k:1]. **(**c) UV-visible absorption spectra of *5nmAuNPs:liposome nanohybrids* using GCPQ20 at different ratio: [20:1], [500:1], [1k:1], [3k:1],

[6k:1] and [16k:1]. (d) Plasmonic peak of *5nmAuNPs:liposome nanohybrids* using CTAB, GCPQ19 and GCPQ20 at different ratio.

All these nanohybrids have a surface plasmon band below 555 nm. In summary, CTAB is a suitable candidate and seems to perform better than the other linkers.

5.2.5 SERS of nanohybrids

Raman measurements were conducted with solutions placed in a Hellma 96-well quartz microplate at room temperature. Figure 5.13 I, II, III, IV shows the Raman spectra of ultrapure water, BPT solution ($9.1 \cdot 10^{-5}$ M in ethanol), 5 nm AuNPs labelled with BPT, 5 nm AuNPs labelled with BPT and CTAB-coated in the presence of liposomes, measured at two wavelengths, 785 and 830 nm. For comparison, the spectrum of BPT in ethanol solution is also shown in Figure 5.13 II. There was no Raman signal arising from the AuNPs themselves when the BPT reporter was not added (see "water" spectrum). Three notable Raman bands from BPT at 1080, 1278 and 1596 cm^{-1} are ascribed to the vibrational modes of C–H rocking, C–C stretching (ν_{8a} mode), and stretching of C–C connecting the phenyl rings, respectively (as shown in Figure 13 with pink lines). After binding with AuNPs, the ν_{8a} band of BPT at 1596 cm^{-1} (a coupled vibration of both phenyl rings) was observed to split into two at 1586 and 1599 cm^{-1}. This suggests that the orientation of the phenyl rings in BPT should be different and they may not lie in the same plane on AuNP surfaces. Excitation at 785 nm was found to produce slightly larger signals than those obtained with 830 nm excitation, as it is expected from the wavelength-dependent scattering intensity. The largest signal was found for BPT and CTAB labelled AuNPs with liposomes ($8.8 \cdot 10^4$ counts) at 1586 cm^{-1} using the 785 nm laser. However, in previous experiments the largest signal was found for BPT labelled 80 nm AuNPs ($2.6 \cdot 10^6$ counts) using the 785 nm laser.

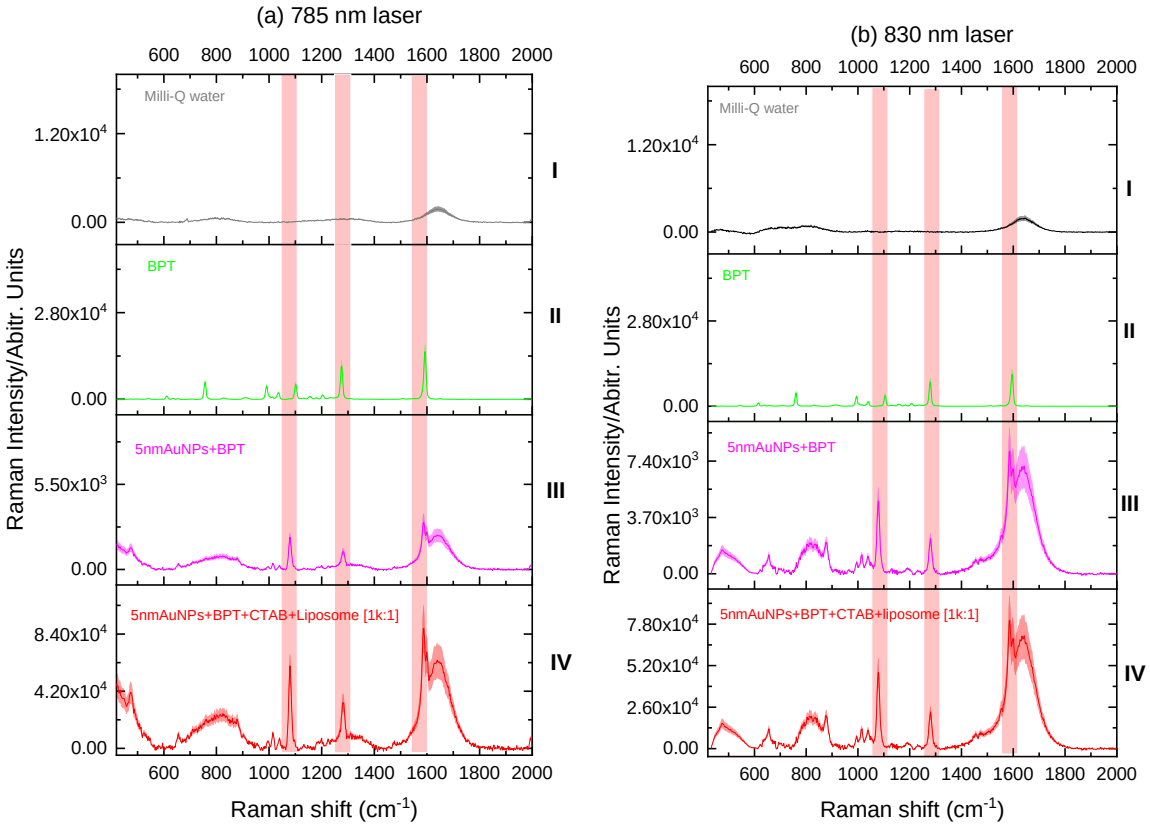

Figure 5.13 Raman spectra of I) water, II) BPT in ethanol (concentration of $9.1 \cdot 10^{-5}$ M), III) 5nmAuNPs+BPT, IV) *5nmAuNPs+BPT+CTAB+liposome* [20:1] measured at (a) 785 nm and (b) 830 nm. Pink lines denote the three most prominent signals of BPT, at 1080, 1278 and 1586 cm^{-1}.

In comparison it can be observed that for *5nmAuNPs+BPT+CTAB+liposome* the Raman signals were stronger than those from BPT-labelled 5nm AuNPs for all three BPT peaks (1080 cm^{-1}, 1278 cm^{-1}, and 1586 cm^{-1}) using both 785 nm and 830 nm lasers which are illustrated in Figure 5.14 below.

However, the noteworthy finding here is that larger signals are produced when excitation was done at a lower wavelength of 785 nm in comparison to those produced at a higher wavelength of 830 nm excitation. The SERS signal was approximately 1.3 times as intense for all three peaks. The largest signal was found for *5nmAuNPs+BPT+CTAB+liposome* at 1080 cm^{-1} at $6 \cdot 10^4$ counts and 1586 cm^{-1} at $8.8 \cdot 10^4$ counts by the use of 785 nm laser. But, approximately 10^6 counts for BPT-labelled 80 nm AuNPs using both 785 nm and 830 nm lasers as shown in Figure 5.14.

Figure 5.15 shows the SERS enhancement factor (EF) for three patterns of labelled AuNPs at 785 and 830 nm excitation wavelength. This graph evaluated the SERS EF using the three peaks of BPT at 1080 cm^{-1}, 1278 cm^{-1}, and 1586 cm^{-1}.

When applying both 785 nm and 830 nm lasers, the greatest EF for *5nmAuNPs+BPT+CTAB+liposome* was around $8 \cdot 10^5$ at 1080 cm^{-1}, and $5 \cdot 10^5$ at 1586 cm^{-1}, as in Figure 5.15.

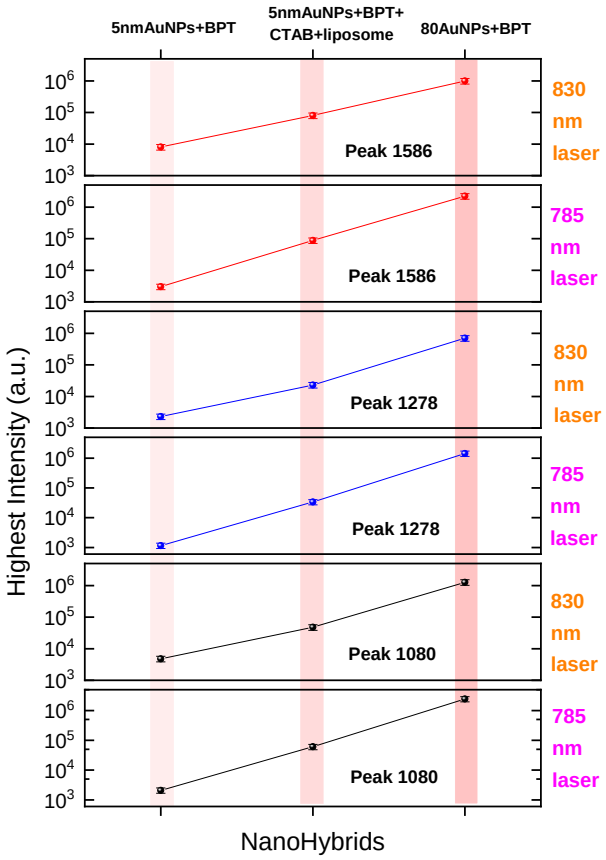

Figure 5.14 Plot of the highest intensity (height) of the three significant peaks of BPT at 1080 cm^{-1}, 1278 cm^{-1}, and 1586 cm^{-1} for BPT-labelled AuNP solutions measured at 785 and 830 nm.

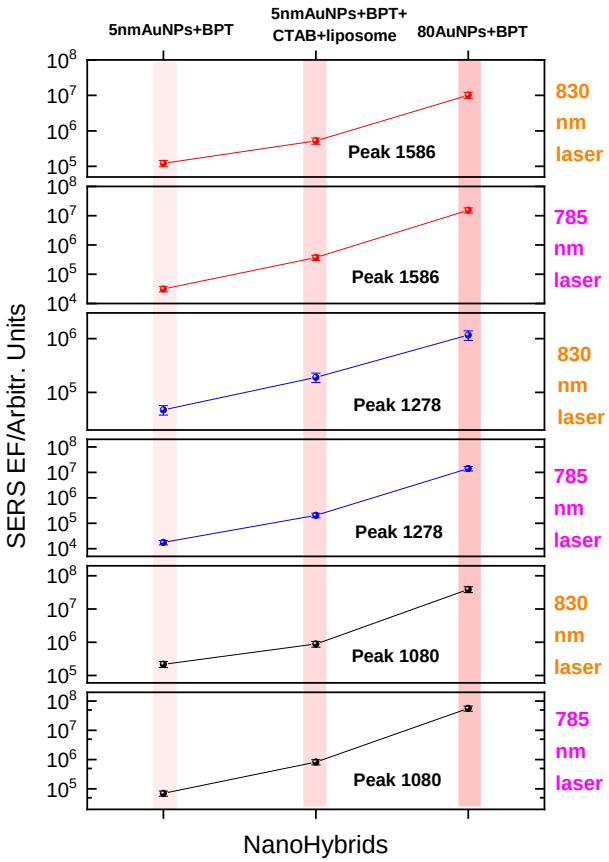

Figure 5.15 Plot of SERS EF of the three main BPT peaks at 1080 cm^{-1}, 1278 cm^{-1}, and 1586 cm^{-1} for labelled AuNP solutions at 785 nm and 830 nm excitation.

5.2.6 Cytotoxicity profile of nanohybrids against triple-negative human breast cancer cell line MDA-MB 231

Figure 5.16a shows the *in vitro* cytotoxicity profile of the selected concentrations (0.05, 0.025, 0.01 and 0.0125 mg/ml) of eleven different structures (where A, B, C, D, E, F, G, H, I, J represent *AuNP+BPT* (100 nm size), *AuNPs+BPT* (80 nm), *AuNPs+BPT* (60 nm), *AuNPs+BPT* (40 nm), *AuNPs+BPT* (15 nm), *AuNPs+BPT* (10 nm), *AuNPs+BPT* (5 nm), *5nmAuNPs+BPT+CTAB+liposome*-5:1 NPs:liposome, *5nmAuNPs+BPT+CTAB+liposome*-10:1 NPs:liposome, *5nmAuNPs+BPT+CTAB+liposome*-20:1 NPs:liposome respectively) against human triple-negative breast cancer cell line MDA-MB-231. This toxicity test was performed after

24 hours of incubation of NPs with cells. MTT assay was performed to investigate the ratio of alive vs. dead cells (represented as % age of cell viability). These results demonstrate that *AuNP+BPT* (100 nm diameter), *AuNPs+BPT* (80 nm), *AuNPs+BPT* (60 nm), *AuNPs+BPT* (40 nm), *AuNPs+BPT* (15 nm), *AuNPs+BPT* (10 nm), *AuNPs+BPT* (5 nm) have more than 80% cell viability while low cell viability was noticed in the case of *5nmAuNPs+BPT+CTAB+liposome*-5:1 NPs:liposome, *5nmAuNPs+BPT+CTAB+liposome*-10:1 NPs:liposome, *5nmAuNPs+BPT+CTAB+liposome*-20:1 NPs:liposome. The toxicity profile of these NPs reveals that the presence of CTAB in the liposome nanohybrids leads to more toxic effects on cancer cells. In summary, these results advocate on the use of PEG-ylation to protect the nanohybrids and screen the cells from unwanted cytotoxicity from CTAB. Furthermore, the liposome nanohybrids were imaged using stimulated Raman scattering microscopy which shows that the nanohybrids were taken up by cells. The Raman spectrum further revealed the selective delivery of nanohybrids towards cancer cells in this untargeted case (by simple diffusion).

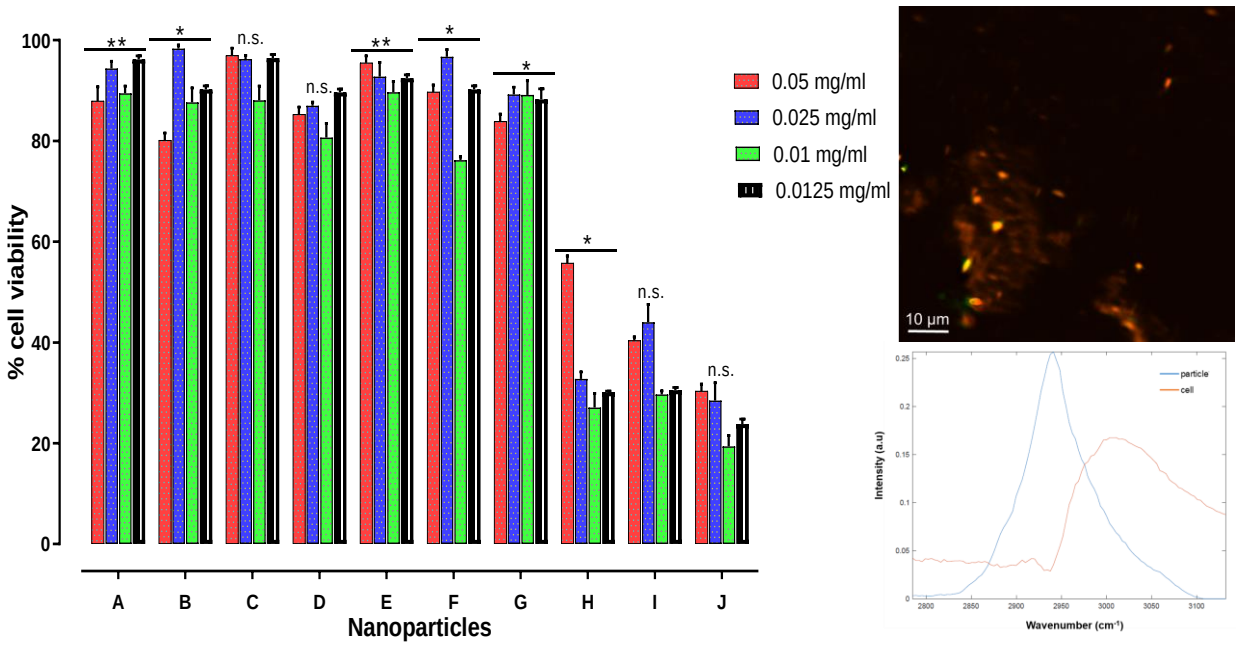

Figure 5.16 Toxicity assay results and hyperspectral SRS imaging of cancer cells with AuNPs (20:1 NPs:liposome). (A) Toxicity results of NPs against triple-negative breast cancer cell line MDA-MB-231 (MTT assay). A, B, C, D, E, F, G, H, I, J represent *AuNP+BPT* (100 nm size), *AuNPs+BPT* (80 nm), *AuNPs+BPT* (60 nm), *AuNPs+BPT* (40 nm), *AuNPs+BPT* (15 nm),

AuNPs+BPT (10 nm), *AuNPs+BPT* (5 nm), *5nmAuNPs+BPT+CTAB+liposome*-5:1 NPs: liposome, *5nmAuNPs+BPT+CTAB+liposome*-10:1 NPs: liposome, *5nmAuNPs+BPT+CTAB+liposome*-20:1 NPs:liposome respectively. Each result arises from three independent experiments. The values have been shown as the mean ± standard deviation of three experiments; * denotes $p < 0.05$ (statistical significance) and ns represents $p \geq 0.05$ (nonstatistical significance). (B) Hyperspectral SRS imaging of cancer cells with AuNPs (*5nmAuNPs+BPT+CTAB+liposome*-20:1 NPs: liposome) while Figure (C) represents the spectrum of NP (*5nmAuNPs+BPT+CTAB+liposome*-20:1 NPs:liposome) and cells.

5.3 Conclusion

For the diagnostic and therapeutic purposes related to cancer, the metallic NPs have been widely addressed in medical research due to their properties of high penetrability, high binding affinity, good biocompatibility, and targeting ability, along with low toxicity. With specific reference to the gold nanoparticles (AuNPs), they can produce ultrasensitive surface-enhanced Raman scattering (SERS) in the near-infrared (NIR) region. This is mainly because they present plasmonic properties, especially in the NIR region for NP aggregates. These properties of AuNPs are beneficial in the sense that with the help of these advantageous properties, AuNPs might be utilized for the selective detection of cancer cells through targeting specific molecules and tailored ablation using radiation therapy or photothermal therapy (PTT). It can prove to be efficacious in the diagnostic and therapeutic management of cancer. For instance, it has widely been reported that the diagnostic and therapeutic efficacy of AuNPs may be improved significantly by attachment of targeting moieties and biomolecules (specific to disease such as antibodies, RNA, DNA). However, these modalities suffer from a wide variety of challenges such as off-target toxicity, biocompatibility, clearance and low SERS signals. The development of novel nanohybrids based on Raman tags and liposomes is a promising solution.

Findings of the study suggest that analytical techniques such as Transmission Electron Microscopy (TEM), PhotoThermal Therapy (PTT), Dynamic Light Scattering (DLS), UV-visible spectroscopy and SRS imaging, are considered reliable to characterize novel nanohybrids hence utilized with AuNPs (gold nanoparticles) for detecting cancer cells. Their combined application can be used for getting proficient results. In addition to this, the different protocols of nanohybrid test results reveal

that the 90-200 nm-sized nanohybrid particles made of unilamellar vesicles (ULVs) and 5 nm spherical AuNPs showed reduced toxicity levels in a living system for delivering systematic working. Furthermore, in AuNPs solutions, the biphenyl-4-thiol (BPT) which is also referred to as Raman reporter (RR) molecule is used to derive SERS signals and the results validated the use of various RR molecules. Moreover, the test results also showed that biocompatibility is highly effective in terms of surface-enhanced Raman spectroscopy (SERS) for the reduction and elimination of tumour cells. In addition to this, it was investigated the use of suitable and safe polymer to enable the binding between AuNPs and ULVs of 100 nm diameter approximately. Moreover, the results of the test also show that using NTA, the maximum of *5nmAuNPs+BPT+CTAB+liposome* size distribution was recorded to be 124 nm and by DLS it was recorded to be 108 nm. On the other hand, the measurement of LPSR of *5nmAuNPs+BPT+CTAB+liposome* was around 544 nm approximately which is relatively similar in size to 80 nm commercial nanospheres. The light-heat conversion efficiency of *5nm AuNPs+BPT+GCPQ20+liposome* and *5nm AuNPs+BPT+CTAB+liposome* were also investigated by measuring their temperature rising over time during 808 nm laser exposure. The results demonstrated that *5nm AuNPs+BPT+GCPQ20+liposome* and *5nmAuNPs+BPT+CTAB+liposome* have a higher temperature rising over time, and these special structures (*5nm AuNPs+BPT+GCPQ20+liposome* and *5nmAuNPs+BPT+CTAB+liposome*) could increase by approximately 226.78% and 175.52%, respectively, the PTT efficiency of *5 nm AuNPs*.

The SERS enhancement was evaluated based on the three Raman peaks of BPT observed at 1080 cm^{-1}, 1278 cm^{-1} and 1586 cm^{-1}. The largest enhancement factor was recorded for the BPT peak at 1080 cm^{-1} using both 785 nm and 830 nm lasers for *5nmAuNPs+BPT+CTAB+liposome* ($8 \cdot 10^5$) which was then selected as a potential candidate to carry forward. In addition to this, for achieving effective results from utilizing *5nmAuNPs+BPT+CTAB+liposome*, an alternative to the cytotoxic CTAB was investigated. Also, it was observed that the synthesis of small, 5nm AuNPs worked more effectively than using the commercial products (5nm AuNPs, NanoXact, 0.05 mg/ml, citrate, 25 mL) and considered more suitable since they produced strong photothermal effect due to absorption in the near-infrared region (NIR). Moreover, the tested ratio of NPs to liposome of [16k:1] is beneficial to saturate the liposome cavity which is the optimal solution for heating and SERS. Therefore, 16k:1 ratio was used as the ratio number while CTAB was employed as the

polymer linker. Findings of the research indicate that the effect of these nanohybrids against MDA-MB-231 (triple-negative breast cancer cell line) in a concentration-dependent manner is cytotoxicity due to the presence of CTAB. Therefore, the study highlights the need for hybrid nanostructures which encompass a PEG coating (along with targeting molecules) for delivering laser-driven therapy based on the utilization of PTT and SERS for Raman diagnostics.

CHAPTER 6
AuNR-LIPOSOME NANOHYBRIDS FOR SURFACE ENHANCED RAMAN SCATTERING AND PHOTOTHERMAL THERAPY

6.1 Introduction

The aim of this section is to report the development of biocompatible noble metallic NP constructs based on AuNPs and liposomes (or lipid vesicles) functionalised with Raman tags for potential applications in SERS diagnostics and photothermal therapy. To this aim, the design previously described in Chapter 5 will be pursued. In terms of the reasoning behind using gold nanorods and liposomes in photothermal therapy, the study by Singh et al. (2016) has shown that the nanorods prove vital in achieving laser light absorption in near infrared region.[216] Practical results of the use of gold nanorods with liposomes can be seen in the study of Chauhan et al., in which MDA-MB-231 cells that are present in breast cancer patients have been effectively disintegrated.[217] This means that gold nanorods provide an effective way of assembly with liposomes, such that cancer cells can be infiltrated and then their normal functions disrupted. However, literature has also shown that gold nanorods are not used as a primary treatment method, instead they are applied as an additional therapeutic stabiliser for chemotherapy. Conjugated but modified gold nanorods, when used to coat liposomes, are effective in synergizing between the chemical and thermal mix of drugs for treating cancer cells.[218] Using this technique, not only is the chemical effect of other drugs stabilised, but the thermal aspects of gold nanorods also enable the cancer cells to be effectively identified and disrupted.

Previous design showed negative results based on UV-vis spectra in that small spherical AuNPs, even assembled with liposomes, failed to express a NIR response. Therefore, they cannot be used in Raman nanotheranostics as foreseen in our NIR application. For this reason, this section focuses on the use of small gold nanorods (15 nm diameter, 55 nm length, giving an aspect ratio of ca. 4). Indeed, AuNRs have two peaks in UV- visible spectra, and the second peak falls within the NIR region. Thanks to this peak, the AuNR assemblies with liposomes are proved to be effective in photothermal therapy with NIR irradiation. Specific to NRs is the notion of CTAB coating for gold nanorods, which Black et al. has found to lead to different optical properties of the gold nanorods, which means that their uptake by cells can be disrupted as well. As a consequence, it can be argued

that CTAB may prove ineffective.[219] However, the advantage of using CTAB is the fact that this product is biofriendly, leading to effective porous layer formation on the gold nanorods.[220]

Moreover, only CTAB has been used while GCPQ has been avoided. Although GCPQ is safe, and CTAB is toxic, the use of CTAB leads to full coating of gold nanorods better that GCPQ. In addition, due to the liposome's long hydrophobic chains interacting with CTAB on NR surfaces, they will form a highly selective network structure, which is well suited for controlling NP aggregation and possessing the capability to control nanotag aggregation.[221] Therefore, only one molecule (CTAB) has been used to reverse the AuNR surface charge for interaction with liposomes. Using the spherical AuNPs previously, it has been determined that the AuNP:liposome ratio of 16k:1 is the most suitable ratio. Therefore, a suitable ratio of AuNR:liposome of 6.9k:1 has been used here, in the presence of (CTAB and) BPT labelling, which also gave the best results previously.

The novelty of this work is in the fabrication and testing of biodegradable AuNR-liposome nanostructures with added Raman labelling and SERS activity to previously demonstrated PTT-active nanohybrids.

Dr Marzieh Salimi collected and analyzed PTT data. SRS imaging, transient absorption microscopy measurements and data analysis were performed by Dr Chun-Chin Wang, a postdoctoral fellow within the "RaNT" programme grant. Finally, cytotoxicity tests and data analysis were conducted by Emad Manni, a PhD student at Prof. Lorna Harries' lab in Exeter Medical School. Everything else is the author's work.

6.2 Results

6.2.1 TEM

In this section, TEM images are reported for liposomal nanoconstructs prepared using both commercial (Nanocomposix) gold nanorods (*55/15nm AuNRs+BPT+CTAB+liposome*) and synthesised gold nanorods (*52/16nm AuNRs+BPT+CTAB+liposome*).

6.2.1.1 55/15nm AuNRs+BPT+CTAB+liposome

The TEM images of AuNRs at 0.016 mg/ml are shown in Figure 6.1, whilst the TEM images of *55/15nm AuNR:liposome nanohybrids* with number ratio [6.9k:1] at 0.4 mg/ml concentration are shown in Figure 6.2.

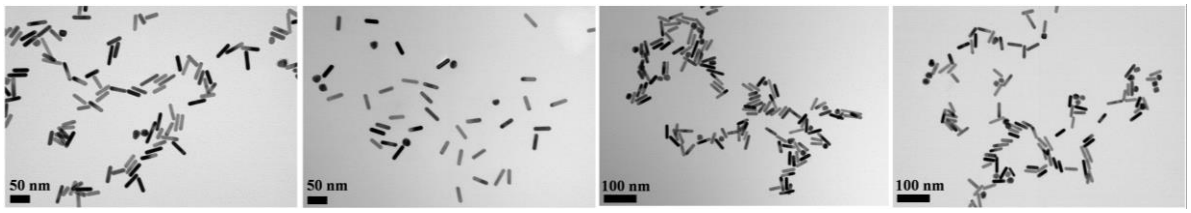

Figure 6.1 *55/15nm AuNRs* at room temperature. Scale bar: 50 and 100 nm.

Figure 6.2 shows excellent results with large clusters of gold nanorods colocalised with liposomes (both internalised in their cavities and deposited on their external surfaces). Nanostructures of various sizes and shapes, from small spheres of ca. 50 nm diameter to large elongated clusters of few hundreds nanometres length, are apparent in these transmission micrographs. Based on ImageJ analysis, the most common structures have a mean NP number of 50 ± 2.

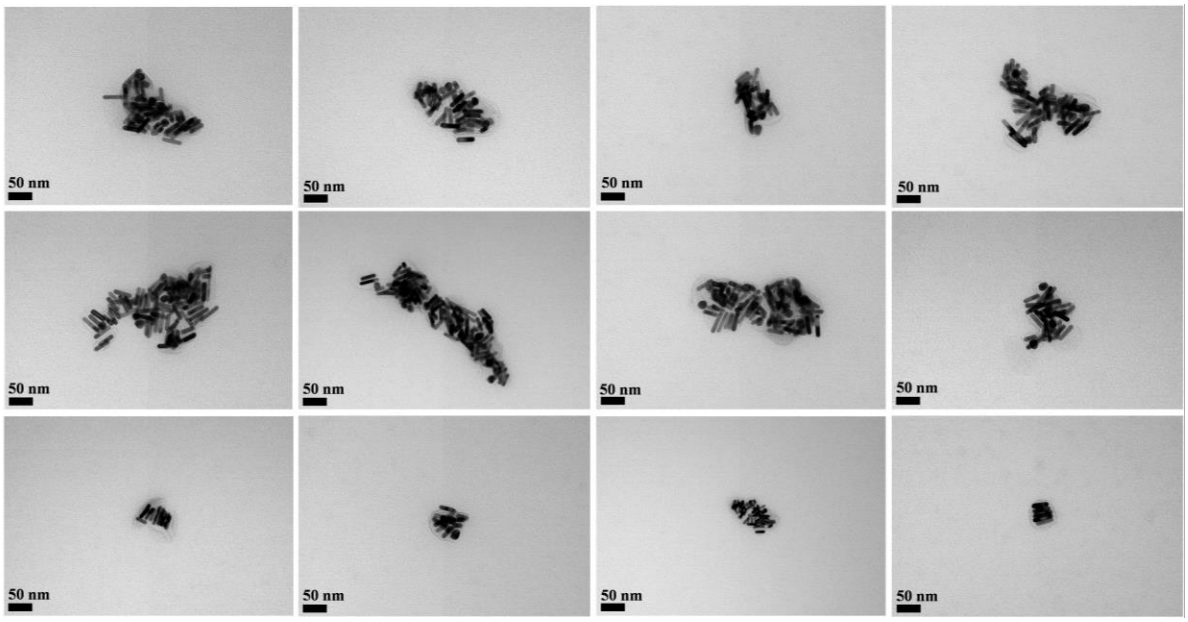

Figure 6.2 *55/15nm AuNR:liposome nanohybrids* with number ratio [6.9k:1] at room temperature. Scale bar: 50 nm.

To investigated the stability and biodegradability of these nanostructures, the effect of preparing the liposome nanohybrids (CTAB-coated BPT-labelled AuNR:liposome; 0.4 mg/ml AuNRs concentration) at different temperatures above the T_m of DSPC (42-43 °C), 44, 46, 48 and 50°C for 20 minutes, was tested by TEM as shown in the following section.

6.2.1.1.1 Temperature effect

When prepared at 44°C, gold nanorods line the interior side of the liposome membrane as shown in Figure 6.3. Increasing the temperature to 46°C (Figure 6.4) still shows that the gold nanorods are within the liposomes, often closely adhered to the membrane. However, there are fewer AuNRs attached to the liposomes when they are prepared at 48°C (Figure 6.5). Since the temperature was the only difference between those samples, then it seems to have an effect on the binding of the AuNRs to the liposomes.

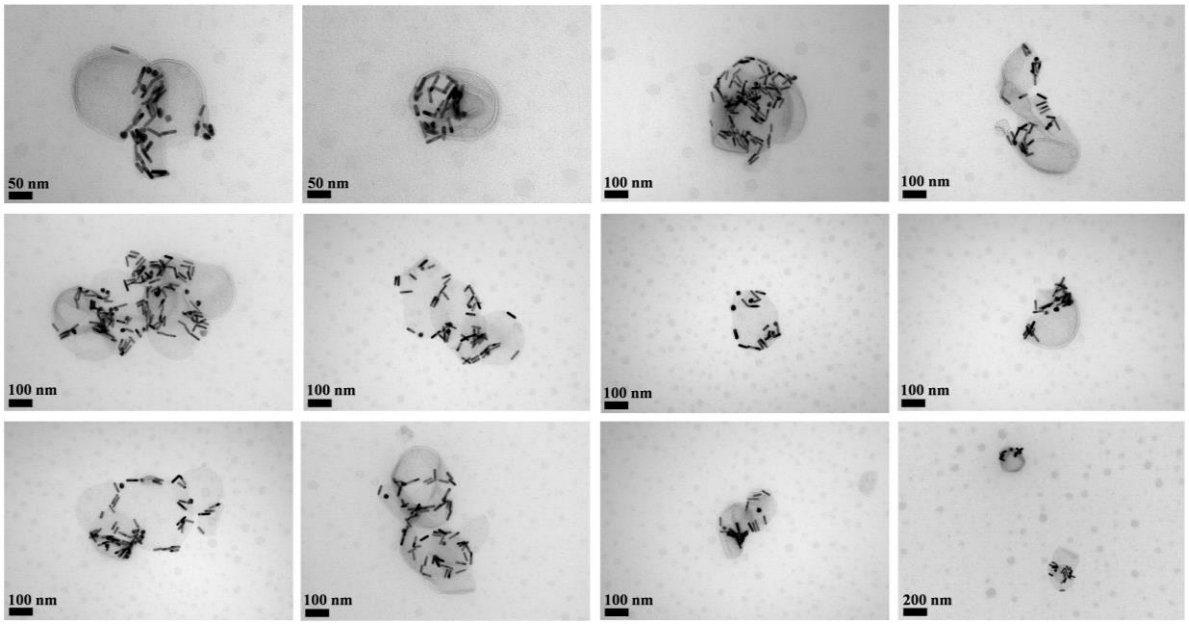

Figure 6.3 *55/15nm AuNR:liposome nanohybrids* with number ratio [6.9k:1] at 44°C. Scale bar: 50, 100 and 200 nm.

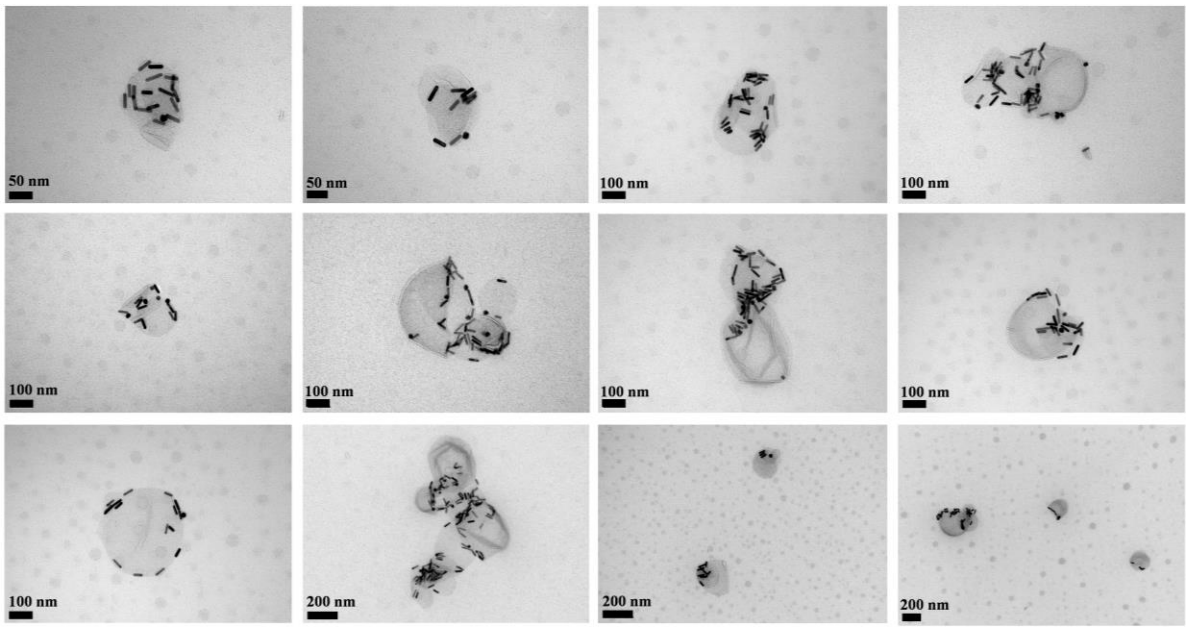

Figure 6.4 *55/15nm AuNR:liposome nanohybrids* with number ratio [6.9k:1] at 46°C. Scale bar: 50, 100 and 200 nm.

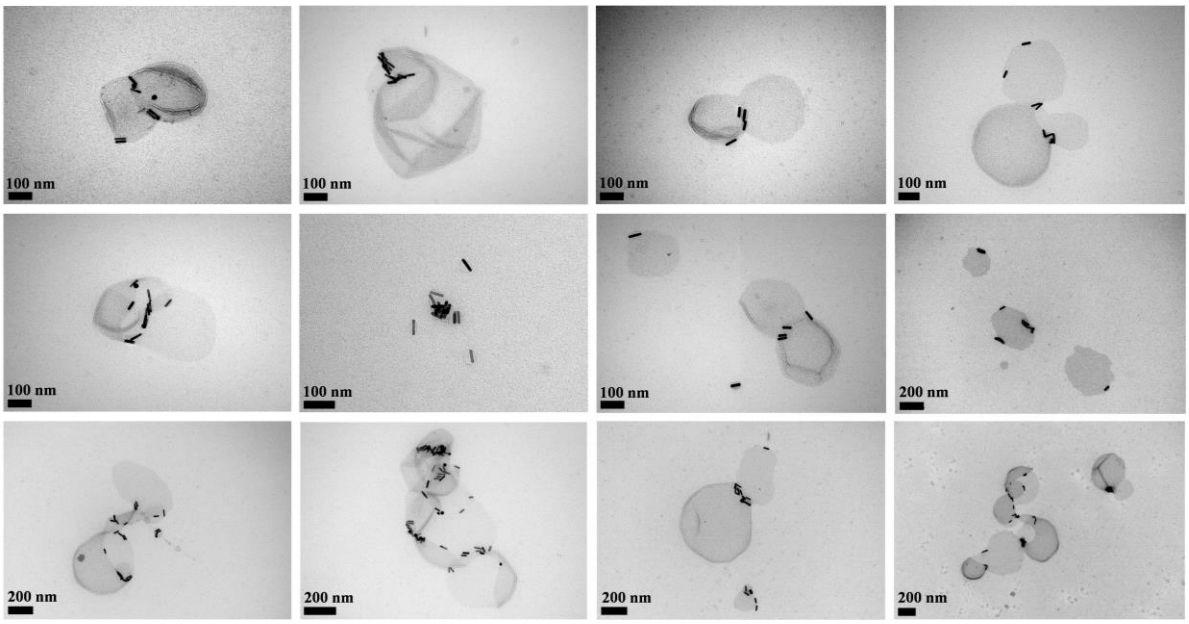

Figure 6.5 *55/15nm AuNR:liposome nanohybrids* with number ratio [6.9k:1] at 48°C. Scale bar: 100 and 200 nm.

Eventually at 50°C, finding areas with nanorods still attached to visible parts of liposomes was difficult, as shown in Figure 6.6. It is seen that the liposomes are definitely fragmented with lots of individual nanorods still wrapped in lipid, and a few empty liposomes are visible without any nanorods attached to them.

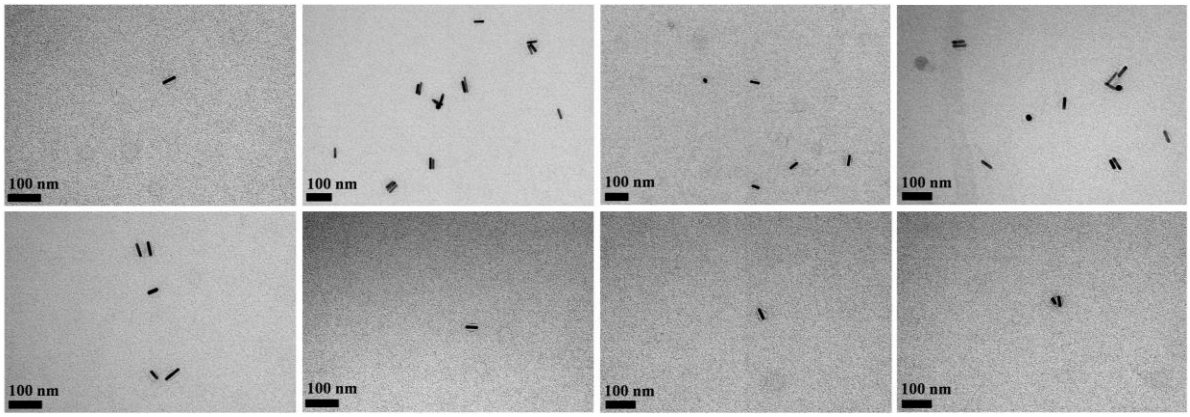

Figure 6.6 *55/15nm AuNR:liposome nanohybrids* with number ratio [6.9k:1] at 50°C. Scale bar: 100 nm.

These results show distinctly that, during preparation, an increase in temperature well above the liposome T_m disrupts the membrane and hence prevents aggregation of the AuNRs with liposomes. They also indicate that the liposomes are integral templates for the assembly of AuNRs, both encapsulated into and adhered to the membrane.

6.2.1.1.2 Determination of the location of NRs by section thickness (inside or outside the liposome surface)

To be able to image cross-sections of liposomes, samples were mixed with 12% pig skin gelatin in PBS, to trap them inside and to then process little cubes of gelatin. AuNRs were visible both within the liposomes and on the outside. As shown in Figure 6.7, it is important to note that the section thickness is 70 nm.

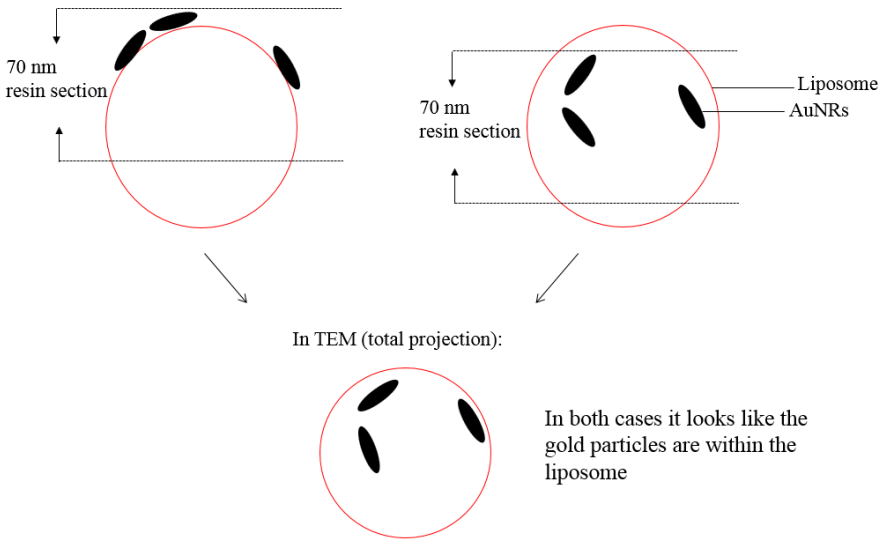

Figure 6.7 Schematic diagram illustrating *55/15nm AuNR:liposome nanohybrids* at thick sections at 70 nm in TEM.

Therefore, with a liposome size of 100 nm, it depends which part of the liposome is displayed in the section. In other words, some of the gold particles that appear to be inside the liposome structures could theoretically also be on the outside. With the TEM we essentially see a total projection of anything within the section, so it could look like the gold is inside although it is on the outside.

With the sections cut at 70 nm as shown in Figure 6.8, as there are plenty of liposomes visible with gold particles inside the boundary of the liposomes, the most likely outcome is that we have a mix of both, particles stuck to the outside of the liposomes and some which are within.

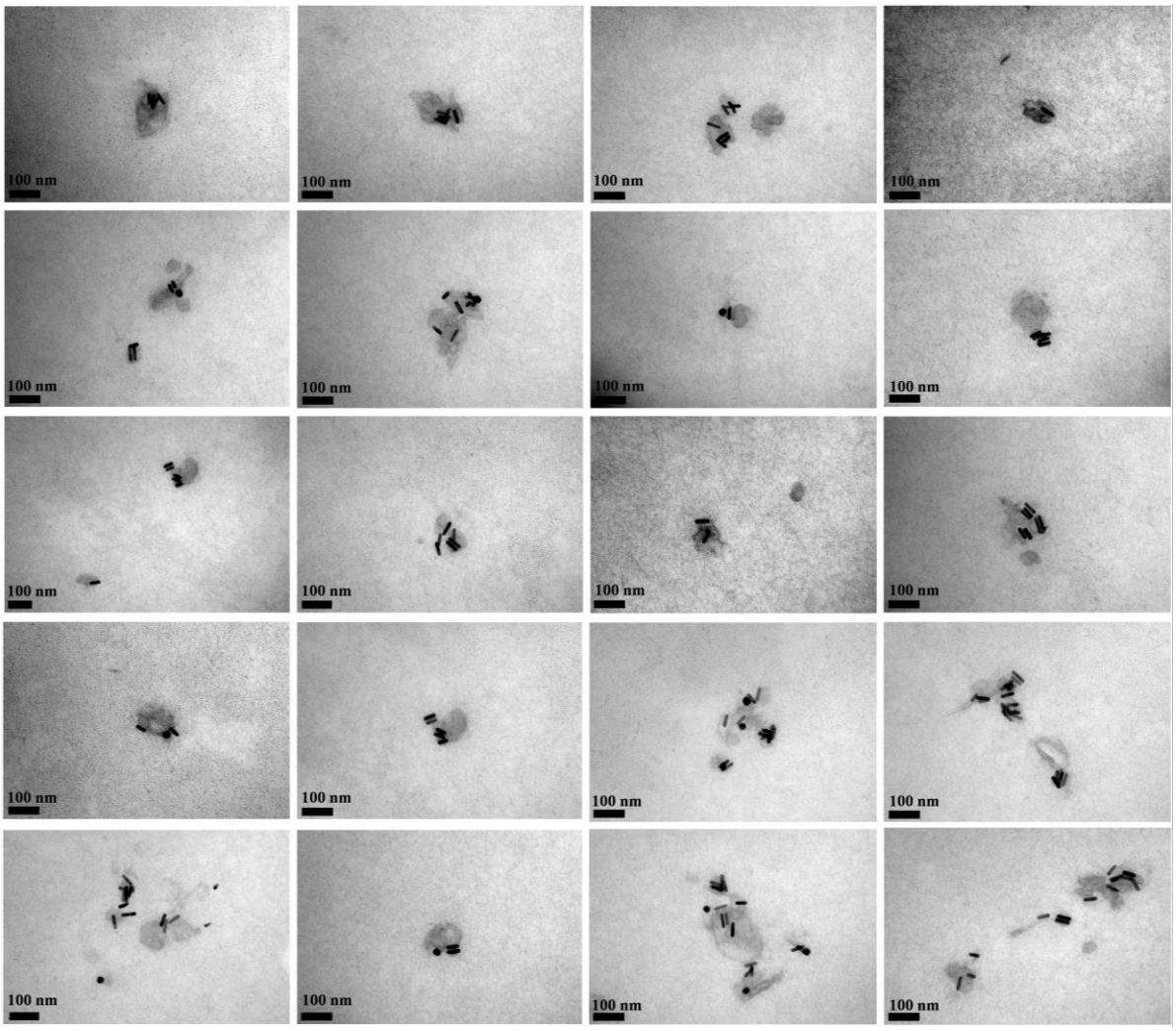

Figure 6.8 *55/15nm AuNR:liposome nanohybrids* with number ratio [6.9k:1] at 70 nm-thick sections. Scale bar: 100 nm.

The outcome of thinner sections at 30 nm (Figure 6.9) is pretty similar. Some AuNPs are nicely surrounded by the liposomes, thus they will be inside of them. However, other AuNPs seem to be bound to the surface, rather than encapsulated in the interior.

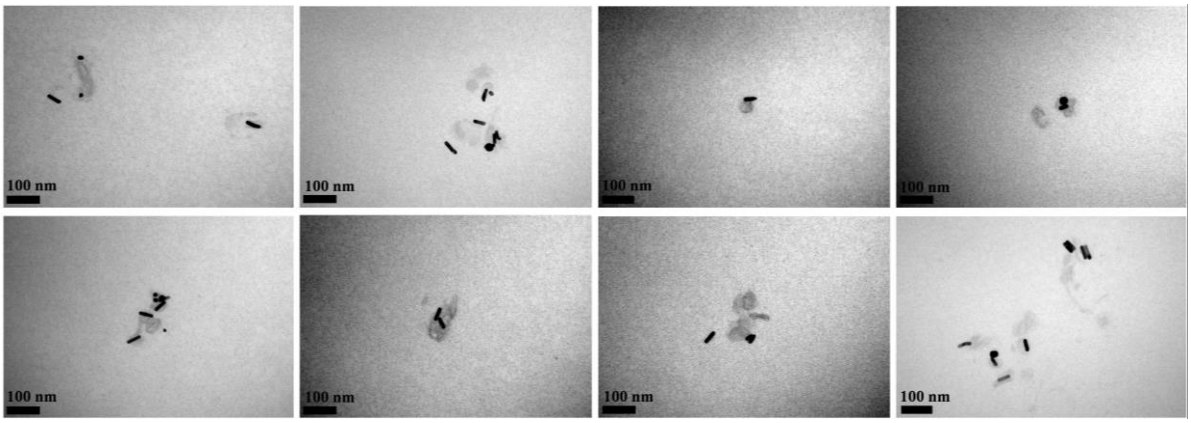

Figure 6.9 *55/15nm AuNR:liposome nanohybrids* with number ratio [6.9k:1] at 30 nm-thick sections. Scale bar: 100 nm.

6.2.1.2 52/16nm AuNRs+BPT+CTAB+liposome

To compare the TEM images of liposomal nanoconstructs prepared from commercial nanorods given in section 6.2.1.1, TEM images of liposomal nanoconstructs prepared using synthetic nanorods are demonstrated here. Synthetic nanorods (*52/16nm AuNRs*) with CTAB and using PBS as solvent were used to prepare liposomal nanohybrids. TEM images of only *52/16nm AuNRs+CTAB* are shown in Figure 6.10. Gold particles appear to be adhered to the outside of membrane structures.

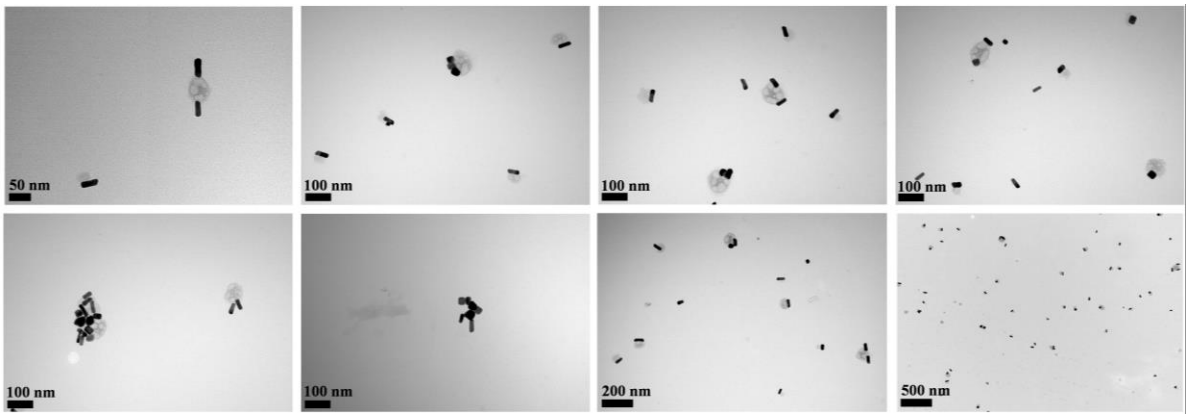

Figure 6.10 TEM images of *52/16nm AuNRs+CTAB*. Scale bar: 50, 100, 200 and 500 nm.

However, after adding liposome to synthetic nanorods (52/16nm *AuNRs+PBS+CTAB+liposome*) as in Figure 6.11, the majority of gold particles appears not bound to any membrane structure. A proportion of the particles appear to form larger aggregates. Some of the particles are visible within smaller liposomes.

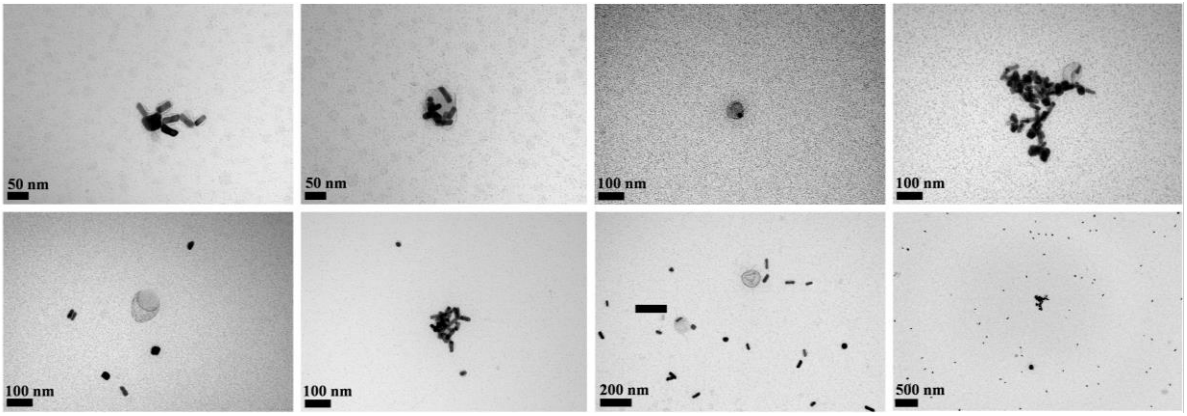

Figure 6.11 TEM images of *52/16nm AuNR:liposome nanohybrids* with number ratio [6.9k:1], PBS solvent. Scale bar: 50, 100, 200 and 500 nm.

In addition, distilled water was used as an alternative solvent to compare with PBS, as shown in Figure 6.12. Gold particles can be identified as adhered to liposome structures, engulfed by the membrane or as unbound particles, not in contact with any membrane.

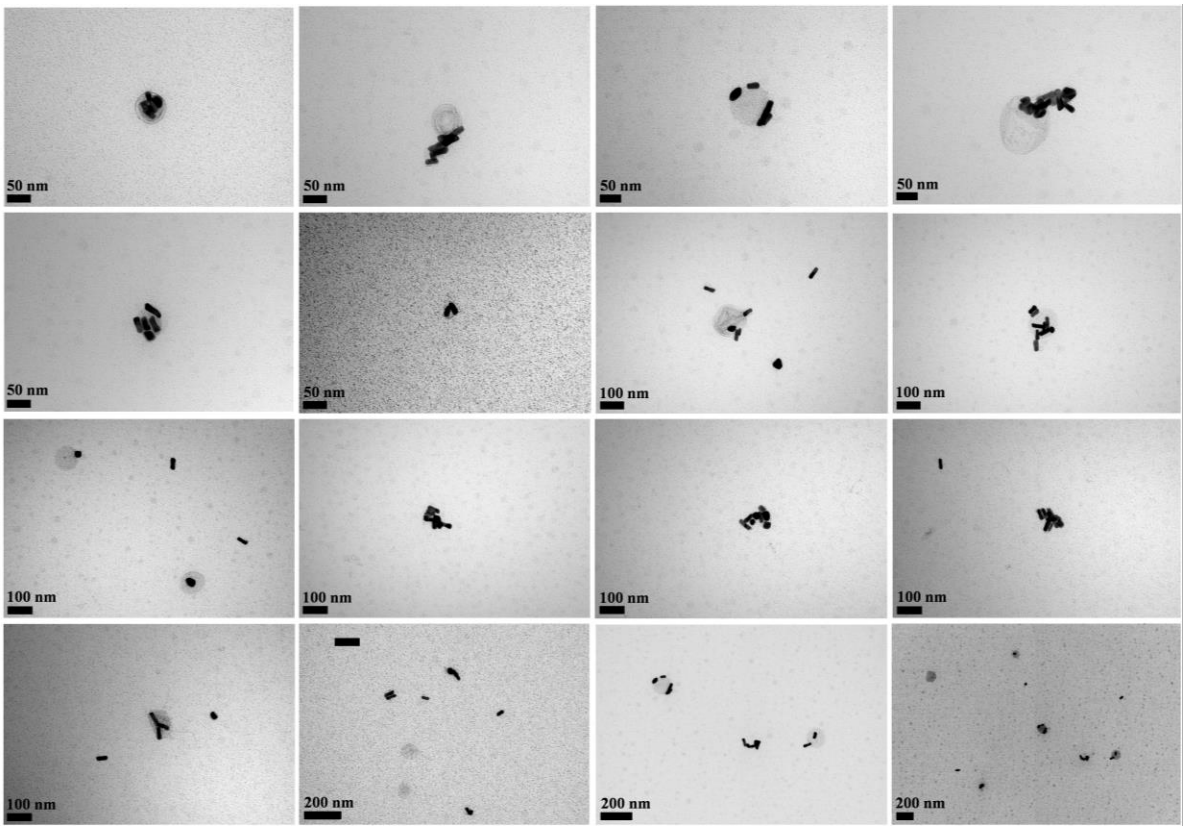

Figure 6.12 *52/16nm AuNR:liposome nanohybrids* with number ratio [6.9k:1], water solvent. Scale bar: 50, 100 and 200 nm.

6.2.1.2.1 Laser power effect

In this project, the effect of laser power was studied for AuNRs+CTAB+liposome at 0.5 and 1 W. It is observed that, after illumination by laser at 0.5 W and 1 W, finding an intact liposome is difficult, as shown in Figure 6.13 and 6.14.

At 0.5 W, we find the occasional intact liposome (Figure 6.13). For example, some images show the liposome with a few gold nanorods attached. Other structures could represent damaged liposomes. A small membrane structure (micelle) or a small liposome can be observed in the TEM images. As for the NRs, there is definitely a mix of elongated and more round ones. The laser treatment appears to have affected the majority of liposomes structures. Gold particles still associate with membrane structures, however some nanorods are turned into nanospheres by rearrangement of their structures due to laser irradiance.

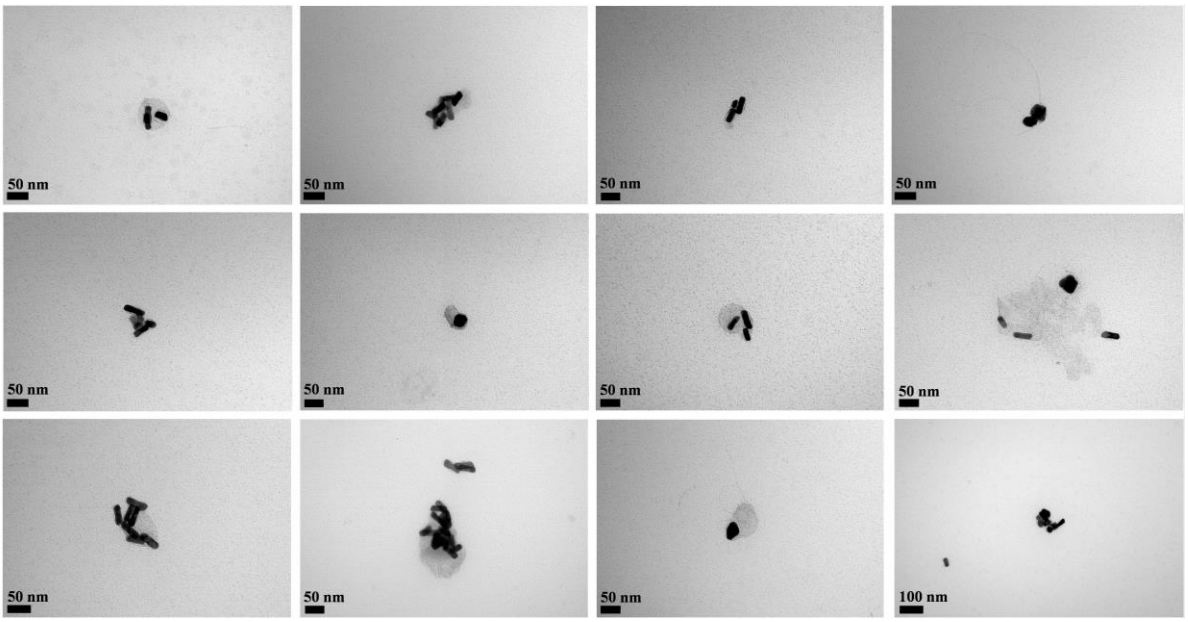

Figure 6.13 *55/15nm AuNR:liposome nanohybrids* with number ratio [6.9k:1] after illumination of laser power at 0.5 W. Scale bar: 50 and 100 nm.

At 1 W, this effect is even more apparent, as shown in Figure 6.14. The TEM images reveal that gold nanorods are capable of attaching to membrane structures, although in the process it is likely that the liposomes may be damaged. Certain cases of non-attachment are also common.

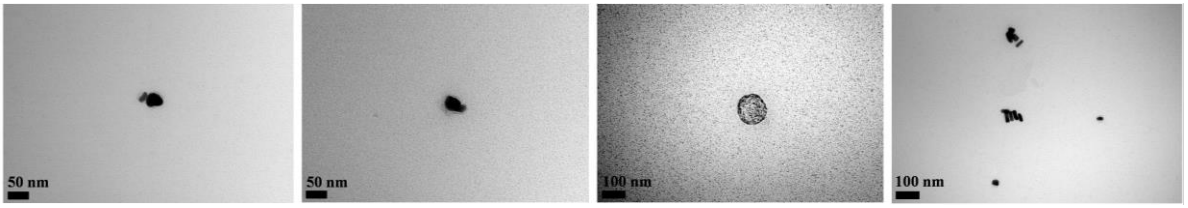

Figure 6.14 *55/15nm AuNR:liposome nanohybrids* with number ratio [6.9k:1] after illumination of laser power at 1.0 W. Scale bar: 50 and 100 nm.

These data warn of the use of suitable laser powers for illumination, such that nanohybrids are not badly affected during Raman or PTT measurements.

6.2.2 DLS data

Figure 6.15a I, II, III, IV, V, VI, VI* show the size distribution of *55/15nm AuNRs*, CTAB labelled *55/15nmAuNRs*, *55/15nm AuNRs+BPT+CTAB+liposome* at 4 µg/ml AuNPs concentration, *55/15nm AuNRs+BPT+CTAB+liposome* at 10 µg/ml AuNPs concentration, *55/15nm AuNRs+BPT+CTAB+liposome* at 200 µg/ml AuNPs concentration, *55/15nm AuNRs+BPT+CTAB+liposome* at 400 µg/ml AuNPs concentration, *55/15nm AuNRs+BPT+CTAB+liposome* at 400 µg/ml AuNPs concentration (50°C). The size distribution of *55/15nm AuNRs*, and CTAB labelled *55/15nm AuNRs* were 59±3 and 63±3, respectively (Figure 6.15a I, II). The DLS size distribution increases upon increasing concentration of *55/15nm AuNRs+BPT+CTAB+liposome* (Figure 6.16a III, IV, V, VI). They are 67±3, 80±3, 85±2 and 108±4 nm, respectively. However, heating up the *55/15nm AuNRs+BPT+CTAB+liposome* at 400 µg/ml concentration to 50°C will reduce the size from 108 to 60±4 nm (Figure 6.15a VI*). From NTA testing, the size of *55/15nm AuNRs+BPT+CTAB+liposome* at 400 µg/ml was around 129±8 nm, as shown in Figure 6.15c. The surface charge of *55/15nm* AuNR solution (Figure 6.15d I) reversed from – 42±2 mV to +45±3 mV after adding CTAB (Figure 6.15d II). For *55/15nm AuNR+BPT+CTAB+liposome* at 400 µg/ml (Figure 6.15d VI), the surface charge was ~35±3 mV. A decrease in concentration to 200, 10 and 4 µg/ml (Figure 6.15d V, IV, III, respectively) will reduce the surface charge to 26±3, 21±2, and 10±2 mV.

For the synthetic nanorods (52/16 nm size*)*, the size distribution of stock *52/16 nm AuNRs* was approximately 68.3±6 nm, with +27±2 mV surface charge (Figure 6.15b,d VII). Adding CTAB during *52/16 nm AuNRs* synthesis reversed the charge of AuNRs from negative to positive values. However, dilution of stock *52/16 nm AuNRs* solution in PBS by 1/5, 1/10, 1/100 and 1/1000 reduced the positive charge to 25.3±2, 24.8±1, 16.2±1, and – 13.7±2 mV and increased the particle size distribution to 71.9±3, 85±4, 94.6±5, and 109±7 nm, respectively (Figure 6.15b,d VIII, IX, X, XI). Most importantly, adding liposomes to these synthetic nanorods with and without BPT labelling can increase both the size distribution and the positive surface charge. The size distribution of *52/16 nm AuNRs+CTAB+liposome* and *52/16 nm AuNRs+CTAB+BPT+liposome* after distilled water resuspsion was 73±4 and 95.8±3 nm with surface charge of 37.1 ±2 and 50.7 ±4 mV, respectively (Figure 6.15b,d XII, XIII). However, the DLS size distribution of *52/16 nm AuNRs+CTAB+liposome* and *52/16 nm AuNRs+CTAB+BPT+liposome* (in PBS) was 112±5 and 191±4 nm with surface charge of 28±2 and 35±3 mV, respectively (Figure 6.15b,d XIV, XV).

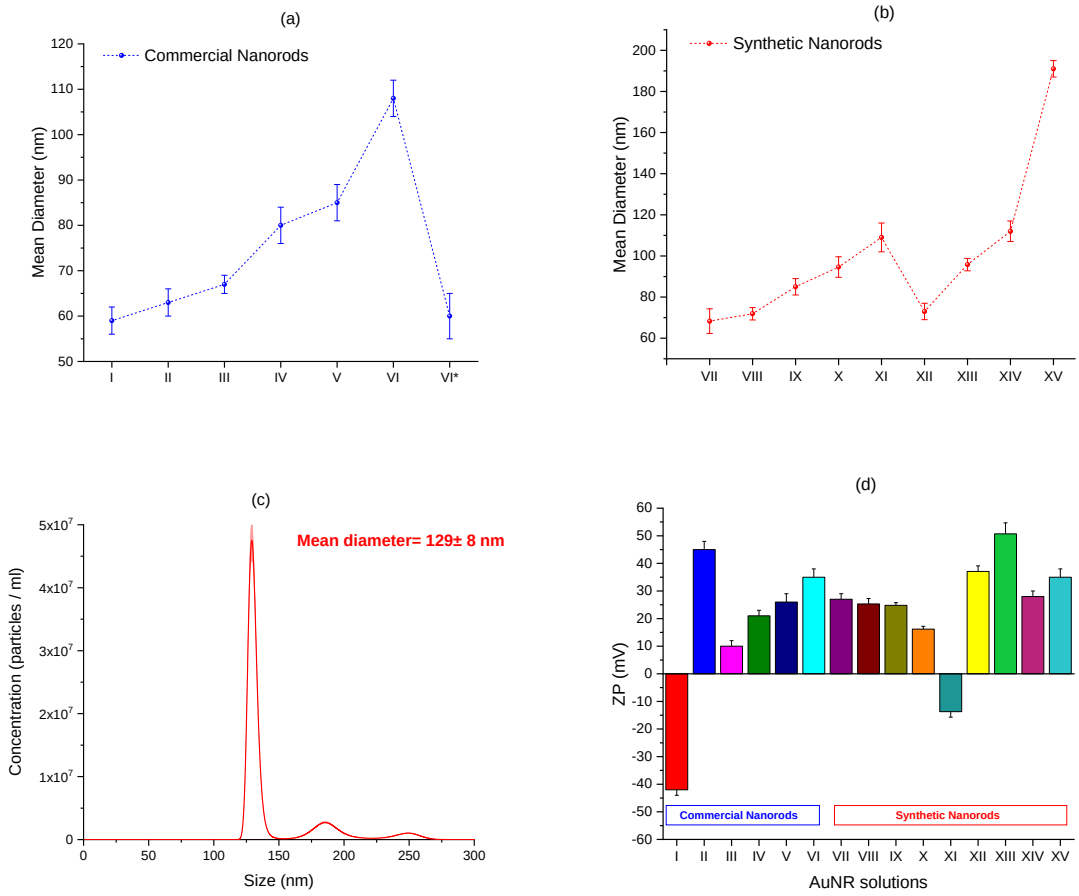

Figure 6.15 The particle size distribution of different AuNR:liposome using (a) commercial *55/15nm AuNRs* and (b) synthetic *52/16nm AuNRs*. (c) *55/15nm AuNRs+BPT+CTAB+liposome* size distribution plotted in terms of concentration in 10^7 particles/ml by NTA. (d) the zeta potential of 55/15nm and *52/16nm AuNRs+BPT+CTAB+Liposome* by using DLS.

In addition, the NanoSight method was used to capture the video data of *55/15nm AuNRs+BPT+CTAB+liposome* solutions. Figure 6.16 displays screenshots of videos from NanoSight LM10 testing, showing optimal light scatter from liposomal nanoconstucts measured both (from left to right) at 5, 10, 30 and 60 s.

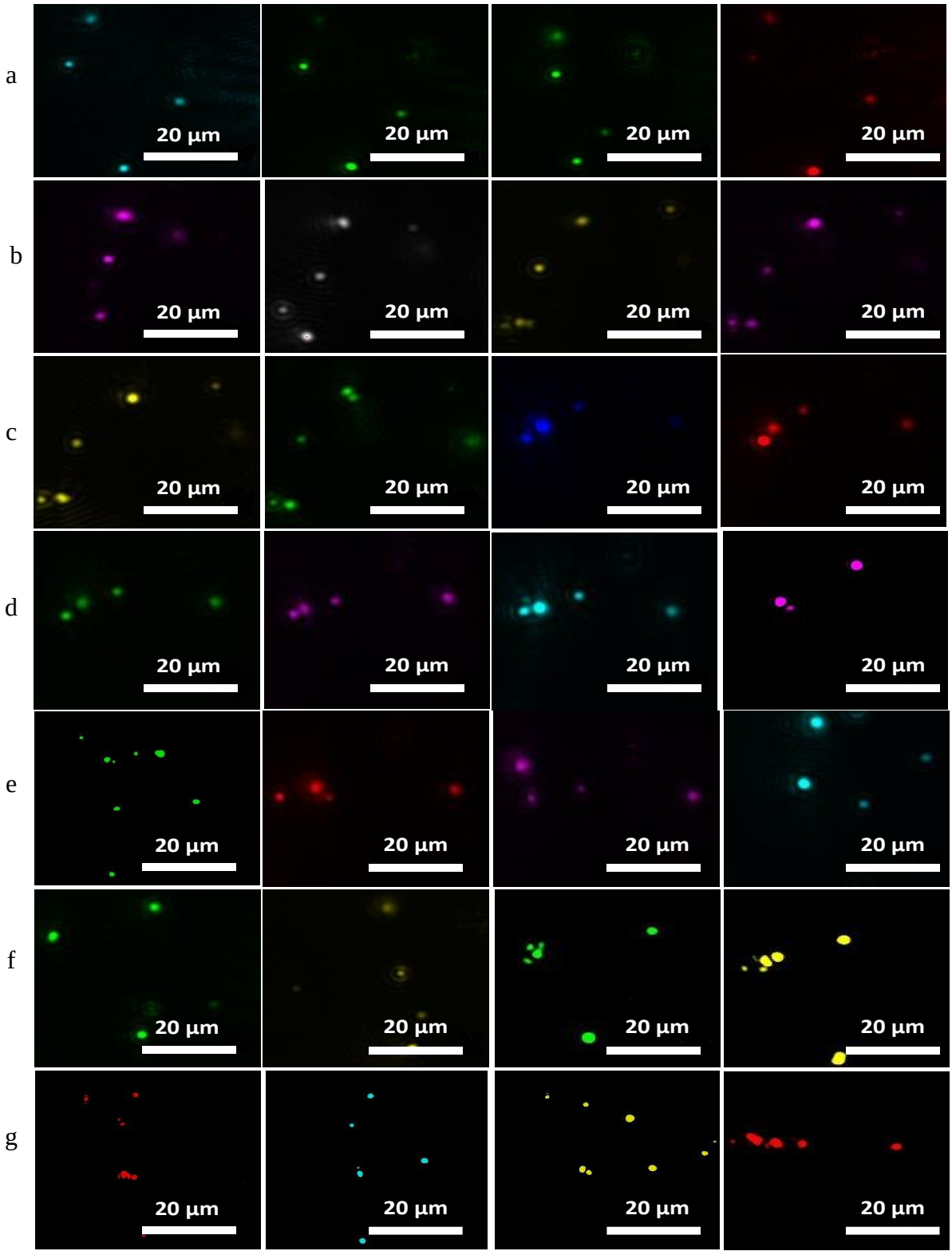

Figure 6.16 NTA images showing light scattered off liposomes; acquisition time: 5 s, 10 s, 30 s and 60 s, in different position a, b, c, d, e, f, g. Scale bar: 10 µm.

6.2.3 Plasmonic light absorption

Figure 6.17a shows the UV-visible absorption spectra of *55/15nm AuNR:liposome nanohybrids* at various concentrations (black curve) 0.016, (red) 0.2, (blue) 0.4, and (green) 0.4 mg/ml heated to 50°C. The surface plasmon band redshifts upon increasing the AuNR:liposome ratio, as shown in Figure 6.17b. The maximum absorption for these concentrations is 795, 797, and 824 nm, respectively. The optimal concentration appears to be 0.4 mg/ml, which has the highest plasmonic peak. Heating the high concentration solution (0.4 mg/ml) up to 50°C for 20 minutes is found to reduce the redshift from 824 nm to 816 nm as well as the maximum absorption by 2.3 times, as shown in (green spectrum) in Figure 6.17a. This result shows the tuneability of lipid membrane based on its T_m, hence the lipid structures can be affected by temperature which is a critical variable.

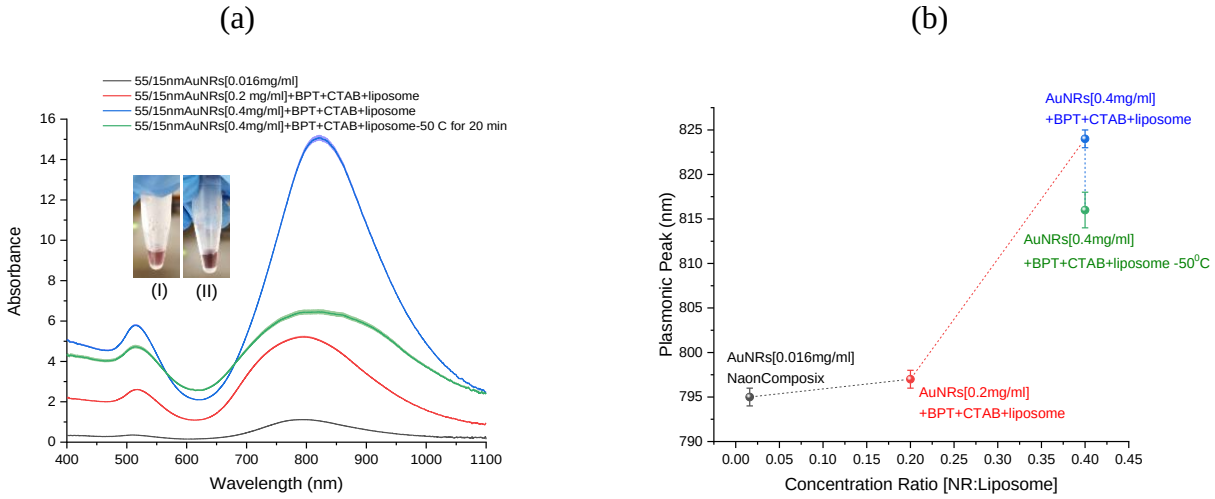

Figure 6.17 (a) UV-visible spectra of liposome nanoconstructs using (CTAB and AuNRs) in different concentrations. Inset: photos of liposome at (low and high ratio concentration (I: II; *55/15nm AuNRs [0.2 mg/ml]+BPT+CTAB+liposome* and *55/15nm AuNRs [0.4 mg/ml]+BPT+CTAB+liposome* respectively). (b) Plasmonic peaks for *55/15nm AuNRs (0.016 mg/ml), 55/15nm AuNRs [0.2 mg/ml]+BPT+CTAB+liposome*, 55/*15nm AuNRs [0.4 mg/ml]+BPT+CTAB+liposome*, and *55/15nm AuNRs [0.4 mg/ml]+BPT+CTAB+liposome* after increasing temperature to 50°C for 20 min.

In contrast, for the synthetic AuNRs, the absorbance of *52/16nm AuNRs+CTAB* with different solvents such as PBS and distilled water was much lower (Figure 6.18), and their peaks were also

at lower max. wavelength, 719 and 712 nm respectively. However, adding liposomes to *52/16nm AuNRs+CTAB* increased the absorbance 12 times with a 3 nm redshift. Moreover, better results are achieved upon BPT labelling of *52/16nm AuNRs+CTAB+liposome* nanoconstructs, since the structure is more uniform which then leads to an increase and redshift of the plasmonic peak.

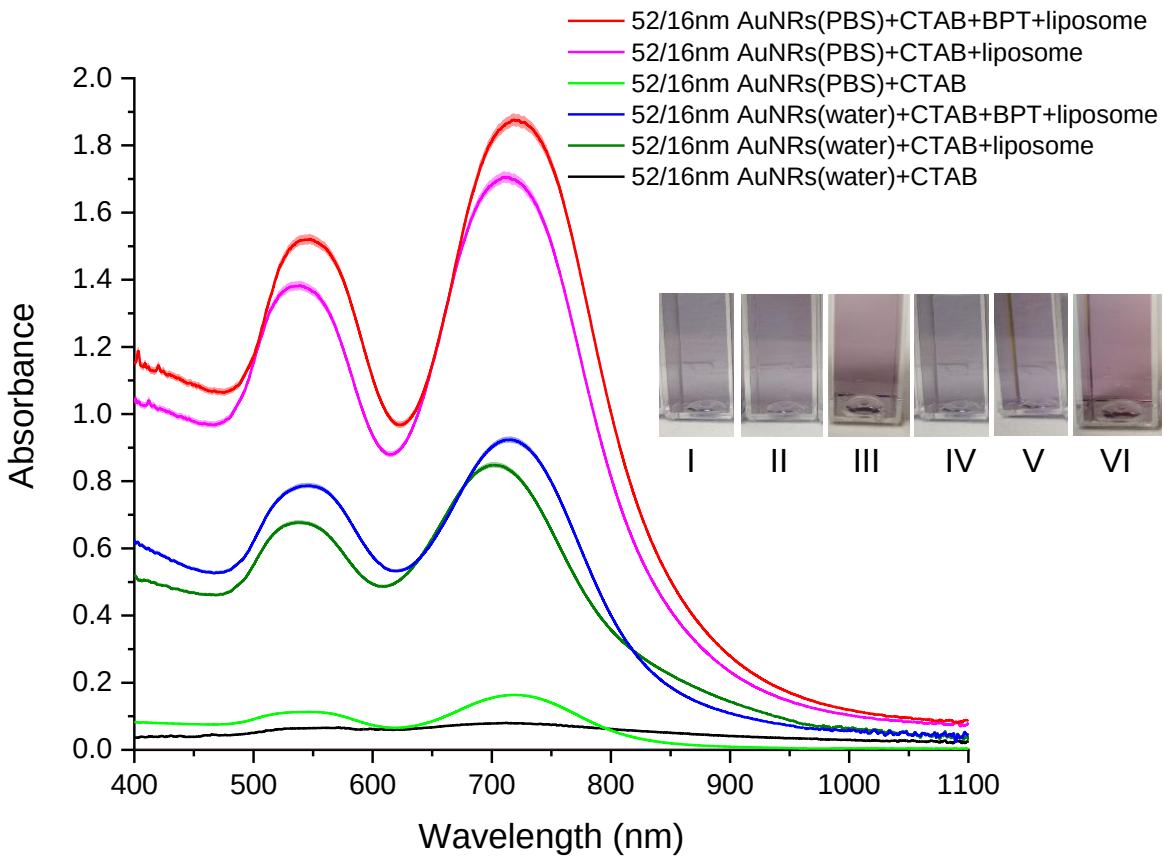

Figure 6.18 UV-visible absorption spectra of various colloidal nanorods: 52/16nm AuNRs(water)+CTAB, 52/16nm AuNRs(water)+CTAB+liposome, 52/16nm AuNRs(water)+BPT+CTAB+liposome, 52/16nm AuNRs(PBS)+CTAB, 52/16nm AuNRs(PBS)+CTAB+liposome, and 52/16nm AuNRs(PBS)+BPT+CTAB+liposome. Inset: photos of (I) 52/16nm AuNRs(PBS)+CTAB+liposome, (II) 52/16nm AuNRs(PBS)+CTAB+liposome, (III) 52/16nm AuNRs(PBS)+CTAB, (IV) 52/16nm AuNRs(water)+BPT+CTAB+liposome, (V) 52/16nm AuNRs(water)+CTAB+liposome and (VI) 52/16nm AuNRs(water)+CTAB.

6.2.4 SERS

Figure 6.19 I, II, III, IV, V, VI, VII show the Raman spectra of water, BPT in ethanol solution at $9.1 \cdot 10^{-5}$ M concentration, BPT labelled *55/15nm AuNRs*, CTAB coated *55/15nm AuNRs* with liposomes, CTAB coated and BPT labelled *55/15nm AuNRs* with liposomes (as wet drop), CTAB coated and BPT labelled *55/15nm AuNRs* with liposomes (as dried drop), and CTAB coated and BPT labelled *55/15nm AuNRs* with liposomes treated at 50°C, measured at (a) 785 and (b) 830 nm. The AuNRs concentration was 0.4 mg/ml. There were no Raman signal arising from the AuNRs (Figure 6.19 I) or CTAB coated AuNRs with liposomes (Figure 6.19 IV) when BPT was not added. However, the three notable Raman peaks from BPT at 1080, 1278, and 1586 cm^{-1} are apparent when BPT is added to CTAB coated AuNRs with liposomes, as in Figure 6.19 V, VI. The SERS signal is increased by approximately an order of magnitude upon drying of a drop of sample (Figure 6.19 VI) compared to the wet drop (Figure 6.19 V, Table 6.1). However, no SERS signal is apparent for the nanostructure with AuNRs after heating at 50°C (Figure 6.19 VII).

Excitation at 830 nm was found to produce larger Raman signals than those obtained with 785 nm excitation, as it is expected. The SERS signal measured at 830 nm was approximately five to six times as large when compared to using 785 nm laser illumination at all three peaks. The highest signal was found for CTAB coated and BPT labelled AuNRs with liposomes evaluated at 1080 cm^{-1} using the 830 nm laser ($6.47 \cdot 10^{7}$). This results is likely arising due to the NIR resonance (Figure 6.17).

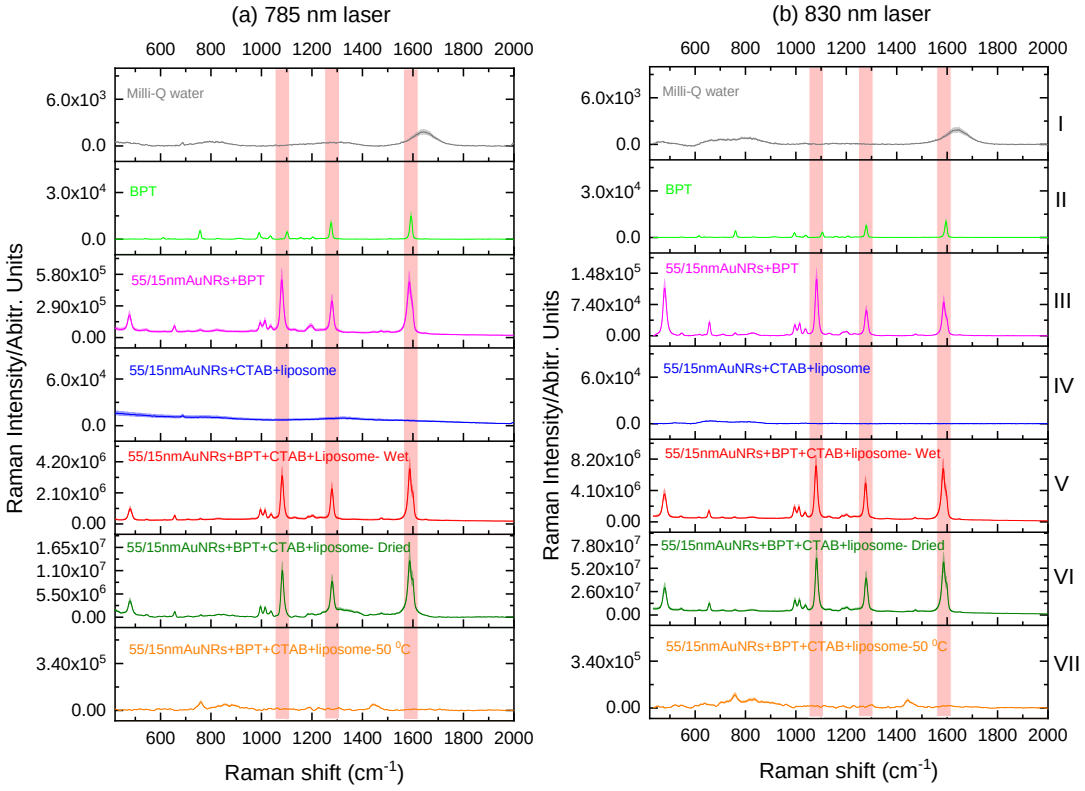

Figure 6.19 Raman spectra of (I) water, (II) BPT in ethanol solution ($9.1 \cdot 10^{-5}$ M concentration), (III) *55/15nm AuNRs+BPT*, (IV) *55/15nm AuNRs+CTAB+liposome*, (V) *55/15nm AuNRs+BPT+CTAB+liposome* as wet drop, (VI) as dried drop, and (VII) *55/15nm AuNRs+BPT+CTAB+liposome* at 50°C. The AuNRs concentration was 0.4 mg/ml.

Table 6.1 List of Raman spectra of *55/15nm AuNRs+BPT+CTAB+liposome* as wet drop and dried drop. The AuNRs concentration was 400 µg/ml.

Laser wavelengths	785 nm			830 nm		
Peaks (cm^{-1})	1080	1278	1586	1080	1278	1586
Dried drop	$1.14 \cdot 10^7$	$8.62 \cdot 10^6$	$1.34 \cdot 10^7$	$6.47 \cdot 10^7$	$4.17 \cdot 10^7$	$5.94 \cdot 10^7$
Wet drop	$3.36 \cdot 10^6$	$2.43 \cdot 10^6$	$3.79 \cdot 10^6$	$7.45 \cdot 10^6$	$5.14 \cdot 10^6$	$7.05 \cdot 10^6$

The nanostructures with AuNRs at different concentrations were investigated at 4 µg/ml and 10 µg/ml for different depths of probing: (-0, -100, -200, -300, -400, -500, -600 and -700) µm depth. When BPT was not added, no Raman signal was found, as shown in Figure 6.20a,b,c,d. However, the SERS signal is obtained significantly for the nanostructures with AuNRs (Figure 6.21a,b,c,d).

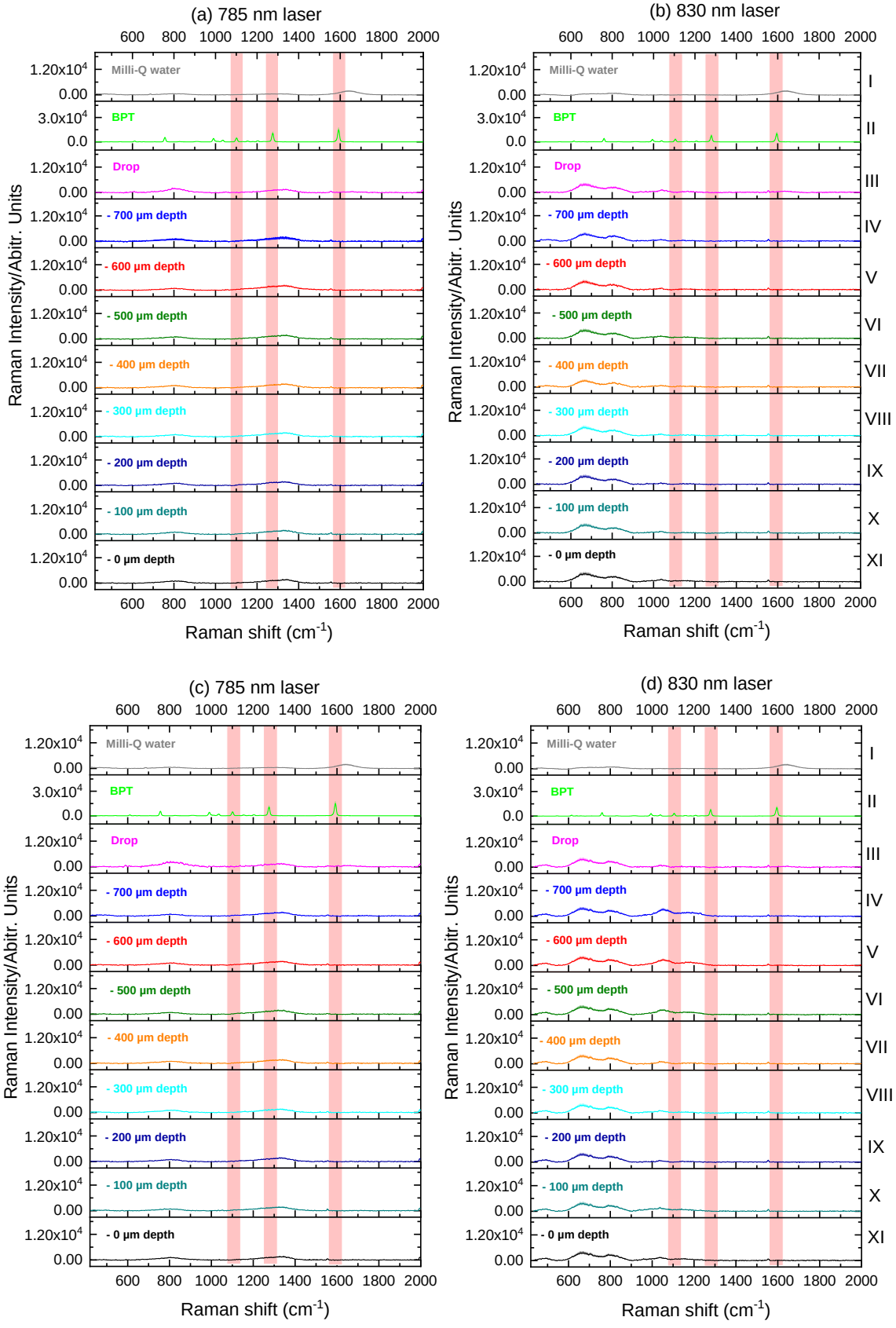
(a) 785 nm laser
(b) 830 nm laser
(c) 785 nm laser
(d) 830 nm laser
Milli-Q water
BPT
Drop
- 700 µm depth
- 600 µm depth
- 500 µm depth
- 400 µm depth
- 300 µm depth
- 200 µm depth
- 100 µm depth
- 0 µm depth
I
II
III
IV
V
VI
VII
VIII
IX
X
XI
Raman Intensity/Abitr. Units
Raman shift (cm-1)
600 800 1000 1200 1400 1600 1800 2000
1.20x10^4
0.00
3.0x10^4
0.0

Figure 6.20 Raman spectra of (I) water, (II) BPT in ethanol solution ($9.1 \cdot 10^{-5}$ M concentration), (III) drop of *55/15nm AuNRs*, and at different depth (IV) -700 µm depth, (V) -600 µm depth, (VI) -500 µm depth, (VII) -400 µm depth, (VIII) -300 µm depth, (IX) -200 µm depth, (X) -100 µm depth and (XI) -0 µm depth) at (a) 785 nm in 4 µg/ml concentration and (b) 830 nm laser in 4 µg/ml concentration, (c) 785 nm in 10 µg/ml concentration and (d) 830 nm laser in 10 µg/ml concentration.

At different depths from -0 µm to 700 µm depth at 4 µg/ml and 10 µg/ml concentrations, the largest SERS signals were obtained at approximately 300 to 400 µm depth and increased more for 10 µg/ml concentration with 830 nm laser ($1.16 \cdot 10^{6}$ at 1080 and 1586 cm^{-1}) as presented in Table 6.2. Furthermore, the SERS signal increased significantly when measuring the sample as a drop on quartz microplate. Moreover, The SERS signal at 830 nm was approximately twice as large as that at 785 nm for all three peaks (1080, 1278 and 1586 cm^{-1}). The largest signal was obtained for CTAB coated and BPT labelled AuNRs with liposomes at 1080 cm^{-1} using the 830 nm laser ($8.24 \cdot 10^{7}$).

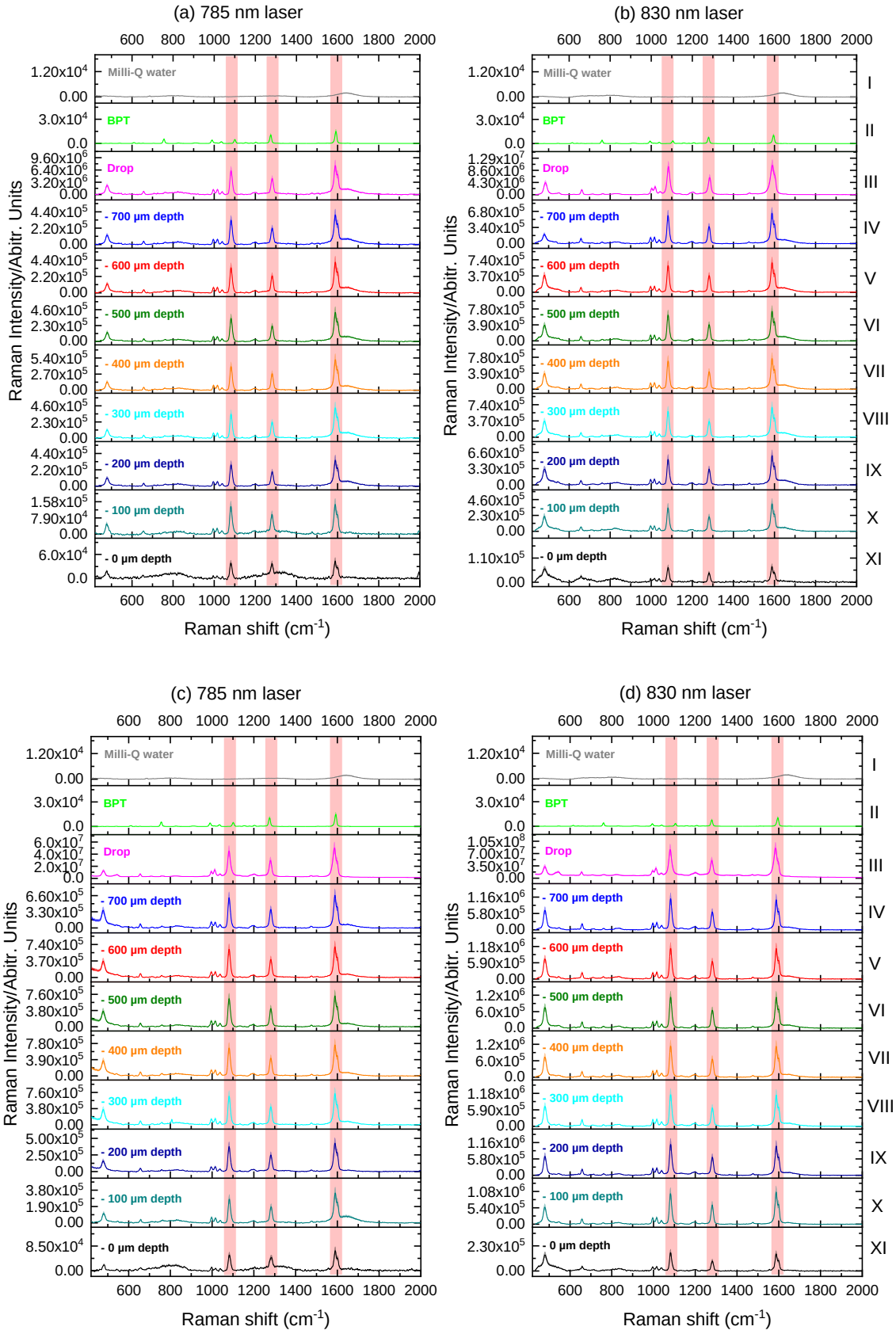
(a) 785 nm laser
(b) 830 nm laser
(c) 785 nm laser
(d) 830 nm laser
Milli-Q water
BPT
Drop
- 700 µm depth
- 600 µm depth
- 500 µm depth
- 400 µm depth
- 300 µm depth
- 200 µm depth
- 100 µm depth
- 0 µm depth
I
II
III
IV
V
VI
VII
VIII
IX
X
XI
Raman Intensity/Abitr. Units
Raman shift (cm-1)
600 800 1000 1200 1400 1600 1800 2000

Figure 6.21 Raman spectra of (I) water, (II) BPT in ethanol solution ($9.1 \cdot 10^{-5}$ M concentration), (III) a drop of *55/15nm AuNRs+BPT+CTAB+liposome*, and at different depths (IV) -700 µm depth, (V) -600 µm depth, (VI) -500 µm depth, (VII) -400 µm depth, (VIII) -300 µm depth, (IX) -200 µm depth, (X) -100 µm depth and (XI) -0 µm depth at (a) 785 nm in 4µg/ml concentration and (b) 830 nm laser in 4µg/ml concentration, (c) 785 nm in 10 µg/ml concentration and (d) 830 nm laser in 10 µg/ml concentration.

Table 6.2 List of Raman spectral intensity of a drop of *55/15nm AuNRs+BPT+CTAB+liposome* and at different depths from -0 to 700 µm. The AuNRs concentrations were 4 and 10 µg/ml.

Laser wavelengths		785 nm			830 nm		
Peaks ($cm^{-}1$)		1080	1278	1586	1080	1278	1586
4 µg/ml	drop	$5.98 \cdot 10^6$	$5.16 \cdot 10^6$	$8.10 \cdot 10^6$	$1.0 \cdot 10^7$	$6.10 \cdot 10^6$	$1.05 \cdot 10^7$
	0	$5.46 \cdot 10^4$	$4.37 \cdot 10^4$	$7.03 \cdot 10^4$	$6.98 \cdot 10^4$	$4.41 \cdot 10^4$	$7.23 \cdot 10^4$
	-100	$2.80 \cdot 10^5$	$1.91 \cdot 10^5$	$3.56 \cdot 10^5$	$3.47 \cdot 10^5$	$2.16 \cdot 10^5$	$4.05 \cdot 10^5$
	-200	$2.91 \cdot 10^5$	$2.00 \cdot 10^5$	$3.55 \cdot 10^5$	$5.29 \cdot 10^5$	$3.27 \cdot 10^5$	$6.05 \cdot 10^5$
	-300	$3.48 \cdot 10^5$	$2.28 \cdot 10^5$	$4.37 \cdot 10^5$	$5.98 \cdot 10^5$	$3.68 \cdot 10^5$	$6.92 \cdot 10^5$
	-400	$4.04 \cdot 10^5$	$2.84 \cdot 10^5$	$5.21 \cdot 10^5$	$7.04 \cdot 10^5$	$4.26 \cdot 10^5$	$7.58 \cdot 10^5$
	-500	$3.45 \cdot 10^5$	$2.31 \cdot 10^5$	$4.29 \cdot 10^5$	$6.39 \cdot 10^5$	$4.01 \cdot 10^5$	$7.34 \cdot 10^5$
	-600	$3.41 \cdot 10^5$	$2.24 \cdot 10^5$	$4.19 \cdot 10^5$	$6.18 \cdot 10^5$	$3.87 \cdot 10^5$	$6.83 \cdot 10^5$
	-700	$3.32 \cdot 10^5$	$2.28 \cdot 10^5$	$4.04 \cdot 10^5$	$6.05 \cdot 10^5$	$3.65 \cdot 10^5$	$6.46 \cdot 10^5$
10 µg/ml	drop	$4.64 \cdot 10^7$	$3.01 \cdot 10^7$	$5.09 \cdot 10^7$	$8.24 \cdot 10^7$	$5.10 \cdot 10^7$	$8.37 \cdot 10^7$
	0	$3.95 \cdot 10^4$	$3.80 \cdot 10^4$	$4.51 \cdot 10^4$	$1.69 \cdot 10^4$	$9.30 \cdot 10^4$	$1.57 \cdot 10^4$
	-100	$1.38 \cdot 10^5$	$9.97 \cdot 10^4$	$1.47 \cdot 10^5$	1024776	$6.44 \cdot 10^5$	$1.06 \cdot 10^6$
	-200	$3.88 \cdot 10^5$	$2.56 \cdot 10^5$	$4.34 \cdot 10^5$	$1.12 \cdot 10^6$	$6.47 \cdot 10^5$	$1.06 \cdot 10^6$
	-300	$6.93 \cdot 10^5$	$4.36 \cdot 10^5$	$7.52 \cdot 10^5$	$1.16 \cdot 10^6$	$6.68 \cdot 10^5$	$1.12 \cdot 10^6$
	-400	$6.87 \cdot 10^5$	$4.39 \cdot 10^5$	$7.62 \cdot 10^5$	$1.16 \cdot 10^6$	$6.67 \cdot 10^5$	$1.16 \cdot 10^6$
	-500	$6.79 \cdot 10^5$	$4.37 \cdot 10^5$	$7.40 \cdot 10^5$	$1.15 \cdot 10^6$	$6.57 \cdot 10^5$	$1.13 \cdot 10^6$
	-600	$6.49 \cdot 10^5$	$4.17 \cdot 10^5$	$7.00 \cdot 10^5$	$1.13 \cdot 10^6$	$6.48 \cdot 10^5$	$1.11 \cdot 10^6$
	-700	$6.39 \cdot 10^5$	$3.89 \cdot 10^5$	$6.79 \cdot 10^5$	$1.13 \cdot 10^6$	$6.42 \cdot 10^5$	$1.08 \cdot 10^6$

However, testing the nanostructure with synthetic AuNRs in different solvents (PBS and water) showed that the SERS signals using 785 and 830 nm excitations were approximately the same value. It was $4 \cdot 10^6$ (in water) and $6 \cdot 10^6$ (in PBS) at 1080 and 1586 cm^{-1} (Figure 6.22).

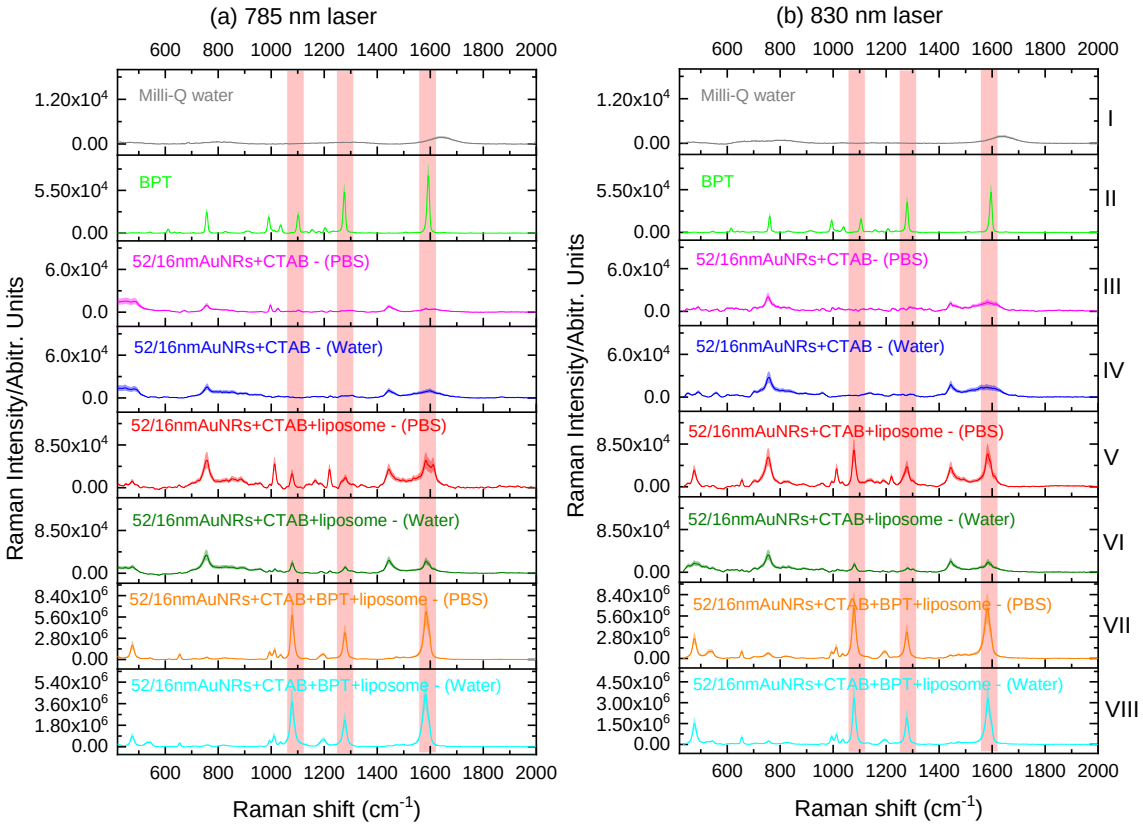

Figure 6.22 Raman spectra of (I) water, (II) BPT in ethanol solution ($9.1 \cdot 10^{-5}$ M concentration), (III) *52/16nm AuNRs+CTAB* in PBS solution, (IV) *52/16nm AuNRs+CTAB* in water, (V) *52/16nm AuNRs+CTAB+liposome* in PBS solution, (VI) 5*2/16nm AuNRs+CTAB+liposome* in water, (VII) *52/16nm AuNRs+CTAB+BPT+liposome* in PBS solution, (VIII) *52/16nm AuNRs+CTAB+BPT+liposome* in water at (a) 785 nm and (b) 830 nm lasers.

Figure 6.23 I, II, III, IV, V, VI, VII presents the SERS EF of BPT labelled *60nmAuNPs*, BPT labelled *80nm AuNPs*, CTAB coated and BPT labelled *52/16nm AuNRs* with liposomes (dissolved in water), CTAB coated and BPT labelled *52/16nm AuNRs* with liposomes (dissolved in PBS), CTAB coated and BPT labelled *55/15nm AuNRs* with liposomes (4 µg/ml), CTAB coated and BPT labelled *55/15nm AuNRs* with liposomes (400 µg/ml), and CTAB coated and BPT labelled *55/15nm AuNRs* with liposomes (10 µg/ml) at 785 and 830 nm. This figure evaluated the SERS

EF in the three highest peaks which are 1080 cm^{-1}, 1278 cm^{-1}, and 1586 cm^{-1}. The greatest enhancement factors (of around $2 \cdot 10^9$) were observed for CTAB coated and BPT labelled *55/15nm AuNRs* with liposomes (10 µg/ml) and CTAB coated and BPT labelled *55/15nm AuNRs* with liposomes (400 µg/ml) at 1080 cm^{-1}, as seen in Figure 6.23.

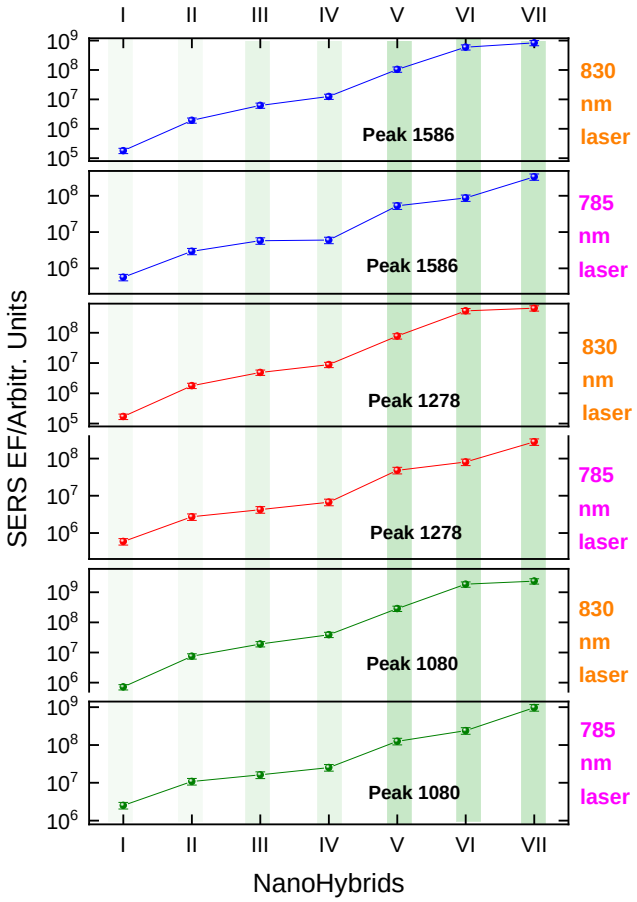

Figure 6.23 Plot of SERS EF of the three main peaks at 1080 cm^{-1}, 1278 cm^{-1}, and 1586 cm^{-1} for labelled AuNP solutions; (I) *60nm AuNPs+BPT*, (II) *80nm AuNPs+BPT*, (III) *52/16nm AuNRs+BPT+CTAB+liposome* (dissolved in water), (IV) *52/16nm AuNRs +BPT+CTAB+liposome* (dissolved in PBS), (V) *55/15nm AuNRs+BPT+CTAB+liposome* (4 µg/ml), (VI) *55/15nm AuNRs+BPT+CTAB+liposome* (400 µg/ml), (VII) *55/15nm AuNRs +BPT+CTAB+liposome* (10 µg/ml) at 785 nm and 830 nm excitation.

6.2.5 Potential photothermal therapeutic responses

Figure 6.24a,b presents the PTT results for liposomal nanoconstructs based on AuNRs. The calculated Q/E (0.5 W) is 74% for *55/15nm AuNRs*, 36% for *55/15nm AuNRs+BPT+CTAB+liposome*, 13% for *52/16nm AuNRs+CTAB*, 20% for *52/16nm AuNRs+ BPT+CTAB+liposome*. However, the calculated Q/E (1.0 W) is 18% for *52/16nm AuNRs+CTAB* and 19% for *52/16nm AuNRs+ BPT+CTAB+liposome*. The listing of results of photothermal experiments conducted on nanohybrids using a PTT system is been presented in Table 6.3.

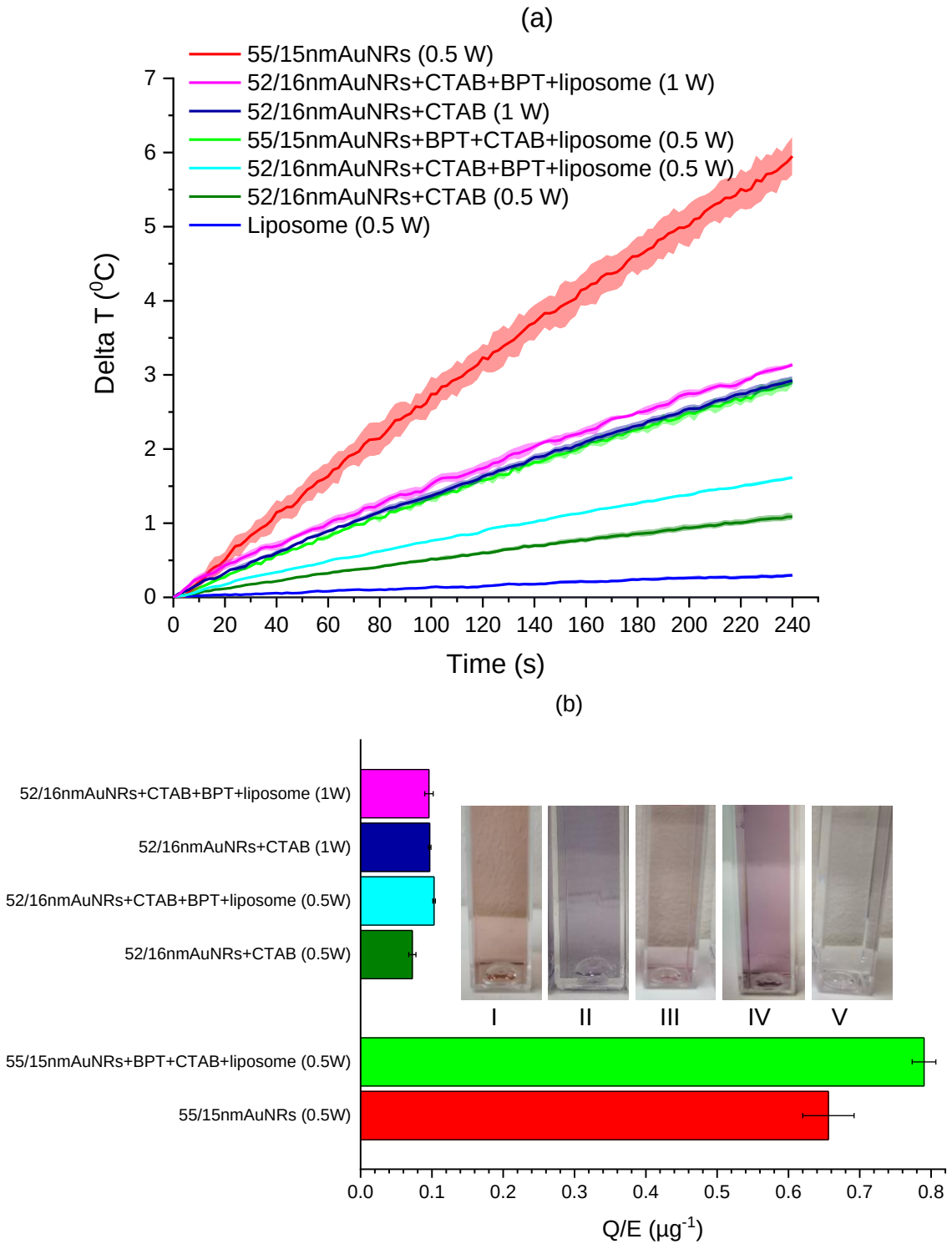

Figure 6.24 (a) Differential temperature-time curves and b) Q/E for *55/15nm AuNRs*, *52/16nm AuNRs+CTAB*, *55/15nm AuNRs+BPT+CTAB+liposome*, *52/16nm AuNRs+CTAB+BPT +liposome* and liposome solutions. During the 808 nm laser exposure (0.5 W/ 0.1 W), the

temperature of samples was measured using a thermocouple thermometer. Inset: photos of (I) *55/15nm AuNRs*, (II) *52/16nm AuNRs+CTAB*, (III) *55/15nm AuNRs+BPT+CTAB+liposome*, (IV) *52/16nm AuNRs+CTAB+BPT +liposome* and (V) liposome solutions.

Table 6.3 The light-heat conversion efficiency calculated from the initial slope of the differential temperature-time curve (first 60 s). The transduction efficiency per µg of *55/15nm AuNRs, 52/16nm AuNRs+CTAB, 55/15nm AuNRs+BPT+CTAB+liposome* and *52/16nm AuNRs+CTAB+BPT +liposome* were also calculated using the mass of Au in the heating volume.

	55/15nm NR 0.5 W	**55/15nm NR:Lipo (CTAB) 0.5 W**	**52/16nm NR (CTAB) 0.5 W**	**52/16nm NR:Lipo (CTAB) 0.5 W**	**52/16nm NR (CTAB) 1.0 W**	**52/16nm NR:Lipo (CTAB) 1.0 W**
Concentration mg/ml	0.016	0.0065	0.026	0.028	0.026	0.028
Temperature increase in first time period / K	1.766	0.864	0.321	0.488	0.857	0.907
First time period (t) / s	60	60	60	60	60	60
Initial gradient of heating slope / $dK.dt^{-1}$	0.029	0.014	0.005	0.008	0.014	0.015
Q/E	0.742	0.363	0.135	0.205	0.180	0.191
Efficiency of transduction (Eff) / ug^{-1} Au	0.656 SD=±0.036	0.790 SD=±0.017	0.073 SD=±0.005	0.103 SD=±0.002	0.097 SD=±0.002	0.096 SD=±0.006

From the results across different mixtures, it can be seen that highest concentration was 0.03 mg/ml for *52/16nm AuNRs+CTAB* and *52/16nm AuNRs+ BPT+CTAB+liposome*, while the lowest

concentration is that of *55/15nm AuNRs+BPT +CTAB+liposome*, with the value of 0.0065. At these concentrations, the efficiency of transduction has also shown variance, as one value has not been calculated for any of the samples. For *52/16nm AuNRs+CTAB*, it is at approximately 0.10, which is equal to *52/16nm AuNRs+BPT+CTAB+liposome*. Values of transduction efficiency are also highest at 0.79, for *55/15nm AuNRs+BPT+CTAB+liposome*.

The *55/15nm AuNRs* have a higher concentration compared to *55/15nm AuNRs+BPT+CTAB+liposome*, and hence can be expected to produce more heat during a specific period of time. But when calculating the conversion efficiency per µg of AuNRs, the *55/15nm AuNRs+BPT+CTAB+liposome* present an efficiency of transduction that is 20% larger than that of the AuNRs themselves. This is a promising result that shows that the AuNRs based nanoconstructs are viable candidates for PTT.

6.2.6 Cytotoxicity profile of nanohybrids against Primary Normal Human Dermal Fibroblast (NHDF) cells

Figure 6.25 and 6.26 presents images and the *in vitro* cell viability percentage of the selected concentrations [(I) 0 or not treated, (II) 0.05, (III) 0.025 and (IV) 0.0125 mg/ml] of BPT labelled AuNRs at 0.05 mg/ml concentration (NR1), BPT labelled AuNRs at 0.025 mg/ml concentration (NR2), and BPT labelled AuNRs at 0.125 mg/ml concentration (NR3) against primary normal human dermal fibroblast (NHDF) cells. In contrast, Figure 6.25b shows images of BPT labelled AuNRs with liposomes at 0.05 mg/ml concentration (NL1), BPT labelled AuNRs with liposomes at 0.025 mg/ml concentration (NL2), and BPT labelled AuNRs with liposomes at 0.0125 mg/ml concentration (NL3) against NHDF cells.

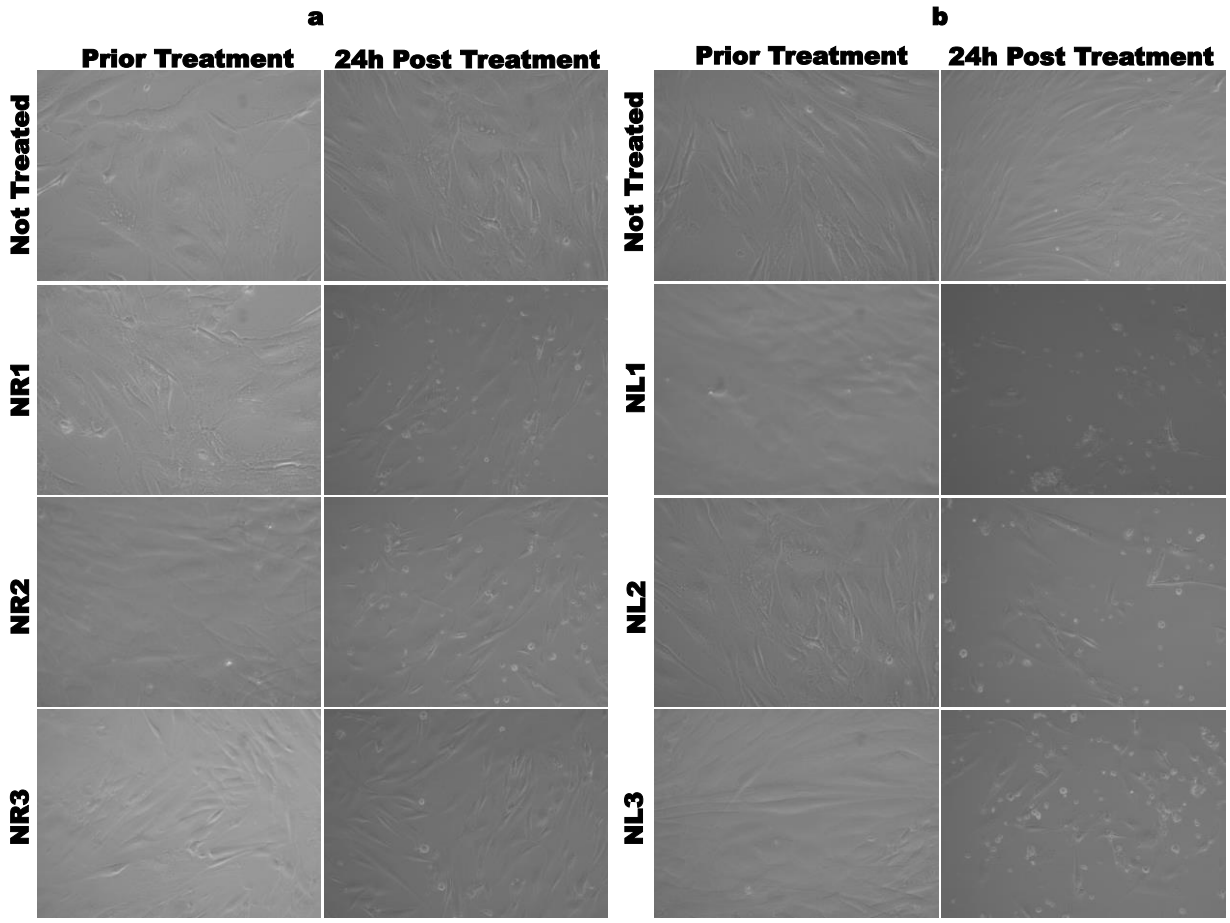

Figure 6.25 Comparison of cell viability of Primary Normal Human Dermal Fibroblast (NHDF) cells upon treatment with BPT labelled AuNRs (NR) and AuNR:liposome hybrids (NL) at different concentrations (1: 0.05 mg/ml; 2: 0.025 mg/ml; 3: 0.0125 mg/ml). (a) Images of NR1, NR2, NR3 before and after 24 hrs treatment with NHDF cells. (b) Images of NL1, NL2, NL3 before and after 24 hrs treatment with NHDF cells.

Cell viability of cells was performed before and after treatment. We use the automated CellDrop (nexcelom) device to measure the ratio of live versus dead cell (represented as percentage of cell viability). These results indicate that NR1, NR2, NR3 have more than 88% cell viability, while low cell viability was noticed in the case of NL1, NL2, NL3 (as shown in Figure 6.26). The toxicity profile of these NRs shows that liposomes functionalised with NRs have more toxic effects towards NHDF cells. However, NL3 at the lowest concentration of 0.0125 mg/ml shows approximately 70% cell viability. As shown in Figure 6.26, BPT labelled AuNRs (NR1-3) present

high cell viability even after 24 hr exposure of the NHDF cells. However, in the presence of CTAB-coated NPs with liposomes, the cell viability decreases with increasing CTAB concentration. This can be explained based on the well-documented cytotoxic effect of CTAB.[207-210] Note that these are labelled AuNRs, therefore citrate has already been replaced by the Raman label. Liposomes themselves are biocompatible drug carriers and therefore should not affect the cell viability.[222, 223] In summary, these results show the suitability of these NRs for cancer theranostics.

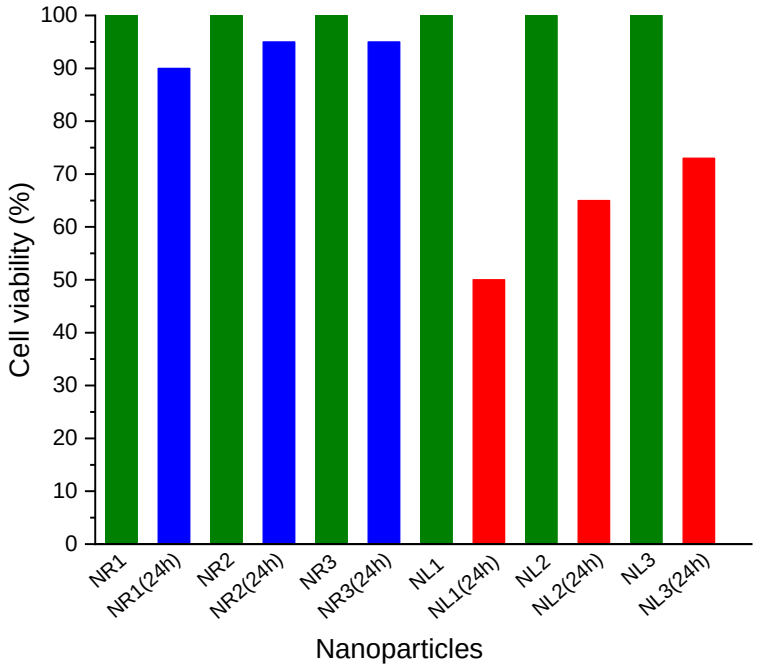

Figure 6.26 Percentage of cell viability at two points (prior treatment and 24 hours post treatment) of NR1, NR2, NR3, NL1, NL2, NL3 in the NHDF cells.

6.2.7 Hyperspectral data and 3D imaging of *55/15nm AuNRs+BPT+CTAB+liposome* dosed 4T1 cells

Firstly, we performed high-speed hyperspectral imaging of 4T1 cancer cells and *55/15nm AuNRs+BPT+CTAB+liposome* using stimulated Raman scattering and transient absorption (TA) microscopy (Figure 6.27a). By adjusting the delay time between pump and probe laser beams, we

collected SRS and TA spectra of 4T1 cancer cells and *55/15nm AuNRs+BPT+CTAB+liposome*, respectively (Figure 6.27b).

Transient absorption (TA), based on the time-resolved technique, is a secondary absorption which occurs once the material has been excited through primary absorption. Varying the delay between pump and probe beams provides the information on metastable states or transient species. Several mechanisms contribute to the pump-probe transient absorption signal, such as excited state absorption (ESA) and ground state depletion (GSD), and are suitable for mapping gold nanoparticles such as gold nanorods and nanospheres, respectively.

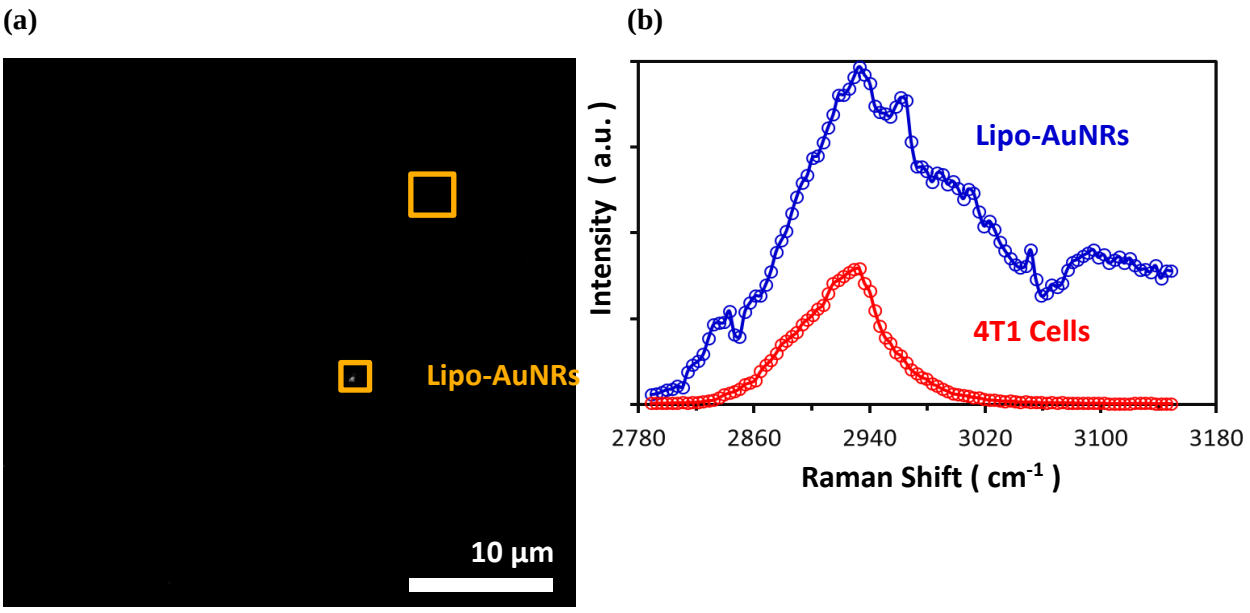

Figure 6.27 Hyperspectral scan of *55/15nm AuNRs+BPT+CTAB+liposome* dosed 4T1 cells. Scale bar: 10 µm.

Secondly, we performed 3D imaging of 4T1 cells and *55/15nm AuNRs+BPT+CTAB+liposome* (Figure 6.28), based on the differential contrast of cells and AuNRs spectra at 2928 cm^{-1} and 3141 cm^{-1}.

Furthermore, 3D reconstruction and orthogonal views of TA and SRS images allowing identification of *55/15nm AuNRs+BPT+CTAB+liposome* uptake by 4T1 cancer cells. In the orthogonal views of TA and SRS signals, the TA signal depicts the lipo+AuNRs distribution, which is concentrated inside the cell body and clustered on the cell surface.

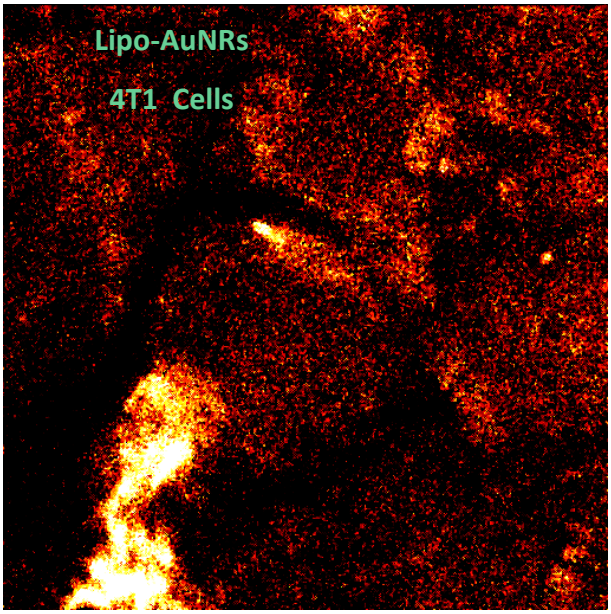
Lipo-AuNRs
4T1 Cells

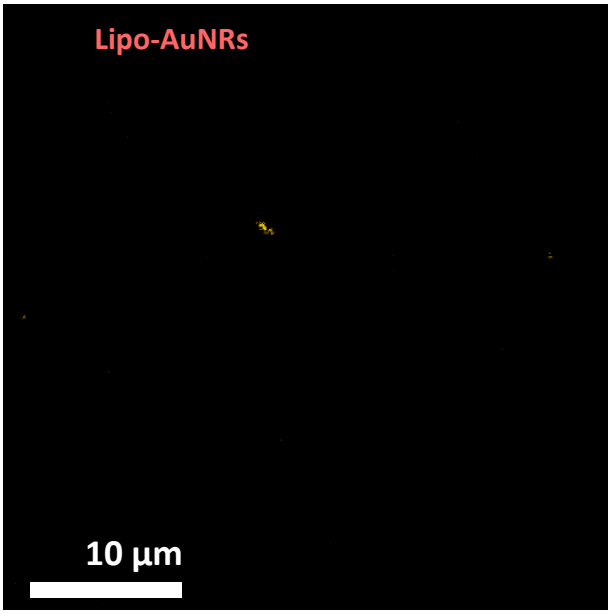
Lipo-AuNRs
10 µm

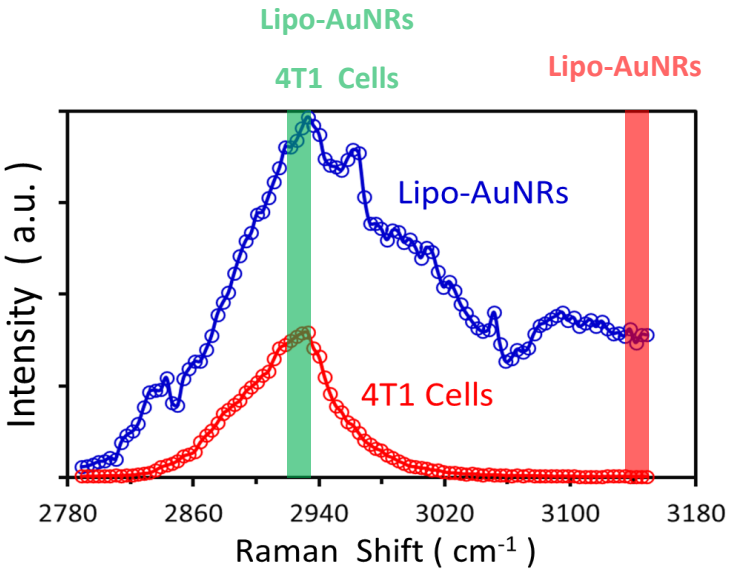
Lipo-AuNRs
4T1 Cells
Lipo-AuNRs
Lipo-AuNRs
4T1 Cells
Intensity (a.u.)
2780
2860
2940
3020
3100
3180
Raman Shift (cm-1)

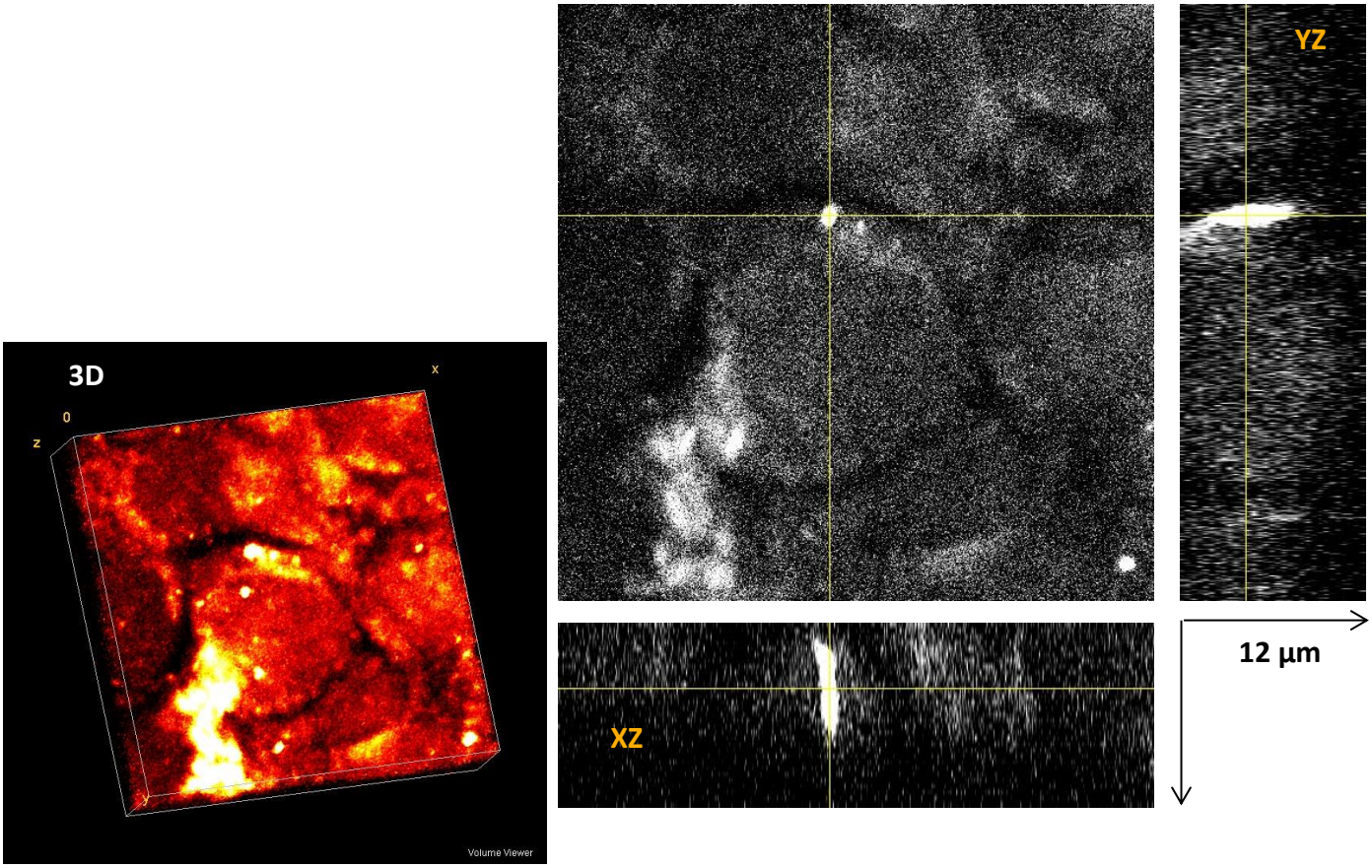

Figure 6.28 3D imaging of *55/15nm AuNRs+BPT+CTAB+liposome* dosed 4T1 cells. Scale bar: 10 µm.

The 3D imaging capability of SRS enables us to conclude, based on these data, that BPT labelled AuNRs-liposome constructs are predominantly attached to the 4T1 cell membrane with some nanoconstructs passively uptaken by the cells and present in the cytoplasm. This is an important result which, if confirmed in a larger-scale study, indicates that the addition of tumour-targeting moieties to the nanoconstructs can even further increase the uptake by tumour cells.

The Transient Absorption (TA) signal,[224] which is the secondary absorption occurring after the primary absorption of AuNRs, first increased and then decreased when adjusting the time delay of SF-TRU. NIR excitation and time delay enable selective observation of AuNRs as their TA signal has a longer lifetime than the SRS signal.

6.3 Conclusion

The purpose of conducting this study was to ascertain the role that gold nanorods play in causing photothermal reactions, such that cancerous cells can be targeted and disrupted. The results revealed that the liposome is an integral part of the nanoconstruct, showing degradation above the T_m. The liposomes with T_m = 42-43 °C remained intact throughout the preparation but an increase in temperature above the T_m would increase the permeability of the liposomal membrane, thereby releasing the contents. Addition of liposome to synthetic nanorods with and without BPT labelling led to an increase in both the size distribution as well as in positive surface charge. In terms of *AuNRs+CTAB+liposome* with or without BPT, it can be seen that results for BPT are much more promising than those without BPT labelling. BPT added as a Raman reporter to liposomal nanoconstructs leads to a more uniform structure, which then subsequently leads to an increase and redshift in the plasmonic peak. Using the longer wavelength, 830 nm, all three peaks of BPT produced a SERS signal that was larger than when using the shorter wavelength, 785 nm, which has to do with the NIR absorption of these nanohybrids. Another important conclusion to make is that toxicity profiles of gold nanorods indicated that AuNRs-liposomes hybrids are considerably more toxic when it comes to tackling NHDF cells. However, lowest concentrations of NL3 still shows a cell viability of 70%. Similarly, for *55/15nm AuNRs+BPT+CTAB+liposome*, a efficiency of transduction that is 20% larger than that of AuNRs alone was noted.

In addition, we demonstrated that the combined imaging modalities of transient absorption (TA) and stimulated Raman scattering (SRS) allow to selectively image *55/15nm AuNRs+BPT+CTAB+liposome* in cancer cells. Transient absorption is a secondary absorption that happens after a material has been excited through primary absorption. This universal photophysical process exists in most types of gold nanoparticles, making it an ideal modality to monitor the location and dynamics of AuNRs in cells. Furthermore, the nonlinear multiphoton response provides SRS and TA with intrinsic 3D optical sectioning capability and high spatial resolution, making it a suitable for imaging cellular uptake of *55/15nm AuNRs+BPT+CTAB+liposome*. With the long wavelength excitation provided by pulsed lasers, combined TA and SRS is a promising imaging platform for tissue imaging, which would be hard for dark-field microscopy. Moreover, the absorption nature in the TA process creates the possibility to quantitatively analyse single liposome-AuNRs uptaken by cancer cells in the near future.

In conclusion, it can therefore be stated that AuNRs have a considerable effect on cancer cells, and therefore are capable of providing together with liposomes an invaluable platform for cancer nanotheranostics.

CHAPTER 7
CONCLUSIONS AND FUTURE PERSPECTIVES

Cancer is considered amongst the leading causes of death globally. Cancer was the biggest cause of death worldwide in 2017, with millions of fatalities. Cancer mortality is anticipated to rise globally, with an estimated 12 million deaths globally by 2030. As a result, developing efficient cancer diagnostic, monitoring, and therapeutic approaches is a pressing societal challenge. Currently, cancer is conventionally cured based primarily on surgical excision and medical approaches, and the most common treatment interventions aimed at treating cancer are known to be chemotherapy, surgery, radiation therapy, or a combination of these treatments. Despite the fact that these procedures have been recognized and used for years, they do have some disadvantages and negative effects. These procedures suffer from a renown problem that is that these treatments are not capable of removing all the cancerous cells during surgery, because of invasiveness, or inoperability due to their adjacency to critical tissue structures. Surgical excision of tumours, for instance, is limited to big, resectable, and visible tumours. Chemotherapeutic medications only induce apoptosis and may sometimes target healthy tissue such as bone marrow since they only attack rapidly dividing cells. Radiation therapy using for example gamma rays, invariably has harmful effects on normal tissue along the route of radiation. Given the limitations of existing therapeutic approaches, a major step towards treating cancer is to focus therapeutic drugs directly to cancer cells whilst protecting normal tissue. Fortunately, thermal medicine (including both diagnostic and therapeutic sides) demonstrates promising advantages over conventional approaches owing to its non-invasiveness, simplicity, and potential applicability to tumours surrounded by vital human organs/regions that are not feasible using the traditional approaches. But the requirement of sufficient activation energy capable of reaching underlying tumours or treating large tumours encourages investigation on the use of energy-absorbing agents localized within tumour tissues to facilitate localized heating.

Usually, materials at the nanoparticle level show improved energy absorption properties compared to bulk counterparts. For example, noble metal nanoparticles, such as gold nanoparticles (AuNPs), feature ultra-sensitive Surface-Enhanced Raman Scattering (SERS) signal due to their plasmonic properties in the visible and near-infrared (NIR) regions of the spectrum, making them suitable

candidates for a range of biomedical Raman applications including the potential for selective detection of tumours and tailored ablation (through, e.g., photothermal therapy (PTT) or radiation therapy).

Gold-based nanostructures that are SERS active in the NIR range and of sufficient transduction efficiency to be deployed in PTT are generally larger than 20 nm in size, rendering the accumulation of such metallic nanostructures harmful to human health, due to limited renal clearance. This necessitates investigations on novel biodegradable gold nanostructures made of smaller AuNPs that can be easily excreted after achieving the SERS-based diagnostics and PTT treatment.

Nanotechnology has advanced to the point that it can nowadays be used in healthcare settings. AuNPs have distinct physicochemical characteristics, which are mostly shown in the following areas: they are reasonably safe, robust, and simple to make, and they also have a number of distinct properties, including large surface-to-volume ratio, quantum size implications, electrical effects, and optical transmittance. AuNPs have higher absorption than standard medications and are more likely to be used in therapy and diagnostics. As a result, AuNPs have a wide range of applications in biomedicine, particularly in the treatment of cancer. Cancer detection and management are now being addressed using multifunctional tuneable nanoparticles, which are a prominent area of research. AuNPs, for instance, can be utilised for MRI detection and can be combined with polyethylene glycol (PEG) monomers to extend nanoparticle circulation time *in vivo*, and so forth. Tumour-specific F3 peptides could be employed as targeted transportation in the adenocarcinoma animal model, and adriamycin transport agents have shown to be efficacious.

Because the value of AuNPs is primarily determined by their safe use in human, toxicological studies are required prior to their use in cancer care. The cytotoxic impacts of AuNPs was shown to be linked to nanoparticle size, charge density, and chemical functional groups. AuNPs have been documented in the literature up to date, however they have been found to have no ability to cause deleterious or acute toxic effects, and hence are considered biocompatible substances for use in biological applications. Recent research has revealed that there may be more to AuNP toxicity than previously thought, and that the severity of the toxicity reaction is comparable to the size and concentration of the AuNPs. For the therapeutic and diagnostic intents associated with cancer, the metallic NPs have been addressed adequately in the medical study for cancer because of their

characteristics of high permeation, strong affinity, strong biocompatibility, and targeted capability, together with low neurotoxic effects. These nanoparticles are capable of producing high-sensitivity surface-enhanced Raman Scattering (SERS) in the near-infrared (NIR) region of the spectrum, when assembled to a size above 100 nm or so. This is mostly due to their plasmonic capabilities, which are particularly attractive for SERS application when they are expressed in the near-infrared region. These features of AuNPs are significant in that they enable the selective identification of cancerous cells by focusing certain molecules and targeted ablation utilizing radiotherapy or photothermal therapy (PTT). They may prove to be beneficial in the diagnosis and treatment of cancer.

This project aimed to develop a biodegradable noble metal nanoparticle construct or hybrid fabricated based on smaller AuNPs and lipid nanoparticles (liposomes or lipid vesicles) with added SERS activity and PTT capability. Specifically, the work focused on the optimization of the NP assembly according to current protocols, assessment of the NP suitability for SERS application to cell samples, the addition of specific tags (reporters) to the NP construct for the investigation of Raman labelling, and validation of the NP's response to photothermal therapy (PTT) as the strategic way to achieve the main objective.

For simplicity, the work was divided into three main segments. ***The first segment*** dealt with the synthesis and characterization of labelled AuNPs for SERS application. AuNPs offer varied physical features that make them appropriate for applicability in the biomedical field. Regarding tiny molecules or single cancer cells, their detection range for imaging technology could be several orders of magnitude greater, dramatically lessening limits of detection. In this study, Raman spectroscopy and complementary analytical techniques were applied to characterize and validate the use of four distinct different Raman labels with colloidal gold nanospheres in the distinct range 5 nm to 100 nm as SERS substrate. The results demonstrated that the strongest SERS EFs were obtained for *80 nm AuNPs* with BPT labelling, followed by *60 nm AuNPs* labelled with 4-AATP. Based on this, BPT was selected as the label to take forward in the subsequent segments.

In the second segment, the potential of AuNP-liposome constructs based on small (5 nm) spherical nanoparticles was tested by using SERS and photothermal therapy. The current study indicates

that analytical techniques such as Transmission Electron Microscopy (TEM), nanoparticle tracking analysis (NTA), Dynamic Light Scattering (DLS), UV-visible spectroscopy, and stimulated Raman scattering (SRS) imaging are appropriate for the characterization of the novel nanohybrids when utilized for detecting cancer cells. In line with this, the results of different protocols of the nanohybrids test revealed reduced toxicity levels in a living system for the 90-200 nm-sized unilamellar vesicles (ULVs) based nanohybrids with 5 nm spherical AuNPs. The Raman signals of the AuNPs solutions were measured using biphenyl-4-thiol (BPT) as the Raman reporter (RR) molecules. Materials capable of generating SERS signals are required to be biocompatible to enable the feasible reduction and elimination of tumour cells. In this work, CTAB (cytotoxic) was utilized allowing the internalisation of AuNPs into the cavity of ULVs of approximately 100 nm diameter. Going forward, to mitigate the effect of CTAB, using low CTAB-to-AuNP ratios and adding PEG coating to shield and increase stability of the nanohybrid may be appropriate.

NTA and DLS analysis showed that the nanohybrids (*5nmAuNPs+BPT+CTAB+liposome*) has a size distribution peaking at around 124 nm and 108 nm, respectively. UV-visible spectra indicated that the maximum absorption for *5nmAuNPs+BPT+CTAB+liposome* was approximately 544 nm, relatively similar to that of larger, 80 nm gold nanosphere, hence demonstrating a good approach but still not significant for use with NIR excitation light. Furthermore, the light-heat conversion efficiency of *5nmAuNPs+BPT+CTAB+liposome* investigated by measuring the temperature rise over time during exposure to 808 nm radiation was much better (175.52%) than that of monodispersed 5 nm AuNPs colloidal solution when scaled to the same mass of gold.

Regarding the Raman analysis of *5nmAuNPs+BPT+CTAB+liposome*, three BPT peaks were observed at 1080 cm^{-1}, 1278 cm^{-1}, and 1586 cm^{-1}. The last two peaks disappeared upon addition of CTAB, while the largest enhancement factor was recorded at 1080 cm^{-1} for *5nmAuNPs+BPT+CTAB+liposome* ($8 \cdot 10^5$), which implies its effectiveness for the diagnosis and treatment of cancer in the future. Furthermore, to optimize nanohybrids synthesis, the polymer GCPQ was also tested against CTAB to reduce cytotoxicity effects; despite GCPQ effectiveness in linking AuNPs together forming larger clusters, the liposomes were not detected using TEM and this prevented its used in subsequent preparations (where CTAB was retained). It was also observed that synthetic 5 nm AuNPs were more effective than the commercial products

(*5nmAuNPs*, NanoXact, 0.05 mg/mL, citrate, 25mL) in liposome nanohybrid preparation. This was indicated by a strong photothermal effect due to absorption in the NIR region. Finally, a test of the optimal AuNP-to-liposome ratio found a value of [16k:1], which is essential to saturate the liposome's internal cavity and achieve optimal SERS and PTT performance. The result indicates that these nanohybrids with [16k:1] AuNP:liposome ratio and CTAB as a linker, when tested against MDA-MB-231 (triple-negative breast cancer cell line) in a concentration-dependent manner, have significantly higher toxicity against the tumour cells and so can be good candidates.

In the third and final segment, the potential application of AuNR-liposome constructs was investigated for SERS activity and PTT response at NIR wavelengths. Specifically, the role of AuNRs in triggering photothermal reactions and rendering cancerous cells targetable and destructible was studied. Liposomes demonstrated degradation above their T_m = 42-43 °C following its integration to the nanoconstruct. However, the liposomes remained intact throughout the preparation. Still, an increase in the permeability of the liposomal membrane was observed when the temperature rose above the T_m, thereby releasing contents through the membrane. This is an important result which shows that these are biodegradable structures that degrade releasing their constituent smaller AuNPs when heated up to a temperature that is capable of killing cancer cells. This property, along with the tuneability of the phase of the membrane based on its composition, can further be exploited by developing tumour-targeting nanohybrids based on this design. Concerning *AuNRs+CTAB+liposome* with and without BPT, the result of the former is much better, which proved its better structural uniformity as well as increased and redshifted plasmonic peak. Also, the intensity of the SERS signal is higher when measured at 830 nm compared with 785 nm. Typically, the SERS signals of CTAB coated and BPT labelled *55/15nm AuNRs* at a concentration of 400 µg/mL (and 10 µg/mL AuNRs concentration) were $6.47 \cdot 10^7$ counts and $8.24 \cdot 10^7$ counts at 1080 cm^{-1} ($2 \cdot 10^9$ enhanced factor) for 830 and 785 nm, respectively.

In another development, the toxicity profiles indicated that the nanohybrids made from 55/15nm *AuNRs+BPT+CTAB* with liposomes are toxic when tackling NHDF cells. Nevertheless, even at the lowest levels of NL3 (*55/15nm AuNRs+BPT+CTAB+liposome* at 0.0125 mg/ml concentration), cell viability is still 70%. Moreover, a greater level of transduction efficiency was observed for the *55/15nm AuNRs+BPT+CTAB+liposome*, amounting to 20% enhancement

compared to the *55/15nm AuNRs* alone. Interestingly, it was demonstrated that the combined imaging modalities transient absorption (TA) and stimulated Raman scattering (SRS) can selectively image *55/15nm AuNRs+BPT+CTAB+liposome* in cancer cells. Furthermore, the optical sectioning capability and high spatial resolution of SRS and TA allow the imaging of cellular uptake for *55/15nm AuNRs+BPT+CTAB+liposome*. Using pulsed laser generated long-wavelength excitation, combined TA and SRS could be a promising imaging platform for tissue imaging, which would be difficult to attain for dark-field microscopy. Soon, single liposome-AuNRs uptaken by cancer cells can be analyzed quantitatively due to the absorption nature of the TA process. Therefore, it is safe to say that AuNR-liposome nanohybrids are effective in potentially detecting cancer cells using SERS (ideally through a tumour-targeting approach) and treating cancer more selectively than current modalities based on chemo- or radio-therapy.

Overall, the findings of this research will underpin the development of novel Raman-labelled nanostructures for applications in nanotheranostics. The work has also demonstrated the significance of hybrid nanostructures toward achieving laser-driven therapy based on the utilization of PTT and SERS activity for Raman diagnostics. Additionally, the cell disruption potential of gold nanostructures in non-invasive and biocompatible ways has been established.

Certain clinical imaging modalities, such as CT, might benefit significantly from the development of novel nanoparticle-based contrast media that provide prolonged circulation time and localised deposition at the tumour site to aid in diagnosis. Additionally, platforms based on AuNPs can be utilised to augment or allow a number of therapies, including medication administration, nucleic acid distribution, photothermal treatment, and radiation. The flexibility to tailor the size, shape, and hence physicochemical parameters of AuNPs, together with their low cytotoxic effects, good biocompatibility, and variety of surface chemistries, make them attractive prospects for clinical usage. This is demonstrated by the availability and approval of AuNP-based diagnostic tools, as well as a variety of preparations in clinical studies as medicines.

Future perspective is tuning the size and aspect ratio of the AuNRs using synthetic approaches, for further use in SERS and photothermal therapy. There is a current PhD project (Ioana Blein) looking at this effects. Her project aimed to develop an all-in-one approach of cancer diagnosis and

treatment using gold nanostructures. Therefore, the PhD student will complete my work by finding the best protocol of synthetic AuNRs with appropriate aspect ratio, and then adding a specific ligand to the constructs to investigate tumour-targeting (Figure 7.1). These promising gold nanoconstructs should be expressing non-toxicity, high SERS signal and PTT response.

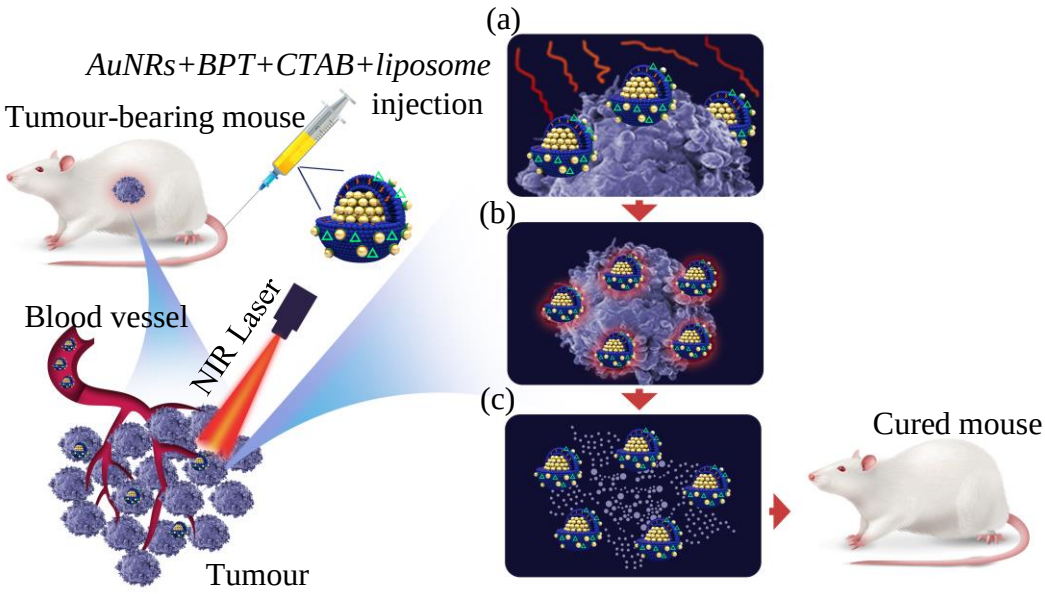

Figure 7.1 Schematic illustration of *in vivo* PTT. Three steps after injecting the mouse and targeting the tumour: (a) NIR laser irradiation, (b) heat is localised in the tumour and (c) cancer cells death.

Contemporary oncological studies have revealed that a variety of cancer treatment approaches could benefit significantly from newly developed nanotechnology. AuNPs have been lately identified as a useful reagent amongst the various nanomaterials currently studied for treatment of cancer. AuNPs have already shown promising future in a variety of cancer therapeutic interventions, such as via PTT and ultrasound hyperthermia, due to their intrinsic bioinertness. Notwithstanding encouraging results on the use of AuNPs in anticancer therapy, additional preclinical studies are required to determine the toxic effects of AuNPs, particularly the long-term morbidity associated with liver buildup and exudation of such nanomaterials.

Bibliography

[1] W. H. Organization. [online] Available on Cancer: www.who.int/health-topics/cancer (accessed 1st November, 2021).

[2] A. C. Society. "Cancer Facts & Figures." https://www.cancer.org/research/cancer-facts-statistics/all-cancer-facts-figures/cancer-facts-figures-2021.html (accessed 2021).

[3] J. Guo, K. Rahme, Y. He, L.-L. Li, J. D. Holmes, and C. M. O'Driscoll, "Gold nanoparticles enlighten the future of cancer theranostics," *International Journal of Nanomedicine,* vol. 12, p. 6131, 2017.

[4] E. Darrigues *et al.*, "Raman spectroscopy using plasmonic and carbon-based nanoparticles for cancer detection, diagnosis, and treatment guidance. Part 2: Treatment," *Drug Metabolism Reviews,* vol. 49, no. 2, pp. 253-283, 2017.

[5] I. P. Santos *et al.*, "Raman spectroscopy for cancer detection and cancer surgery guidance: translation to the clinics," *Analyst,* vol. 142, no. 17, pp. 3025-3047, 2017.

[6] R. Ravanshad *et al.*, "Application of nanoparticles in cancer detection by Raman scattering based techniques," *Nano Reviews & Experiments,* vol. 9, no. 1, p. 1373551, 2018.

[7] E. Versi, "" Gold standard" is an appropriate term," *BMJ: British Medical Journal,* vol. 305, no. 6846, p. 187, 1992.

[8] H. Fox, "Is H&E morphology coming to an end?," *Journal of Clinical Pathology,* vol. 53, no. 1, pp. 38-40, 2000.

[9] R. Rubin, D. S. Strayer, and E. Rubin, *Rubin's pathology: clinicopathologic foundations of medicine*. Lippincott Williams & Wilkins, 2008.

[10] L. FILIPPONI and D. Sutherland, "Nanotechnologies: Principles, Applications, Implications and Hands-on Activities. 2013," *Editado por: European Commission–Directorate-General for Research and Innovation Industrial Technologies programme. Disponível em:<* *https://ec.europa.eu/research/industrial_technologies/pdf/nano-hands-on-activities_en.pdf*>. *Acesso em,* vol. 21, 2017.

[11] N. Grobert and D. Hutton, "Nanoscience and nanotechnologies: opportunities and uncertainties," *London The Royal Society The Royal Academy of Engineering Report,* vol. 46, pp. 618-618, 2004.

[12] E. Smith and G. Dent, *Modern Raman spectroscopy: a practical approach*. John Wiley & Sons, 2019.

[13] L. Fabris, "Gold-based SERS tags for biomedical imaging," *Journal of Optics,* vol. 17, no. 11, p. 114002, 2015.

[14] R. Pilot, R. Signorini, C. Durante, L. Orian, M. Bhamidipati, and L. Fabris, "A review on surface-enhanced Raman scattering," *Biosensors,* vol. 9, no. 2, p. 57, 2019.

[15] W. Zhang, L. Jiang, J. A. Piper, and Y. Wang, "SERS nanotags and their applications in biosensing and bioimaging," *Journal of Analysis and Testing,* vol. 2, no. 1, pp. 26-44, 2018.

[16] B. Kuestner *et al.*, "SERS Labels for Red Laser Excitation: Silica-Encapsulated SAMs on Tunable Gold/Silver Nanoshells," *Angewandte Chemie International Edition,* vol. 48, no. 11, pp. 1950-1953, 2009.

[17] F. Wang, S. Cao, R. Yan, Z. Wang, D. Wang, and H. Yang, "Selectivity/specificity improvement strategies in surface-enhanced Raman spectroscopy analysis," *Sensors,* vol. 17, no. 11, p. 2689, 2017.

[18] M. Fleischmann, P. J. Hendra, and A. J. McQuillan, "Raman spectra of pyridine adsorbed at a silver electrode," *Chemical Physics Letters,* vol. 26, no. 2, pp. 163-166, 1974.

[19] W. A. El-Said, H.-Y. Cho, and J.-W. Choi, "SERS Application for Analysis of Live Single Cell," *Nanoplasmonics*, p. 361, 2017.
[20] K. De Victoria, "Successful European Nanotechnology Research," *Outstanding science and technology to match the needs of future society, edited by the European Commission Directorate-General for Research and Innovation Directorate Industrial Technologies*, 2011.
[21] M. C. Roco, C. A. Mirkin, and M. C. Hersam, *Nanotechnology research directions for societal needs in 2020: retrospective and outlook*. Springer Science & Business Media, 2011.
[22] D. Lombardo, M. A. Kiselev, and M. T. Caccamo, "Smart nanoparticles for drug delivery application: development of versatile nanocarrier platforms in biotechnology and nanomedicine," *Journal of Nanomaterials*, vol. 2019, 2019.
[23] M. Grzelczak, J. Vermant, E. M. Furst, and L. M. Liz-Marzán, "Directed self-assembly of nanoparticles," *ACS Nano*, vol. 4, no. 7, pp. 3591-3605, 2010.
[24] K. Pacławski, B. Streszewski, W. Jaworski, M. Luty-Błocho, and K. Fitzner, "Gold nanoparticles formation via gold (III) chloride complex ions reduction with glucose in the batch and in the flow microreactor systems," *Colloids and Surfaces A: Physicochemical and Engineering Aspects*, vol. 413, pp. 208-215, 2012.
[25] L. Freitas de Freitas, G. H. C. Varca, J. G. dos Santos Batista, and A. Benévolo Lugão, "An overview of the synthesis of gold nanoparticles using radiation technologies," *Nanomaterials*, vol. 8, no. 11, p. 939, 2018.
[26] M. Azharuddin *et al.*, "A repertoire of biomedical applications of noble metal nanoparticles," *Chemical Communications*, vol. 55, no. 49, pp. 6964-6996, 2019.
[27] G. Wypych, "Selection of adhesion promoters for different substrates," *Handbook of Adhesion Promoters; ChemTec Publishing: Toronto, ON, Canada*, pp. 139-175, 2018.
[28] S. K. Maurya, A. Rout, R. A. Ganeev, and C. Guo, "Effect of size on the saturable absorption and reverse saturable absorption in silver nanoparticle and ultrafast dynamics at 400 nm," *Journal of Nanomaterials*, vol. 2019, 2019.
[29] W. Faulk and G. Taylor, "An immunocolloid method for the electron microscope. Immunocytochemistry 8, 1081—1083 5 Roth, J.(1983) The colloidal gold marker system for light and electron microscopic cytochemistry, inImmunocytochemistry, vol. 2 (Bullock, GR and Petrusz, P, eds.)," ed: Academic, London, 1971.
[30] I. Sondi and B. Salopek-Sondi, "Silver nanoparticles as antimicrobial agent: a case study on E. coli as a model for Gram-negative bacteria," *Journal of Colloid and Interface Science*, vol. 275, no. 1, pp. 177-182, 2004.
[31] K. Saha, S. S. Agasti, C. Kim, X. Li, and V. M. Rotello, "Gold nanoparticles in chemical and biological sensing," *Chemical Reviews*, vol. 112, no. 5, pp. 2739-2779, 2012.
[32] S. Suri, G. Ruan, J. Winter, and C. E. Schmidt, "Chapter I. 2.19-Microparticles and Nanoparticles," *Ratner, BD, Hoffman, AS, Schoen, FJ, Lemons, JEBTBS (Third E.(Eds.),. Academic Press, pp. 360–388.* https://doi.org/https://doi.org/10.1016/B978-0-08-087780-8.00034-6, 2013.
[33] Z. Guo and L. Tan, *Fundamentals and applications of nanomaterials*. Artech House, 2009.
[34] G. Schmid *et al.*, "Small dimensions and material properties," *A Definition of Nanotechnology*, vol. 11, no. 03, 2003.

[35] A. K. Wanekaya, W. Chen, N. V. Myung, and A. Mulchandani, "Nanowire-based electrochemical biosensors," *Electroanalysis: An International Journal Devoted to Fundamental and Practical Aspects of Electroanalysis,* vol. 18, no. 6, pp. 533-550, 2006.

[36] X. Luo, A. Morrin, A. J. Killard, and M. R. Smyth, "Application of nanoparticles in electrochemical sensors and biosensors," *Electroanalysis: An International Journal Devoted to Fundamental and Practical Aspects of Electroanalysis,* vol. 18, no. 4, pp. 319-326, 2006.

[37] J. M. Pingarrón, P. Yanez-Sedeno, and A. González-Cortés, "Gold nanoparticle-based electrochemical biosensors," *Electrochimica Acta,* vol. 53, no. 19, pp. 5848-5866, 2008.

[38] L. R. Hirsch *et al.*, "Nanoshell-mediated near-infrared thermal therapy of tumors under magnetic resonance guidance," *Proceedings of the National Academy of Sciences,* vol. 100, no. 23, pp. 13549-13554, 2003.

[39] F. Danhier, O. Feron, and V. Préat, "To exploit the tumor microenvironment: passive and active tumor targeting of nanocarriers for anti-cancer drug delivery," *Journal of Controlled Release,* vol. 148, no. 2, pp. 135-146, 2010.

[40] M. R. Ali, H. R. Ali, C. R. Rankin, and M. A. El-Sayed, "Targeting heat shock protein 70 using gold nanorods enhances cancer cell apoptosis in low dose plasmonic photothermal therapy," *Biomaterials,* vol. 102, pp. 1-8, 2016.

[41] J. A. Yang, H. T. Phan, S. Vaidya, and C. J. Murphy, "Nanovacuums: Nanoparticle uptake and differential cellular migration on a carpet of nanoparticles," *Nano Letters,* vol. 13, no. 5, pp. 2295-2302, 2013.

[42] U. Kreibig and M. Vollmer, *Optical properties of metal clusters*. Springer Science & Business Media, 2013.

[43] J. Doster, G. Baraldi, J. Gonzalo, J. Solis, J. Hernandez-Rueda, and J. Siegel, "Tailoring the surface plasmon resonance of embedded silver nanoparticles by combining nano-and femtosecond laser pulses," *Applied Physics Letters,* vol. 104, no. 15, p. 153106, 2014.

[44] J. Prakash, R. Harris, and H. Swart, "Embedded plasmonic nanostructures: synthesis, fundamental aspects and their surface enhanced Raman scattering applications," *International Reviews in Physical Chemistry,* vol. 35, no. 3, pp. 353-398, 2016.

[45] L. Roach *et al.*, "Evaluating Phospholipid-Functionalized Gold Nanorods for In Vivo Applications," *Small,* vol. 17, no. 13, p. 2006797, 2021.

[46] J. Wu, G. R. Williams, S. Niu, F. Gao, R. Tang, and L. M. Zhu, "A multifunctional biodegradable nanocomposite for cancer theranostics," *Advanced Science,* vol. 6, no. 14, p. 1802001, 2019.

[47] T. A. Tabish *et al.*, "Smart gold nanostructures for light mediated cancer theranostics: combining optical diagnostics with photothermal therapy," *Advanced Science,* vol. 7, no. 15, p. 1903441, 2020.

[48] J. Y. Kah, E. L. Yeo, S. He, and G. Engudar, "Gold nanorods in photomedicine," in *Applications of Nanoscience in Photomedicine*: Elsevier, 2015, pp. 221-248.

[49] Q. Sun *et al.*, "A photoresponsive and rod-shape nanocarrier: Single wavelength of light triggered photothermal and photodynamic therapy based on AuNRs-capped & Ce6-doped mesoporous silica nanorods," *Biomaterials,* vol. 122, pp. 188-200, 2017.

[50] M. Chisanga, H. Muhamadali, D. I. Ellis, and R. Goodacre, "Surface-enhanced Raman scattering (SERS) in microbiology: illumination and enhancement of the microbial world," *Applied Spectroscopy,* vol. 72, no. 7, pp. 987-1000, 2018.

[51] I. Minn *et al.*, "Molecular-genetic imaging of cancer," *Advances in Cancer Research,* vol. 124, pp. 131-169, 2014.
[52] D. Peer, J. M. Karp, S. Hong, O. C. Farokhzad, R. Margalit, and R. J. N. n. Langer, "Nanocarriers as an emerging platform for cancer therapy," vol. 2, no. 12, pp. 751-760, 2007.
[53] C. O. Noble *et al.*, "Development of ligand-targeted liposomes for cancer therapy," *Expert Opinion on Therapeutic Targets,* vol. 8, no. 4, pp. 335-353, 2004.
[54] K. Paunovska, D. Loughrey, and J. E. Dahlman, "Drug delivery systems for RNA therapeutics," *Nature Reviews Genetics,* pp. 1-16, 2022.
[55] R. Fanciullino, J. Ciccolini, and G. Milano, "COVID-19 vaccine race: watch your step for cancer patients," *British Journal of Cancer,* vol. 124, no. 5, pp. 860-861, 2021.
[56] A. K. Rengan, M. Jagtap, A. De, R. Banerjee, and R. Srivastava, "Multifunctional gold coated thermo-sensitive liposomes for multimodal imaging and photo-thermal therapy of breast cancer cells," *Nanoscale,* vol. 6, no. 2, pp. 916-923, 2014.
[57] A. K. Rengan *et al.*, "In vivo analysis of biodegradable liposome gold nanoparticles as efficient agents for photothermal therapy of cancer," *Nano Letters,* vol. 15, no. 2, pp. 842-848, 2015.
[58] A. Mohammed, N. Weston, A. Coombes, M. Fitzgerald, and Y. J. I. j. o. p. Perrie, "Liposome formulation of poorly water soluble drugs: optimisation of drug loading and ESEM analysis of stability," vol. 285, no. 1-2, pp. 23-34, 2004.
[59] N. Karimi, B. Ghanbarzadeh, H. Hamishehkar, F. KEYVANI, A. Pezeshki, and M. M. Gholian, "Phytosome and liposome: the beneficial encapsulation systems in drug delivery and food application," 2015.
[60] D. R. Arifin, A. F. J. A. c. Palmer, blood substitutes,, and biotechnology, "Stability of liposome encapsulated hemoglobin dispersions," vol. 33, no. 2, pp. 113-136, 2005.
[61] E. Rideau, R. Dimova, P. Schwille, F. R. Wurm, and K. J. C. S. R. Landfester, "Liposomes and polymersomes: a comparative review towards cell mimicking," vol. 47, no. 23, pp. 8572-8610, 2018.
[62] D. Lasic and F. Martin, "On the mechanism of vesicle formation," *Journal of Membrane Science,* vol. 50, no. 2, pp. 215-222, 1990.
[63] W. Liu, Y. Hou, Y. Jin, Y. Wang, X. Xu, and J. Han, "Research progress on liposomes: Application in food, digestion behavior and absorption mechanism," *Trends in Food Science & Technology,* 2020.
[64] S. Emami, S. Azadmard-Damirchi, S. H. Peighambardoust, H. Valizadeh, and J. Hesari, "Liposomes as carrier vehicles for functional compounds in food sector," *Journal of Experimental Nanoscience,* vol. 11, no. 9, pp. 737-759, 2016.
[65] K. Prathyusha, M. Muthukumaran, and B. Krishnamoorthy, "Liposomes as targetted drug delivery systems present and future prospectives: A review," *Journal of Drug Delivery and Therapeutics,* vol. 3, no. 4, pp. 195-201, 2013.
[66] M. Thomas and A. M. Klibanov, "Conjugation to gold nanoparticles enhances polyethylenimine's transfer of plasmid DNA into mammalian cells," *Proceedings of the National Academy of Sciences,* vol. 100, no. 16, pp. 9138-9143, 2003.
[67] S. M. Tabakman, K. Welsher, G. Hong, and H. Dai, "Optical properties of single-walled carbon nanotubes separated in a density gradient: length, bundling, and aromatic stacking effects," *The Journal of Physical Chemistry C,* vol. 114, no. 46, pp. 19569-19575, 2010.

[68] J. Xavier, S. Vincent, F. Meder, and F. Vollmer, "Advances in optoplasmonic sensors–combining optical nano/microcavities and photonic crystals with plasmonic nanostructures and nanoparticles," *Nanophotonics,* vol. 7, no. 1, pp. 1-38, 2018.

[69] A. Otto, I. Mrozek, H. Grabhorn, and W. Akemann, "Surface-enhanced Raman scattering," *Journal of Physics: Condensed Matter,* vol. 4, no. 5, p. 1143, 1992.

[70] K. Kneipp, H. Kneipp, I. Itzkan, R. R. Dasari, and M. S. Feld, "Ultrasensitive chemical analysis by Raman spectroscopy," *Chemical Reviews,* vol. 99, no. 10, pp. 2957-2976, 1999.

[71] M. Kahl and E. Voges, "Analysis of plasmon resonance and surface-enhanced Raman scattering on periodic silver structures," *Physical Review B,* vol. 61, no. 20, p. 14078, 2000.

[72] L. Cao, P. Diao, L. Tong, T. Zhu, and Z. Liu, "Surface-Enhanced Raman Scattering of p-Aminothiophenol on a Au (core)/Cu (shell) Nanoparticle Assembly," *ChemPhysChem,* vol. 6, no. 5, pp. 913-918, 2005.

[73] H. Ueba, "Theory of charge transfer excitation in surface enhanced Raman scattering," *Surface Science,* vol. 131, no. 2-3, pp. 347-366, 1983.

[74] J. F. Arenas, M. S. Woolley, J. C. Otero, and J. I. Marcos, "Charge-Transfer Processes in Surface-Enhanced Raman Scattering. Franck− Condon Active Vibrations of Pyrazine," *The Journal of Physical Chemistry,* vol. 100, no. 8, pp. 3199-3206, 1996.

[75] P. Nordlander, C. Oubre, E. Prodan, K. Li, and M. Stockman, "Plasmon hybridization in nanoparticle dimers," *Nano Letters,* vol. 4, no. 5, pp. 899-903, 2004.

[76] K. L. Wustholz *et al.*, "Structure− activity relationships in gold nanoparticle dimers and trimers for surface-enhanced Raman spectroscopy," *Journal of the American Chemical Society,* vol. 132, no. 31, pp. 10903-10910, 2010.

[77] W. Li, P. H. Camargo, X. Lu, and Y. Xia, "Dimers of silver nanospheres: facile synthesis and their use as hot spots for surface-enhanced Raman scattering," *Nano Letters,* vol. 9, no. 1, pp. 485-490, 2009.

[78] G. Chen *et al.*, "High-purity separation of gold nanoparticle dimers and trimers," *Journal of the American Chemical Society,* vol. 131, no. 12, pp. 4218-4219, 2009.

[79] W. Xie and S. Schlücker, "Medical applications of surface-enhanced Raman scattering," *Physical Chemistry Chemical Physics,* vol. 15, no. 15, pp. 5329-5344, 2013.

[80] A. S. D. Indrasekara, B. J. Paladini, D. J. Naczynski, V. Starovoytov, P. V. Moghe, and L. Fabris, "Dimeric Gold Nanoparticle Assemblies as Tags for SERS-Based Cancer Detection," *Advanced Healthcare Materials,* vol. 2, no. 10, pp. 1370-1376, 2013.

[81] S. Schlücker, B. Küstner, A. Punge, R. Bonfig, A. Marx, and P. Ströbel, "Immuno-Raman microspectroscopy: In situ detection of antigens in tissue specimens by surface-enhanced Raman scattering," *Journal of Raman Spectroscopy: An International Journal for Original Work in all Aspects of Raman Spectroscopy, Including Higher Order Processes, and also Brillouin and Rayleigh Scattering,* vol. 37, no. 7, pp. 719-721, 2006.

[82] X. Qian *et al.*, "In vivo tumor targeting and spectroscopic detection with surface-enhanced Raman nanoparticle tags," *Nature Biotechnology,* vol. 26, no. 1, pp. 83-90, 2008.

[83] H. Karabeber *et al.*, "Guiding brain tumor resection using surface-enhanced Raman scattering nanoparticles and a hand-held Raman scanner," *ACS Nano,* vol. 8, no. 10, pp. 9755-9766, 2014.

[84] M.-A. Woo *et al.*, "Multiplex immunoassay using fluorescent-surface enhanced Raman spectroscopic dots for the detection of bronchioalveolar stem cells in murine lung," *Analytical Chemistry,* vol. 81, no. 3, pp. 1008-1015, 2009.

[85] D. Yadav, K. Sandeep, D. Pandey, and R. K. Dutta, "Liposomes for drug delivery," *J. Biotechnol. Biomater,* vol. 7, no. 4, 2017.
[86] D. Yang *et al.*, "Assembly of Au plasmonic photothermal agent and iron oxide nanoparticles on ultrathin black phosphorus for targeted photothermal and photodynamic cancer therapy," *Advanced Functional Materials,* vol. 27, no. 18, p. 1700371, 2017.
[87] G. von Maltzahn *et al.*, "SERS-coded gold nanorods as a multifunctional platform for densely multiplexed near-infrared imaging and photothermal heating," *Advanced Materials,* vol. 21, no. 31, pp. 3175-3180, 2009.
[88] L. Y. Chou, K. Ming, and W. C. Chan, "Strategies for the intracellular delivery of nanoparticles," *Chemical Society Reviews,* vol. 40, no. 1, pp. 233-245, 2011.
[89] T. K. Sau and C. J. Murphy, "Seeded high yield synthesis of short Au nanorods in aqueous solution," *Langmuir,* vol. 20, no. 15, pp. 6414-6420, 2004.
[90] B. Nikoobakht and M. A. El-Sayed, "Preparation and growth mechanism of gold nanorods (NRs) using seed-mediated growth method," *Chemistry of Materials,* vol. 15, no. 10, pp. 1957-1962, 2003.
[91] C. J. Murphy *et al.*, "Gold nanoparticles in biology: beyond toxicity to cellular imaging," *Accounts of Chemical Research,* vol. 41, no. 12, pp. 1721-1730, 2008.
[92] W. E. Doering and S. Nie, "Spectroscopic tags using dye-embedded nanoparticles and surface-enhanced Raman scattering," *Analytical Chemistry,* vol. 75, no. 22, pp. 6171-6176, 2003.
[93] S. P. Mulvaney, M. D. Musick, C. D. Keating, and M. J. Natan, "Glass-coated, analyte-tagged nanoparticles: a new tagging system based on detection with surface-enhanced Raman scattering," *Langmuir,* vol. 19, no. 11, pp. 4784-4790, 2003.
[94] W. Stöber, A. Fink, and E. Bohn, "Controlled growth of monodisperse silica spheres in the micron size range," *Journal of Colloid and Interface Science,* vol. 26, no. 1, pp. 62-69, 1968.
[95] A. Khan, R. Rashid, G. Murtaza, and A. Zahra, "Gold nanoparticles: synthesis and applications in drug delivery," *Tropical Journal of Pharmaceutical Research,* vol. 13, no. 7, pp. 1169-1177, 2014.
[96] M. Benkovicova, K. Vegso, P. Siffalovic, M. Jergel, S. Luby, and E. Majkova, "Preparation of gold nanoparticles for plasmonic applications," *Thin Solid Films,* vol. 543, pp. 138-141, 2013.
[97] T. S. Rezende, G. R. Andrade, L. S. Barreto, N. B. Costa Jr, I. F. Gimenez, and L. Almeida, "Facile preparation of catalytically active gold nanoparticles on a thiolated chitosan," *Materials Letters,* vol. 64, no. 7, pp. 882-884, 2010.
[98] P. Rai and S. A. Morris, *Nanotheranostics for cancer applications*. Springer, 2019.
[99] M. Salimi, S. Mosca, B. Gardner, F. Palombo, P. Matousek, and N. Stone, "Nanoparticle-Mediated Photothermal Therapy Limitation in Clinical Applications Regarding Pain Management," *Nanomaterials,* vol. 12, no. 6, p. 922, 2022.
[100] X. Bao *et al.*, "In vivo theranostics with near-infrared-emitting carbon dots—highly efficient photothermal therapy based on passive targeting after intravenous administration," *Light: Science & Applications,* vol. 7, no. 1, pp. 1-11, 2018.
[101] J. Zhang *et al.*, "Multifunctional envelope-type mesoporous silica nanoparticles for tumor-triggered targeting drug delivery," *Journal of the American Chemical Society,* vol. 135, no. 13, pp. 5068-5073, 2013.

[102] Y. Lu, P. Wu, Y. Yin, H. Zhang, and C. Cai, "Aptamer-functionalized graphene oxide for highly efficient loading and cancer cell-specific delivery of antitumor drug," *Journal of Materials Chemistry B,* vol. 2, no. 24, pp. 3849-3859, 2014.

[103] C. Cai *et al.,* "Polydopamine-coated gold core/hollow mesoporous silica shell particles as a nanoplatform for multimode imaging and photothermal therapy of tumors," *Chemical Engineering Journal,* vol. 362, pp. 842-850, 2019.

[104] Y.-W. Chen, Y.-L. Su, S.-H. Hu, and S.-Y. Chen, "Functionalized graphene nanocomposites for enhancing photothermal therapy in tumor treatment," *Advanced Drug Delivery Reviews,* vol. 105, pp. 190-204, 2016.

[105] S. D. Brown *et al.,* "Gold nanoparticles for the improved anticancer drug delivery of the active component of oxaliplatin," *Journal of the American Chemical Society,* vol. 132, no. 13, pp. 4678-4684, 2010.

[106] L. Zhou *et al.*, "Injectable self-healing antibacterial bioactive polypeptide-based hybrid nanosystems for efficiently treating multidrug resistant infection, skin-tumor therapy, and enhancing wound healing," *Advanced Functional Materials,* vol. 29, no. 22, p. 1806883, 2019.

[107] X. Deng *et al.,* "Ultrafast low-temperature photothermal therapy activates autophagy and recovers immunity for efficient antitumor treatment," *ACS Applied Materials & Interfaces,* vol. 12, no. 4, pp. 4265-4275, 2020.

[108] J. Conde, N. Oliva, Y. Zhang, and N. Artzi, "Local triple-combination therapy results in tumour regression and prevents recurrence in a colon cancer model," *Nature Materials,* vol. 15, no. 10, pp. 1128-1138, 2016.

[109] A. Vogel and V. Venugopalan, "Mechanisms of pulsed laser ablation of biological tissues," *Chemical Reviews,* vol. 103, no. 2, pp. 577-644, 2003.

[110] D. P. O'Neal, L. R. Hirsch, N. J. Halas, J. D. Payne, and J. L. West, "Photo-thermal tumor ablation in mice using near infrared-absorbing nanoparticles," *Cancer Letters,* vol. 209, no. 2, pp. 171-176, 2004.

[111] W. Chen, M. Qin, X. Chen, Q. Wang, Z. Zhang, and X. Sun, "Combining photothermal therapy and immunotherapy against melanoma by polydopamine-coated Al2O3 nanoparticles," *Theranostics,* vol. 8, no. 8, p. 2229, 2018.

[112] P. Huang *et al.,* "Biodegradable gold nanovesicles with an ultrastrong plasmonic coupling effect for photoacoustic imaging and photothermal therapy," *Angewandte Chemie,* vol. 125, no. 52, pp. 14208-14214, 2013.

[113] P. Wu, D. Deng, J. Gao, and C. Cai, "Tubelike Gold Sphere–Attapulgite Nanocomposites with a High Photothermal Conversion Ability in the Near-Infrared Region for Enhanced Cancer Photothermal Therapy," *ACS Applied Materials & Interfaces,* vol. 8, no. 16, pp. 10243-10252, 2016.

[114] C. F. Babbs and D. P. DeWitt, "Physical principles of local heat therapy for cancer," *Medical Instrumentation,* 1981.

[115] T. Takada *et al.,* "Growth inhibition of re-challenge B16 melanoma transplant by conjugates of melanogenesis substrate and magnetite nanoparticles as the basis for developing melanoma-targeted chemo-thermo-immunotherapy," *Journal of Biomedicine and Biotechnology,* vol. 2009, 2009.

[116] T. Sugahara *et al.,* "Kadota fund international forum 2004. Application of thermal stress for the improvement of health, 15–18 June 2004, Awaji Yumebutai international

conference center, Awaji island, Hyogo, Japan. Final report," *International Journal of Hyperthermia,* vol. 24, no. 2, pp. 123-140, 2008.
[117] Z. Qin and J. C. Bischof, "Thermophysical and biological responses of gold nanoparticle laser heating," *Chemical Society Reviews,* vol. 41, no. 3, pp. 1191-1217, 2012.
[118] X. Yang, M. Yang, B. Pang, M. Vara, and Y. Xia, "Gold nanomaterials at work in biomedicine," *Chemical Reviews,* vol. 115, no. 19, pp. 10410-10488, 2015.
[119] A. Bettaieb, P. K. Wrzal, and D. A. Averill-Bates, "Hyperthermia: Cancer treatment and beyond," *Cancer Treatment-Conventional and Innovative Approaches,* pp. 257-283, 2013.
[120] T.-C. Lin, F.-H. Lin, and J.-C. Lin, "In vitro feasibility study of the use of a magnetic electrospun chitosan nanofiber composite for hyperthermia treatment of tumor cells," *Acta Biomaterialia,* vol. 8, no. 7, pp. 2704-2711, 2012.
[121] P. Dey *et al.*, "Surface enhanced deep Raman detection of cancer tumour through 71 mm of heterogeneous tissue," *Nanotheranostics,* vol. 6, no. 3, pp. 337-349, 2022.
[122] B. Gardner, N. Stone, and P. Matousek, "Noninvasive simultaneous monitoring of pH and depth using surface-enhanced deep Raman spectroscopy," *Journal of Raman Spectroscopy,* vol. 51, no. 7, pp. 1078-1082, 2020.
[123] P. Matousek and N. Stone, "Development of deep subsurface Raman spectroscopy for medical diagnosis and disease monitoring," *Chemical Society Reviews,* vol. 45, no. 7, pp. 1794-1802, 2016.
[124] M. Z. Vardaki, P. Matousek, and N. Stone, "Characterisation of signal enhancements achieved when utilizing a photon diode in deep Raman spectroscopy of tissue," *Biomedical Optics Express,* vol. 7, no. 6, pp. 2130-2141, 2016.
[125] B. Gardner, P. Matousek, and N. Stone, "Subsurface chemically specific measurement of pH levels in biological tissues using combined surface-enhanced and deep Raman," *Analytical Chemistry,* vol. 91, no. 17, pp. 10984-10987, 2019.
[126] M. Mathiyazhakan, C. Wiraja, and C. Xu, "A concise review of gold nanoparticles-based photo-responsive liposomes for controlled drug delivery," *Nano-Micro Letters,* vol. 10, no. 1, pp. 1-10, 2018.
[127] A. Y. Rwei, W. Wang, and D. S. Kohane, "Photoresponsive nanoparticles for drug delivery," *Nano Today,* vol. 10, no. 4, pp. 451-467, 2015.
[128] G. Wang, "Liposomes as Drug Delivery vehicles," *Drug Delivery: Principles and Applications,* pp. 272-298, 2016.
[129] Z. Yang *et al.*, "Self-assembly of semiconducting-plasmonic gold nanoparticles with enhanced optical property for photoacoustic imaging and photothermal therapy," *Theranostics,* vol. 7, no. 8, p. 2177, 2017.
[130] H. Deng *et al.*, "Theranostic self-assembly structure of gold nanoparticles for NIR photothermal therapy and X-Ray computed tomography imaging," *Theranostics,* vol. 4, no. 9, p. 904, 2014.
[131] J. Song, J. Zhou, and H. Duan, "Self-assembled plasmonic vesicles of SERS-encoded amphiphilic gold nanoparticles for cancer cell targeting and traceable intracellular drug delivery," *Journal of the American Chemical Society,* vol. 134, no. 32, pp. 13458-13469, 2012.
[132] J. Song, L. Cheng, A. Liu, J. Yin, M. Kuang, and H. Duan, "Plasmonic vesicles of amphiphilic gold nanocrystals: self-assembly and external-stimuli-triggered destruction," *Journal of the American Chemical Society,* vol. 133, no. 28, pp. 10760-10763, 2011.

[133] S. Liu *et al.*, "High-performance Ba1− xKxFe2As2 superconducting tapes with grain texture engineered via a scalable fabrication," *Science China Materials,* vol. 64, no. 10, pp. 2530-2540, 2021.
[134] L. Viitala *et al.*, "Photothermally triggered lipid bilayer phase transition and drug release from gold nanorod and indocyanine green encapsulated liposomes," *Langmuir,* vol. 32, no. 18, pp. 4554-4563, 2016.
[135] T. Lister, P. A. Wright, and P. H. Chappell, "Optical properties of human skin," *Journal of Biomedical Optics,* vol. 17, no. 9, p. 090901, 2012.
[136] S.-H. Park, S.-G. Oh, J.-Y. Mun, and S.-S. Han, "Loading of gold nanoparticles inside the DPPC bilayers of liposome and their effects on membrane fluidities," *Colloids and Surfaces B: Biointerfaces,* vol. 48, no. 2, pp. 112-118, 2006.
[137] M. Mathiyazhakan *et al.*, "Non-invasive controlled release from gold nanoparticle integrated photo-responsive liposomes through pulse laser induced microbubble cavitation," *Colloids and Surfaces B: Biointerfaces,* vol. 126, pp. 569-574, 2015.
[138] X. Han *et al.*, "Crystal Structures of Saturn-Like C50Cl10 and Pineapple-Shaped C64Cl4: Geometric Implications of Double-and Triple-Pentagon-Fused Chlorofullerenes," *Angewandte Chemie International Edition,* vol. 47, no. 29, pp. 5340-5343, 2008.
[139] T. S. Troutman, J. K. Barton, and M. Romanowski, "Biodegradable plasmon resonant nanoshells," *Advanced Materials,* vol. 20, no. 13, pp. 2604-2608, 2008.
[140] Y.-C. Ou *et al.*, "Gold nanoantenna-mediated photothermal drug delivery from thermosensitive liposomes in breast cancer," *ACS Omega,* vol. 1, no. 2, pp. 234-243, 2016.
[141] A. Agarwal, M. A. Mackey, M. A. El-Sayed, and R. V. Bellamkonda, "Remote triggered release of doxorubicin in tumors by synergistic application of thermosensitive liposomes and gold nanorods," *ACS Nano,* vol. 5, no. 6, pp. 4919-4926, 2011.
[142] R. D. Issels, "Hyperthermia adds to chemotherapy," *European Journal of Cancer,* vol. 44, no. 17, pp. 2546-2554, 2008.
[143] J. Song, L. Pu, J. Zhou, B. Duan, and H. Duan, "Biodegradable theranostic plasmonic vesicles of amphiphilic gold nanorods," *ACS Nano,* vol. 7, no. 11, pp. 9947-9960, 2013.
[144] B. Gardner, P. Matousek, and N. Stone, "Self-absorption corrected non-invasive transmission Raman spectroscopy (of biological tissue)," *Analyst,* vol. 146, no. 4, pp. 1260-1267, 2021.
[145] L. Paasonen, T. Laaksonen, C. Johans, M. Yliperttula, K. Kontturi, and A. Urtti, "Gold nanoparticles enable selective light-induced contents release from liposomes," *Journal of Controlled Release,* vol. 122, no. 1, pp. 86-93, 2007.
[146] X. An, F. Zhang, Y. Zhu, and W. Shen, "Photoinduced drug release from thermosensitive AuNPs-liposome using a AuNPs-switch," *Chemical Communications,* vol. 46, no. 38, pp. 7202-7204, 2010.
[147] N. Zhang *et al.*, "Gold conjugate-based liposomes with hybrid cluster bomb structure for liver cancer therapy," *Biomaterials,* vol. 74, pp. 280-291, 2016.
[148] J.-H. Lee *et al.*, "General and programmable synthesis of hybrid liposome/metal nanoparticles," *Science Advances,* vol. 2, no. 12, p. e1601838, 2016.
[149] T. Lajunen *et al.*, "Light induced cytosolic drug delivery from liposomes with gold nanoparticles," *Journal of Controlled Release,* vol. 203, pp. 85-98, 2015.
[150] M. Mathiyazhakan *et al.*, "In situ synthesis of gold nanostars within liposomes for controlled drug release and photoacoustic imaging," *Science China Materials,* vol. 59, no. 11, pp. 892-900, 2016.

[151] K. Sivasubramanian, M. Mathiyazhakan, C. Wiraja, P. K. Upputuri, C. Xu, and M. Pramanik, "Near-infrared light-responsive liposomal contrast agent for photoacoustic imaging and drug release applications," *Journal of Biomedical Optics,* vol. 22, no. 4, p. 041007, 2016.

[152] T. K. Sau *et al.*, "Controlling loading and optical properties of gold nanoparticles on liposome membranes," *Colloids and Surfaces A: Physicochemical and Engineering Aspects,* vol. 342, no. 1-3, pp. 92-96, 2009.

[153] N. Dave and J. Liu, "Protection and Promotion of UV Radiation-Induced Liposome Leakage via DNA-Directed Assembly with Gold Nanoparticles," *Advanced Materials,* vol. 23, no. 28, pp. 3182-3186, 2011.

[154] M. W. Schmitt, L. A. Loeb, and J. J. Salk, "The influence of subclonal resistance mutations on targeted cancer therapy," *Nature Reviews Clinical Oncology,* vol. 13, no. 6, pp. 335-347, 2016.

[155] K. Kong, C. Kendall, N. Stone, and I. Notingher, "Raman spectroscopy for medical diagnostics—From in-vitro biofluid assays to in-vivo cancer detection," *Advanced Drug Delivery Reviews,* vol. 89, pp. 121-134, 2015.

[156] J. C. Day and N. Stone, "A subcutaneous Raman needle probe," *Applied Spectroscopy,* vol. 67, no. 3, pp. 349-354, 2013.

[157] S. Pahlow *et al.*, "Application of vibrational spectroscopy and imaging to point-of-care medicine: A review," *Applied Spectroscopy,* vol. 72, no. 101, pp. 52-84, 2018.

[158] M. Sung, D. H. Shin, H. J. Lee, K. H. Jang, K. Shin, and J. W. Kim, "Enhancing Skin Permeation of Nanoemulsions through Associative Polymeric Micelles-Mediated Drop-to-Skin Dipolar Interactions," *Journal of Molecular Liquids,* p. 117741, 2021.

[159] G. Bozzuto and A. Molinari, "Liposomes as nanomedical devices," *International Journal of Nanomedicine,* vol. 10, p. 975, 2015.

[160] Y.-C. Yeh, B. Creran, and V. M. Rotello, "Gold nanoparticles: preparation, properties, and applications in bionanotechnology," *Nanoscale,* vol. 4, no. 6, pp. 1871-1880, 2012.

[161] J. A. Yang, S. E. Lohse, S. P. Boulos, and C. J. Murphy, "The early life of gold nanorods: temporal separation of anisotropic and isotropic growth modes," *Journal of Cluster Science,* vol. 23, no. 3, pp. 799-809, 2012.

[162] P. Dey, T. A. Tabish, S. Mosca, F. Palombo, P. Matousek, and N. Stone, "Plasmonic nanoassemblies: tentacles beat satellites for boosting broadband NIR plasmon coupling providing a novel candidate for SERS and photothermal therapy," *Small,* vol. 16, no. 10, p. 1906780, 2020.

[163] M. L. Passos and M. L. M. Saraiva, "Detection in UV-visible spectrophotometry: Detectors, detection systems, and detection strategies," *Measurement,* vol. 135, pp. 896-904, 2019.

[164] A. Shalaby, D. Nihtianova, P. Markov, A. Staneva, R. Iordanova, and Y. Dimitriev, "Structural analysis of reduced graphene oxide by transmission electron microscopy," *Bulgarian Chemical Communications,* vol. 47, no. 1, pp. 291-295, 2015.

[165] P. Martinez Pancorbo *et al.*, "Novel Au–SiO2–WO3 Core–Shell Composite Nanoparticles for Surface-Enhanced Raman Spectroscopy with Potential Application in Cancer Cell Imaging," *Advanced Functional Materials,* vol. 29, no. 46, p. 1903549, 2019.

[166] S. Behera, S. Ghanty, F. Ahmad, S. Santra, and S. Banerjee, "UV-visible spectrophotometric method development and validation of assay of paracetamol tablet formulation," *J Anal Bioanal Techniques,* vol. 3, no. 6, pp. 151-7, 2012.

[167] O. Thomas and C. Burgess, *UV-visible spectrophotometry of water and wastewater*. Elsevier, 2017.
[168] A. Feist, K. E. Echternkamp, J. Schauss, S. V. Yalunin, S. Schäfer, and C. Ropers, "Quantum coherent optical phase modulation in an ultrafast transmission electron microscope," *Nature,* vol. 521, no. 7551, pp. 200-203, 2015.
[169] H. Davies, V. Popov, I. Kraev, and M. Stewart, "Digital Imaging in a Multi-User Electron Microscopy Facility: Progress since 1995," *Microscopy,* 2013.
[170] T. Misono, "Dynamic Light Scattering (DLS)," *Measurement Techniques and Practices of Colloid and Interface Phenomena,* pp. 65-69, 2019.
[171] J. Panchal, J. Kotarek, E. Marszal, and E. M. Topp, "Analyzing subvisible particles in protein drug products: a comparison of dynamic light scattering (DLS) and resonant mass measurement (RMM)," *The AAPS Journal,* vol. 16, no. 3, pp. 440-451, 2014.
[172] A. E. James and J. D. Driskell, "Monitoring gold nanoparticle conjugation and analysis of biomolecular binding with nanoparticle tracking analysis (NTA) and dynamic light scattering (DLS)," *Analyst,* vol. 138, no. 4, pp. 1212-1218, 2013.
[173] R. Ishikawa, K. Ueno, and H. Shirai, "Improved efficiency of methylammonium-free perovskite thin film solar cells by fluorinated ammonium iodide treatment," *Organic Electronics,* vol. 78, p. 105596, 2020.
[174] X. Su, J. A. Ditlev, M. K. Rosen, and R. D. Vale, "Reconstitution of TCR signaling using supported lipid bilayers," in *The Immune Synapse*: Springer, 2017, pp. 65-76.
[175] H. Pi *et al.*, "Passivation of the surface imperfection of TiO 2 by using ZIF-8 for efficient carrier separation/transfer," *Dalton Transactions,* vol. 47, no. 1, pp. 209-214, 2018.
[176] M. Tong, O. Brown, P. Stone, L. Cree, and L. Chamley, "Flow speed alters the apparent size and concentration of particles measured using NanoSight nanoparticle tracking analysis," *Placenta,* vol. 38, pp. 29-32, 2016.
[177] K. M. Curtis, "Comparing Coherent and Spontaneous Raman Modalities for the Investigation of Gastrointestinal Cancers," 2017.
[178] E. C. Le Ru, E. Blackie, M. Meyer, and P. G. Etchegoin, "Surface enhanced Raman scattering enhancement factors: a comprehensive study," *The Journal of Physical Chemistry C,* vol. 111, no. 37, pp. 13794-13803, 2007.
[179] M. D. Porter and J. H. Granger, "Surface-enhanced Raman scattering II: concluding remarks," *Faraday Discussions,* vol. 205, pp. 601-613, 2017.
[180] M. J. Natan, "Concluding remarks surface enhanced Raman scattering," *Faraday Discussions,* vol. 132, pp. 321-328, 2006.
[181] D. Han, J. Yao, Y. Quan, M. Gao, and J. Yang, "plasmon-coupled charge transfer in fSZA core-shell Microspheres with High SeRS Activity and pesticide Detection," *Scientific Reports,* vol. 9, no. 1, pp. 1-6, 2019.
[182] S. Lee *et al.*, "Au nanolenses for near-field focusing," *Chemical Science,* vol. 12, no. 18, pp. 6355-6361, 2021.
[183] P. Guo, X. Huang, L. Li, and S. Zhao, "Interfacial self-assembly approach of plasmonic nanostructures for efficient SERS and recyclable catalysts applications," *Chemical Research in Chinese Universities,* vol. 33, no. 1, pp. 135-142, 2017.
[184] S. Managò *et al.*, "Tailoring lab-on-fiber SERS optrodes towards biological targets of different sizes," *Sensors and Actuators B: Chemical,* vol. 339, p. 129321, 2021.
[185] A. Zeytunyan, T. Baldacchini, and R. Zadoyan, "Module for multiphoton high-resolution hyperspectral imaging and spectroscopy," in *Multiphoton Microscopy in the Biomedical*

Sciences XVIII, 2018, vol. 10498: International Society for Optics and Photonics, p. 104980K.

[186] T. Hellerer, A. M. Enejder, and A. Zumbusch, "Spectral focusing: High spectral resolution spectroscopy with broad-bandwidth laser pulses," *Applied Physics Letters,* vol. 85, no. 1, pp. 25-27, 2004.

[187] D. Zhang, P. Wang, M. N. Slipchenko, D. Ben-Amotz, A. M. Weiner, and J.-X. Cheng, "Quantitative vibrational imaging by hyperspectral stimulated Raman scattering microscopy and multivariate curve resolution analysis," *Analytical Chemistry,* vol. 85, no. 1, pp. 98-106, 2013.

[188] L. Hamm, A. Gee, and A. S. De Silva Indrasekara, "Recent advancement in the surface-enhanced Raman spectroscopy-based biosensors for infectious disease diagnosis," *Applied Sciences,* vol. 9, no. 7, p. 1448, 2019.

[189] S. Mosca, P. Dey, T. A. Tabish, F. Palombo, N. Stone, and P. Matousek, "Determination of inclusion depth in ex vivo animal tissues using surface enhanced deep Raman spectroscopy," *Journal of Biophotonics,* vol. 13, no. 1, p. e201960092, 2020.

[190] M. Pannico, A. Calarco, G. Peluso, and P. Musto, "Functionalized gold nanoparticles as biosensors for monitoring cellular uptake and localization in normal and tumor prostatic cells," *Biosensors,* vol. 8, no. 4, p. 87, 2018.

[191] G. P. Szekeres and J. Kneipp, "SERS probing of proteins in gold nanoparticle agglomerates," *Frontiers in Chemistry,* vol. 7, p. 30, 2019.

[192] S. B. Gunnarsson, K. Bernfur, U. Englund-Johansson, F. Johansson, and T. J. P. o. Cedervall, "Analysis of complexes formed by small gold nanoparticles in low concentration in cell culture media," *PloS One,* vol. 14, no. 6, p. e0218211, 2019.

[193] S. Hong and X. Li, "Optimal size of gold nanoparticles for surface-enhanced Raman spectroscopy under different conditions," *Journal of Nanomaterials,* vol. 2013, 2013.

[194] Y. Li, Q. Wei, F. Ma, X. Li, F. Liu, and M. Zhou, "Surface-enhanced Raman nanoparticles for tumor theranostics applications," *Acta Pharmaceutica Sinica B,* vol. 8, no. 3, pp. 349-359, 2018.

[195] M. V. Rigo, J. Seo, W.-J. Kim, and S. Jung, "Plasmon coupling of R6G-linked gold nanoparticle assemblies for surface-enhanced Raman spectroscopy," *Vibrational Spectroscopy,* vol. 57, no. 2, pp. 315-318, 2011.

[196] K.-Q. Lin *et al.*, "Size effect on SERS of gold nanorods demonstrated via single nanoparticle spectroscopy," *The Journal of Physical Chemistry C,* vol. 120, no. 37, pp. 20806-20813, 2016.

[197] R. E. Darienzo, O. Chen, M. Sullivan, T. Mironava, and R. Tannenbaum, "Au nanoparticles for SERS: Temperature-controlled nanoparticle morphologies and their Raman enhancing properties," *Materials Chemistry and Physics,* vol. 240, p. 122143, 2020.

[198] A. Lombardi *et al.*, "Pulsed molecular optomechanics in plasmonic nanocavities: from nonlinear vibrational instabilities to bond-breaking," *Physical Review X,* vol. 8, no. 1, p. 011016, 2018.

[199] S. Jang *et al.*, "Adsorption of 4-biphenylmethanethiolate on different-sized gold nanoparticle surfaces," *Langmuir,* vol. 20, no. 5, pp. 1922-1927, 2004.

[200] S. R. Emory, W. E. Haskins, and S. Nie, "Direct observation of size-dependent optical enhancement in single metal nanoparticles," *Journal of the American Chemical Society,* vol. 120, no. 31, pp. 8009-8010, 1998.

[201] Y. Gao, N. Yang, T. You, L. Jiang, and P. Yin, "Ultra-thin Au tip structure: a novel SERS substrate for in situ observation of ap-aminothiophenol surface-catalytic reaction," *RSC Advances,* vol. 7, no. 8, pp. 4541-4546, 2017.

[202] C. Hu *et al.*, "Highly narrow nanogap-containing Au@ Au core–shell SERS nanoparticles: size-dependent Raman enhancement and applications in cancer cell imaging," *Nanoscale,* vol. 8, no. 4, pp. 2090-2096, 2016.

[203] S. Harmsen, M. A. Wall, R. Huang, and M. F. Kircher, "Cancer imaging using surface-enhanced resonance Raman scattering nanoparticles," *Nature Protocols,* vol. 12, no. 7, pp. 1400-1414, 2017.

[204] C. Song, P. Wang, and H. A. Makse, "A phase diagram for jammed matter," *Nature,* vol. 453, no. 7195, pp. 629-632, 2008.

[205] M. Faried, K. Suga, Y. Okamoto, K. Shameli, M. Miyake, and H. Umakoshi, "Membrane surface-enhanced Raman spectroscopy for cholesterol-modified lipid systems: effect of gold nanoparticle size," *ACS Omega,* vol. 4, no. 9, pp. 13687-13695, 2019.

[206] Y.-W. Won, A. N. Patel, and D. A. Bull, "Cell surface engineering to enhance mesenchymal stem cell migration toward an SDF-1 gradient," *Biomaterials,* vol. 35, no. 21, pp. 5627-5635, 2014.

[207] E. Yasun *et al.*, "BSA modification to reduce CTAB induced nonspecificity and cytotoxicity of aptamer-conjugated gold nanorods," *Nanoscale,* vol. 7, no. 22, pp. 10240-10248, 2015.

[208] J. G. Nirmala, S. Akila, R. Narendhirakannan, and S. Chatterjee, "Vitis vinifera peel polyphenols stabilized gold nanoparticles induce cytotoxicity and apoptotic cell death in A431 skin cancer cell lines," *Advanced Powder Technology,* vol. 28, no. 4, pp. 1170-1184, 2017.

[209] N. Tiwari, E. R. Osorio-Blanco, A. Sonzogni, D. Esporrín-Ubieto, H. Wang, and M. Calderon, "Nanocarriers for Skin Applications: Where Do We Stand?," *Angewandte Chemie International Edition,* vol. 61, no. 3, p. e202107960, 2022.

[210] D. Schachter, *The source of toxicity in CTAB and CTAB-stabilized gold nanorods*. Rutgers The State University of New Jersey-New Brunswick and University of Medicine and Dentistry of New Jersey, 2013.

[211] A. Siew, H. Le, M. Thiovolet, P. Gellert, A. Schatzlein, and I. Uchegbu, "Enhanced oral absorption of hydrophobic and hydrophilic drugs using quaternary ammonium palmitoyl glycol chitosan nanoparticles," *Molecular Pharmaceutics,* vol. 9, no. 1, pp. 14-28, 2012.

[212] X. Qu *et al.*, "Carbohydrate-based micelle clusters which enhance hydrophobic drug bioavailability by up to 1 order of magnitude," *Biomacromolecules,* vol. 7, no. 12, pp. 3452-3459, 2006.

[213] K. W. Chooi *et al.*, "Physical characterisation and long-term stability studies on quaternary ammonium palmitoyl glycol chitosan (GCPQ)—A new drug delivery polymer," *Journal of Pharmaceutical Sciences,* vol. 103, no. 8, pp. 2296-2306, 2014.

[214] R. D. Mellor, A. G. Schätzlein, and I. F. Uchegbu, "Development of Bio-Functionalized, Raman Responsive, and Potentially Excretable Gold Nanoclusters," *Nanomaterials,* vol. 11, no. 9, p. 2181, 2021.

[215] U. Odunze, "Engineering of Polymeric Nanoparticles Based on Structure-Activity Relationships (SARs) for Oral Drug Delivery," UCL (University College London), 2018.

[216] M. Singh *et al.*, "Application of gold nanorods for photothermal therapy in ex vivo human oesophagogastric adenocarcinoma," *Journal of Biomedical Nanotechnology*, vol. 12, no. 3, pp. 481-490, 2016.
[217] D. S. Chauhan, R. Prasad, J. Devrukhkar, K. Selvaraj, and R. Srivastava, "Disintegrable NIR light triggered gold nanorods supported liposomal nanohybrids for cancer theranostics," *Bioconjugate Chemistry*, vol. 29, no. 5, pp. 1510-1518, 2017.
[218] T. Wang *et al.*, "Stable gold nanorods conjugated liposomal podophyllotoxin nanocomposites for synergistic chemo-photothermal cancer therapy," *Journal of Biomedical Nanotechnology*, vol. 13, no. 11, pp. 1435-1445, 2017.
[219] K. C. Black, J. Yi, J. G. Rivera, D. C. Zelasko-Leon, and P. B. Messersmith, "Polydopamine-enabled surface functionalization of gold nanorods for cancer cell-targeted imaging and photothermal therapy," *Nanomedicine*, vol. 8, no. 1, pp. 17-28, 2013.
[220] Y. Yu *et al.*, "Rattle-type gold nanorods/porous-SiO2 nanocomposites as near-infrared light-activated drug delivery systems for cancer combined chemo–photothermal therapy," *Molecular Pharmaceutics*, vol. 16, no. 5, pp. 1929-1938, 2019.
[221] G. Zhang *et al.*, "Controlling carbon encapsulation of gold nano-aggregates as highly sensitive and spectrally stable SERS tags for live cell imaging," *Journal of Materials Chemistry B*, vol. 1, no. 35, pp. 4364-4369, 2013.
[222] M. Singh, S. Devi, V. S. Rana, B. B. Mishra, J. Kumar, and V. Ahluwalia, "Delivery of phytochemicals by liposome cargos: Recent progress, challenges and opportunities," *Journal of Microencapsulation*, vol. 36, no. 3, pp. 215-235, 2019.
[223] J. Zhang, H. Tang, Z. Liu, and B. Chen, "Effects of major parameters of nanoparticles on their physical and chemical properties and recent application of nanodrug delivery system in targeted chemotherapy," *International Journal of Nanomedicine*, vol. 12, p. 8483, 2017.
[224] T. Chen, S. Chen, J. Zhou, D. Liang, X. Chen, and Y. Huang, "Transient absorption microscopy of gold nanorods as spectrally orthogonal labels in live cells," *Nanoscale*, vol. 6, no. 18, pp. 10536-10539, 2014.